SOME APPLICATIONS OF ENGINEERING MECHANICS IN PRESSURE VESSEL ANALYSIS

PROEFSCHRIFT

TER VERKRIJGING VAN DE GRAAD VAN DOCTOR IN DE TECHNISCHE WETENSCHAPPEN AAN DE TECHNISCHE HOGESCHOOL DELFT, OP GEZAG VAN DE RECTOR MAGNIFICUS IR. H. R. VAN NAUTA LEMKE, HOOGLERAAR IN DE AFDELING DER ELEKTROTECHNIEK, VOOR EEN COMMISSIE UIT DE SENAAT TE VERDEDIGEN OP
WOENSDAG 3 MEI 1972
TE 16.00 UUR

DOOR

DICK HANS VAN CAMPEN

werktuigkundig ingenieur

geboren te Apeldoorn

Dit proefschrift is goedgekeurd door de promotoren
Prof. Ir. D. G. H. Latzko en Prof. Dr. Ir. J. G. Lekkerkerker

Aan mijn ouders
Aan Aatje,
Edgar en Niels

CONTENTS

Page

CHAPTER 1. INTRODUCTION 7

1.1. Motives for the need of pressure vessel analysis. 7
1.2. Foundations of the linear thin shell theory. 9
1.3. Philosophy of the finite element procedure. 12
1.4. Outline of the present thesis. 14

CHAPTER 2. A CONTRIBUTION TO FINITE ELEMENT ANALYSIS 15

2.1. Introduction. 15
2.2. Finite element analysis of solids of revolution under non-axisymmetric loads. 16
2.2.1. Theoretical basis of the method of analysis. 16
2.2.2. The triangular ring element with six nodal points. 18
2.3. The ana-element in the finite element approach. 22
2.3.1. General aspects of the introduction of the ana-element. 22
2.3.2. The infinitely large flat plate with a circular hole under in-plane harmonic loading. 24
2.3.3. The infinitely large flat plate with a circular hole under harmonic loading perpendicular to its plane. 28
2.3.4. The semi-infinite circular cylindrical shell under harmonic loading. 32

CHAPTER 3. ANALYSIS OF LARGE-DIAMETER, HIGH-PRESSURE VESSEL FLANGES 39

3.1. Introduction. 39
3.2. A systematic semi-empirical bolt-tightening procedure. 42
3.2.1. Experimental equipment. 42
3.2.2. Experiments on the interaction among groups of bolts. 43
3.2.3. A systematic tightening procedure. 54
3.2.4. Verification of the tightening procedures. 57
3.3. Deformation of large taper hub flanges. 60
3.3.1. Tapered hub behaviour. 60
3.3.2. Experimental data on flange ring deformation and comparison with numerical results. 71
3.3.2.1. Test results on behaviour of metal-to-metal contact sealing faces and on bolt forces. 71
3.3.2.2. Comparison of numerical and experimental results on flange deformation. 75

CHAPTER 4. ANALYSIS OF NOZZLE-TO-CYLINDER CONNECTIONS FOR SMALL DIAMETER RATIOS 79

4.1. Introduction. 79
4.2. Computational method for the biaxially loaded nozzle-to-flat plate connection. 80
4.3. Generalization for the nozzle-to-cylinder connection. 83
4.3.1. Introductory remarks. 83
4.3.2. Influence coefficients for the reinforced nozzle and cylindrical pipe part. 84
4.3.3. Influence coefficients for the cylindrical vessel. 86
4.3.3.1. Loadings and deformations in Lekkerkerker's notation. 86
4.3.3.2. Adaptation of the boundary loadings. 87
4.3.3.3. Adaptation of the edge deformations. 90
4.3.4. Adaptation of the internal pressure membrane solution. 92
4.3.5. Continuity conditions at the cylindrical vessel juncture. 94

Page

4.4. Evaluation by comparison with experimental results. 97
4.4.1. Description of test arrangement. 97
4.4.2. Comparison of experimental and numerical model vessel and flat plate results. 103
4.4.2.1. Introductory remarks. 103
4.4.2.2. Discussion of the results for the flat plate nozzles. 110
4.4.2.3. Discussion of the results for the model vessel nozzles. 110
4.4.2.4. Comparison of experimental model vessel and flat plate results. 111
4.4.3. Comparison of various boundary conditions in the computational method for the nozzle-to-cylinder connection. 112

APPENDICES

Appendix 1. Compatibility conditions at the intersection between a shell element and other finite elements. 122
Appendix 2. Formulae for the integral expressions R(p,q). 124
Appendix 3. Summary of governing equations for circular cylindrical shells. 126
Appendix 4. Influence coefficients for the tapered hub considered as an assemblage of TRIAX 6 elements. 128
Appendix 5. Determination of relative gasket face rotations from sensing pin displacements. 134
Appendix 6. Summary of Lekkerkerker's shallow thin shell theory method. 136

REFERENCES

References Chapter 1. 142
References Chapter 2. 144
References Chapter 3. 145
References Chapter 4. 146
References Appendices. 149

ACKNOWLEDGEMENTS 150

SAMENVATTING 151

1.1. Motives for the need of pressure vessel analysis.

Once the shape, overall dimensions and service loads for a pressure vessel have been determined by the process requirements, the traditional method for its further mechanical design is characterized by the existence of Design Codes such as the "Grondslagen waarop de beoordeling van de constructie en het materiaal van stoomtoestellen, damptoestellen en drukhouders berust" (Principles for the assessment of the construction and of the materials used in the construction of boilers and pressure vessels) [1.1] in The Netherlands and Division 1 of Section VIII (Pressure Vessels) of the ASME Boiler and Pressure Vessel Code [1.2] in the U.S.A. The traditional Codes have two main limitations:

a. They only take into account the so-called primary stresses, which are in equilibrium with the external loadings and do not vary across the vessel thickness. Additional bending stresses and stress concentrations are allowed for in so-called safety factors, which are based on previous experience and therefore often are ignorance factors. These factors enlarge the thickness which does not always lead to an economic and more safe design. For instance for nuclear pressure vessels we have
   - enlarging of thermal stresses due to increasing of neutron and γ-absorption
   - raised chance of inhomogeneities and local defects (wall thickness P(ressurized)W(ater)R(eactor) vessels 200-300 mm, steam generator tube plates up to about 650 mm).

b. They do not account for low-cycle fatigue failure. This type of fatigue, with local plastic deformation at each loading cycle, may lead to an unsafe design under certain operating conditions such as rapid changes in temperature or pressure. For instance for nuclear pressure vessels we have
   - loading dependent variations of thermal stresses due to neutron and γ-absorption
   - danger for fast growth of fatigue cracks due to embrittlement of the vessel wall by fast neutron radiation.

For nuclear pressure vessels the above considerations have led to the following ideas, formalized originally in the 1963 edition of Section III (Nuclear Vessels) of the ASME Boiler and Pressure Vessel Code [1.3]:

a. Classification of the stresses in stress categories, i.e. primary, secondary and peak stresses, depending on their effect on the structure

b. Applying of different stress limits to the stresses of the different categories, depending on the relevant mode of failure, such as
   - plastic instability
   - incremental collapse
   - low-cycle fatigue ★)

A more detailed explanation of the philosophy underlying [1.3] can be found in [1.4].

★) *[1.3] does not provide a design criterion for another important mode of failure, i.e. brittle fracture.*

The design of pressure vessels in accordance with this philosophy requires

- detailed information about the stresses in each category under all possible operating conditions
- experimentally verified knowledge about the effect of each stress type on the integrity of the structure.

This second requirement constitutes a tremendous challenge to the metallurgist and as yet requires continuing investigations on to the mechanisms of creep, low-cycle fatigue and brittle fracture, together with their interactions.
The present thesis restricts itself to contributing to the first requirement, resulting in a detailed stress analysis.
The financial consequences of designing on the basis of the above philosophy and of utilizing the results of a detailed stress analysis are illustrated in figure 1.1.1 (the dimensions in this figure have been extracted from figure 2 of [1.5]) for a B(oiling)W(ater)R(eactor) and a PWR vessel.

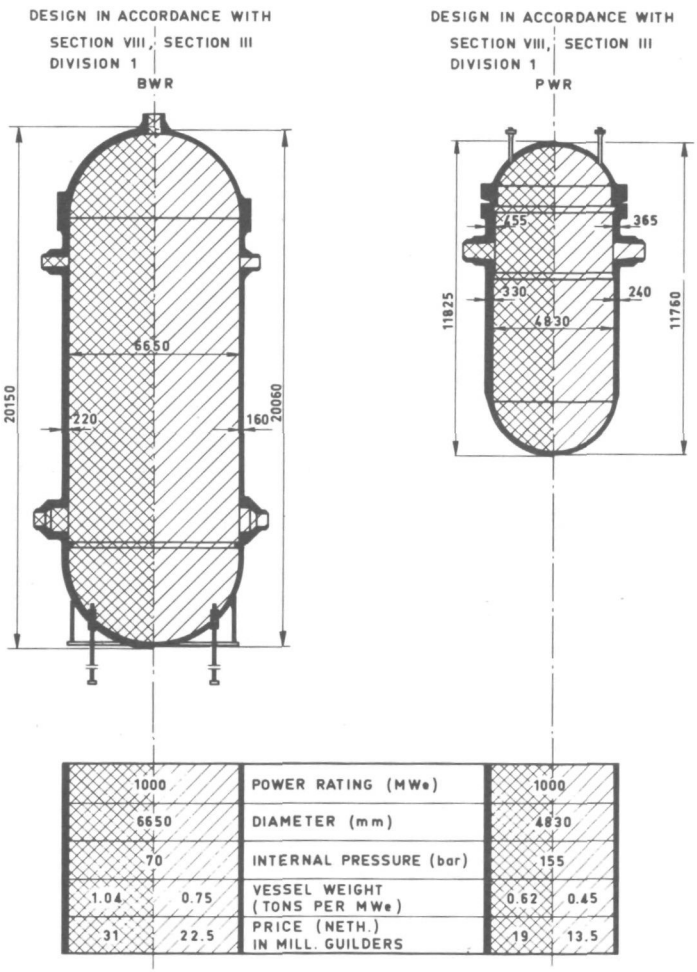

FIGURE 1.1.1.

Comparison between traditional and progressive pressure vessel design.

From this figure the most important areas for stress and deformation analysis can be seen to be the flange connection, the nozzles attached to the cylindrical vessel, the nozzles attached to the spherical head or bottom and the skirt transition. The first two areas of these are of major importance, the former because of the extremely stringent leak-tightness requirements and the latter because it includes the region of highest stresses.

Recognizing the importance of the above safety and financial considerations the ASME in 1968 introduced Division 2 of Section VIII of the ASME Boiler and Pressure Vessel Code [1.6], providing alternative rules for the design of conventional pressure vessels. In fact, these rules constitute the same philosophy as established in [1.3] for nuclear pressure vessels.

The requirements for detailed stress and deformation analysis of pressure vessels defined in [1.3] or [1.6] are so far ★) limited to the elastic range.

★) *In the case of low-cycle fatigue this is done by "converting" plastic strains to (imaginary) stresses by multiplying by Young's modulus. The 1971 edition of [1.3] permits the use of limit analysis for demonstrating the adequacy of nozzle reinforcements.*

Such analyses are usually carried out through one or two of the following basic concepts

- linear thin shell theory analysis
- finite element analysis.

The analysis on the basis of linear thin shell theory has now become sufficiently well established to be generally accepted. Its physical justification can be found in the fact that the vast majority of pressure vessels contain parts, where the ratio of the wall thickness to smallest middle surface radius of curvature does not exceed (say) 1/10. However, its utilization in design practice is mostly restricted to the case of axisymmetric shells under axisymmetric loadings. Although, as indicated by the formulas established in the Appendices of [1.3] and [1.6] and by the analyses of pressure vessel components presented e.g. in [1.7], this case covers an important number of practical problems, it excludes for example the nozzle attached to a cylindrical shell which is known to include the region of highest stresses in a pressure vessel. In the present thesis the thin shell theory concept has been utilized for the analysis of this non-axisymmetric connection. It should be noticed already in this stage that any thin shell theory remains essentially incapable of giving information about peak stresses. For this purpose the finite element concept has been incorporated into the treatment of the non-axisymmetric case given in the present thesis.
As the application of both the thin shell theory and the finite element concept requires basic knowledge about their foundations, these are summarized in the next two sections. The last section of this chapter reviews the scope of the present thesis.

1.2. Foundations of the linear thin shell theory.

In its essence the use of a thin shell theory implies the simplification of a three-dimensional problem to a two-dimensional problem by considering the behaviour of the middle surface to be representative for the behaviour of the three-dimensional shell. Mention should be made at this point of the analogy with the theory of beams, where the behaviour of the axis is considered to be representative for the behaviour of the three-dimensional beam. Thus any thin shell theory is necessarily of an approximate character.
In order to realize the simplification just mentioned, the three-dimensional concepts strain and stress are replaced respectively by the two-dimensional concepts middle surface strain and change of curvature on the one hand and stress resultant (force) and stress couple (moment) on the other hand.

A first step in the study of the theory of shells usually consists of the investigation of the geometrical properties of the *deformations of shells*. For pressure vessel analysis this implies expressing the functional relationships between the (generally three) middle surface strains and the (generally three) middle surface changes of curvature on the one hand and the (generally three) middle surface displacements on the other hand. The only assumption made in this step is that the displacements and their derivatives are small everywhere in the shell (linear theory).

As usual in the theory of elasticity, the analysis of the deformations of shells is followed by that of the corresponding stresses, resulting in the *equations of equilibrium* and the *dynamic boundary conditions*. The classical equations of equilibrium, as formulated by LOVE [1.8, Chapter XXIV, Article 331], are six in number, viz. three force equations and three moment equations, and involve ten unknowns, viz. two membrane normal forces, two membrane shear forces, two transverse shear forces, two bending moments and two twisting moments. On the basis of the work done by GOL'DENVEIZER [1.9] and LUR'E [1.10], it was pointed out by NOVOZHILOV [1.11, Chapter I, par. 8]

that these six equations in ten unknowns may be reduced to a system of three equations involving no more than six unknowns, viz. two membrane normal forces, one modified shear force, two bending moments and one modified torsional moment (half the sum of the two original twisting moments). It becomes clear from this reduction that the difference between the two original twisting moments does not appear in the modified equilibrium equations. The physical explanation for this remarkable reduction has been given by Koiter [1.12] and originates in the principle of virtual work. It may be concluded from this explanation that the equations of equilibrium do not involve any approximation.

The study of the state of stress in thin shells has to be completed with the dynamic boundary conditions to which the forces and moments are subjected. Starting from the original system of ten stress resultants and stress couples, introduced before, one would think that the number of dynamic boundary conditions must be equal to five. However, the number of independent kinematic boundary quantities to be prescribed along an edge curve in the middle surface is equal to four, viz. three edge displacements and the rotation around the edge curve. Hence the principle of virtual work yields four independent so-called natural dynamic boundary conditions, completely determining the solution for the stresses in a shell. This controversy has been resolved by KELVIN and TAIT [1.13] for the special case of thin plate theory, replacing the twisting couple and transverse shear force distributions along a plate edge by a statically equivalent distribution of reduced transverse shear forces. A similar argument has been applied in the theory of thin shells (see e.g. [1.8, Chapter XXIV, Article 332] and [1.11, Chapter I, par. 11]). It involves an appeal to St.-Venant's principle and assumes that the replacement of the original edge loads by statically equivalent loads has a negligible effect on the stress distribution in the interior of the shell at a distance from the edges equal to at most a few times the shell thickness. Thus the reduced dynamic boundary conditions appear to have an approximative character. However, by introducing the modified membrane shear force and the modified torsional moment, mentioned in the discussion of the equilibrium equations, KOITER [1.14] proved that appropriately formulated reduced dynamic boundary conditions are rigorously valid. Again it turns out that the difference between the two original internal twisting moments does not appear in the reduced dynamic boundary conditions.

The previous discussion of the compatibility conditions for the middle surface strains and changes of curvature and of the equations of equilibrium and the boundary conditions for the stress resultants and stress couples did not include any approximation, except for the assumption that the displacements and their derivatives are small everywhere in the shell. The approximate nature of shell theory enters the picture at the final and critical stage, where the *constitutive relations* are introduced between the stress resultants and stress couples on the one hand and the middle surface strains and curvatures on the other hand.
In classical thin shell theory these relations are derived on the basis of the well-known Kirchhoff-Love assumptions:

a. The effect of the normal stress on surfaces parallel to the middle surface may be neglected in the stress-strain relations.

b. Points which lie on one and the same normal to the undeformed middle surface also lie on one and the same normal to the deformed middle surface.

c. The displacements in the direction of the normal to the middle surface are equal for all points on the same normal.

For homogeneous and isotropic materials obeying Hooke's law, the Kirchhoff-Love hypotheses are mutually contradictory, as Poisson's ratio implies a

strain in the direction normal to the shell middle surface under the neglection of the normal stress on surfaces parallel to the middle surface in the stress-strain relations.
Considerable progress with regard to this inconsistency of the classical thin shell theory foundations was achieved by KOITER [1.15, 1.16] by replacing the Kirchhoff-Love hypotheses by the *single* assumption of an approximately plane state of stress parallel to the middle surface. After rigorous elaborations he showed that the elastic energy on the basis of this assumption may always be approximated by Love's so-called first approximation [1.8, Chapter XXIV, Article 329, equation (38)], as the sum of stretching or extensional energy and bending or flexural energy, and that no refinement of this first approximation is justified, if the basic Kirchhoff-Love assumptions are retained. The relative error of this approximation (i.e. the error, as compared with the energy on the basis of the plane stress assumption) is of order h/R or h^2/L^2 (whichever may be critical), where h is the wall thickness of the shell, R the minimum principal radius of curvature, and L the wave length of the deformation pattern *). Moreover it was shown that the bending energy may be modified, without loss in accuracy of the approximation, by adding terms of order ε/R to the measures for the changes of curvature, where ε is a middle surface strain. Thus it appeared in [1.15, 1.16] that most of the different expressions for the changes of curvature occurring in literature are equivalent. An inherent inadequacy of the foregoing thin shell theory foundations is that no information is obtained on the actual magnitude of the errors. In this respect major progress was achieved by JOHN [1.17] and KOITER [1.18].
It may be concluded from their analyses that the relative error in Love's approximate decomposition of elastic energy (i.e. the error, as compared with the energy for the three-dimensional shell) is of order h/R or h^2/L^2. Moreover the analysis given in [1.18] enables one to make precise error estimates once the two-dimensional (approximate) shell solution is available.

The system of partial differential equations resulting for the general linear theory of thin elastic shells within the basic assumptions discussed above appears to be of eighth-order and is extremely complicated. Some simplification is obviously desirable for application to a particular problem and a wide variety of shell theories with a more or less approximate character are known from literature. A systematic classification of possible simplifications of the general field equations has been given in [1.19]. The two important parameters in this simplification process are shown to be $h\kappa/\varepsilon$ and L^2/hR, where κ is the maximum (absolute) curvature and ε the maximum (absolute) middle surface strain.
One of the best known versions of simplified shell equations is referred to as shallow shell theory and is utilized in Chapter 4 of the present thesis. Although it is very difficult to estimate a priori the errors due to the simplifying assumptions made during the presentations of this theory in

---

*) *The wave length L is defined by*

$$\left|\frac{d\varepsilon}{ds}\right| = O\left[\frac{\varepsilon}{L}\right] \quad ; \quad \left|\frac{d\kappa}{ds}\right| = O\left[\frac{\kappa}{L}\right]$$

where ε is a middle surface strain and κ a middle surface change of curvature, while ds denotes the arc element along any curve on the middle surface and the symbol O [..] denotes the order of magnitude.

literature *), it seems justified to conclude from [1.19] that the applicability of shallow shell theory is restricted to the following order of magnitude of the two parameters mentioned above.

$$\frac{h\kappa}{\varepsilon} = 0\ [1] \qquad \frac{L^2}{hR} = 0\ [1]$$

In view of the basic assumptions underlying the thin shell theory it may be concluded from the order of magnitude of the second parameter that the wave length L of the deformation pattern has to be small compared with the minimum principal radius of curvature R.

1.3. Philosophy of the finite element procedure.

Essentially the finite element method can be considered as a generalization of standard structural analysis procedures. It permits a detailed stress and deflection analysis in two- and three-dimensional structures, such as pressure vessels, by the same techniques which are applied in the analysis of ordinary framed structures.
The method, having originally been developed in the aerospace industry, in response to the need for a procedure providing refined solutions for extremely complex airframe configurations [1.20, 1.21], has now a fast broadening field of non-aeronautical applications (such as the nuclear one), particularly thanks to the availability of powerful automatic digital computer facilities.

The basic concept of the finite element method is that every structure may be considered to be an assemblage of individual structural components or elements. The mathematical model which describes the real construction consits of a finite number of such elements, interconnected at a finite number of joints or nodal points. In the matrix displacement method, to which the present thesis is restricted, the displacements of these nodal points will be the basic unknown parameters of the problem.
The finite element analysis of a structure may be divided into four phases: structural idealization, evaluation of element properties, structural analysis of the element assemblage, and interpretation (presentation) of the results. The structural idealization being merely the subdivision of the original system into an assemblage of discrete elements the evaluation of the element properties forms the critical phase of the analysis. Since the elements are assumed to be interconnected only at a limited number of nodal points the essential characteristics of an element are represented by the relationship between a system of forces concentrated at the nodes and their resulting deflections. In the matrix displacement method (also called direct stiffness method) this force-deflection relationship may be expressed most conveniently by the stiffness matrix of the element. A more general basis for the development of the element properties can be found in the virtual work equation or in the principle of minimum potential energy: for a prescribed set of displacements and strains the equilibrium conditions are satisfied when the values of these displacements are such that the total potential energy reaches its minimum value.

Once the element properties have been defined, the stress and deflection analysis of the element assemblage resulting from any given loading

---

*) *A general treatment of shallow shell theory is given among others by NOVOZHILOV [1.11, Chapter I, par. 17a].*

condition is a standard structural problem, which for a displacement method analysis consists of the following basic operations [1.22]:

1. Evaluation of the stiffness properties of the individual elements, expressed in any convenient local (element) co-ordinate system.
2. Transformation of the element stiffness matrix from the local co-ordinate system to a form relating to the global co-ordinate system of the complete structural assemblage by means of transformation of the nodal displacements.
3. Superposition of the individual element stiffnesses contributing to each nodal point to obtain the total assemblage nodal stiffness matrix.
4. Formulation and solution of the "equilibrium equations" resulting from the virtual work equation.
5. Evaluation of the element deformations from the computed nodal displacements by kinematic relationships.
6. Determination of element stresses by means of the stress-strain relations.
7. Interpretation of the results. This includes presentation in an appropriate form.

A comprehensive discussion of the analogy between the matrix equations representing the finite element method and the field equations of continuum mechanics by BESSELING [1.23], demonstrates that the finite element equations are the complete equivalent in finite form of the standard equations of elasticity. In order that the finite element idealization may provide a reasonable representation of the actual continuum each element must be required to deform similarly to the deformations developed in the corresponding region of the continuum. This objective may be accomplished most conveniently by prescribing the deformation patterns which may develop within each finite element by means of functions defining uniquely the state of displacement in terms of its nodal point displacements. Thus the basic and critical operation in the definition of an element stiffness matrix is the choice of the displacement functions.
To ensure convergence of the finite element solution to the solution of the continuum field equations the following restrictions may be imposed [1.24]:

1. The deformation characteristics chosen should be such that straining of an element is excluded when the nodal displacements are caused by rigid body displacements.
2. The deformation characteristics should include all uniform strain states to obtain meaningful solutions for the case of nearly constant strain conditions which will occur as the elements get smaller.
3. To ensure compatibility between two elements, the displacements at their interconnecting boundary should be uniquely determined by their values at the nodal points along this boundary.

The first two conditions, referred to in literature as the *completeness requirements* for the displacements, are necessary for convergence to the true state of strain, while the third criterion, mentioned in literature as the *conformity requirement*, is a sufficient condition for this convergence.

1.4. Outline of the present thesis.

The primary scope of the present thesis is to contribute to the elastic analysis of two important pressure vessel components, i.e. the flange connection and the nozzle-to-cylindrical vessel connection.
In order to realize this purpose Chapter 2 presents a twofold contribution to the finite element analysis. Firstly, a triangular ring element with six nodal points is developed for finite element analysis of solids of revolution under non-axisymmetric loads (Chapter 2.2). Secondly, the so-called ana-element concept is introduced so as to incorporate parts of the structure, whose equations of elasticity have a known analytical solution, into the finite element approach (Chapter 2.3). This concept is applied to a number of plate and shell elements of interest in pressure vessel analysis.

The contribution on the analysis of flanges presented in Chapter 3, concentrates on large-diameter, high-pressure vessel flanges. Firstly, the development is described of a systematic semi-empirical groupwise bolt-tightening procedure for obtaining a bolt load distribution as uniform as possible in a single loading cycle (Chapter 3.2).
Secondly, a comparison between two alternative computational methods for tapered hub behaviour is offered using a finite element analysis for reference (Chapter 3.3.1). These methods consider the tapered hub either as a thin cylindrical shell with varying wall thickness or as a ring with undeformable radial cross section. An improved version of the existing thin shell approaches is presented for large values of the taper angle; in addition the influence coefficients for the finite element approach are given in graphical form.
Finally, some experimental information is presented pertinent to the problem of determining the exact location of the point of application of the gasket face reaction (Chapter 3.3.2.1), while, on the basis of this information, an experimental check is given on the validity of the most accurate method for predicting tapered hub behaviour in flange analysis, considering the hub as assemblage of finite elements (Chapter 3.3.2.2).

As regards the nozzle-to-cylindrical vessel connection the present thesis investigates the potential of the flat plate analogy as a first step for analysis of this intersection at nozzle-to-cylinder diameter ratios not exceeding $\sim 1/4$ (Chapter 4.2). This analogy enables to treat the problem as a solid of revolution under non-axisymmetric loading.
Moreover, a generalization of this approach is offered for the nozzle-to-cylindrical vessel problem, which still treats the nozzle itself as geometrically axisymmetric, but considers the cylindrical vessel as a shallow circular cylindrical shell with a circular cutout (Chapter 4.3).
Finally, the two methods (nozzle-to-flat plate and nozzle-to-cylindrical vessel) are compared with each other and the reliability of both is evaluated by comparison with experimental evidence (Chapter 4.4).

2.1. Introduction.

Historically speaking, the first types of structural elements for the matrix displacement method were based upon very simple displacement patterns with a linearly varying displacement distribution [1.21]. These primitive elements are however being superseded by more sophisticated elements, which nevertheless satisfy, in general, the basic requirements of the displacement method mentioned in Chapter 1.3.
In nearly all these elements *assumed* displacement modes form the basis for the evaluation of the stiffness matrix. However, a considerable number of practical structures, particularly in pressure vessel technology, contain parts where the solution of the elasticity equations is known to have a special character (e.g. ring elements under non-axisymmetric loads) or may even be completely known (e.g. plates and shells). In these cases a more efficient use of computing time and of computer memory may be made by utilizing this special character of the solution during the evaluation of the element stiffness matrix in stead of using elements with an arbitrarily assumed displacement distribution.

The case of solids of revolution under non-axisymmetric loads covers for example the nozzle-to-spherical vessel connection under moment or shear force loading and also the biaxially loaded nozzle-to-flat plate connection as a first approximation of the pressurized nozzle-to-cylindrical vessel connection, which is one of the subjects of the present thesis (cf. Chapter 4). Section 2.2 of the present chapter contributes to the analysis of this type of structure by developing a triangular ring element with six nodal points and a harmonic displacement distribution varying quadratically within the element cross section.

The application of finite elements whose stiffness matrices can be obtained from known analytical solutions of the elasticity equations to pressure vessel analysis may cover for instance the thin-walled vessel and pipe regions adjacent to reinforced nozzle attachments and also the flange ring of large-diameter, high-pressure vessel flanges, if this is considered as a ring with undeformable radial cross section (cf. Chapter 3.3). Some general consequences of the introduction of the so-called ana-element concept in the finite element approach are discussed in Sub-section 2.3.1 of this chapter, while the stiffness matrices for a number of plate and shell elements of interest in pressure vessel analysis are derived in the Sub-sections 2.3.2 through 2.3.4.

In solving structural problems - such as the above-mentioned reinforced nozzle-to-vessel connection - by means of combinations of shell (ana-) elements and two- or three-dimensional finite elements, the deformation patterns of the former elements meet the Kirchhoff-Love assumptions underlying linear thin shell theory (cf. Chapter 1.2). One of the consequences of these assumptions in the continuous theory is that we have ultimately four independant kinematic boundary conditions along an arbitrary edge curve in the middle surface (three edge displacements and the rotation of the normal to the middle surface around the edge curve). These conditions, which also have to be met for shell elements in the finite element approach, result in a linear distribution of the edge displacements about the wall thickness and thereby form the basis for the compatibility conditions at the intersection between a shell element and other finite elements. Some general formulae resulting from these compatibility conditions are given in Appendix 1.

2.2. Finite element analysis of solids of revolution under non-axisymmetric loads.

2.2.1. Theoretical basis of the method of analysis.

In the finite element approximation of axisymmetric solids under axisymmetric loads, the continuous structure is known to be replaced by a system of axisymmetrically loaded ring elements, which are interconnected at circumferential joints or nodal circles.
The general outline for the finite element analysis of axisymmetric structures under non-axisymmetric loads has been given by WILSON [2.1]. This method, which will be summarized in this subsection more systematically, is also based upon the replacement of the structure by a system of ring elements, but involves expansion of the nodal circle displacements and of the temperature distribution in Fourier's series.

Denoting the co-ordinate and displacement notations as shown in figure 2.2.1, z being the symmetry axis, the strain displacement relations become (see e.g. [1.8], p. 56)

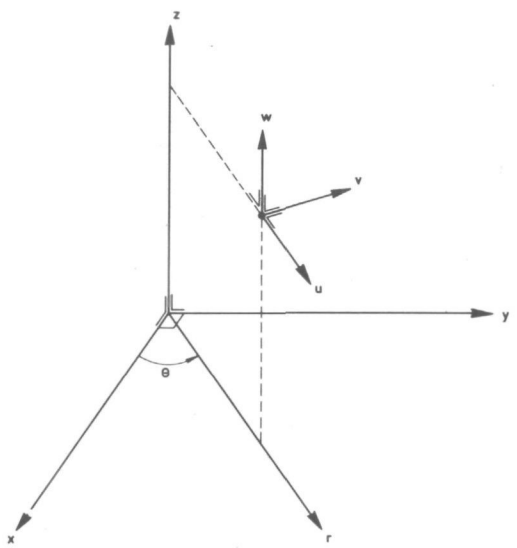

$$
\begin{aligned}
\varepsilon_r &= \frac{\partial u}{\partial r} \\
\varepsilon_\theta &= \frac{1}{r}\left[u + \frac{\partial v}{\partial \theta}\right] \\
\varepsilon_z &= \frac{\partial w}{\partial z} \\
\gamma_{r\theta} &= \frac{1}{r}\frac{\partial u}{\partial \theta} + \frac{\partial v}{\partial r} - \frac{v}{r} \\
\gamma_{\theta z} &= \frac{\partial v}{\partial z} + \frac{1}{r}\frac{\partial w}{\partial \theta} \\
\gamma_{rz} &= \frac{\partial u}{\partial z} + \frac{\partial w}{\partial r}
\end{aligned}
\qquad (2.2.1)
$$

FIGURE 2.2.1.

General co-ordinate and displacement notations.

LOVE ([1.8], p. 102) derived a general expression for the elastic energy of homogeneous isotropic solids for the case of mechanical loadings. In polar co-ordinates and including thermal loadings, this expression has the following form *)

*) *Throughout the whole thesis E denotes Young's modulus, while ν denotes Poisson's ratio.*

$$E_{el} = \tfrac{1}{2} \int_r \int_{\theta=0}^{\theta=2\pi} \int_z \left\{ \frac{E}{2(1+\nu)} \left[\frac{2(1-\nu)}{1-2\nu} (\varepsilon_r^2+\varepsilon_\theta^2+\varepsilon_z^2) + \frac{4\nu}{1-2\nu} (\varepsilon_r\varepsilon_\theta+\varepsilon_\theta\varepsilon_z+\varepsilon_z\varepsilon_r) + \right. \right. \tag{2.2.2}$$

$$\left. \left. + \gamma_{r\theta}^2+\gamma_{\theta z}^2+\gamma_{rz}^2 \right] - \frac{2E}{1-2\nu} \lambda T(\varepsilon_r+\varepsilon_\theta+\varepsilon_z) + \frac{3E}{1-2\nu} [\lambda T]^2 \right\} dr\, rd\theta\, dz$$

T being the difference between the temperature which is a function of the co-ordinates and a reference temperature. The Fourier's series expansions for the displacements and for the temperature distribution are supposed to describe the case of loads, which are symmetric about the x-z plane (θ=0)

$$u = \sum_{n=0}^{\infty} u_n \cos n\theta \qquad v = \sum_{n=1}^{\infty} v_n \sin n\theta \qquad w = \sum_{n=0}^{\infty} w_n \cos n\theta \tag{2.2.3}$$

$$T = \sum_{n=0}^{\infty} T_n \cos n\theta \tag{2.2.4}$$

where u_n, v_n, w_n and T_n are functions of r and z only. The strains corresponding to these displacements are

$$\varepsilon_r = \sum_{n=0}^{\infty} \varepsilon_{rn} \cos n\theta \qquad \varepsilon_\theta = \sum_{n=0}^{\infty} \varepsilon_{\theta n} \cos n\theta \qquad \varepsilon_z = \sum_{n=0}^{\infty} \varepsilon_{zn} \cos n\theta \tag{2.2.5}$$

$$\gamma_{r\theta} = \sum_{n=1}^{\infty} \gamma_{r\theta n} \sin n\theta \qquad \gamma_{\theta z} = \sum_{n=1}^{\infty} \gamma_{\theta zn} \sin n\theta \qquad \gamma_{rz} = \sum_{n=0}^{\infty} \gamma_{rzn} \cos n\theta$$

where

$$\varepsilon_{rn} = \frac{\partial u_n}{\partial r} \qquad \varepsilon_{\theta n} = \frac{1}{r} [u_n+nv_n] \qquad \varepsilon_{zn} = \frac{\partial w_n}{\partial z} \tag{2.2.6}$$

$$\gamma_{r\theta n} = -\frac{1}{r} [nu_n+v_n] + \frac{\partial v_n}{\partial r} \qquad \gamma_{\theta zn} = \frac{\partial v_n}{\partial z} - \frac{1}{r} nw_n \qquad \gamma_{rnz} = \frac{\partial u_n}{\partial z} + \frac{\partial w_n}{\partial r}$$

Substituting from (2.2.4) and (2.2.5) into (2.2.2) and making use of the orthogonality, properties of the harmonic functions

$$\int_0^{2\pi} \cos n\theta \cos k\theta\, d\theta = \begin{cases} 2\pi \text{ if } n = k = 0 \\ \pi \text{ if } n = k \neq 0 \\ 0 \text{ if } n \neq k \neq 0 \end{cases}$$

$$\int_0^{2\pi} \sin n\theta \sin k\theta\, d\theta = \begin{cases} \pi \text{ if } n = k \neq 0 \\ 0 \begin{cases} \text{if } n \neq k \\ \text{if } n = k = 0 \end{cases} \end{cases}$$

leads to the following matrix expression for E_{el}

$$E_{el} = \pi \int_r \int_z (\bar{\varepsilon}'_0 - \bar{\varepsilon}'_{T0}) G (\bar{\varepsilon}_0 - \bar{\varepsilon}_{T0}) r \, dr \, dz +$$

$$+ \frac{\pi}{2} \sum_{n=1}^{\infty} \int_r \int_z (\bar{\varepsilon}'_n - \bar{\varepsilon}'_{Tn}) G (\bar{\varepsilon}_n - \bar{\varepsilon}_{Tn}) r \, dr \, dz \qquad (2.2.7)$$

where

$$\bar{\varepsilon}_0 = \begin{bmatrix} \varepsilon_{r0} \\ \varepsilon_{\theta 0} \\ \varepsilon_{z0} \\ 0 \\ 0 \\ \gamma_{rz0} \end{bmatrix} \qquad \bar{\varepsilon}_n = \begin{bmatrix} \varepsilon_{rn} \\ \varepsilon_{\theta n} \\ \varepsilon_{zn} \\ \gamma_{r\theta n} \\ \gamma_{\theta zn} \\ \gamma_{rzn} \end{bmatrix} \text{, if } n \neq 0 \qquad \bar{\varepsilon}_{Tn} = \begin{bmatrix} \lambda T_n \\ \lambda T_n \\ \lambda T_n \\ 0 \\ 0 \\ 0 \end{bmatrix} \qquad (2.2.8)$$

while G is the matrix of elastic coefficients

$$G = \frac{E}{2(1+\nu)} \begin{bmatrix} e_1 & e_2 & e_2 & 0 & 0 & 0 \\ e_2 & e_1 & e_2 & 0 & 0 & 0 \\ e_2 & e_2 & e_1 & 0 & 0 & 0 \\ 0 & 0 & 0 & 1 & 0 & 0 \\ 0 & 0 & 0 & 0 & 1 & 0 \\ 0 & 0 & 0 & 0 & 0 & 1 \end{bmatrix} \quad \text{with} \left\{ \begin{array}{l} e_1 = \dfrac{2(1-\nu)}{1-2\nu} \\ \\ e_2 = \dfrac{2\nu}{1-2\nu} \end{array} \right\} \qquad (2.2.9)$$

It thus follows from expression (2.2.7) that the three-dimensional analysis is divided into a series of uncoupled two-dimensional analyses in which the displacement amplitudes u_n, v_n and w_n are the unknowns.
Once the choice of the displacement functions has been made, expression (2.2.7) can be used as a starting point for the development of the element stiffness matrix.

2.2.2. The triangular ring element with six nodal points.

For bodies of revolution under axisymmetric loading the TRIAX 6 element developed by ARGYRIS [2.2] has been applied extensively and proven reliable and economic. This ring element has a triangular cross section with six nodal points, describing a fully quadratic displacement distribution within the element.
A generalization of the TRIAX 6 element to the case of harmonic loadings has been developed simultaneously and independently by BUCK [2.3] and by the author [2.4]. This generalization will be described now.

Starting from solution (2.2.3) for the displacements the following quadratic expressions for u_n, v_n and w_n describe a displacement distribution that meets the conformity requirement (cf. Chapter 1.3) in a triangular ring element with six nodal points (cf. figure 2.2.2)

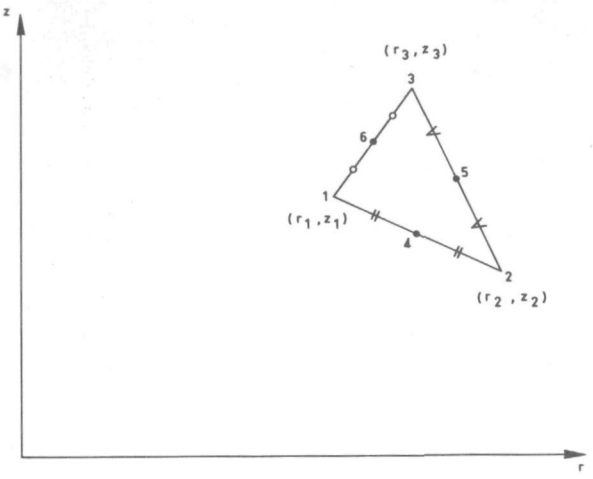

FIGURE 2.2.2.

Cross-section triangular ring element with six nodal points.

$$u_n = A_{n1} + A_{n2}r + A_{n3}z + A_{n4}r^2 + A_{n5}rz + A_{n6}z^2$$

$$v_n = B_{n1} + B_{n2}r + B_{n3}z + B_{n4}r^2 + B_{n5}rz + B_{n6}z^2 \qquad (2.2.10)$$

$$w_n = C_{n1} + C_{n2}r + C_{n3}z + C_{n4}r^2 + C_{n5}rz + C_{n6}z^2$$

where A_{nk}, B_{nk} and C_{nk} (k=1, 2, ..., 6) are constants, while for n=0, B_{nk}=0. Substitution from (2.2.10) into (2.2.6) and introduction of the vector *)

$$\bar{a}_n' = \begin{vmatrix} A_{n1} & A_{n2} & A_{n3} & A_{n4} & A_{n5} & A_{n6} & & & & & & \\ & & & & & & B_{n1} & B_{n2} & B_{n3} & B_{n4} & B_{n5} & B_{n6} \\ & & & & & & C_{n1} & C_{n2} & C_{n3} & C_{n4} & C_{n5} & C_{n6} \end{vmatrix} \qquad (2.2.11)$$

leads to the following matrix relation

$$\bar{\varepsilon}_n = C_n \bar{a}_n \qquad (2.2.12)$$

where the (6 x 18) matrix C_n has been defined in table 2.2.1.

$$\bar{a}_n' = \begin{vmatrix} A_{n1} & A_{n2} & A_{n3} & A_{n4} & A_{n5} & A_{n6} & B_{n1} & B_{n2} & B_{n3} & B_{n4} & B_{n5} & B_{n6} & C_{n1} & C_{n2} & C_{n3} & C_{n4} & C_{n5} & C_{n6} \end{vmatrix}$$

$$C_n = \begin{bmatrix} 0 & 1 & 0 & 2r & z & 0 & 0 & 0 & 0 & 0 & 0 & 0 & 0 & 0 & 0 & 0 & 0 & 0 \\ \frac{1}{r} & 1 & \frac{z}{r} & r & z & \frac{z^2}{r} & \frac{n}{r} & n & \frac{nz}{r} & nr & nz & \frac{nz^2}{r} & 0 & 0 & 0 & 0 & 0 & 0 \\ 0 & 0 & 0 & 0 & 0 & 0 & 0 & 0 & 0 & 0 & 0 & 0 & 0 & 0 & 1 & 0 & r & 2z \\ -\frac{n}{r} & -n & -\frac{nz}{r} & -nr & -nz & -\frac{nz^2}{r} & -\frac{1}{r} & 0 & -\frac{z}{r} & r & 0 & -\frac{z^2}{r} & 0 & 0 & 0 & 0 & 0 & 0 \\ 0 & 0 & 0 & 0 & 0 & 0 & 0 & 0 & 1 & 0 & r & 2z & -\frac{n}{r} & -n & -\frac{nz}{r} & -nr & -nz & -\frac{nz^2}{r} \\ 0 & 0 & 1 & 0 & r & 2z & 0 & 0 & 0 & 0 & 0 & 0 & 0 & 1 & 0 & 2r & z & 0 \end{bmatrix}$$

TABLE 2.2.1.

The C_n matrix.

*) *The transposed vector of $\bar{a}_n$ will be denoted by $\bar{a}_n'$. The introduction of transposed vectors is only a matter of convenience.*

$H_n = \frac{E}{2(1+\nu)}$

$\frac{1}{a_n}$ =	A_{n1}	A_{n2}	A_{n3}	A_{n4}	A_{n5}	A_{n6}	B_{n1}	B_{n2}	B_{n3}
	$[e_1 + n^2]R(-2,0)$								
	$[e_1 + e_2 + n^2]R(-1,0)$	$[2(e_1 + e_2) + n^2]R(0,0)$							
	$[e_1 + n^2]R(-2,1)$	$[e_1 + e_2 + n^2]R(-1,1)$	$[e_1 + n^2]R(-2,2) + R(0,0)$						
	$[e_1 + 2e_2 + n^2]R(0,0)$	$[3(e_1 + e_2) + n^2]R(1,0)$	$[e_1 + 2e_2 + n^2]R(0,1)$	$[5e_1 + 4e_2 + n^2]R(2,0)$					
	$[e_1 + e_2 + n^2]R(-1,1)$	$[2(e_1 + e_2) + n^2]R(0,1)$	$[e_1 + e_2 + n^2]R(-1,2) + R(1,0)$	$[3(e_1 + e_2) + n^2]R(1,1)$	$[2(e_1 + e_2) + n^2]R(0,2) + R(2,0)$				
	$[e_1 + n^2]R(-2,2)$	$[e_1 + e_2 + n^2]R(-1,2)$	$[e_1 + n^2]R(-2,3) + 2R(0,1)$	$[e_1 + 2e_2 + n^2]R(0,2)$	$[e_1 + e_2 + n^2]R(-1,3) + 2R(1,1)$	$[e_1 + n^2]R(-2,4) + 4R(0,2)$			
	$n[e_1 + 1]R(-2,0)$	$n[e_1 + e_2 + 1]R(-1,0)$	$n[e_1 + 1]R(-2,1)$	$n[e_1 + 2e_2 + 1]R(0,0)$	$n[e_1 + e_2 + 1]R(-1,1)$	$n[e_1 + 1]R(-2,2)$	$[n^2 e_1 + 1]R(-2,0)$		
	$n e_1 R(-1,0)$	$n[e_1 + e_2]R(0,0)$	$n e_1 R(-1,1)$	$n[e_1 + 2e_2]R(1,0)$	$n[e_1 + e_2]R(0,1)$	$n e_1 R(-1,2)$	$n^2 e_1 R(-1,0)$	$n^2 e_1 R(0,0)$	
	$n[e_1 + 1]R(-2,1)$	$n[e_1 + e_2 + 1]R(-1,1)$	$n[e_1 + 1]R(-2,2)$	$n[e_1 + 2e_2 + 1]R(0,1)$	$n[e_1 + e_2 + 1]R(-1,2)$	$n[e_1 + 1]R(-2,3)$	$[n^2 e_1 + 1]R(-2,1)$	$n^2 e_1 R(-1,1)$	$[n^2 e_1 + 1]R(-2,2) + R(0,0)$
	$n[e_1 - 1]R(0,0)$	$n[e_1 + e_2 - 1]R(1,0)$	$n[e_1 - 1]R(0,1)$	$n[e_1 + 2e_2 - 1]R(2,0)$	$n[e_1 + e_2 - 1]R(1,1)$	$n[e_1 - 1]R(0,2)$	$[n^2 e_1 - 1]R(0,0)$	$n^2 e_1 R(1,0)$	$[n^2 e_1 - 1]R(0,1)$
	$n e_1 R(-1,1)$	$n[e_1 + e_2]R(0,1)$	$n e_1 R(-1,2)$	$n[e_1 + 2e_2]R(1,1)$	$n[e_1 + e_2]R(0,2)$	$n e_1 R(-1,3)$	$n^2 e_1 R(-1,1)$	$n^2 e_1 R(0,1)$	$n^2 e_1 R(-1,2) + R(1,0)$
	$n[e_1 + 1]R(-2,2)$	$n[e_1 + e_2 + 1]R(-1,2)$	$n[e_1 + 1]R(-2,3)$	$n[e_1 + 2e_2 + 1]R(0,2)$	$n[e_1 + e_2 + 1]R(-1,3)$	$n[e_1 + 1]R(-2,4)$	$[n^2 e_1 + 1]R(-2,2)$	$n^2 e_1 R(-1,2)$	$[n^2 e_1 + 1]R(-2,3) + 2R(0,1)$
	0	0	0	0	0	0	0	0	$-nR(-1,0)$
	0	0	$R(0,0)$	0	$R(1,0)$	$2R(0,1)$	0	0	$-nR(0,0)$
	$e_2 R(-1,0)$	$2e_2 R(0,0)$	$e_2 R(-1,1)$	$3e_2 R(1,0)$	$2e_2 R(0,1)$	$e_2 R(-1,2)$	$n e_2 R(-1,0)$	$n e_2 R(0,0)$	$n[e_2 - 1]R(-1,1)$
	0	0	$2R(1,0)$	0	$2R(2,0)$	$4R(1,1)$	0	0	$-nR(1,0)$
	$e_2 R(0,0)$	$2e_2 R(1,0)$	$[e_2 + 1]R(0,1)$	$3e_2 R(2,0)$	$(2e_2 + 1)R(1,1)$	$(e_2 + 2)R(0,2)$	$n e_2 R(0,0)$	$n e_2 R(1,0)$	$n[e_2 - 1]R(0,1)$
	$2e_2 R(-1,1)$	$4e_2 R(0,1)$	$2e_2 R(-1,2)$	$6e_2 R(1,1)$	$4e_2 R(0,2)$	$2e_2 R(-1,3)$	$2n e_2 R(-1,1)$	$2n e_2 R(0,1)$	$n[2e_2 - 1]R(-1,2)$

	B_{n4}	B_{n5}	B_{n6}	C_{n1}	C_{n2}	C_{n3}	C_{n4}	C_{n5}	C_{n6}
	SYMMETRIC								
	$[n^2 e_1 + 1]R(2,0)$								
	$n^2 e_1 R(1,1)$	$n^2 e_1 R(0,2) + R(2,0)$							
	$[n^2 e_1 - 1]R(0,2)$	$n^2 e_1 R(-1,3) + 2R(1,1)$	$[n^2 e_1 + 1]R(-2,4) + 4R(0,2)$						
	0	$-nR(0,0)$	$-2nR(-1,1)$	$n^2 R(-2,0)$					
	0	$-nR(1,0)$	$-2nR(0,1)$	$n^2 R(-1,0)$	$[n^2 + 1]R(0,0)$				
	$n e_2 R(1,0)$	$n[e_2 - 1]R(0,1)$	$n[e_2 - 2]R(-1,2)$	$n^2 R(-2,1)$	$n^2 R(-1,1)$	$e_1 R(0,0) + n^2 R(-2,2)$			
	0	$-nR(2,0)$	$-2nR(1,1)$	$n^2 R(0,0)$	$[n^2 + 2]R(1,0)$	$n^2 R(0,1)$	$[n^2 + 4]R(2,0)$		
	$n e_2 R(2,0)$	$n[e_2 - 1]R(1,1)$	$n[e_2 - 2]R(0,2)$	$n^2 R(-1,1)$	$[n^2 + 1]R(0,1)$	$e_1 R(1,0) + n^2 R(-1,2)$	$[n^2 + 2]R(1,1)$	$e_1 R(2,0) + [n^2 + 1]R(0,2)$	
	$2n e_2 R(1,1)$	$n[2e_2 - 1]R(0,2)$	$2n[e_2 - 1]R(-1,3)$	$n^2 R(-2,2)$	$n^2 R(-1,2)$	$2e_1 R(0,1) + n^2 R(-2,3)$	$n^2 R(0,2)$	$2e_1 R(1,1) + n^2 R(-1,3)$	$4e_1 R(0,2) + n^2 R(-2,4)$

TABLE 2.2.2. The H_n matrix.

Substitution from (2.2.12) into (2.2.7) leads to the following basic integral, characterizing the stiffness of the triangular ring element

$$E_n = \int_\Delta \int \bar{\varepsilon}_n' \, G \, \bar{\varepsilon}_n \, r dr dz = \bar{a}_n' \, H_n \, \bar{a}_n \tag{2.2.13}$$

where the (18 x 18) matrix

$$H_n = \int_\Delta \int \bar{C}_n' \, G \, C_n \, r dr dz \tag{2.2.14}$$

is shown in table 2.2.2. The integral expressions

$$R(p,q) = \int_\Delta \int r^p \, z^q \, r dr dz \tag{2.2.15}$$

can be computed by means of the formulae given in Appendix 2.
The last step in the evaluation of the stiffness matrix consists of the determination of the relationship between the unknown constants and the values of u_n, v_n and w_n in the nodal points (denoted by u_{ni}, v_{ni}, w_{ni} in nodal point i). From (2.2.10) it follows

$$\bar{u}_n = Q \, \bar{A}_n \qquad \bar{v}_n = Q \, \bar{B}_n \qquad \bar{w}_n = Q \, \bar{C}_n \tag{2.2.16}$$

where

$$\left.\begin{aligned} \bar{u}_n' &= |u_{n1} \;\; u_{n4} \;\; u_{n2} \;\; u_{n5} \;\; u_{n3} \;\; u_{n6}| \\ \bar{v}_n' &= |v_{n1} \;\; v_{n4} \;\; v_{n2} \;\; v_{n5} \;\; v_{n3} \;\; v_{n6}| \\ \bar{w}_n' &= |w_{n1} \;\; w_{n4} \;\; w_{n2} \;\; w_{n5} \;\; w_{n3} \;\; w_{n6}| \end{aligned}\right\} \tag{2.2.17}$$

$$\left.\begin{aligned} \bar{A}_n' &= |A_{n1} \;\; A_{n2} \;\; A_{n3} \;\; A_{n4} \;\; A_{n5} \;\; A_{n6}| \\ \bar{B}_n' &= |B_{n1} \;\; B_{n2} \;\; B_{n3} \;\; B_{n4} \;\; B_{n5} \;\; B_{n6}| \\ \bar{C}_n' &= |C_{n1} \;\; C_{n2} \;\; C_{n3} \;\; C_{n4} \;\; C_{n5} \;\; C_{n6}| \end{aligned}\right\} \tag{2.2.18}$$

while the (6 x 6) matrix Q (independent of n!) has been defined in table 2.2.3.

$$\bar{A}_n' = |A_{n1} \quad A_{n2} \quad A_{n3} \quad A_{n4} \quad A_{n5} \quad A_{n6}|$$

$$Q = \begin{bmatrix} 1 & r_1 & z_1 & r_1^2 & r_1 z_1 & z_1^2 \\ 1 & \frac{1}{2}(r_1+r_2) & \frac{1}{2}(z_1+z_2) & \frac{1}{4}(r_1+r_2)^2 & \frac{1}{4}(r_1+r_2)(z_1+z_2) & \frac{1}{4}(z_1+z_2)^2 \\ 1 & r_2 & z_2 & r_2^2 & r_2 z_2 & z_2^2 \\ 1 & \frac{1}{2}(r_2+r_3) & \frac{1}{2}(z_2+z_3) & \frac{1}{4}(r_2+r_3)^2 & \frac{1}{4}(r_2+r_3)(z_2+z_3) & \frac{1}{4}(z_2+z_3)^2 \\ 1 & r_3 & z_3 & r_3^2 & r_3 z_3 & z_3^2 \\ 1 & \frac{1}{2}(r_3+r_1) & \frac{1}{2}(z_3+z_1) & \frac{1}{4}(r_3+r_1)^2 & \frac{1}{4}(r_3+r_1)(z_3+z_1) & \frac{1}{4}(z_3+z_1)^2 \end{bmatrix}$$

TABLE 2.2.3.
The Q matrix.

Inverting (2.2.16) leads to

$$\bar{A}_n = Q^{-1}\,\bar{u}_n \qquad \bar{B}_n = Q^{-1}\,\bar{v}_n \qquad \bar{C}_n = Q^{-1}\,\bar{w}_n \tag{2.2.19}$$

These vector relations can be combined to

$$\bar{a}_n = P\,\bar{U}_n \tag{2.2.20}$$

where the (18 x 1) vector $\bar{a}_n$ combines the three vectors (2.2.18), the (18 x 1) vector $\bar{U}_n$ combines the three vectors (2.2.17), and the (18 x 18) matrix P is equal to

$$P = \begin{bmatrix} Q^{-1} & 0 & 0 \\ 0 & Q^{-1} & 0 \\ 0 & 0 & Q^{-1} \end{bmatrix} \tag{2.2.21}$$

The stiffness matrix S_n of the triangular ring element follows after substitution from (2.2.20) into (2.2.13)

$$E_n = \bar{U}_n'\,P'\,H_n\,P\,\bar{U}_n = \bar{U}_n'\,S_n\,\bar{U}_n \tag{2.2.22}$$

where

$$S_n = P'\,H_n\,P \tag{2.2.23}$$

2.3. The ana-element in the finite element approach.

2.3.1. General aspects of the introduction of the ana-element.

In Section 2.1 an ana-element has been defined as an element, the stiffness matrix of which has been obtained from known analytical solutions of the equations of elasticity. Some general consequences of the introduction of the ana-element in the finite element approach will be discussed in the present sub-section.

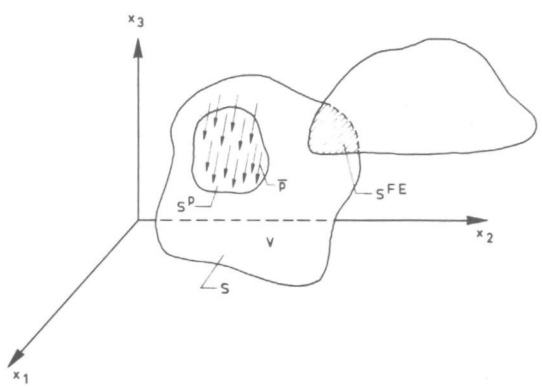

FIGURE 2.3.1.

Schematic representation of an ana-element.

Figure 2.3.1 shows an ana-element with volume V and surface S, which will be described referring to a cartesian co-ordinate system x_1, x_2 and x_3, denoted generally by x_i. This element will now be considered a finite element in a more complicated structure, interconnected with other finite elements at the surface S^{FE}. Due to the external loadings, a point of the ana-element with co-ordinate x_i undergoes a displacement, the component of which in the direction x_i will be denoted by u_i. Under the assumption of small deformations, the linearized strain tensor

$$\varepsilon_{ij} = \tfrac{1}{2}\left[u_{i,j}+u_{j,i}\right] \tag{2.3.1}$$

describes the deformed state of the ana-element, where a comma, followed by an index indicates partial differentiation with respect to the corresponding co-ordinate according to a convention that is usual in tensor analysis, e.g.

$$u_{i,j} = \frac{\partial u_i}{\partial x_j} \tag{2.3.2}$$

The stresses, belonging to this state of deformation, will be denoted by the stress tensor σ_{ij}.

Let now δu_i be a system of arbitrary additional displacements referred to as *virtual* displacements. The corresponding virtual deformations will be defined by the linearized virtual strain tensor

$$\delta\varepsilon_{ij} = \tfrac{1}{2}\left[\delta u_{i,j}+\delta u_{j,i}\right] \tag{2.3.3}$$

The body-forces acting on the ana-element will be denoted by X_i, while $\bar{p}_i$ represents a system of external surface loadings, acting on the surface S^p of S.
Under the assumption that the conformity requirement at the intersection between the ana-element and the other finite elements, mentioned in Chapter 1.3, is met, the contribution of the ana-element to the virtual work equation of the complete construction is equal to

$$\int_V \sigma_{ij}\,\delta\varepsilon_{ij}\,dv - \int_V X_i\,\delta u_i\,dv - \int_{S^p} \bar{p}_i\,\delta u_i\,ds \tag{2.3.4}$$

In this expression use has been made of the summation convention, which implies summation of an index from 1 to 3 if this index occurs twice in a product term. The first term of expression (2.3.4) will be evaluated by making use of the symmetry of the stress tensor

$$\sigma_{ij} = \sigma_{ji} \tag{2.3.5}$$

resulting from moment equilibrium of an infinitesimal element

$$\begin{aligned}\int_V \sigma_{ij}\,\delta\varepsilon_{ij}\,dv &= \int_V \sigma_{ij}\,\delta u_{i,j}\,dv = \\ &= \int_V \left[\sigma_{ij}\,\delta u_i\right]_{,j}\,dv - \int_V \sigma_{ij,j}\,\delta u_i\,dv\end{aligned} \tag{2.3.6}$$

The first term in the right-hand member of this expression can be transformed by applying the divergence theorem

$$\int_V \left[\sigma_{ij}\,\delta u_i\right]_{,j}\,dv = \int_S \left[\sigma_{ij}\,\delta u_i\right] n_j\,ds \tag{2.3.7}$$

where n_j stands for the component in the direction x_j of the unit vector, normal to the surface S. Substitution from (2.3.6) and (2.3.7) into (2.3.4) results in the following contribution of the ana-element to the virtual work equation for the complete structure

$$\int_S \sigma_{ij}\, n_j\, \delta u_i\, ds - \int_V [\sigma_{ij,j} + X_i]\, \delta u_i\, dv - \int_{S^p} \bar{p}_i\, \delta u_i\, ds \qquad (2.3.8)$$

At this point we take into account that the (known) analytical solution satisfies the force equilibrium conditions of an infinitesimal element

$$\sigma_{ij,j} + X_i = 0 \qquad (2.3.9)$$

and the boundary conditions for the surface loadings

$$\sigma_{ij}\, n_j = \bar{p}_i \text{ on } S^p \qquad (2.3.10)$$

$$\sigma_{ij}\, n_j = p_i^{FE} \text{ on } S^{FE} \qquad (2.3.11)$$

Thus we arrive at the final expression for the contribution of the ana-element to the virtual work equation for the complete construction

$$\int_{S^{FE}} p_i^{FE}\, \delta u_i\, ds \qquad (2.3.12)$$

This expression represents the virtual work due to a system of stresses acting at the intersection between the ana-element and the other finite elements.

It can be shown that this contribution is equal to the virtual work done by a general equilibrium system of boundary loadings acting at S^{FE} (homogeneous solution), diminished by the virtual work done by a system of so-called kinematically consistent edge loadings p_i^{KC}, defined by

$$\int_{S^{FE}} p_i^{KC}\, \delta u_i\, ds \equiv \int_V X_i\, \delta u_i\, dv + \int_{S^p} \bar{p}_i\, \delta u_i\, ds \qquad (2.3.13)$$

Thus complete similarity is obtained with the way of analyzing beam-type structures by means of the finite element method (cf. e.g. [2.5]).

2.3.2. The infinitely large flat plate with a circular hole under in-plane harmonic loading.

In this sub-section the element stiffness matrix will be derived for the infinitely large flat plate with a circular hole under in-plane harmonic loading.
Denoting the stress notations as shown in figure 2.3.2 and introducing a stress function ψ, we have the following stress components (see e.g. [2.6], pp. 55-57)

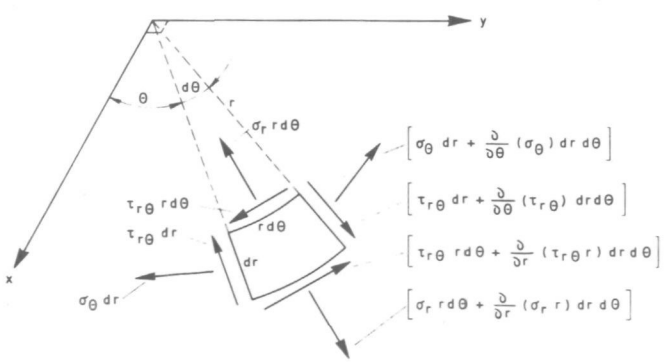

FIGURE 2.3.2.

Stress notations for the in-plane loaded flat plate.

$$\sigma_r = \frac{1}{r}\frac{\partial\psi}{\partial r} + \frac{1}{r^2}\frac{\partial^2\psi}{\partial\theta^2} \qquad \sigma_\theta = \frac{\partial^2\psi}{\partial r^2} \qquad \tau_{r\theta} = -\frac{\partial}{\partial r}\left[\frac{1}{r}\frac{\partial\psi}{\partial\theta}\right] \tag{2.3.14}$$

The compatibility conditions for the strains lead for a material obeying Hooke's law to the following equation for the homogeneous part of ψ *)

$$\left(\frac{\partial^2}{\partial r^2} + \frac{1}{r}\frac{\partial}{\partial r} + \frac{1}{r^2}\frac{\partial^2}{\partial\theta^2}\right)\left(\frac{\partial^2\psi}{\partial r^2} + \frac{1}{r}\frac{\partial\psi}{\partial r} + \frac{1}{r^2}\frac{\partial^2\psi}{\partial\theta^2}\right) = 0 \tag{2.3.15}$$

The general series solution for ψ, being symmetrically with regard to $\theta=0$ and satisfying (2.3.15) is [2.7]

$$\begin{aligned}\psi = {} & A_0 r^2 + B_0 + C_0 r^2 \ln\rho + D_0 \ln\rho + \\ & + A_1 r\,\theta \sin\theta + \{B_1 r^{-1} + [C_1 r^2 + D_1 \ln\rho]r\}\cos\theta + \\ & + \sum_{n=2}^{\infty} \{[A_n r^2 + B_n]r^{-n} + [C_n r^2 + D_n]r^n\}\cos n\theta\end{aligned} \tag{2.3.16}$$

where A_n, B_n, C_n and D_n are constants while $\rho = r/r_0$, r_0 being the radius of the circular hole. Substitution from (2.3.16) into (2.3.14) leads to

$$\sigma_r = \sum_{n=0}^{\infty} \sigma_{rn} \cos n\theta \qquad \sigma_\theta = \sum_{n=0}^{\infty} \sigma_{\theta n} \cos n\theta$$

$$\tau_{r\theta} = \sum_{n=1}^{\infty} \tau_{r\theta n} \sin n\theta \tag{2.3.17}$$

where

$$\left.\begin{aligned}\sigma_{r0} &= 2A_0 + C_0\,[2\ln\rho + 1] + D_0 r^{-2} \\ \sigma_{\theta 0} &= 2A_0 + C_0\,[2\ln\rho + 3] - D_0 r^{-2}\end{aligned}\right\} \tag{2.3.18}$$

$$\left.\begin{aligned}\sigma_{r1} &= 2A_1 r^{-1} - 2B_1 r^{-3} + 2C_1 r + D_1 r^{-1} \\ \sigma_{\theta 1} &= 2B_1 r^{-3} + 6C_1 r + D_1 r^{-1} \\ \tau_{r\theta 1} &= -2B_1 r^{-3} + 2C_1 r + D_1 r^{-1}\end{aligned}\right\} \tag{2.3.19}$$

---

*) *In the absence of thermal and surface loadings this equation yields the complete solution for ψ.*

$$\left.\begin{aligned}
\sigma_{rn} &= -\left[(n+2)(n-1)A_n r^2 + n(n+1)B_n\right]r^{-(n+2)} + \\
&\quad -\left[(n-2)(n+1)C_n r^2 + n(n-1)D_n\right]r^{n-2} \\
\sigma_{\theta n} &= \left[(n-2)(n-1)A_n r^2 + n(n+1)B_n\right]r^{-(n+2)} + \\
&\quad +\left[(n+2)(n+1)C_n r^2 + n(n-1)D_n\right]r^{n-2} \\
\tau_{r\theta n} &= -\left[n(n-1)A_n r^2 + n(n+1)B_n\right]r^{-(n+2)} + \\
&\quad +\left[n(n+1)C_n r^2 + n(n-1)D_n\right]r^{n-2}
\end{aligned}\right\} \quad \text{if } n > 1 \qquad (2.3.20)$$

As the plate is considered to be of infinite size the solution must be finite at $r = \infty$, which results in

$$\begin{aligned} C_n &= 0 \qquad (n = 0, 1, \ldots) \\ D_n &= 0 \qquad \text{if } n > 2 \end{aligned} \qquad (2.3.21)$$

In considering only the homogeneous solution (see Section 2.3.1) we have no boundary forces at $r = \infty$. Thus we may put $A_0 = 0$, $D_2 = 0$.
Substitution from (2.3.18), (2.3.19) and (2.3.20) into Hooke's law and using (2.3.21) and the first, second and fourth expression of (2.2.1) leads to the following solutions for the in-plane displacements

$$u = \sum_{n=0}^{\infty} u_n \cos n\theta \qquad v = \sum_{n=1}^{\infty} v_n \sin n\theta \qquad (2.3.22)$$

where

$$u_0 = -\frac{1+\nu}{E} D_0 r^{-1} \qquad (2.3.23)$$

$$\left.\begin{aligned}
u_1 &= \frac{1}{E}\{2A_1 \ln\rho + (1+\nu)B_1 r^{-2} + (1-\nu)\,D_1 \ln\rho + \\
&\quad + \left[A_1(1-\nu) + 2D_1\right]\theta \tan\theta\} + K \\
v_1 &= \frac{1}{E}\{-2A_1\left[\ln\rho+\nu\right] + (1+\nu)B_1 r^{-2} - (1-\nu)\,D_1\left[\ln\rho-1\right] + \\
&\quad + \left[A_1(1-\nu) + 2D_1\right]\left[\theta \operatorname{cotan}\theta - 1\right]\} - K
\end{aligned}\right\} \qquad (2.3.24)$$

$$\left.\begin{aligned}
u_n &= \frac{1}{E}\left[\{n+2+\nu(n-2)\}\,A_n r^2 + (1+\nu)nB_n\right]r^{-(n+1)} \\
v_n &= \frac{1}{E}\left[\{n-4+\nu n\}\,A_n r^2 + (1+\nu)nB_n\right]r^{-(n+1)}
\end{aligned}\right\} \quad \text{if } n > 1 \qquad (2.3.25)$$

In the above expressions the solution $u = K \cos\theta$, $v = -K \sin\theta$ (K being an integration constant) represents a (stress-free) rigid body translation of the plate in the $\theta = 0$ direction.
The displacements should be single-valued functions of θ, which leads with (2.3.24) to

$$A_1(1-\nu) + 2D_1 = 0 \qquad \text{or} \qquad D_1 = -\frac{(1-\nu)}{2} A_1 \tag{2.3.26}$$

The condition of equilibrium of forces along the central circular hole in the $\theta = 0$ direction leads with (2.3.17) to

$$[\sigma_{r1}]_{r=r_0} - [\tau_{r\theta 1}]_{r=r_0} = 0 \tag{2.3.27}$$

By means of (2.3.19), (2.3.21), (2.3.26) and (2.3.27) follows

$$A_1 = D_1 = 0 \tag{2.3.28}$$

In order to obtain the in-plane stiffness of the plate we have to find the relationship between the unknown constants and the values $\overset{0}{u}_n$ and $\overset{0}{v}_n$ of u_n and v_n at the circular hole (radius r_0). By means of (2.3.23), (2.3.24), (2.3.25) and (2.3.28) follows

$$D_0 = -\frac{r_0 E}{1+\nu} \overset{0}{u}_0 \qquad B_1 = \frac{r_0^2 E}{2(1+\nu)} [\overset{0}{u}_1 + \overset{0}{v}_1] \tag{2.3.29}$$

$$\left.\begin{aligned} A_n r_0^2 &= \frac{r_0^{n+1} E}{2(3-\nu)} [\overset{0}{u}_n - \overset{0}{v}_n] \\ B_n &= \frac{r_0^{n+1} E}{2n(1+\nu)(3-\nu)} [-\{(1+\nu)n - 4\}\overset{0}{u}_n + \{n+2+\nu(n-2)\}\overset{0}{v}_n] \end{aligned}\right\} \text{ if } n > 1 \tag{2.3.30}$$

After substitution from (2.3.21), (2.3.28), (2.3.29) and (2.3.30) into (2.3.18), (2.3.19) and (2.3.20) the virtual work $\delta V_{pl,in}$ done by a general equilibrium system of boundary loadings acting at $r = r_0$ can be computed

$$\begin{aligned} \delta V_{pl,in} &= -2\pi r_0 h_{pl} [\sigma_{r0}]_{r=r_0} \delta\overset{0}{u}_0 + \\ &\quad - \pi r_0 h_{pl} \sum_{n=1}^{\infty} \{[\sigma_{rn}]_{r=r_0} \delta\overset{0}{u}_n + [\tau_{r\theta n}]_{r=r_0} \delta\overset{0}{v}_n\} = \\ &= 2\pi \frac{Eh_{pl}}{1+\nu} \overset{0}{u}_0 \delta\overset{0}{u}_0 + \pi \frac{Eh_{pl}}{1+\nu} (\overset{0}{u}_1 + \overset{0}{v}_1) \delta(\overset{0}{u}_1 + \overset{0}{v}_1) + \\ &\quad + \pi \frac{Eh_{pl}}{(1+\nu)(3-\nu)} \sum_{n=2}^{\infty} [(2n+1-\nu)(\overset{0}{u}_n \delta\overset{0}{u}_n + \overset{0}{v}_n \delta\overset{0}{v}_n) + \\ &\quad + (n+2-\nu n)(\overset{0}{v}_n \delta\overset{0}{u}_n + \overset{0}{u}_n \delta\overset{0}{v}_n)] \end{aligned} \tag{2.3.31}$$

h_{pl} being the wall thickness of the plate.

2.3.3. The infinitely large flat plate with a circular hole under harmonic loading perpendicular to its plane.

In this sub-section the element stiffness matrix will be derived for the infinitely large flat plate with a circular hole, loaded perpendicularly to its plane by harmonic loading.

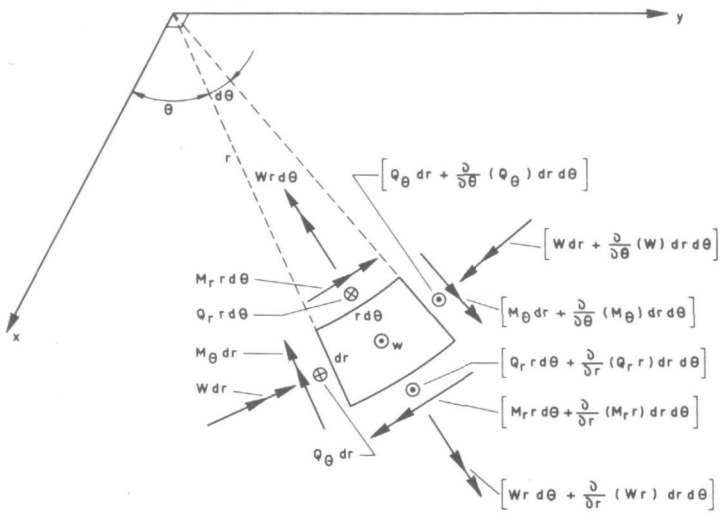

Denoting the shear forces and moments per unit arc length of middle surface as shown in figure 2.3.3 we have the following (homogeneous) equilibrium equations

FIGURE 2.3.3.

Shear forces, moments and axial displacement for the flat plate, loaded perpendicular to its plane.

$$\frac{\partial}{\partial r}(Q_r r) + \frac{\partial}{\partial \theta}(Q_\theta) = 0 \tag{2.3.32}$$

$$\left.\begin{aligned} Q_r &= -\frac{1}{r}\left[\frac{\partial}{\partial r}(M_r r) + \frac{\partial}{\partial \theta}(W) - M_\theta\right] \\ Q_\theta &= -\frac{1}{r}\left[\frac{\partial}{\partial \theta}(M_\theta) + \frac{\partial}{\partial r}(Wr) + W\right] \end{aligned}\right\} \tag{2.3.33}$$

The constitutive equations are (see [2.8], p. 283)

$$\left.\begin{aligned} M_r &= \frac{Eh_{pl}^3}{12(1-\nu^2)}\left[\frac{\partial^2 w}{\partial r^2} + \nu\left(\frac{1}{r^2}\frac{\partial^2 w}{\partial \theta^2} + \frac{1}{r}\frac{\partial w}{\partial r}\right)\right] \\ M_\theta &= \frac{Eh_{pl}^3}{12(1-\nu^2)}\left[\frac{1}{r^2}\frac{\partial^2 w}{\partial \theta^2} + \frac{1}{r}\frac{\partial w}{\partial r} + \nu\frac{\partial^2 w}{\partial r^2}\right] \\ W &= \frac{Eh_{pl}^3}{12(1+\nu)}\left[\frac{1}{r}\frac{\partial^2 w}{\partial r \partial \theta} - \frac{1}{r^2}\frac{\partial w}{\partial \theta}\right] \end{aligned}\right\} \tag{2.3.34}$$

where w is the normal displacement (cf. figure 2.3.3).
Substitution from (2.3.33) and (2.3.34) into (2.3.32) leads to the following differential equation for w

$$\left(\frac{\partial^2}{\partial r^2} + \frac{1}{r}\frac{\partial}{\partial r} + \frac{1}{r^2}\frac{\partial^2}{\partial \theta^2}\right)\left(\frac{\partial^2 w}{\partial r^2} + \frac{1}{r}\frac{\partial w}{\partial r} + \frac{1}{r^2}\frac{\partial^2 w}{\partial \theta^2}\right) = 0 \tag{2.3.35}$$

The solution of (2.3.35) is assumed to be a Fourier's series in θ direction

$$w = \sum_{n=0}^{\infty} w_n \cos n\theta \tag{2.3.36}$$

where

$$\begin{aligned} w_0 &= A_0 r^2 + B_0 + C_0 r^2 \ln\rho + D_0 \ln\rho \\ w_1 &= [A_1 r^2 + B_1] r^{-1} + [C_1 r^2 + D_1 \ln\rho] r \\ w_n &= [A_n r^2 + B_n] r^{-n} + [C_n r^2 + D_n] r^n \quad , \text{ if } n > 1 \end{aligned} \tag{2.3.37}$$

In this solution A_n, B_n, C_n and D_n are constants while $\rho = r/r_0$, r_0 being the radius of the circular hole.
By means of (2.3.36) and (2.3.37) the following solution for the rotation ϕ in radial direction can be derived

$$\phi = \frac{\partial w}{\partial r} = \sum_{n=0}^{\infty} \phi_n \cos n\theta \tag{2.3.38}$$

where

$$\begin{aligned} \phi_0 &= 2A_0 r + C_0 [2 \ln\rho + 1] r + D_0 r^{-1} \\ \phi_1 &= [A_1 r^2 - B_1] r^{-2} + 3C_1 r^2 + D_1 [\ln\rho + 1] \\ \phi_n &= [-(n-2)A_n r^2 - n B_n] r^{-(n+1)} + [(n+2)C_n r^2 + n D_n] r^{n-1} \quad , \text{ if } n > 1 \end{aligned} \tag{2.3.39}$$

In the above expressions the solution $w = A_1 r \cos\theta$, $\phi = A_1 \cos\theta$ represents a (stress-free) rigid body rotation of the plate about the $\theta = \pi/2$ axis.
Substitution from the solution for w into (2.3.34) and (2.3.33) leads to

$$Q_r = \sum_{n=0}^{\infty} Q_{rn} \cos n\theta \qquad M_r = \sum_{n=0}^{\infty} M_{rn} \cos n\theta$$

$$W = \sum_{n=1}^{\infty} W_n \sin n\theta \tag{2.3.40}$$

where

$$
\left.
\begin{aligned}
Q_{r0} &= -\frac{Eh_{pl}^3}{12(1-\nu^2)}\, 4\, C_0 r^{-1} \\
M_{r0} &= \frac{Eh_{pl}^3}{12(1-\nu^2)}\, \{2(1+\nu)\, A_0 + \\
&\quad + C_0\, [2(1+\nu)\, \ln\rho + 3 + \nu] - (1-\nu)\, D_0 r^{-2}\}
\end{aligned}
\right\} \qquad (2.3.41)
$$

$$
\left.
\begin{aligned}
Q_{r1} &= -\frac{Eh_{pl}^3}{12(1-\nu^2)}\, \frac{1}{r}\, \{8\, C_1\, r - 2D_1 r^{-1}\} \\
M_{r1} &= \frac{Eh_{pl}^3}{12(1-\nu^2)}\, \{2(1-\nu)\, B_1\, r^{-3} + 2(3+\nu)\, C_1 r + (1+\nu)\, D_1 r^{-1}\} \\
W_1 &= \frac{Eh_{pl}^3}{12(1-\nu^2)}\, (1-\nu)\, \{2B_1 r^{-3} - 2C_1 r - D_1 r^{-1}\}
\end{aligned}
\right\} \qquad (2.3.42)
$$

$$
\left.
\begin{aligned}
Q_{rn} &= -\frac{Eh_{pl}^3}{12(1-\nu^2)}\, \frac{1}{r}\, [4n(n-1)\, A_n r^{-n} + 4n(n+1)\, C_n r^n] \\
M_{rn} &= \frac{Eh_{pl}^3}{12(1-\nu^2)}\, \Big[\{(n-1)\, [n-2+\nu(n+2)]\, A_n r^2 + n(n+1)(1-\nu)\, B_n\} r^{-(n+2)} + \\
&\quad + \{(n+1)\, [n+2-\nu(n-2)]\, C_n r^2 + n(n-1)(1-\nu)\, D_n\}\, r^{n-2}\Big] \\
W_n &= \frac{Eh_{pl}^3}{12(1-\nu^2)}\, (1-\nu)\, \Big[\{n(n-1)\, A_n r^2 + n(n+1)\, B_n\} r^{-(n+2)} + \\
&\quad - \{n(n+1)\, C_n r^2 + n(n-1)\, D_n\} r^{n-2}\Big]
\end{aligned}
\right\} \text{if } n > 1 \qquad (2.3.43)
$$

The stresses must tend to zero at $r = \infty$, which results in

$$
\begin{aligned}
A_0 &= 0 \\
C_n &= 0 \qquad (2.3.44) \\
D_n &= 0, \quad \text{if } n > 1
\end{aligned}
$$

The reduced shear force along the central circular hole (radius r_0) is equal to

$$\overline{Q}_{red} = \left[Q_r - \frac{1}{r}\frac{\partial W}{\partial \theta}\right]_{r=r_0} = \sum_{n=0}^{\infty} \overline{Q}_n \cos n\theta \qquad (2.3.45)$$

where

$$\overline{Q}_0 = 0 \text{ (homogeneous solution)}$$

$$\overline{Q}_1 = -\frac{Eh_{pl}^3}{12(1-\nu^2)}\frac{1}{r_0}\{2(1-\nu)\, B_1 r_0^{-3} - (3-\nu)\, D_1 r_0^{-1}\} \qquad (2.3.46)$$

$$\overline{Q}_n = -\frac{Eh_{pl}^3}{12(1-\nu^2)}\frac{1}{r_0}\{n(n-1)\,(n+4-\nu n)\, A_n r_0^{2} + n^2\,(n+1)(1-\nu)\, B_n\}\, r_0^{-(n+2)}, \quad \text{if } n > 1$$

The moment equilibrium condition along the circular hole in $\theta = \pi/2$ direction leads with (2.3.40) and (2.3.45) to

$$r_0\,[\overline{Q}_1] + [M_{r1}]_{r=r_0} = 0 \qquad (2.3.47)$$

By means of (2.3.42), (2.3.46) and (2.3.47) follows

$$D_1 = 0 \qquad (2.3.48)$$

In order to obtain the stiffness of the plate we have to find the relationship between the unknown constants and the values $\overset{0}{w}_n$ and $\overset{0}{\phi}_n$ of w_n and ϕ_n at the circular hole. By means of (2.3.37), (2.3.39), (2.3.44) and (2.3.48) follows

$$D_0 = r_0 \overset{0}{\phi}_0 \qquad (2.3.49)$$

$$\left.\begin{aligned} A_n &= \tfrac{1}{2}\left[n\overset{0}{w}_n + r_0\overset{0}{\phi}_n\right] r_0^{n-2} \\ B_n &= \tfrac{1}{2}\left[-(n-2)\overset{0}{w}_n - r_0\overset{0}{\phi}_n\right] r_0^{n} \end{aligned}\right\} \quad \text{if } n > 0 \qquad (2.3.50)$$

After substitution from (2.3.49) and (2.3.50) into (2.3.41), (2.3.42), (2.3.43) and (2.3.46) the virtual work $\delta V_{pl,\perp}$ done by a general equilibrium system of boundary loadings acting at $r = r_0$ can be computed

$$\delta V_{pl,\perp} = -2\pi\, r_0\, [M_{r0}]_{r=r_0}\, \delta\overset{0}{\phi}_0 +$$

$$- \pi\, r_0 \sum_{n=1}^{\infty} \{\overline{Q}_n\, \delta\overset{0}{w}_n + [M_{rn}]_{r=r_0}\, \delta\overset{0}{\phi}_n\} =$$

$$= 2\pi \frac{Eh_{pl}^3}{12(1-\nu^2)} (1-\nu) \overset{0}{\phi}_0 \delta\overset{0}{\phi}_0 +$$

$$+ \pi \frac{Eh_{pl}^3 r_0^{-2}}{12(1-\nu^2)} (1-\nu) (\overset{0}{w}_1 - r_0 \overset{0}{\phi}_1) \delta(\overset{0}{w}_1 - r_0 \overset{0}{\phi}_1) +$$

$$+ \pi \frac{Eh_{pl}^3 r_0^{-2}}{12(1-\nu^2)} \sum_{n=2}^{\infty} \{[2n - (1+\nu)] [n^2 \overset{0}{w}_n \delta\overset{0}{w}_n + r_0 \overset{0}{\phi}_n \delta(r_0 \overset{0}{\phi}_n)] +$$

$$+ n[-2+n(1+\nu)] [r_0 \overset{0}{\phi}_n \delta\overset{0}{w}_n + \overset{0}{w}_n \delta(r_0 \overset{0}{\phi}_n)]\} \qquad (2.3.51)$$

h_{pl} being the wall thickness of the plate.

2.3.4. The semi-infinite circular cylindrical shell under harmonic loading.

In this sub-section the element stiffness matrix will be derived for the semi-infinite circular cylindrical shell with mid-surface radius R and wall thickness h under harmonic loading. Figure 2.3.4 shows the shell middle surface with co-ordinates, displacements, rotations and loadings along an arbitrary edge curve.

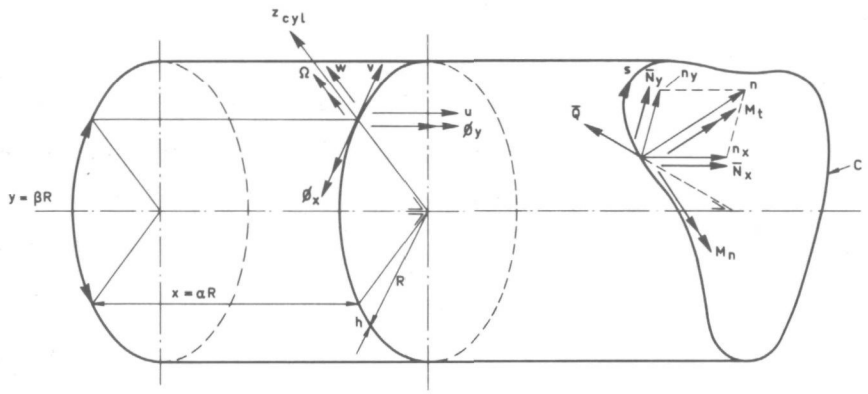

FIGURE 2.3.4.

Cylindrical shell middle surface with co-ordinates, deformations and edge loadings.

Instead of the co-ordinates x (parallel with the axis of the cylinder) and y (perpendicular to x) in the middle surface, the following dimensionless co-ordinates α and β are defined

$$\alpha = x/R \qquad \beta = y/R \qquad (2.3.52)$$

Differentiations to α and β will be denoted respectively by

$$\frac{\partial}{\partial\alpha} (\ldots) = (\ldots)' \qquad \frac{\partial}{\partial\beta} (\ldots) = (\ldots)^{\cdot} \qquad (2.3.53)$$

The Laplacian Δ with respect to a α and β is defined by

$$\Delta (\ldots) = (\ldots)'' + (\ldots)^{\cdot\cdot} \qquad (2.3.54)$$

A summary of the governing equations for circular cylindrical shells is given in Appendix 3. The general solution of eq. (A.3.8) is again assumed to be a Fourier's series in β direction

$$w = \sum_{n=0}^{\infty} W_n \cos n\beta \tag{2.3.55}$$

where W_n for each value of n is a function of α only. Substitution from (2.3.55) into (A.3.8) leads to an ordinary differential equation for W_n, the solution of which has the following form

$$W_n = C_n e^{\lambda_n \alpha} \tag{2.3.56}$$

where C_n is an integration constant and λ_n satisfies the following characteristic equation

$$(1-\nu^2)\,\lambda_n^4 + \frac{h^2}{12R^2}\,(\lambda_n^2-n^2)^2\,(\lambda_n^2-n^2+1)^2 = 0 \tag{2.3.57}$$

This equation has eight roots λ_n for each value of n, being generally complex

$$\begin{aligned} \lambda_{n1,2} &= -\kappa_{n1} \pm i\,\mu_{n1} & \lambda_{n5,6} &= \kappa_{n1} \pm i\,\mu_{n1} \\ \lambda_{n3,4} &= -\kappa_{n2} \pm i\,\mu_{n2} & \lambda_{n7,8} &= \kappa_{n2} \pm i\,\mu_{n2} \end{aligned} \tag{2.3.58}$$

where κ_{n1}, κ_{n2}, μ_{n1} and μ_{n2} are positive real numbers, dependent on n. As the cylindrical shell is considered to be semi-infinite, the stresses must tend to zero at $\alpha = \infty$. This results in the following homogeneous solution for W_n only valid without edge loadings at $\alpha = \infty$ [2.9]

$$\begin{aligned} W_0 &= \exp(-\kappa_{01}\alpha)\,[C_{01}^1 \cos \mu_{01}\alpha + C_{02}^1 \sin \mu_{01}\alpha] \\ W_1 &= \exp(-\kappa_{11}\alpha)\,[C_{11}^1 \cos \mu_{11}\alpha + C_{12}^1 \sin \mu_{11}\alpha] + D_1 + D_2\,\alpha \\ W_n &= \sum_{i=1}^{2} \exp(-\kappa_{ni}\alpha)\,[C_{n1}^i \cos \mu_{ni}\alpha + C_{n2}^i \sin \mu_{ni}\alpha], \quad \text{if } n > 1 \end{aligned} \tag{2.3.59}$$

where C_{nj}^i $(i=1,2;\ j=1,2)$, D_1 and D_2 are integration constants. The solution corresponding to D_1 represents a (stress-free) rigid body translation of the cylinder in the $\beta = 0$ direction, while the solution corresponding to D_2 represents a rigid body rotation of the cylinder about the line $\alpha = 0$, $\beta = \pi/2$.
Substitution from (2.3.55) and (2.3.59) into (A.3.7) leads to the following solution for u and v

$$u = \sum_{n=0}^{\infty} U_n \cos n\beta \qquad v = \sum_{n=1}^{\infty} V_n \sin n\beta \tag{2.3.60}$$

where

$$U_0 = \exp(-\kappa_{01}\alpha)\left[A^1_{01}\cos\mu_{01}\alpha + A^1_{02}\sin\mu_{01}\alpha\right] + D_3$$

$$U_1 = \exp(-\kappa_{11}\alpha)\left[A^1_{11}\cos\mu_{11}\alpha + A^1_{12}\sin\mu_{11}\alpha\right] - D_2 \qquad (2.3.61)$$

$$U_n = \sum_{i=1}^{2} \exp(-\kappa_{ni}\alpha)\left[A^i_{n1}\cos\mu_{ni}\alpha + A^i_{n2}\sin\mu_{ni}\alpha\right], \quad \text{if } n > 1$$

and

$$V_1 = \exp(-\kappa_{11}\alpha)\left[B^1_{11}\cos\mu_{11}\alpha + B^1_{12}\sin\mu_{11}\alpha\right] - D_1 - D_2\,\alpha \qquad (2.3.62)$$

$$V_n = \sum_{i=1}^{2} \exp(-\kappa_{ni}\alpha)\left[B^i_{n1}\cos\mu_{ni}\alpha + B^i_{n2}\sin\mu_{ni}\alpha\right], \quad \text{if } n > 1$$

while the solution corresponding to the integration constant D_3 represents a (stress-free) rigid body displacement in the direction of the shell axis. The relationship between the constants A^i_{nj}, B^i_{nj} on one hand and the constants C^i_{nj} on the other hand follows from the above mentioned substitution and has the following form

$$A^i_{nj} = \sum_{k=1}^{2} a^i_{njk}\, C^i_{nk} \qquad B^i_{nj} = \sum_{k=1}^{2} b^i_{njk}\, C^i_{nk} \qquad (2.3.63)$$

where the equations determining a^i_{njk} and b^i_{njk} are shown in table 2.3.1.

$\left[\varkappa_i^4 - 6\varkappa_i^2\mu_i^2 + \mu_i^4 - 2n^2(\varkappa_i^2 - \mu_i^2) + n^4\right] A^i_{n1} - 4\varkappa_i\mu_i\left[\varkappa_i^2 - \mu_i^2 - n^2\right] A^i_{n2} = \varkappa_i\left[\nu(\varkappa_i^2 - 3\mu_i^2) + n^2\right] C^i_{n1} - \mu_i\left[\nu(3\varkappa_i^2 - \mu_i^2) + n^2\right] C^i_{n2}$	
$4\varkappa_i\mu_i\left[\varkappa_i^2 - \mu_i^2 - n^2\right] A^i_{n1} + \left[\varkappa_i^4 - 6\varkappa_i^2\mu_i^2 + \mu_i^4 - 2n^2(\varkappa_i^2 - \mu_i^2) + n^4\right] A^i_{n2} = \mu_i\left[\nu(3\varkappa_i^2 - \mu_i^2) + n^2\right] C^i_{n1} + \varkappa_i\left[\nu(\varkappa_i^2 - 3\mu_i^2) + n^2\right] C^i_{n2}$	
$\left[\varkappa_i^4 - 6\varkappa_i^2\mu_i^2 + \mu_i^4 - 2n^2(\varkappa_i^2 - \mu_i^2) + n^4\right] B^i_{n1} - 4\varkappa_i\mu_i\left[\varkappa_i^2 - \mu_i^2 - n^2\right] B^i_{n2} = n\left[(2+\nu)(\varkappa_i^2 - \mu_i^2) - n^2\right] C^i_{n1} - 2(2+\nu)n\,\varkappa_i\mu_i C^i_{n2}$	
$4\varkappa_i\mu_i\left[\varkappa_i^2 - \mu_i^2 - n^2\right] B^i_{n1} + \left[\varkappa_i^4 - 6\varkappa_i^2\mu_i^2 + \mu_i^4 - 2n^2(\varkappa_i^2 - \mu_i^2) + n^4\right] B^i_{n2} = 2(2+\nu)n\,\varkappa_i\mu_i C^i_{n1} + n\left[(2+\nu)(\varkappa_i^2 - \mu_i^2) - n^2\right] C^i_{n1}$	

TABLE 2.3.1.
Equations determining a^i_{njk} and b^i_{njk}.

The rotation ϕ_x in α direction follows from (A.3.1), (2.3.55) and (2.3.59)

$$\phi_x = \sum_{n=0}^{\infty} \phi_{xn}\cos n\beta \qquad (2.3.64)$$

where

$$\phi_{x0} = \frac{1}{R} \exp(-\kappa_{01}\alpha) \left[(-C^1_{01}\,\kappa_{01} + C^1_{02}\,\mu_{01}) \cos \mu_{01}\alpha + \right.$$

$$\left. - (C^1_{02}\,\kappa_{01} + C^1_{01}\,\mu_{01}) \sin \mu_{01}\alpha\right]$$

$$\phi_{x1} = \frac{1}{R} \exp(-\kappa_{11}\alpha) \left[(-C^1_{11}\,\kappa_{11} + C^1_{12}\,\mu_{11}) \cos \mu_{11}\alpha + \right. \qquad (2.3.65)$$

$$\left. - (C^1_{12}\,\kappa_{11} + C^1_{11}\,\mu_{11}) \sin \mu_{11}\alpha\right] + \frac{1}{R} D_2$$

$$\phi_{xn} = \sum_{i=1}^{2} \frac{1}{R} \exp(-\kappa_{ni}\alpha) \left[(-C^i_{n1}\,\kappa_{ni} + C^i_{n2}\,\mu_{ni}) \cos \mu_{ni}\alpha + \right.$$

$$\left. - (C^i_{n2}\,\kappa_{ni} + C^i_{n1}\,\mu_{ni}) \sin \mu_{ni}\alpha\right] , \quad \text{if } n > 1$$

Substitution from (2.3.59) to (2.3.63) into (A.3.2) and (A.3.3) leads to the series solution for the modified stress resultants and stress couples. Now the boundary loadings at the edge $\alpha = 0$ of the cylindrical shell can be found by substitution from this solution into (A.3.5) and taking $\alpha = 0$

$$[\overline{N}_x]_{\alpha=0} = \sum_{n=1}^{\infty} [\overline{N}_{xn}]_{\alpha=0} \cos n\beta \qquad [\overline{N}_{y_{red}}]_{\alpha=0} = \sum_{n=1}^{\infty} [\overline{N}_{yn}]_{\alpha=0} \sin n\beta \qquad (2.3.66)$$

$$[\overline{Q}_{red}]_{\alpha=0} = \sum_{n=0}^{\infty} [\overline{Q}_n]_{\alpha=0} \cos n\beta \qquad [M_n]_{\alpha=0} = \sum_{n=0}^{\infty} [M_{nn}]_{\alpha=0} \cos n\beta$$

where

$$[\overline{N}_{xn}]_{\alpha=0} = \frac{Eh}{(1-\nu^2)R} \sum_{i=1}^{2} \left[\{-a^i_{n11}\,\kappa_{ni} + a^i_{n21}\,\mu_{ni} + \left[\nu + (1-\nu)\,\frac{h^2}{12R^2}\right] nb^i_{n11} + \right.$$

$$+ \left[\nu + (1-\nu)\,\frac{h^2}{12R^2}\,n^2\right]\} C^i_{n1} + \{-a^i_{n12}\,\kappa_{ni} + a^i_{n22}\,\mu_{ni} +$$

$$\left. + \left[\nu + (1-\nu)\,\frac{h^2}{12R^2}\right] nb^i_{n12}\}C^i_{n2}\right] \qquad (2.3.67a)$$

$$[\bar{N}_{yn}]_{\alpha=0} = \frac{Eh}{(1-\nu^2)R}(1-\nu)\sum_{i=1}^{2}\Big[\{(-\tfrac{1}{2}+\frac{h^2}{12R^2})\,n a^i_{n11} - \tfrac{1}{2}\,b^i_{n11}\,\kappa_{ni} +$$

$$+\tfrac{1}{2}\,b^i_{n21}\,\mu_{ni} - \frac{h^2}{12R^2}\,n\,\kappa_{ni}\}C^i_{n1} + \{(-\tfrac{1}{2}+\frac{h^2}{12R^2})\,n\,a^i_{n12} +$$

$$-\tfrac{1}{2}\,b^i_{n12}\,\mu_{ni} + \frac{h^2}{12R^2}\,n\,\mu_{ni}\}C^i_{n2}\Big] \qquad (2.3.67b)$$

$$[\bar{Q}_n]_{\alpha=0} = \frac{Eh^3}{12(1-\nu^2)R^3}\sum_{i=1}^{2}\Big[\{\kappa_{ni}\,[\kappa^2_{ni} - 3\mu^2_{ni} - (2-\nu)\,n^2 + 1] +$$

$$+(1-\nu)\,n^2\,a^i_{n11}\}\,C^i_{n1} + \{\mu_{ni}\,[-3\kappa^2_{ni} + \mu^2_{ni} + (2-\nu)\,n^2 - 1] +$$

$$-\tfrac{1}{2}\,b^i_{n12}\,\kappa_{ni} + \tfrac{1}{2}\,b^i_{n22}\,\mu_{ni} + \frac{h^2}{12R^2}\,n\,\mu_{ni}\}C^i_{n2}\Big] \qquad (2.3.67b)$$

$$[M_{nn}]_{\alpha=0} = \frac{Eh^3}{12(1-\nu^2)R^2}\sum_{i=1}^{2}\Big[\{\kappa^2_{ni} - \mu^2_{ni} + (1-\nu n^2) + (1-\nu)\,n b^i_{n11}\}\,C^i_{n1} +$$

$$+\{-2\kappa_{ni}\,\mu_{ni} + (1-\nu)\,n b^i_{n12}\}\,C^i_{n2}\Big] \qquad (2.3.67d)$$

The condition of equilibrium of forces along the edge $\alpha = 0$ in the $\beta = 0$ direction and the moment equilibrium condition along the same edge in the $\beta = \pi/2$ direction lead with (2.3.66) to

$$[\bar{N}_{y1}]_{\alpha=0} = [\bar{Q}_1]_{\alpha=0}$$
$$[\bar{N}_{x1}]_{\alpha=0} = [\tfrac{1}{R}\,M_{n1}]_{\alpha=0} \qquad (2.3.68)$$

After utilizing the solution for a^1_{1jk} and b^1_{1jk} ($j=1,2$; $k=1,2$) resulting from table 2.3.1 for $n = 1$ and realizing that κ_{11} and μ_{11} are roots of the characteristic equation (2.3.57) it can be shown that the solution (2.3.67) automatically satisfies the conditions (2.3.68).

For the sake of brevity the relationship between the boundary loadings and the integration constants will be written in matrix notation as follows

$$\bar{q}_n = K_n \bar{c}_n \qquad (2.3.69)$$

where

$$\left.\begin{aligned}
\overline{q}'_n &= \left|\left[\overline{Q}_n\right]_{\alpha=0}\ \left[\tfrac{1}{R}M_{nn}\right]_{\alpha=0}\right|, \quad \text{if } n \leq 1 \\
\overline{q}'_n &= \left|\left[\overline{N}_{xn}\right]_{\alpha=0}\ \left[\overline{N}_{yn}\right]_{\alpha=0}\ \left[\overline{Q}_n\right]_{\alpha=0}\ \left[\tfrac{1}{R}M_{nn}\right]_{\alpha=0}\right|, \quad \text{if } n > 1
\end{aligned}\right\} \tag{2.3.70}$$

$$\left.\begin{aligned}
\overline{c}'_n &= \left|C^1_{n1}\ C^1_{n2}\right|, \quad \text{if } n \leq 1 \\
\overline{c}'_n &= \left|C^1_{n1}\ C^1_{n2}\ C^2_{n1}\ C^2_{n2}\right|, \quad \text{if } n > 1
\end{aligned}\right\} \tag{2.3.71}$$

while the K_n matrices follow from (2.3.67).
From (2.3.59), (2.3.61), (2.3.62), (2.3.63) and (2.3.65) follows the relationship between the Fourier's coefficients of the kinematic boundary quantities at $\alpha = 0$ and the unknown constants

$$\overline{w}_n = L_n \overline{c}_n \tag{2.3.72}$$

where

$$\left.\begin{aligned}
\overline{w}'_0 &= \left|\left[W_0\right]_{\alpha=0}\ \left[R\,\phi_{x0}\right]_{\alpha=0}\right| \\
\overline{w}'_1 &= \left|\left[W_1 + V_1\right]_{\alpha=0}\ \left[R\,\phi_{x1} + U_1\right]_{\alpha=0}\right| \\
\overline{w}'_n &= \left|\left[U_n\right]_{\alpha=0}\ \left[V_n\right]_{\alpha=0}\ \left[W_n\right]_{\alpha=0}\ \left[R\,\phi_{xn}\right]_{\alpha=0}\right|, \quad \text{if } n > 1
\end{aligned}\right\} \tag{2.3.73}$$

and

$$\left.\begin{aligned}
L_0 &= \begin{bmatrix} 1 & 0 \\ -\kappa_{01} & \mu_{01} \end{bmatrix} \\
L_1 &= \begin{bmatrix} (1+b^1_{111}) & b^1_{112} \\ (-\kappa_{11}+a^1_{111}) & (\mu_{11}+a^1_{112}) \end{bmatrix} \\
L_n &= \begin{bmatrix} a^1_{n11} & a^1_{n12} & a^2_{n11} & a^2_{n12} \\ b^1_{n11} & b^1_{n12} & b^2_{n11} & b^2_{n12} \\ 1 & 0 & 1 & 0 \\ -\kappa_{n1} & \mu_{n1} & -\kappa_{n2} & \mu_{n2} \end{bmatrix}, \quad \text{if } n > 1
\end{aligned}\right\} \tag{2.3.74}$$

From (2.3.72) and (2.3.69) follows

$$\overline{q}_n = K_n L_n^{-1} \overline{w}_n \tag{2.3.75}$$

The virtual work δV_{cyl} done by a general equilibrium system of boundary loadings acting at $\alpha = 0$ is equal to

$$\delta V_{cyl} = - \left[2 \pi R \overline{q}'_0 \overline{\delta w}_0 + \pi R \overline{q}'^{*}_1 \overline{\delta w}^{*}_1 + \pi R \sum_{n=2}^{\infty} \overline{q}'_n \overline{\delta w}_n \right] \tag{2.3.76}$$

where

$$\overline{q}'^{*}_1 = \left| \left[\overline{N}_{x1} \right]_{\alpha=0} \left[\overline{N}_{y1} \right]_{\alpha=0} \left[\overline{Q}_1 \right]_{\alpha=0} \left[\frac{1}{R} M_{n1} \right]_{\alpha=0} \right| \tag{2.3.77}$$

while

$$\overline{w}'^{*}_1 = \left| \left[U_1 \right]_{\alpha=0} \left[V_1 \right]_{\alpha=0} \left[W_1 \right]_{\alpha=0} \left[R \phi_{x1} \right]_{\alpha=0} \right| \tag{2.3.78}$$

Substitution from (2.3.68) and (2.3.75) into (2.3.76) leads to the following expression for δV_{cyl}

$$\delta V_{cyl} = - \left[2 \pi R \overline{w}'_0 \left[L'^{-1}_0 \right] K'_0 \overline{\delta w}_0 + \pi R \overline{w}'_1 \left[L'^{-1}_1 \right] K'_1 \overline{\delta w}_1 + \right.$$

$$\left. + \pi R \sum_{n=2}^{\infty} \overline{w}'_n \left[L'^{-1}_n \right] K'_n \overline{\delta w}_n \right] \tag{2.3.79}$$

CHAPTER 3. ANALYSIS OF LARGE-DIAMETER, HIGH-PRESSURE VESSEL FLANGES

3.1. Introduction.

Interest in the behaviour of high-pressure flanges has been stimulated by the advent of light-water-cooled and moderated nuclear reactors. The bolted flange joint between the pressure vessel head and body combines large size (typically, PWR with inside vessel diameter ≈ 3.5 - 4.5 m for ≈ 155 bar internal pressure and BWR with inside vessel diameter ≈ 5.5 - 6.5 m for ≈ 70 bar internal pressure) with unusually stringent leak-tightness requirement (typically, zero leakage past the outer O-ring during normal operation and transients). Figure 3.1.1 shows the tapered hub design and metal-to-metal gasket aided by concentric metal O-rings typical for such flange joints. The most significant difference between the type of flange joint shown and the more common low-pressure flanges concerns the flange ring thickness to width ratio, whose magnitude is of order unity for the high-pressure case while it is relatively small (say $\lesssim \frac{1}{3}$) for the low-pressure case. Therefore the (elastic) thin plate approach for the flange ring, underlying flange design according to the Divisions 1 and 2 of Section VIII of the ASME Boiler and Pressure Vessel Code [1.2, 1.6], and developed in the classic paper by WATERS, WESSTROM, ROSSHEIM and WILLIAMS [3.1], cannot be utilized for the purpose of the present thesis.
As pointed out in Chapter 1.1 the (overall) behaviour of the flange connection is assumed to be elastic, thereby excluding methods of analysis which account for plastic hinges near the juncture between the flange and the vessel. These methods have been developed e.g. by LAKE and BOYD [3.2] (thin plate approach for flange ring), underlying the British Code BS 1500 [3.3], and by SIEBEL and KRÄGELOH [3.4] (rigid ring approach for flange ring), underlying the German Code [3.5]. They should be excluded for the large-diameter high-pressure flanges of interest because of the extremely stringent leak-tightness requirements mentioned before which enforce the deformation of the flange ring to be restricted within narrow limits.

An essential step in meeting the leak-tightness requirements consists of tightening the bolted flange connection in such a way that the total load is distributed as uniformly as possible over the individual bolts. This problem has been known for a long time and has been solved satisfactorily for most applications by straightforward practical engineering, e.g. the use of torque wrenches. In the case of the flange joints for large-diameter, high-pressure vessels of interest for the present thesis, however, the problem acquires a new importance due to the extremely high requirements for leak-tightness. Size and accessibility of the bolts having led to the almost exclusive use of hydraulic bolt tensioners (cf. figure 3.1.1), one solution -patented in some countries- has been to provide a "crown" of such hydraulic jacks for simultaneous extension of *all* the bolts. The next section of the present chapter describes the development of an alternative method for obtaining the desired uniform load distribution, in which the bolts are tightened groupwise in a single loading cycle.

Starting from a supposedly uniform distribution of bolt load, all methods commonly used in flange analysis assume both the loading and the geometry of the flange to be axisymmetric. An appraisal of this approximation has been given by MENKEN [3.6] who investigated an integral flange model without weakening by bolt holes and with concentrated bolt loads at the bolt pitch circle. From the numerical results given in [3.6] the important conclusion can be drawn that the influence of the local character of bolt loads on the average flange deformation pattern is negligibly small for the range of flange dimensions of interest for large-diameter, high-pressure vessels, i.e.

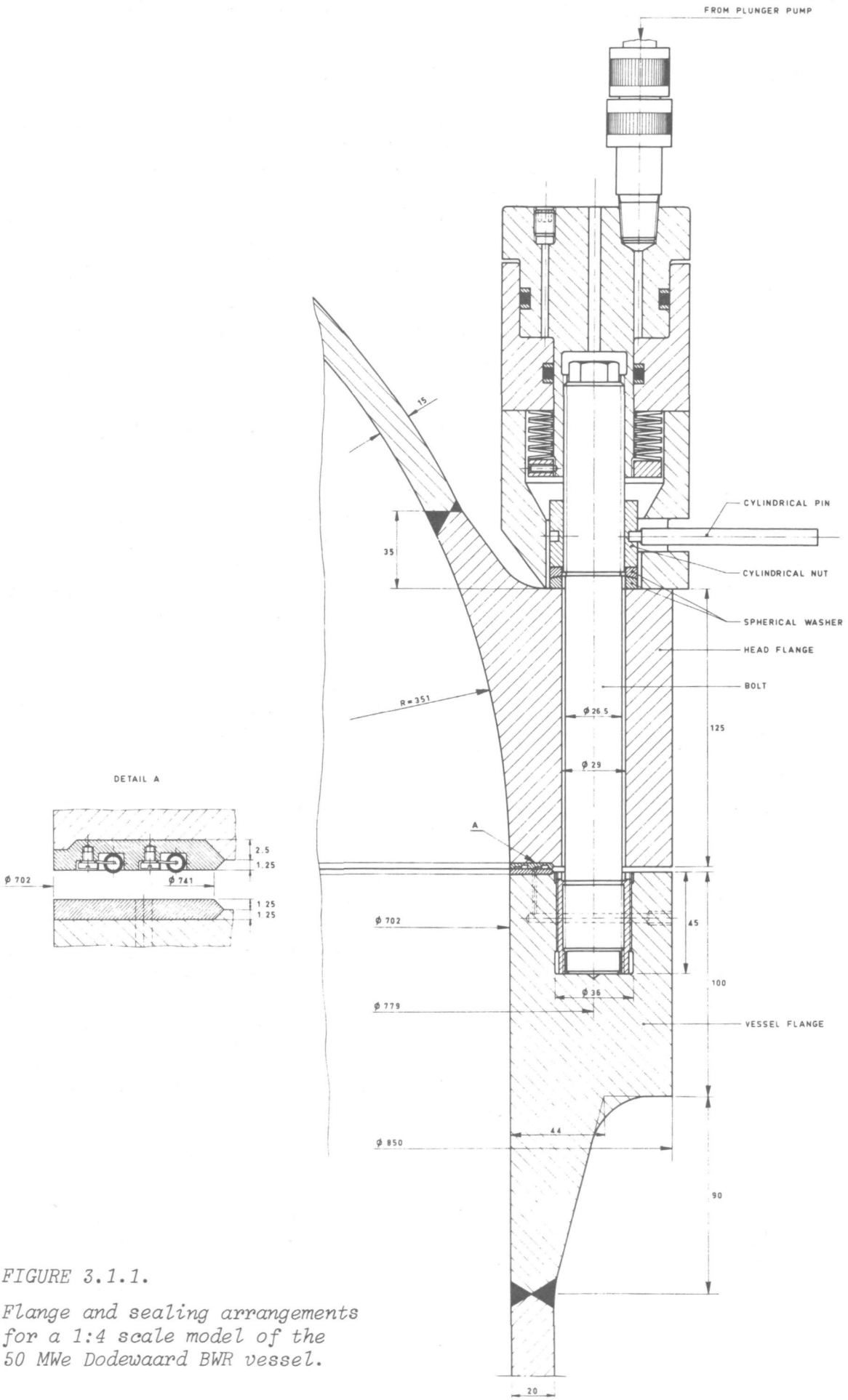

FIGURE 3.1.1.

Flange and sealing arrangements for a 1:4 scale model of the 50 MWe Dodewaard BWR vessel.

$$0.5 \leqslant \frac{t}{b_F} \leqslant 2.0; \qquad \frac{b_F}{r_{cf}} \leqslant 0.3,$$

r_{cf} being the radius of the flange ring center of gravity circle, b_F the flange ring width and t the thickness of the flange ring (cf. figure 3.1.2).

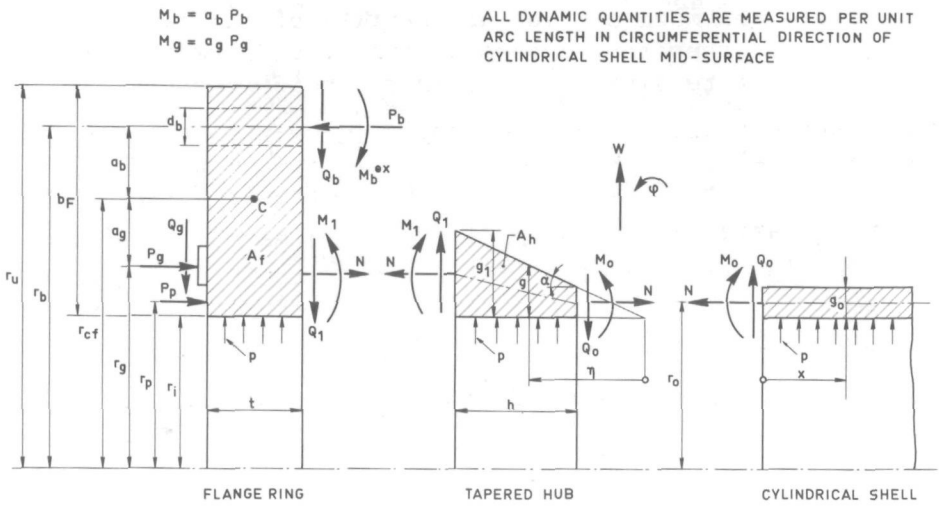

FIGURE 3.1.2.

Constituent elements with in- and external loading.

On the basis of the axisymmetric character of loading and geometry, the general practice in deformation and stress analysis of pressure vessel flanges is to divide each member into its three constituent elements, i.e. ring, hub and shell (cf. figure 3.1.2). After determining the external loadings, the deformation of each of the three elements can be expressed in terms of the redundant shear forces and moments at their junctions. By applying the conditions of equilibrium and compatibility at the junctions, a set of simultaneous linear equations is obtained, which can be solved for the redundant forces and moments. Evaluation of the flange deformation is then a straightforward matter. In determining the deformation of the separate elements the following schematizations are usual:

a. The flange ring is supposed to have an undeformable radial cross section. A rigorous numerical investigation carried out by VISSER [3.7] on the basis of the finite element method for the representative case

$$\frac{t}{b_F} = 1.35; \qquad \frac{b_F}{r_{cf}} = 0.19; \qquad \frac{g_0}{r_0} = 0.06$$

showed, as one might expect, that this is a realistic assumption, except for a small region in the neighbourhood of the gasket face, where plastic deformation can be expected to occur. The implications of this local effect will be discussed later. Experimental results reported by VAN CAMPEN and BROEKHOVEN [3.8] for the same case completely confirmed the numerical results.

b. The cylindrical or the spherical shell is treated by thin shell theory, using the GECKELER approximation [3.9] in the case of hemispherical head.

c. The tapered hub is considered either as a thin cylindrical shell with linearly varying thickness and a small taper [3.10, 3.11, 3.12] or as a ring with undeformable radial cross section [3.13]. Particularly for the tapered hub of the head flange shown in figure 3.1.1, the former approach may become doubtful because of the large taper and the short length of the hub. At the same time this squat shape suggests the much simpler alternative of the latter approach. Section 3.3.1 therefore offers a comparison between these alternatives using a finite element analysis for reference.

An important consequence of the compact geometry of large-diameter, high-pressure vessel flanges is the small difference between the bolt pitch radius r_b and that of the centroid of the (full) flange cross section r_{cf}. Thus, their radial distance ($r_b - r_{cf} = a_b$) may be considerably smaller than the radial distance from the centroid to the point of application of the gasket force P_g ($r_{cf} - r_g = a_g$), which enhances the relative importance of the gasket reaction moment M_g (figure 3.1.2) as compared to the bolting moment M_b. The importance of this effect can be exemplified by the geometry of the vessel flange shown in figure 3.1.1. For initial bolt loading, where P_g equals P_b, the resulting moment M_g will vary between the extreme values 24 M_b and 12 M_b, corresponding to the point of application being taken at the inner rim or at the outer rim of the gasket surface respectively. By contrast the geometry of the low-pressure (18.7 bar) flange investigated by MURRAY and STUART [3.10] is such that the radial distance from the bolt circle to the centroid exceeds that from the possible point of application of P_g by a factor of about 8. Thus, the relative importance of M_g is almost negligible. The above discussion poses the problem of determining the exact location of the point of application of the gasket force P_g. The last sub-section of this chapter presents some experimental information pertinent to this problem and, on the basis of this information, offers an experimental check on the validity of the computational method.

3.2. A systematic semi-empirical bolt-tightening procedure.

3.2.1. Experimental equipment.

The experiments from which the tightening procedure was gleaned have been carried out on a 1:4 scale model of the reactor pressure vessel of the 50 MWe Dodewaard BWR (design pressure 87.9 atm; design temperature 301.6 ^{o}C). The 36 bolts of the flange connection (shown in figure 3.1.1) of this model vessel were prestressed by nine hydraulic jacks, in four groups of nine bolts each. The nine hydraulic jacks were pressurized simultaneously by a hand-operated plunger pump through a manifold and nine high-pressure hoses. The maximum jack loading achievable with the plunger pump is about 28 tf, corresponding to a jack pressure of 1,000 bar.
After prestressing, the nine cylindrical nuts of the group were turned hand-tight, after which the jacks were relieved. Tightening of each of the nuts was done with a cylindrical pin, fitting in radial holes in the nut. The bolt forces have been determined with strain gages of flat-wire grid construction and of 3 mm filament length. In order to obtain detailed information on the distribution of bolt moments acting in the plane through the bolt axis and the vessel axis, each bolt has been provided with four

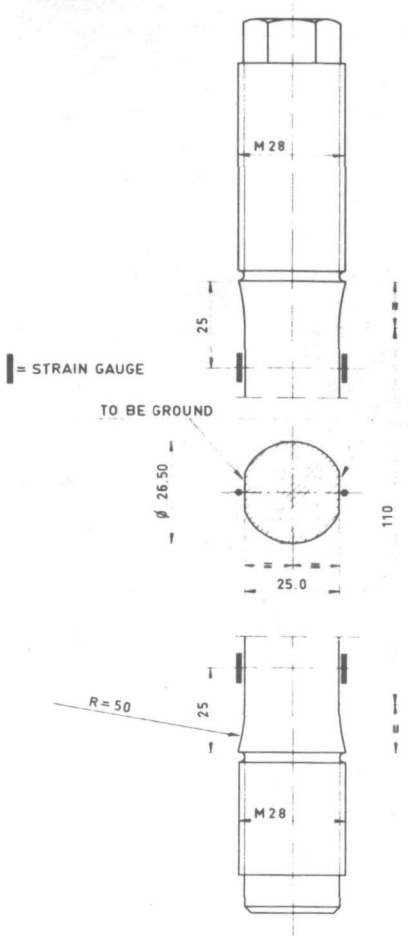

FIGURE 3.2.1.

Measuring bolt with strain gauges.

gages in this plane (cf. figure 3.2.1). Due to the small clearance between the bolt shaft and the bolt holes in the head flange, it has been necessary to grind two flat faces on the bolts to minimize the risk of damaging the strain gauges during the assembly of the head flange.

Figure 3.2.2 shows the test arrangement for hydraulic tightening of the flange connection of the model vessel. The strains were measured by means of a fully automatical digital installation which could scan 400 strain gauges at a speed of 4 gauges per second. The strains measured were punched by an 8-channel tape puncher and were consecutively fed into an electronic digital computer in order to correct for zero-drift, k-factor and wire resistance and to calculate all strains and stresses required.

The four groups of nine bolts each mentioned before will be denoted further as series 1 through 4, series 1 starting with bolt 1, series 2 starting with bolt 3, series 3 starting with bolt 2, and series 4 starting with bolt 4 (cf. figure 3.2.3, see p. 45).

3.2.2. Experiments on the interaction between groups of bolts.

In order to determine the behaviour of the bolts and to obtain information on the interaction between the various groups of bolts during prestressing, the following experiments have been carried out consecutively:

Experiment 1.
The strains in the bolts of series 1 were determined for 50 bar jack pressure loading. Subsequently the nuts were turned handtight, jack pressure was released, and the remaining strains in the bolts were measured. Similar measurements have been performed at jack pressures increasing in steps of 50 bar up to 800 bar inclusive. This last pressure is representative for the mean jack pressure required for tightening the flange connection for an internal vessel pressure of 120 bar (the test pressure).
After this procedure, the nuts of series 1 were loosened, and the same measurements were performed on the series 2, 3 and 4.

Experiment 2.
The bolts of series 1 were tightened by loading the bolts with a jack pressure of 500 bar, fastening the nuts handtight, and relieving the jacks. After measuring the strains, the bolts of series 2 were tightened at a jack pressure of 50 bar and the strains in the bolts of series 1

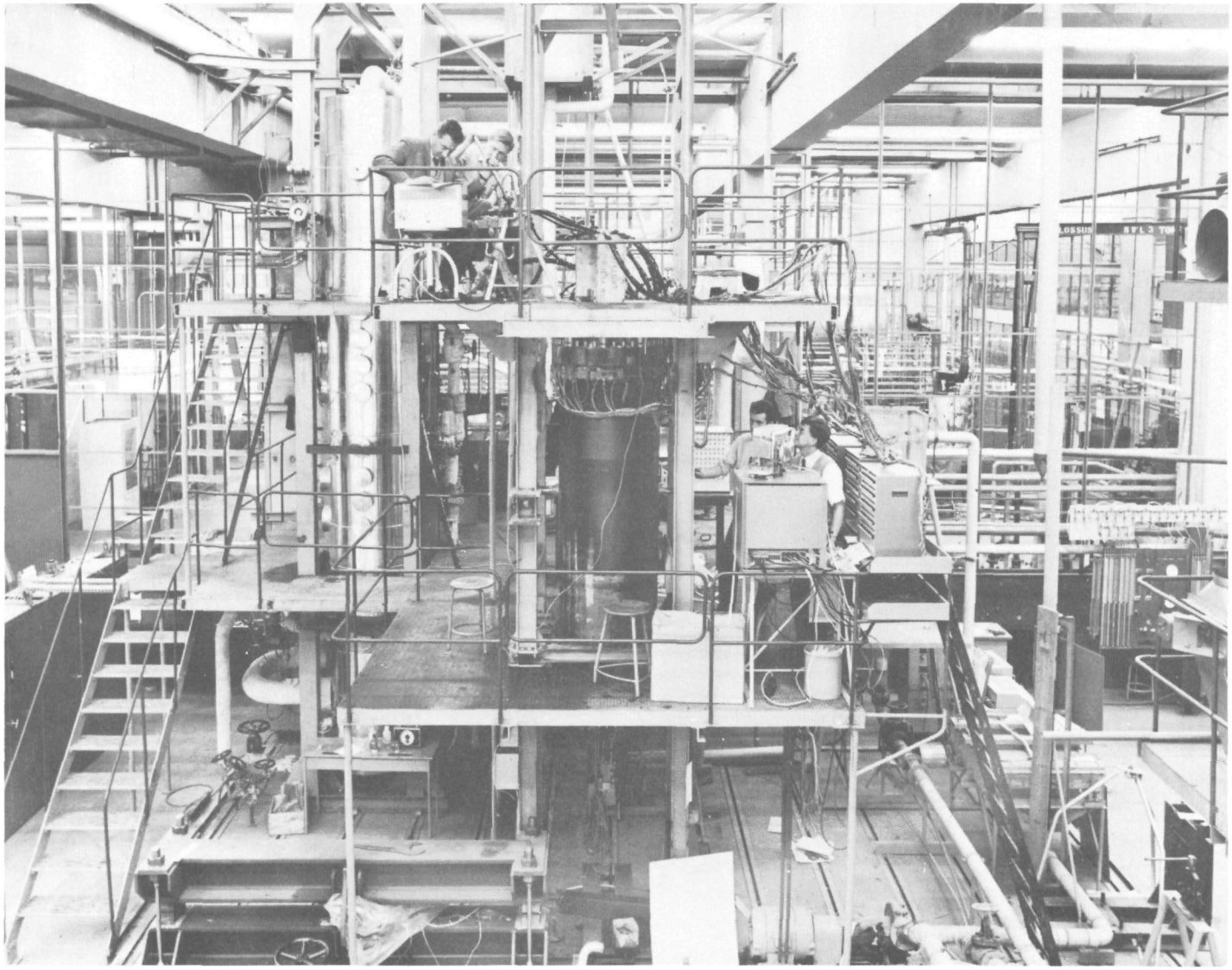

FIGURE 3.2.2.

Hydraulic bolt tightening of the flange connection of the model vessel.

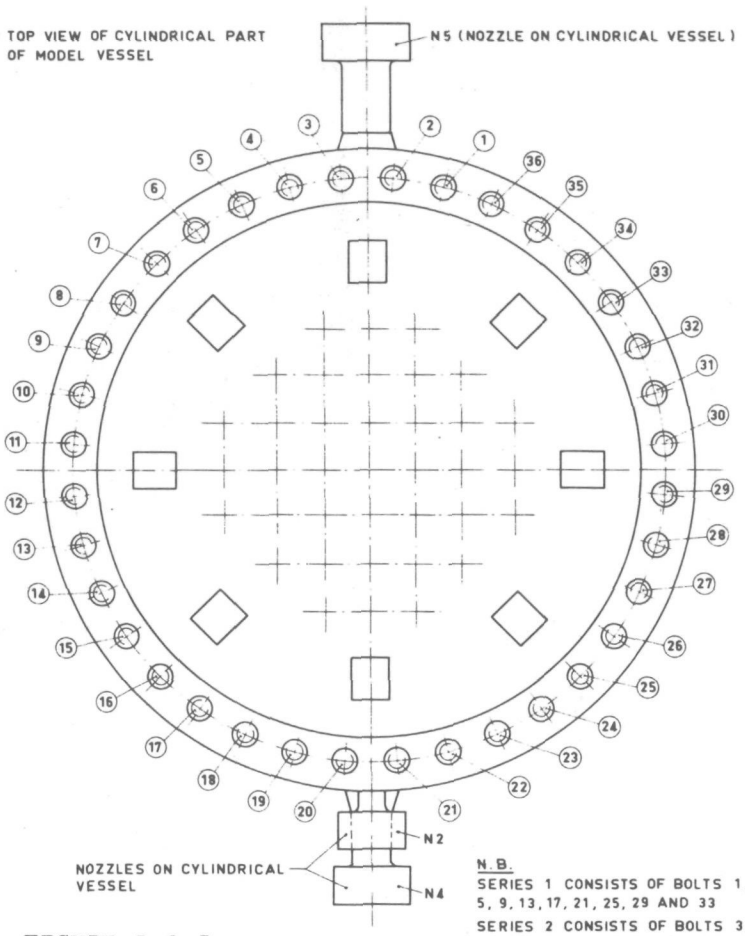

FIGURE 3.2.3.

Numbering of bolts and groups of bolts.

and 2 were measured both under jack pressure loading and after fastening the nuts at released pressure. Similar measurements have been performed at jack pressures increasing in steps of 50 bar up to 500 bar inclusive. Subsequently the same procedure has been applied to the series 3 and 4, measuring at each jack pressure step the strains in all the stressed bolts at pressure loading and after fastening the nuts at released jack pressure.

Experiment 3.
This experiment was identical to the preceding experiment, except that the ultimate jack pressure for each of the bolt series was equal to 800 bar in stead of 500 bar. Again tightening of the series 2, 3 and 4 took place in steps of 50 bar.

Experiment 4.
The bolts of series 1 were tightened at a jack pressure of 50 bar and the strains were measured. After this, the bolts of series 2 were tightened at a jack pressure of 500 bar and the strains in the bolts of series 1 and 2 were measured both at jack pressure loading and after fastening the nuts at released pressure. Subsequently the bolts of series 2 were tightened at a jack pressure of 800 bar and the same measurements were performed.
After this procedure, the nuts of series 2 and 1 were loosened and similar measurements performed at jack pressures for series 1 increasing in steps of 50 bar up to 800 bar inclusive, while in each

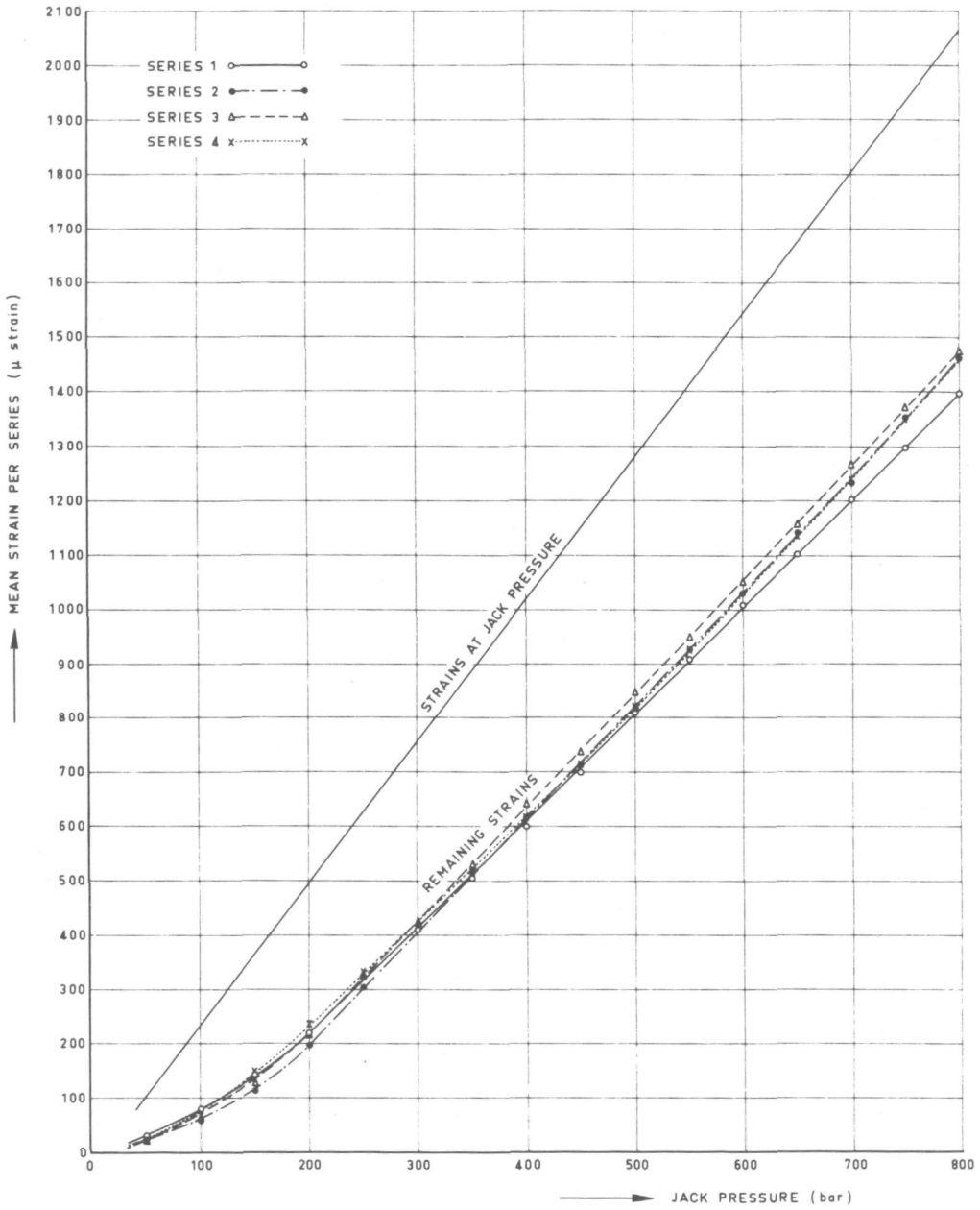

FIGURE 3.2.4.

Results of experiment 1:

Relation between jack pressure, mean strain per series at this pressure and mean remaining strains.

case the jack pressures applied for series 2 were 500 bar and 800 bar respectively.

Experiment 5.
The bolts of series 1 and 2 were tightened successively at a jack pressure of 50 bar and the strains were measured. After this, the bolts of series 3 were tightened at a jack pressure of 500 bar and the strains in the bolts of series 1, 2 and 3 were measured both at jack pressure loading and after fastening the nuts at released pressure. Subsequently the bolts of series 3 were tightened at a jack pressure of 800 bar and the same measurements were performed.
After this procedure, the nuts of series 3, 2 and 1 were loosened and similar measurements have been performed at jack pressures for series 1 and 2 increasing in steps of 50 bar up to 800 bar inclusive, while the jack pressures applied for series 2 again were 500 bar and 800 bar respectively.

The results of the experiments described above will be *discussed* now in some detail.

Experiment 1.
Figure 3.2.4 shows the relation between the oil pressure in the jacks and the mean strain in each of the bolt series occurring at this pressure, together with the remaining mean strains in the bolt series after fastening the nuts and relieving the jacks.
Inasmuch as the mean strain in a bolt is proportional to the normal force in that bolt and the oil pressure in the jack is proportional to the normal force in the bolt occurring at this pressure, the relation between the remaining and the applied mean normal force per series immediately follows from this figure. The ratio between these two forces is defined to be the (mean) jack efficiency (although this efficiency does not depend solely on the jack).
The (relatively small) differences between the remaining mean strains in the bolt series after relieving the jacks are caused by small differences in the measures of the spherical washers under the nuts, and by differences due to the manual nut-tightening procedure following pressurizing of the jacks. These last differences have been kept as small as is feasible by measuring the tightening moment on the nut with strain gauges attached to the cylindrical pin. It should be pointed out that the relative differences between the remaining mean strain in a bolt series and the remaining mean strains in the individual bolts of this series at 800 bar tightening never exceeded 7.5%.
From figure 3.2.4 the important conclusion can be drawn that the relationship between the remaining mean strains and the oil pressure in the jacks becomes linear for each bolt series as the jack pressure rises. The slope in this linear relationship can be assumed to be the same for all the bolt series within sufficient accuracy. On the other hand, this slope differs from the slope in the linear relationship between the mean strains at jack pressure and this pressure itself. This means that the former slope has to be determined by a two-step tightening of each bolt series.

Experiments 2 and 3.
Tables 3.2.1 and 3.2.2 (see p. 50) summarize the results of these experiments, considered as tightening experiments for the head flange at jack pressures of 500 bar and 800 bar respectively. For the sake of brevity only the more detailed results of experiment 3 will be given.
Figures 3.2.5, 3.2.6 and 3.2.7 (see pp. 48, 49 and 51) show the decrease of the mean strains of the bolt series 1, 2 and 3 respectively due to the tightening of subsequent bolt series both at jack pressure loading and after fastening the nuts and relieving the jacks. From these figures

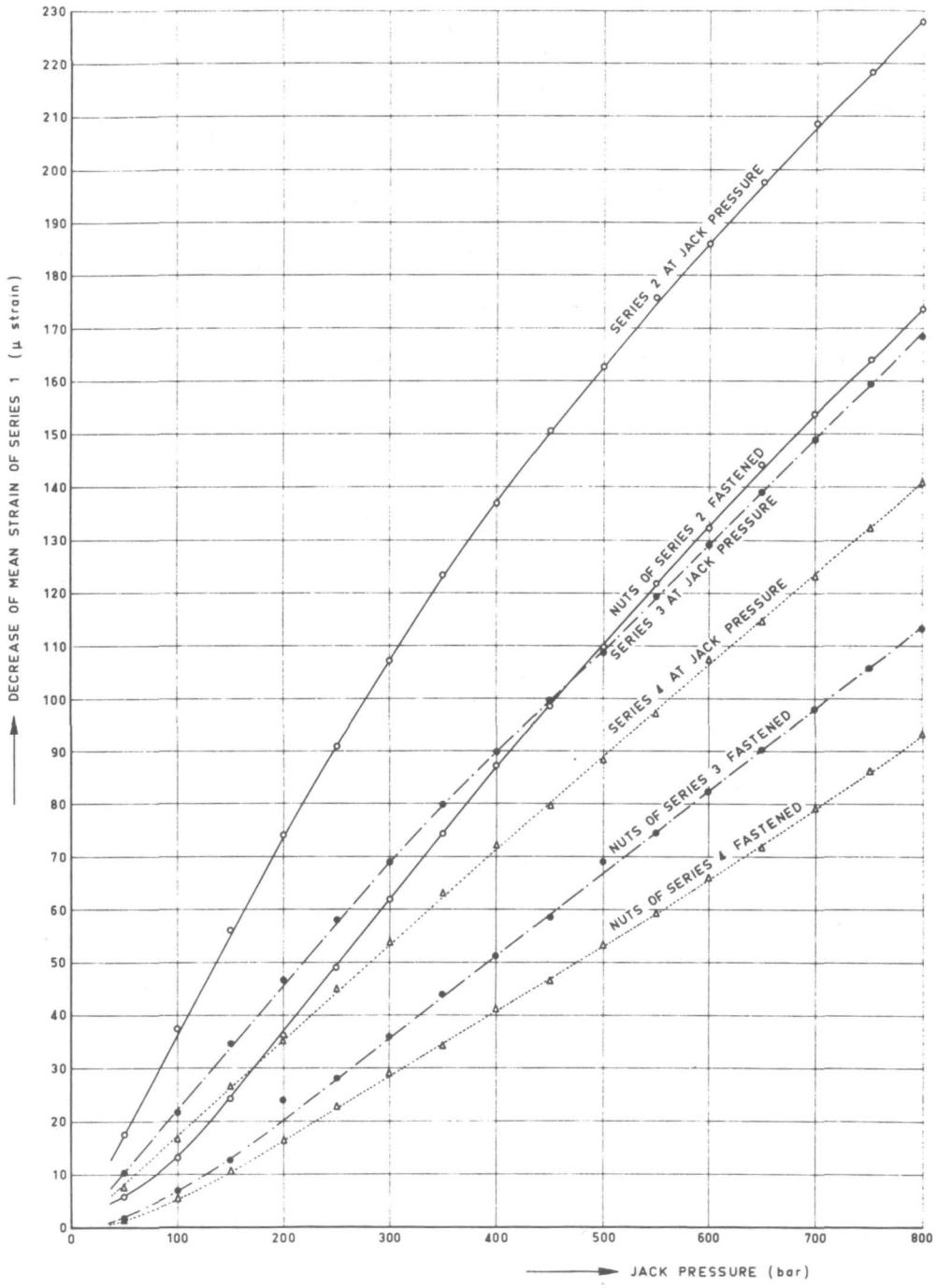

FIGURE 3.2.5.

Results of experiment 3:

Decrease of mean strain of series 1 at tightening of series 2, 3 and 4 respectively.

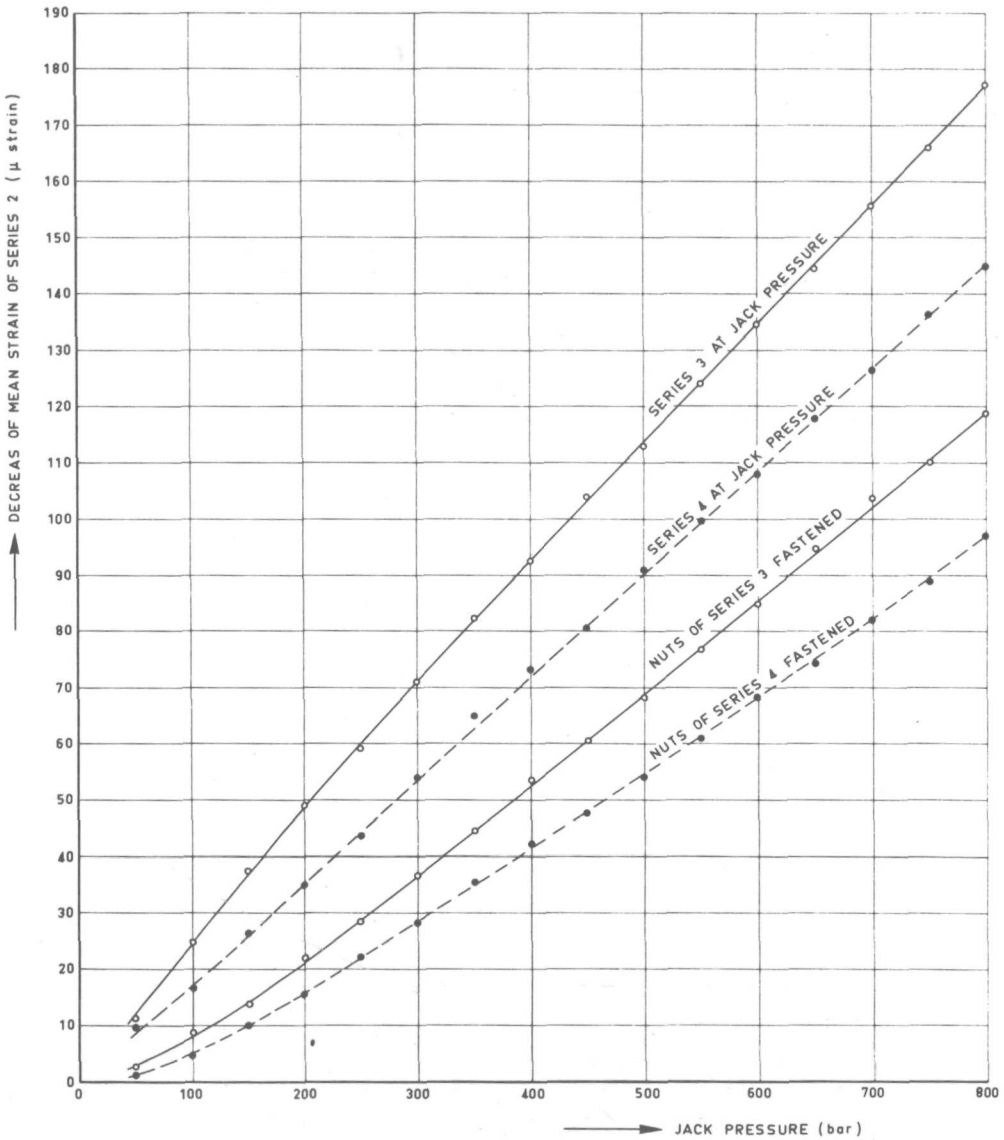

FIGURE 3.2.6.

Results of experiment 3:

Decrease of mean strain of series 2 at tightening of series 3 and 4 respectively.

the important conclusion can be drawn that the relationship between the decrease of mean strain and the jack pressure of subsequently tightened series may assumed to be linear within sufficient accuracy from a practical point of view at jack pressures exceeding about 200 bar. An exception to this conclusion is given by the decrease of the mean strain of series 1 at tightening of series 2 (cf. figure 3.2.5). Due to the relatively small deviation from linearity the relationship mentioned previously is also assumed to be linear in this case. It should be noted that the results of experiment 2 completely justified the above conclusion and did not show a relevant deviation from linearity in the case mentioned before.

TIGHTENED BOLT SERIES		1	1 AND 2	1, 2 AND 3	1, 2, 3 AND 4
JACK PRESSURE (bar)		500	500	500	500
MEAN STRAIN (μ strain) IN EACH BOLT SERIES	1	830	706	611	541
	2		830	725	649
	3			830	769
	4				830

TABLE 3.2.1.

Results of tightening head flange at jack pressures of 500 bar.

TIGHTENED BOLT SERIES		1	1 AND 2	1, 2 AND 3	1, 2, 3 AND 4
JACK PRESSURE (bar)		800	800	800	800
MEAN STRAIN (μ strain) IN EACH BOLT SERIES	1	1450	1276	1163	1071
	2		1450	1332	1235
	3			1450	1378
	4				1450

TABLE 3.2.2.

Results of tightening head flange at jack pressures of 800 bar.

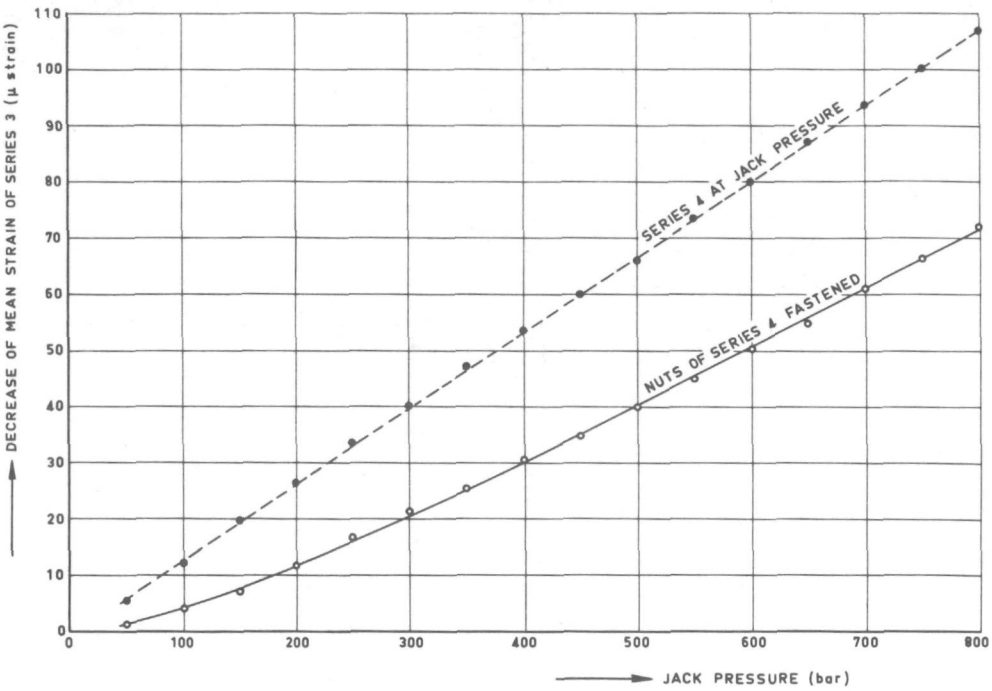

FIGURE 3.2.7.

Results of experiment 3:

Decrease of mean strain of series 3 at tightening of series 4.

Experiments 4 and 5.
Figure 3.2.8 (see p. 52) shows the decrease of the mean strain of bolt series 1 due to subsequent tightening of bolt series 2 at variable jack pressures for series 1. Figure 3.2.9 (see p. 53) gives similar results for the decrease of the mean strain of the bolt series 1 and 2 due to subsequent tightening of bolt series 3. It should be noted in this context that the results did not show a relevant difference between the decrease of the mean strains of the bolt series 1 and 2. From figures 3.2.8 and 3.2.9 it appears that the relationship between the decrease of mean strain of a bolt series and the jack pressure applied during tightening of that series may assumed to be linear from practical point of view at jack pressures exceeding about 350 bar.
As a supplementary result from these experiments it appeared that the mean strains of bolt series during tightening of these series are not influenced by the jack pressures of previously tightened series.

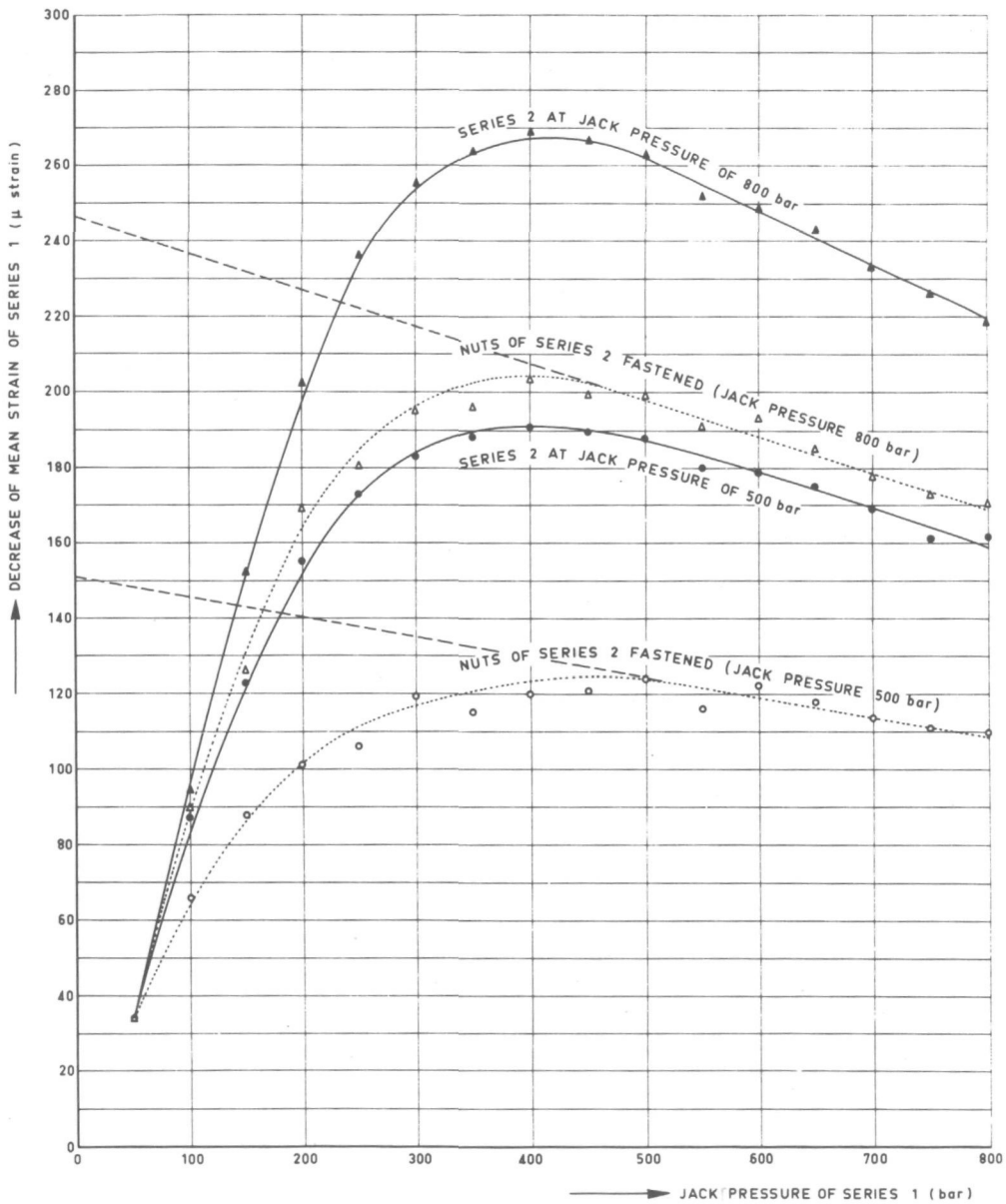

FIGURE 3.2.8.

Results of experiment 4:

Decrease of mean strain of series 1 due to tightening of series 2 at variable jack pressures of series 1.

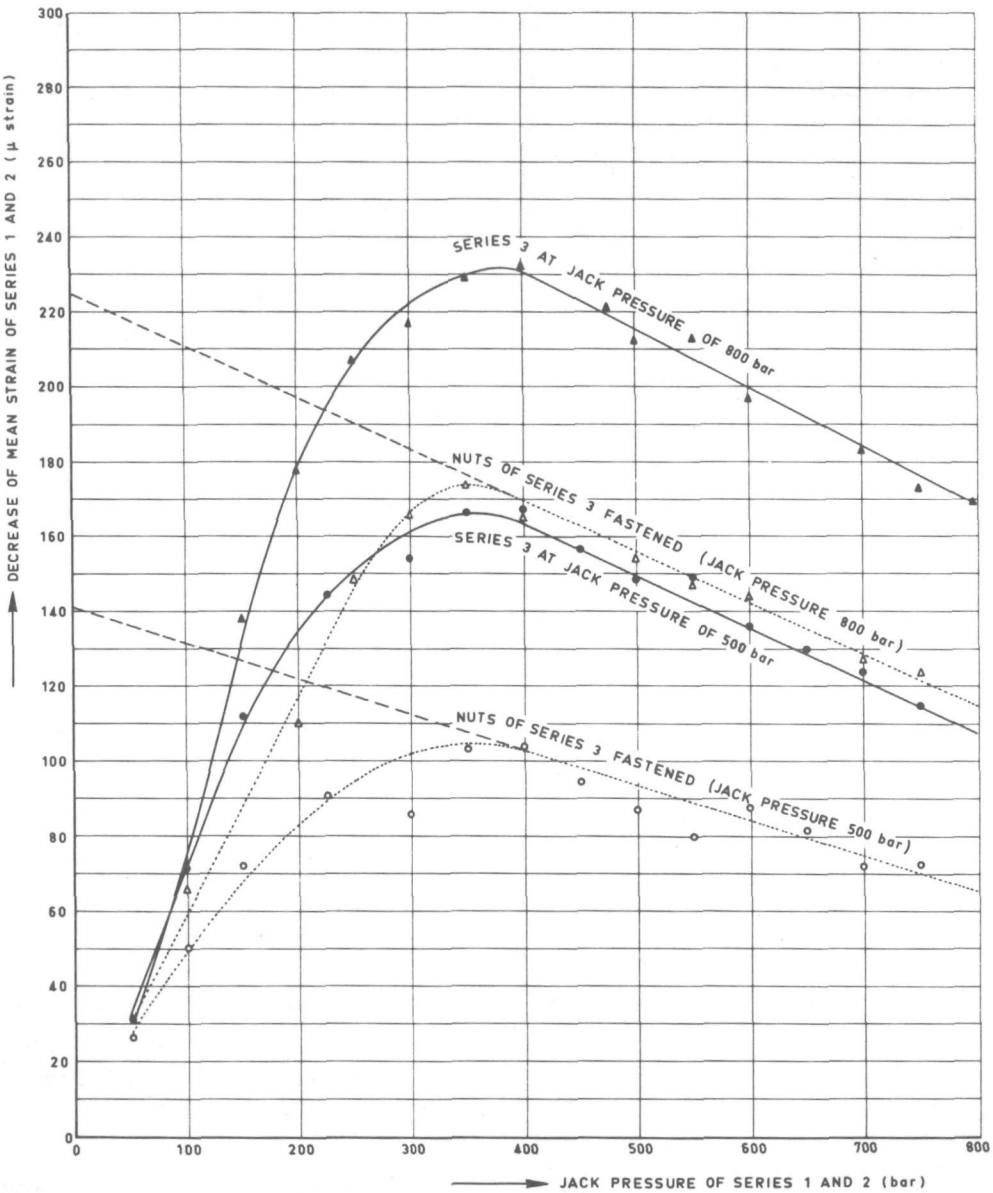

FIGURE 3.2.9.

Results of experiment 5:

Decrease of mean strain of series 1 and 2 due to tightening of series 3 at variable jack pressures of series 1 and 2.

3.2.3. A systematic tightening procedure.

As an introduction to the tightening procedure to be proposed in this sub-section the author should like to recall an earlier more simple procedure developed in [3.14] and based on less rigorous experiments. The basic assumptions of this procedure consisted of:

a. Proportionality between the remaining mean strain in any one bolt series and the jack pressure applied during tightening of that series, together with independence of this strain of the jack pressures of previously tightened series.

b. Proportionality between the decrease of mean strain in any bolt series and the jack pressures of subsequently tightened bolt series, together with independence of this decrease of both the jack pressures of previously tightened series and the jack pressure applied to that series itself.

Under these assumptions, the following formulas describe an arbitrary tightening procedure (to be denoted further as *simplified tightening procedure*)

$$a_{11}p_1 + a_{12}p_2 + a_{13}p_3 + a_{14}p_4 = b_1$$

$$a_{22}p_2 + a_{23}p_3 + a_{24}p_4 = b_2$$

$$a_{33}p_3 + a_{34}p_4 = b_3$$

$$a_{44}p_4 = b_4$$

in which a_{11} through a_{44} are functions of the flange geometry ($a_{ii} > 0$; $a_{ij} < 0$, if $i \neq j$), while p_1 through p_4 are associated with the bolt series 1 through 4, and b_1 through b_4 represent the mean strains remaining in the series 1, 2, 3 and 4 respectively after the tightening procedure. These formulas can be written also as follows

$$\sum_{j=i}^{4} a_{ij}\, p_j = b_i \qquad (i = 1, 2, 3, 4) \qquad (3.2.1)$$

Determination of the "influence coefficients" a_{ij} required a preliminary tightening experiment, which could, in principle, be of arbitrary nature, provided the hydraulic jack pressures for this experiment were selected in reasonable agreement with one of the pressures estimated for the ultimate tightening procedure.

On the basis of the results of the experiments described in the preceding paragraph an *improved tightening procedure* can be obtained by replacing the assumptions underlying (3.2.1) by:

a. Linear relationship between the remaining mean strain in any one bolt series and the jack pressure applied during tightening of that series (experiment 1), together with independence of this strain of the jack pressures of previously tightened series (experiments 4 and 5).

b. Linear relationship between the decrease of mean strain in any one bolt series and the jack pressures of subsequently tightened bolt series (experiments 2 and 3), together with linearity between this decrease

and the jack pressure applied during tightening of that series itself (experiments 4 and 5).

On the basis of these assumptions the following formulas describe an improved tightening procedure

$$\sum_{j=i}^{4} [a_{ij}p_j + c_{ij}] = b_i \qquad (i = 1, 2, 3, 4) \tag{3.2.2}$$

where

$$a_{ij} = a_{ij0} + \sum_{k=1}^{j-1} a_{ijk}p_k \tag{3.2.3}$$

$$c_{ij} = c_{ij0} + \sum_{k=1}^{j-1} c_{ijk}p_k \tag{3.2.4}$$

In these formulas a_{ijk} and c_{ijk} are functions of the flange geometry, while, on the basis of the second part of assumption a, we have

$$\left.\begin{aligned} a_{iik} &= 0 \\ c_{iik} &= 0 \end{aligned}\right\} \text{ if } k > 0 \tag{3.2.5}$$

From the experiments 2, 3, 4 and 5 the following conclusion can be drawn

$$c_{ijk} = 0, \quad \text{if } k > 0 \tag{3.2.6}$$

The following supplementary relations for the coefficients a_{ijk} and c_{ijk} result from symmetry considerations

$$\begin{aligned} &a_{110} = a_{220} = a_{330} = a_{440} \; ; \; c_{110} = c_{220} = c_{330} = c_{440} \\ &a_{130} = a_{230} = a_{140} = a_{240} \; ; \; c_{130} = c_{230} = c_{140} = c_{240} \\ &a_{131} = a_{232} = a_{141} = a_{242} \; ; \; a_{121} = a_{343} \\ &a_{120} = a_{340} \; ; \; c_{120} = c_{340} \; ; \; a_{143} = a_{243} \\ &a_{132} = a_{142} = a_{231} = a_{241} = a_{341} = a_{342} \end{aligned} \tag{3.2.7}$$

Thus we arrive at the final formulas describing an improved tightening procedure, being given in table 3.2.3 (see p. 56). Due to the more complicated character of these formulas, as compared with (3.2.1), the determination of the 7 unknown coefficients a_{ijk} and the 3 unknown coefficients c_{ij0} needs, in general, two preliminary tightening experiments.
Once the coefficients a_{ijk} and c_{ij0} are known, the relationships from table 3.2.3 can be used once more for the determination of a tightening procedure resulting in uniform mean bolt strains for each bolt series if

$$b_1 = b_2 = b_3 = b_4 = b \tag{3.2.8}$$

$$\left[a_{110}p_1 + c_{110}\right] + \left[\left\{a_{120} + a_{121}p_1\right\}p_2 + c_{120}\right] + \left[\left\{a_{130} + a_{131}p_1 + a_{132}p_2\right\}p_3 + c_{130}\right] + \left[\left\{a_{130} + a_{131}p_1 + a_{132}p_2 + a_{143}p_3\right\}p_4 + c_{130}\right] = b_1$$

$$\left[a_{110}p_2 + c_{110}\right] + \left[\left\{a_{130} + a_{132}p_1 + a_{131}p_2\right\}p_3 + c_{130}\right] + \left[\left\{a_{130} + a_{132}p_1 + a_{131}p_2 + a_{143}p_3\right\}p_4 + c_{130}\right] = b_2$$

$$\left[a_{110}p_3 + c_{110}\right] + \left[\left\{a_{120} + a_{132}(p_1 + p_2) + a_{121}p_3\right\}p_4 + c_{120}\right] = b_3$$

$$\left[a_{110}p_4 + c_{110}\right] = b_4$$

TABLE 3.2.3.

Formulas describing an improved tightening procedure.

By prescribing b it is possible, in principle, to determine the remaining four unknown jack pressures by means of the four equations, as a result of which the various jack pressures will not be equal. However, at this point it should be noticed that the first three equations are non-linear in the jack pressures. The best possible way to overcome this difficulty can be found by applying an iterative process. This process is started with a set of equal initial values for the jack pressures

$$p_1^0 = p_2^0 = p_3^0 = p_4 \qquad (3.2.9)$$

where p_4 follows from the fourth equation given in table 3.2.3. Substitution from these pressures into the left-hand members of the first three equations leads to a set of remaining mean strains b_i^0 (i = 1, 2, 3) in the bolt series 1, 2 and 3, the deviation of which from b is equal to

$$\Delta b_i^0 = b - b_i^0 \qquad (i = 1, 2, 3) \qquad (3.2.10)$$

The second step in the iterative process consists of the determination of corrected values for the jack pressures

$$p_i^1 = p_i^0 + \Delta p_i^0 \qquad (i = 1, 2, 3) \qquad (3.2.11)$$

After substituting from these expressions into the first three equations of table 3.2.3 and putting all the right-hand members equal to b, the resulting equations may be linearized with respect to Δp_i^0 if

$$\left|\Delta p_i^0\right| \ll p_4 \qquad (i = 1, 2, 3) \qquad (3.2.12)$$

Subtraction of the equations given in table 3.2.3 from these linearized equations leads to three equations for Δp_i^0 (i = 1, 2, 3) shown in table 3.2.4.

The quality of the corrected jack pressures can be judged by substituting from p_i^1 (i = 1, 2, 3) into the first three equations of table 3.2.3 and checking the right-hand members. If the difference between these right-hand members b_i^1 (i = 1, 2, 3) and b is too large, a third step in the iterative

$$a_{110}\,\Delta p_1^{\circ} + \left[\left\{a_{120} + a_{121}\,p_1^{\circ}\right\}\Delta p_2^{\circ} + a_{121}\,p_2^{\circ}\,\Delta p_1^{\circ}\right] + \left[\left\{a_{130} + a_{131}\,p_1^{\circ} + a_{132}\,p_2^{\circ}\right\}\Delta p_3^{\circ} + a_{131}\,p_3^{\circ}\,\Delta p_1^{\circ} + a_{132}\,p_3^{\circ}\,\Delta p_2^{\circ}\right] + \left[a_{131}\,p_4\,\Delta p_1^{\circ} + a_{132}\,p_4\,\Delta p_2^{\circ} + a_{143}\,p_4\;\Delta p_3^{\circ}\right] = \Delta b_1^{\circ}$$

$$a_{110}\,\Delta p_2^{\circ} + \left[\left\{a_{130} + a_{132}\,p_1^{\circ} + a_{131}\,p_2^{\circ}\right\}\Delta p_3^{\circ} + a_{132}\,p_3^{\circ}\,\Delta p_1^{\circ} + a_{131}\,p_3^{\circ}\,\Delta p_2^{\circ}\right] + \left[a_{132}\,p_4\,\Delta p_1^{\circ} + a_{131}\,p_4\,\Delta p_2^{\circ} + a_{143}\,p_4\;\Delta p_3^{\circ}\right] = \Delta b_2^{\circ}$$

$$a_{110}\,\Delta p_3^{\circ} + \left[a_{132}\,p_4\;\left(\Delta p_1^{\circ} + \Delta p_2^{\circ}\right) + a_{121}\,p_4\;\Delta p_3^{\circ}\right] = \Delta b_3^{\circ}$$

TABLE 3.2.4.

Linearized equations determining corrected jack pressures.

process, similar to the previous one, has to be carried out.
Thus we have obtained, more or less, a mathematical simulation of groupwise bolt-tightening in a number of loading cycles.

In an additional note [3.15] to [3.14] the author proposed a *corrected simplified tightening procedure*, the basic assumptions of which consisted of the first assumption of the improved tightening procedure, together with the second assumption of the simplified tightening procedure

$$\begin{aligned}
\left[a_{11}p_1 + c_{11}\right] + a_{12}p_2 + a_{13}p_3 + a_{14}p_4 &= b_1 \\
\left[a_{22}p_2 + c_{22}\right] + a_{23}p_3 + a_{24}p_4 &= b_2 \\
\left[a_{33}p_3 + c_{33}\right] + a_{34}p_4 &= b_3 \\
\left[a_{44}p_4 + c_{44}\right] &= b_4
\end{aligned} \qquad (3.2.13)$$

In these formulas a_{ij} and c_{ii} are independent of the jack pressures, while the following relations hold because of symmetry considerations

$$a_{11} = a_{22} = a_{33} = a_{44}; \qquad c_{11} = c_{22} = c_{33} = c_{44} \qquad (3.2.14)$$

Due to the lack of experimental information, the practical importance of (3.2.13) could not be discussed in [3.15]. However, it should be noted that the determination of the the influence coefficients a_{ij} and c_{ii} requires only one preliminary tightening experiment, during which the first bolt series has to be tightened in two steps.

3.2.4. Verification of the tightening procedures.

As a first step in the verification process of the tightening procedures, described in the preceding sub-section, the results of the experiments 1, 2 and 3, discussed in the sub-section on the interaction among groups of bolts, will be used to determine the coefficients of the jack pressures and the startup effects in the relations underlying the tightening procedures. The values, concluded from these experiments, are given in table 3.2.5 (see p. 58). It should be noted that both for the simplified tightening procedure and for the corrected simplified tightening procedure two cases are being considered, in which respectively the results from table 3.2.1 (tightening at 500 bar jack pressures) and from table 3.2.2 (tightening at

COEFFICIENTS a_{ij} IN μ strain/bar AND c_{ij} IN μ strain	SIMPLIFIED TIGHTENING PROCEDURE		CORRECTED SIMPLIFIED TIGHTENING PROCEDURE		IMPROVED TIGHTENING PROCEDURE
	CASE 1: BASIS TABLE 3.2.1	CASE 2: BASIS TABLE 3.2.2	CASE 1: BASIS TABLE 3.2.1	CASE 2: BASIS TABLE 3.2.2	
a_{11}	1.660	1.813	2.062	2.062	$a_{110} = 2.062$ μ strain/bar
c_{11}	-	-	- 200	- 200	$c_{110} = -200$ μ strain
a_{12}	- 0.248	- 0.218	- 0.248	- 0.218	$a_{120} = -0.331$ μ strain/bar
					$a_{121} = 1.27 \times 10^{-4}$ μ strain/bar^2
a_{34}	- 0.122	- 0.090	- 0.122	- 0.090	$c_{120} = 10$ μ strain
a_{13}	- 0.190	- 0.141	- 0.190	- 0.141	$a_{130} = -0.309$ μ strain/bar
a_{14}	- 0.140	- 0.115	- 0.140	- 0.115	$a_{131} = 1.29 \times 10^{-4}$ μ strain/bar^2
					$a_{132} = 0.80 \times 10^{-4}$ μ strain/bar^2
a_{23}	- 0.210	- 0.148	- 0.210	- 0.148	$c_{130} = 10$ μ strain
a_{24}	- 0.152	- 0.121	- 0.152	- 0.121	$a_{143} = 0.34 \times 10^{-4}$ μ strain/bar^2

TABLE 3.2.5.

Coefficients for different tightening procedures.

800 bar jack pressures) form the basis of the values.
A first check on the validity of the results for the improved tightening procedure can already be made at this stage by predicting the results of experiments 4 and 5 from the values given in table 3.2.5. Table 3.2.6 shows a comparison between the predicted and the measured decrease of the mean strain in bolt series 1 due to subsequent tightening of the bolt series 2 and 3 as a function of the jack pressure p_1. This comparison sounds reasonably good from practical point of view, particularly if one takes into account the scatter in the experimental results shown in figures 3.2.8 and 3.2.9.

The next step in the verification process consists of a comparison of results obtained by means of two tightening experiments and results predicted by means of the different tightening procedures on the basis of the coefficients from table 3.2.5. The two experiments consisted of determining via trial and error a jack pressure for each bolt series, resulting in the highest bolt-strain uniformity over the whole flange connection in its final tightened stage with desired strains of 675 μ strain and 1250 μ strain respectively. Tables 3.2.7 and 3.2.8 compare the results predicted by means of the different tightening procedures and the results measured during the real tightening. The relative differences between the predicted and the measured results are seen to fall within 5% for the improved tightening procedure and could have been even better if the scatter in the measured remaining mean strains for the

		DECREASE OF MEAN STRAIN OF BOLT SERIES 1	
		PREDICTED	MEASURED
EXPERIMENT 4	$p_2 = 500$ bar	$156 - 0.064\ p_1$	$151 - 0.053\ p_1$
	$p_2 = 800$ bar	$254 - 0.102\ p_1$	$246 - 0.096\ p_1$
EXPERIMENT 5	$p_3 = 500$ bar	$145 - 0.105\ p_1$	$142 - 0.096\ p_1$
	$p_3 = 800$ bar	$237 - 0.167\ p_1$	$225 - 0.139\ p_1$

TABLE 3.2.6.

Comparison between predicted and measured results for experiments 4 and 5.

675 μ case should have been less. The comparison between the predicted and the experimental results is also seen to be very good for the corrected simplified tightening procedure in the case that the jack pressures choosen during the preliminary tightening procedure are in the neighbourhood of those applied at ultimate tightening. This comparison is seen to be reasonably good from practical point of view for the corrected simplified tightening procedure in the case that this restriction is not satisfied and for the simplified tightening procedure in the case that this restriction is satisfied.

		SIMPLIFIED TIGHTENING PROCEDURE		CORRECTED SIMPLIFIED TIGHTENING PROCEDURE		IMPROVED TIGHTENING PROCEDURE WITH ONE ITERATION STEP	EXPERIMENT
		CASE 1: BASIS TABLE 3.2.1	CASE 2: BASIS TABLE 3.2.2	CASE 1: BASIS TABLE 3.2.1	CASE 2: BASIS TABLE 3.2.2		
JACK PRESSURES (bar)	p_1	566	478	555	529	554	565
	p_2	499	429	501	481	497	505
	p_3	436	391	450	443	458	465
	p_4	407	372	424	424	424	425
MEAN STRAIN (μ strain) REMAINING IN EACH BOLT SERIES	b_1	DESIRED REMAINING MEAN STRAINS : $b_1 = b_2 = b_3 = b_4 = 675$ μ strain				674	687
	b_2					675	704
	b_3					674	685
	b_4					675 (DESIRED)	652

TABLE 3.2.7.

Comparison between predicted and measured results at tightening for b = 675 μ strain.

		SIMPLIFIED TIGHTENING PROCEDURE		CORRECTED SIMPLIFIED TIGHTENING PROCEDURE		IMPROVED TIGHTENING PROCEDURE WITH ONE ITERATION STEP	EXPERIMENT
		CASE 1: BASIS TABLE 3.2.1	CASE 2: BASIS TABLE 3.2.2	CASE 1: BASIS TABLE 3.2.1	CASE 2: BASIS TABLE 3.2.2		
JACK PRESSURES (bar)	p_1	1047	884	919	877	860	880
	p_2	924	794	831	797	783	810
	p_3	808	724	745	734	735	750
	p_4	753	689	703	703	703	720
MEAN STRAIN (μ strain) REMAINING IN EACH BOLT SERIES	b_1	DESIRED REMAINING MEAN STRAINS : $b_1 = b_2 = b_3 = b_4 = 1250$ μ strain				1250	1252
	b_2					1252	1260
	b_3					1244	1213
	b_4					1250 (DESIRED)	1253

TABLE 3.2.8.

Comparison between predicted and measured results at tightening for b = 1250 μ strain.

3.3. Deformation of large taper hub flanges.

3.3.1. Tapered hub behaviour.

In order to obtain a systematic approach and to restrict the number of geometrical parameters during the basic phase of the flange analysis the external flange loading has been replaced by two basic external loading components (figure 3.3.1), i.e., unit pressure loading p = 1 and unit moment loading M = 1. The unit pressure loading is in equilibrium with an equivalent external bolting force on the outside of the flange ring. This schematization is allowable because of the supposed rigid ring behaviour of the flange ring.
For the sake of brevity the present sub-section restricts itself to the case that the taper hub flange is connected to a circular cylindrical shell.

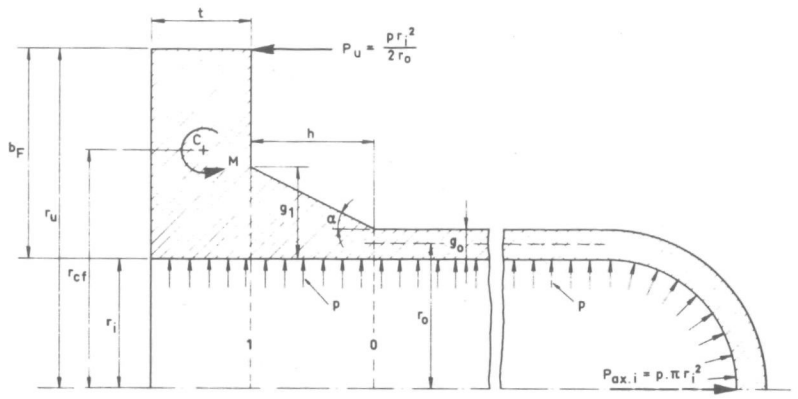

FIGURE 3.3.1.

Equivalent external loading.

The thin shell approach of the tapered hub used by MURRAY and STUART [3.10] as well as in papers on tapered transition joints by RODABAUGH and ATTERBURY [3.11] and HAMADA et al. [3.16] is based upon the solution given by TIMOSHENKO [2.8, Chapter 15, Article 118] and FLÜGGE [3.17, Chapter 5.5.3] for a thin shell with a circular cylindrical shape of the middle plane and a thickness varying linearly as a function of the axial hub co-ordinate. The same solution is used in the present sub-section, yielding the following expression for the radial displacement w (figure 3.1.2)

$$w = \frac{1}{\sqrt{\eta}} \left[C_1 \, \mathrm{ber}'(\xi) + C_2 \, \mathrm{bei}'(\xi) + C_3 \, \mathrm{ker}'(\xi) + C_4 \, \mathrm{kei}'(\xi) \right] + \frac{p r_0^2 (1-\nu/2)}{E \alpha \eta} \qquad (3.3.1)$$

where $\xi = 2\rho \sqrt{\eta}$, with $\rho = \sqrt[4]{\frac{12(1-\nu^2)}{\alpha^2 r_0^2}}$,

while η is the axial hub co-ordinate defined in figure 3.1.2.
In this solution ber' (ξ), bei' (ξ), ker' (ξ) and kei' (ξ) represent the derivatives of the so-called Thomson functions with respect to η. The end rotations ϕ_0 and ϕ_1, the end moments M_0 and M_1 and the end shear forces Q_0 and Q_1 can be expressed in the integration constants C_1 through C_4, considering that

$$\phi = \frac{dw}{d\eta} \qquad M = \frac{Eg^3}{12(1-\nu^2)} \frac{d^2w}{d\eta^2} \qquad Q = \frac{d}{d\eta}\left[\frac{Eg^3}{12(1-\nu^2)} \frac{d^2w}{d\eta^2}\right] \tag{3.3.2}$$

At this point the critical stage in the thin shell approach is reached, where the continuity conditions at the hub boundaries have to be satisfied. In satisfying these conditions MURRAY and STUART in their classical paper on the behaviour of large taper hub flanges [3.10] assume the pressure forces (stress resultants) at the cylindrical shell and the flange ring junctures to act in parallel with the vessel axis and to have their points of application in the hub middle surface (cf. figure 3.3.2). However, this

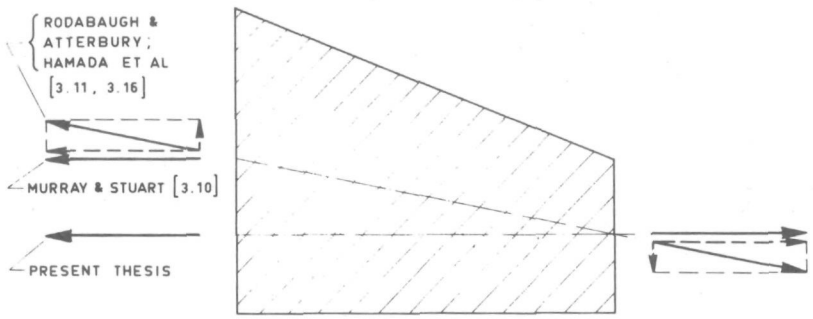

FIGURE 3.3.2.

Pressure forces in satisfying the continuity conditions at the hub boundaries.

is not consistent with the basic thin shell solution mentioned above, as the conical shape of the middle plane, i.e., the difference between the radii $r_i + g_0/2$ and $r_i + g_1/2$, produces an additional moment increasing with η (cf. figure 3.1.2) along the axial length of the hub. As indicated by the experimental evidence presented in [3.11], this effect becomes quite significant for g_1/g_0 ratios exceeding about 1.5 and $h/\sqrt{r_0 g_0}$ values not exceeding about $2\sqrt{2}$, i.e. for hub dimensions relevant in the context of the present thesis. To take this effect into account both the analyses given in [3.11] and [3.16] assume the pressure forces at the cylindrical shell and the flange ring junctures to be located *in* the conical hub middle surface, thereby introducing a radial shear force at each of these junctures (cf. figure 3.3.2). In order to assess the reliability of this correction the present section offers a comparison between the two approaches mentioned above and simultaneously offers a third approach where the shape of the hub middle surface is assumed to be cylindrical in satisfying the continuity conditions (cf. figure 3.3.2). The system of four equations resulting from the continuity conditions at the hub boundaries for the latter case is conveniently presented in tabulated form in table 3.3.1. (see p.62)

The alternative approach mentioned before is to treat the hub as a ring with undeformable cross section, i.e., in the same way as the flange ring. This results in two separate modes of deformation undergone by the hub: (1) rotation of the cross section around the centroid due to the resultant twisting moment M_{wh} and (2) radial displacement of the cross section due to the resultant radial force through the centroid (both M_{wh} and Q_h are measured per unit arc length in circumferential direction of the cylindrical shell midsurface).
It can easily be shown [3.18, pp. 430-438] that the corresponding values for the angle of rotation ϕ_h and the radial displacement of the centroid w_h will be

LEFT-HAND TERMS				RIGHT-HAND TERMS
$C_1^* = \frac{1}{\sqrt{h}} C_1$	$C_2^* = \frac{1}{\sqrt{h}} C_2$	$C_3^* = \frac{1}{\sqrt{h}} C_3$	$C_4^* = \frac{1}{\sqrt{h}} C_4$	
$2\,b_{1,0} - a_1\,b_{9,0} - a_2\,b_{13,0}$	$2\,b_{2,0} - a_1\,b_{10,0} - a_2\,b_{14,0}$	$2\,b_{3,0} - a_1\,b_{11,0} - a_2\,b_{15,0}$	$2\,b_{4,0} - a_1\,b_{12,0} - a_2\,b_{16,0}$	$\frac{p r_o}{E} \frac{2(1-\nu/2)}{[12(1-\nu^2)]^{3/4}} \left(\frac{g_1}{g_o} - 1\right)^{5/2} \left(\frac{\sqrt{r_o g_o}}{h}\right)^3 \frac{r_o}{g_o}$
$4\,b_{5,0} - a_3\,b_{9,0} - 2a_1\,b_{13,0}$	$4\,b_{6,0} - a_3\,b_{10,0} - 2a_1\,b_{14,0}$	$4\,b_{7,0} - a_3 b_{11,0} - 2a_1\,b_{15,0}$	$4\,b_{8,0} - a_3\,b_{12,0} - 2a_1\,b_{16,0}$	$\frac{p r_o}{E} \frac{(1-\nu/2)}{[12(1-\nu^2)]^{3/4}} \left(\frac{g_1}{g_o} - 1\right)^{5/2} \left(\frac{\sqrt{r_o g_o}}{h}\right)^3 \frac{r_o}{g_o} \left[1 + \frac{2\sqrt{2}}{[12(1-\nu^2)]^{1/4}} \left(\frac{g_1}{g_o} - 1\right) \frac{\sqrt{r_o g_o}}{h}\right]$
$2\,b_{1,1} - a_4\,b_{9,1} + a_5\,b_{13,1}$	$2\,b_{2,1} - a_4\,b_{10,1} + a_5\,b_{14,1}$	$2\,b_{3,1} - a_4 b_{11,1} + a_5\,b_{15,1}$	$2\,b_{4,1} - a_4 b_{12,1} + a_5\,b_{16,1}$	$\frac{p r_o}{E} \frac{\left(\frac{g_1}{g_o} - 1\right)^{1/2} \frac{\sqrt{r_o g_o}}{h}}{[12(1-\nu^2)]^{1/4}} \left[-\left(1 - \frac{\nu}{2}\right) \frac{g_o}{g_1} \frac{r_o}{g_o} + \left\{ \frac{1-\nu/2}{1-\nu^2} \left[\left(\frac{g_1}{g_o} - 1\right) \frac{\sqrt{r_o g_o}}{h} \sqrt{\frac{g_o}{r_o}}\right]^2 + \left(\frac{b_F}{r_o}\right)^2 \left(\frac{t}{b_F}\right)^2 + 3\left(1 - \frac{1}{2}\frac{g_o}{r_o}\right)^2 \left(\frac{b_F}{r_o} - \frac{1}{2}\frac{g_o}{r_o}\right) \right\} \left(\frac{r_o}{b_F}\right)^3 \left(\frac{b_F}{t}\right)^2 \left[1 + \frac{1}{2}\left(\frac{b_F}{r_o} - \frac{g_o}{r_o}\right)\right] \right] + \frac{M}{E r_o} \frac{6\left(\frac{g_1}{g_o} - 1\right)^{1/2} \frac{\sqrt{r_o g_o}}{h}}{[12(1-\nu^2)]^{1/4}} \left(\frac{r_o}{b_F}\right)^3 \left(\frac{b_F}{t}\right)^2 \left[1 + \frac{1}{2}\left(\frac{b_F}{r_o} - \frac{g_o}{r_o}\right)\right]$
$4\,b_{5,1} + a_6\,b_{9,1} - 2a_4 b_{13,1}$	$4\,b_{6,1} + a_6\,b_{10,1} - 2a_4\,b_{14,1}$	$4\,b_{7,1} + a_6 b_{11,1} - 2a_4\,b_{15,1}$	$4\,b_{8,1} + a_6\,b_{12,1} - 2a_4\,b_{16,1}$	$\frac{p r_o}{E} \frac{\left(\frac{g_1}{g_o} - 1\right)^{3/2} \left(\frac{\sqrt{r_o g_o}}{h}\right)^2 \sqrt{\frac{g_o}{r_o}}}{[12(1-\nu^2)]^{3/4}} \left[\left(1 - \frac{\nu}{2}\right)\left(\frac{g_1}{g_o} - 1\right) \frac{\sqrt{r_o g_o}}{h} \left(\frac{g_o}{g_1}\right)^2 \left(\frac{r_o}{g_o}\right)^{3/2} - 2\left\{ \frac{1-\nu/2}{1-\nu^2} \left[\left(\frac{g_1}{g_o} - 1\right) \frac{\sqrt{r_o g_o}}{h} \sqrt{\frac{g_o}{r_o}}\right]^2 + 3\left(1 - \frac{1}{2}\frac{g_o}{r_o}\right)^2 \left(\frac{b_F}{r_o} - \frac{1}{2}\frac{g_o}{r_o}\right) \right\} \left(\frac{r_o}{b_F}\right)^4 \left(\frac{b_F}{t}\right)^3 \left[1 + \frac{1}{2}\left(\frac{b_F}{r_o} - \frac{g_o}{r_o}\right)\right] \right] - \frac{M}{E r_o} \frac{12\left(\frac{g_1}{g_o} - 1\right)^{3/2} \left(\frac{\sqrt{r_o g_o}}{h}\right)^2 \sqrt{\frac{g_o}{r_o}}}{[12(1-\nu^2)]^{3/4}} \left(\frac{r_o}{b_F}\right)^4 \left(\frac{b_F}{t}\right)^3 \left[1 + \frac{1}{2}\left(\frac{b_F}{r_o} - \frac{g_o}{r_o}\right)\right]$

$b_1 = \xi^{-1}\,ber'(\xi)$; $b_2 = \xi^{-1}\,bei'(\xi)$; $b_3 = \xi^{-1}\,ker'(\xi)$, $b_4 = \xi^{-1}\,kei'(\xi)$

$b_5 = -\xi^{-3}\left[\xi\,bei(\xi) + 2\,ber'(\xi)\right]$, $b_6 = \xi^{-3}\left[\xi\,ber(\xi) - 2\,bei'(\xi)\right]$

$b_7 = -\xi^{-3}\left[\xi\,kei(\xi) + 2\,ker'(\xi)\right]$; $b_8 = \xi^{-3}\left[\xi\,ker(\xi) - 2\,kei'(\xi)\right]$

$b_9 = \xi\left[-\xi^2\,bei'(\xi) + 4\,\xi\,bei(\xi) + 8\,ber'(\xi)\right]$, $b_{10} = \xi\left[\xi^2\,ber'(\xi) - 4\,\xi\,ber(\xi) + 8\,bei'(\xi)\right]$

$b_{11} = \xi\left[-\xi^2\,kei'(\xi) + 4\,\xi\,kei(\xi) + 8\,ker'(\xi)\right]$, $b_{12} = \xi\left[\xi^2\,ker'(\xi) - 4\,\xi\,ker(\xi) + 8\,kei'(\xi)\right]$

$b_{13} = \xi\left[-\xi\,ber(\xi) + 2\,bei'(\xi)\right]$; $b_{14} = -\xi\left[\xi\,bei(\xi) + 2\,ber'(\xi)\right]$

$b_{15} = \xi\left[-\xi\,ker(\xi) + 2\,kei'(\xi)\right]$, $b_{16} = -\xi\left[\xi\,kei(\xi) + 2\,ker'(\xi)\right]$

A SUBSCRIPT 0 REFERS TO PARTICULAR VALUES AT JUNCTURE OF *THIN-WALL SHELL AND TAPERED HUB*.

A SUBSCRIPT 1 REFERS TO PARTICULAR VALUES AT JUNCTURE OF FLANGE RING AND TAPERED HUB.

$\xi_o = 2\left[12(1-\nu^2)\right]^{1/4} \left[\left(\frac{g_1}{g_o} - 1\right) \frac{\sqrt{r_o g_o}}{h}\right]^{-1}$

$\xi_1 = \sqrt{\frac{g_1}{g_o}}\,\xi_o$

$a_1 = \frac{1}{96(1-\nu^2)} \left[\left(\frac{g_1}{g_o} - 1\right) \frac{\sqrt{r_o g_o}}{h}\right]^4$; $a_4 = \frac{3}{4\left[12(1-\nu^2)\right]^{3/2}} \left[\left(\frac{g_1}{g_o} - 1\right) \frac{\sqrt{r_o g_o}}{h} \sqrt{\frac{g_o}{r_o}}\right]^4 \left(\frac{r_o}{b_F}\right)^3 \left(\frac{b_F}{t}\right)^2 \left[1 + \frac{1}{2}\left(\frac{b_F}{r_o} - \frac{g_o}{r_o}\right)\right]$

$a_2 = \frac{\sqrt{2}}{4\left[12(1-\nu^2)\right]^{3/4}} \left[\left(\frac{g_1}{g_o} - 1\right) \frac{\sqrt{r_o g_o}}{h}\right]^3$, $a_5 = \frac{1}{12(1-\nu^2)} \left[\left(\frac{g_1}{g_o} - 1\right) \frac{\sqrt{r_o g_o}}{h} \sqrt{\frac{g_o}{r_o}}\right]^3 \left(\frac{r_o}{b_F}\right)^2 \frac{b_F}{t} \left[1 + \frac{1}{2}\left(\frac{b_F}{r_o} - \frac{g_o}{r_o}\right)\right]$

$a_3 = \frac{\sqrt{2}}{8\left[12(1-\nu^2)\right]^{5/4}} \left[\left(\frac{g_1}{g_o} - 1\right) \frac{\sqrt{r_o g_o}}{h}\right]^5$, $a_6 = \frac{3}{2\left[12(1-\nu^2)\right]^2} \left[\left(\frac{g_1}{g_o} - 1\right) \frac{\sqrt{r_o g_o}}{h} \sqrt{\frac{g_o}{r_o}}\right]^5 \left(\frac{r_o}{b_F}\right)^4 \left(\frac{b_F}{t}\right)^3 \left[1 + \frac{1}{2}\left(\frac{b_F}{r_o} - \frac{g_o}{r_o}\right)\right]$

TABLE 3.3.1.

Equations for the case that hub is considered as a cilindrical shell with variable wall thickness.

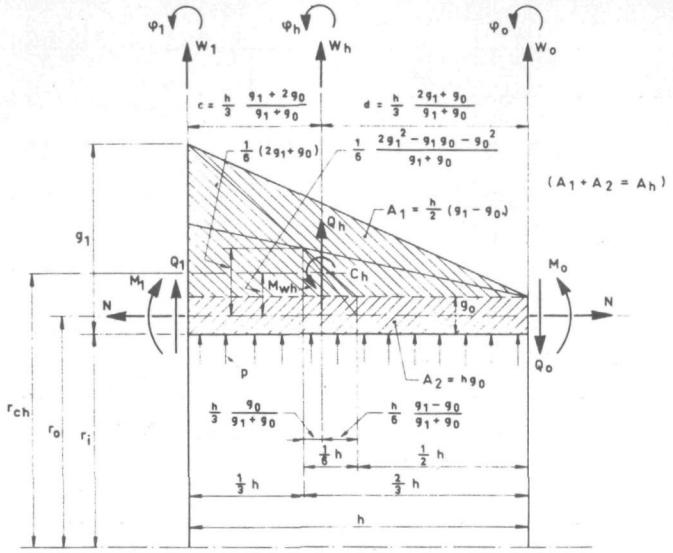

FIGURE 3.3.3.

Hub geometry details (rigid ring approach).

$$\phi_h = \frac{M_{wh}\, r_0\, r_{ch}}{E\, I_h} \qquad w_h = \frac{Q_h\, r_0\, r_{ch}}{E\, A_h} \tag{3.3.3}$$

where the centroid radius r_{ch} may be expressed in terms of figures 3.1.2 and 3.3.3 as follows

$$r_{ch} = \frac{g_1^2 + g_1 g_0 + g_0^2 + 3r_i(g_1+g_0)}{3(g_1+g_0)} \tag{3.3.4}$$

while

$$I_h = \frac{h^3}{36}\,\frac{g_1^2 + 4g_1 g_0 + g_0^2}{g_1+g_0} \tag{3.3.5}$$

The radial displacements w_0 and w_1 at the shell and flange side boundaries, respectively, being

$$w_0 = w_h + \phi_h d \qquad \text{and} \qquad w_1 = w_h - \phi_h c \tag{3.3.6}$$

can then be expressed in terms of the redundant shear forces and moments Q_0, Q_1, M_0 and M_1 by simple geometric and arithmetic considerations. By applying the continuity conditions at the hub boundaries a system of four equations is again obtained, as tabulated in table 3.3.2 (see p. 64).

From tables 3.3.1 and 3.3.2, the remarkable conclusion can be drawn that multiplying all dimensions by the same scale factor does not change the flange ring rotation if the basic pressure loading remains unchanged and the basic moment loading is multiplied by the square of the scale factor. Assuming the real bolt loading to be proportional to the axial pressure reaction and assuming the same (relative) location of the resulting gasket face reaction in the unscaled and the scaled position, it is possible to prove that scaling of the dimensions results in square scaling of the basic moment loading. Therefore, it can be stated that scaling of the dimensions does not change the flange ring rotation under the real external loading conditions. The importance of this conclusion for pressure vessel research using scale models is evident.

The final part of this sub-section offers a comparison between the three thin shell approaches and the rigid ring approach for the tapered hub discussed before, using a finite element analysis as the yardstick for their validity. The finite element approach utilizes the ana-element concept developed in Chapter 2.3 for the flange ring and the cylindrical vessel, while the elements used for the description of the tapered hub behaviour are the TRIAX 6 elements discussed in Chapter 2.2.2. In this approach the displacement continuity conditions at the flange ring and vessel boundaries

LEFT-HAND TERMS				RIGHT-HAND TERMS
M_1	hQ_1	M_o	hQ_o	
$2\left(2\frac{g_1}{g_o}+1\right)$	$\frac{g_1}{g_o}+1$	$-\left[2\left(2\frac{g_1}{g_o}+1\right)+ -\frac{\sqrt{12(1-\nu^2)}}{2}\left(\frac{h}{\sqrt{r_o g_o}}\right)^2 K_o\right]$	$3\frac{g_1}{g_o}+1+ +\frac{[12(1-\nu^2)]^{1/4}}{\sqrt{2}}\frac{h}{\sqrt{r_o g_o}}K_o$	$\left(\frac{h}{\sqrt{r_o g_o}}\right)^2\frac{g_o}{r_o}\left[\frac{g_1}{g_o}-\frac{1-\nu/2}{2}K_o\right]r_o^2 p$
$6\left(\frac{g_1}{g_o}+1\right)$	$2\left(\frac{g_1}{g_o}+2\right)$	$-\left[6\left(\frac{g_1}{g_o}+1\right)+ +\frac{[12(1-\nu^2)]^{3/4}}{\sqrt{2}}\left(\frac{h}{\sqrt{r_o g_o}}\right)^3 K_o\right]$	$2\left(2\frac{g_1}{g_o}+1\right)+ -\frac{\sqrt{12(1-\nu^2)}}{2}\left(\frac{h}{\sqrt{r_o g_o}}\right)^2 K_o$	$\left(\frac{h}{\sqrt{r_o g_o}}\right)^2\frac{g_o}{r_o}\left(\frac{g_1}{g_o}-1\right)r_o^2 p$
$2\left[2\left(\frac{g_1}{g_o}+2\right)+ -3\left(\frac{h}{\sqrt{r_o g_o}}\right)^2 K_1\right]$	$2\left[\frac{g_1}{g_o}+3+ +2\frac{h}{\sqrt{r_o g_o}}\left(\frac{g_o}{r_o}\right)^{3/2}\frac{b_F}{r_o}\frac{t}{b_F}K_1\right]$	$-4\left(\frac{g_1}{g_o}+2\right)$	$2\left(\frac{g_1}{g_o}+1\right)$	$\left(\frac{h}{\sqrt{r_o g_o}}\right)^2\frac{g_o}{r_o}\left[-\left\{2-\frac{g_o}{r_o}\left[\left(\frac{b_F}{r_o}\right)^2\left(\frac{t}{b_F}\right)^2+ +3\left(1-\frac{1}{2}\frac{g_o}{r_o}\right)^2\left(\frac{b_F}{r_o}-\frac{g_o}{r_o}\right)\right]K_1\right\}r_o^2 p+6\frac{g_o}{r_o}K_1 M\right]$
$12\left[\frac{g_1}{g_o}+1+ +\left(\frac{h}{\sqrt{r_o g_o}}\right)^3\left(\frac{g_o}{r_o}\right)^{5/2}\frac{r_o}{b_F}\frac{b_F}{t}K_1\right]$	$2\left[2\left(\frac{g_1}{g_o}+2\right)+ -3\left(\frac{h}{\sqrt{r_o g_o}}\right)^2 K_1\right]$	$-12\left(\frac{g_1}{g_o}+1\right)$	$4\left(2\frac{g_1}{g_o}+1\right)$	$\left(\frac{h}{\sqrt{r_o g_o}}\right)^3\frac{g_o}{r_o}\left[-\left\{2\left(\frac{g_1}{g_o}-1\right)\left(\frac{g_o}{r_o}\right)^{3/2}\frac{r_o}{b_F}\frac{b_F}{t}\times \times\left(1-\frac{1}{2}\frac{g_o}{r_o}\right)^2\left(\frac{b_F}{r_o}-\frac{g_o}{r_o}\right)K_1\right\}r_o^2 p+12\left(\frac{g_o}{r_o}\right)^{3/2}\frac{r_o}{b_F}\frac{b_F}{t}K_1 M\right]$

$$K_o=\frac{\frac{r_o}{g_o}\left(\frac{g_1}{g_o}+1\right)\left[\left(\frac{g_1}{g_o}\right)^2+4\frac{g_1}{g_o}+1\right]}{3\left(\frac{r_o}{g_o}-\frac{1}{2}\right)\left(\frac{g_1}{g_o}+1\right)+\left(\frac{g_1}{g_o}\right)^2+\frac{g_1}{g_o}+1} \quad ; \quad K_1=\left(\frac{r_o}{b_F}\right)^3\left(\frac{b_F}{t}\right)^2\left[1+\frac{1}{2}\left(\frac{b_F}{r_o}-\frac{g_o}{r_o}\right)\right]K_o$$

TABLE 3.3.2.

Equations for the case that the hub is considered as a rigid ring.

are satisfied by specifying the general formulae developed in Appendix 1. A flowchart of the general computer program underlying the numerical investigations is shown in figure 3.3.4.

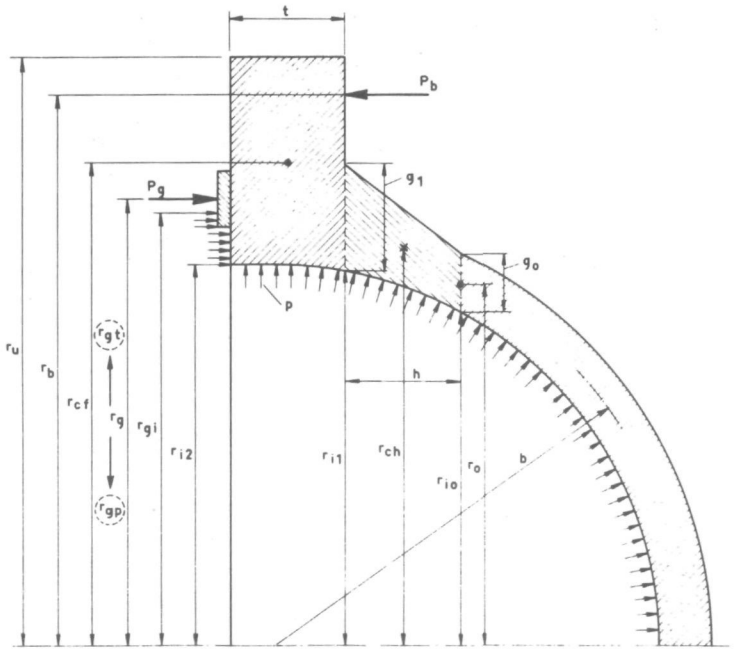

The calculations have been carried out for the representative case

$$\frac{t}{b_F} = 1.25;$$

$$\frac{b_F}{r_{cf}} = 0.2;$$

$$\frac{g_0}{r_0} = 0.05,$$

while $E = 2{,}100{,}000$ kgf/cm^2 and $\nu = 0.3$.

FIGURE 3.3.5.

Flange geometry symbols.

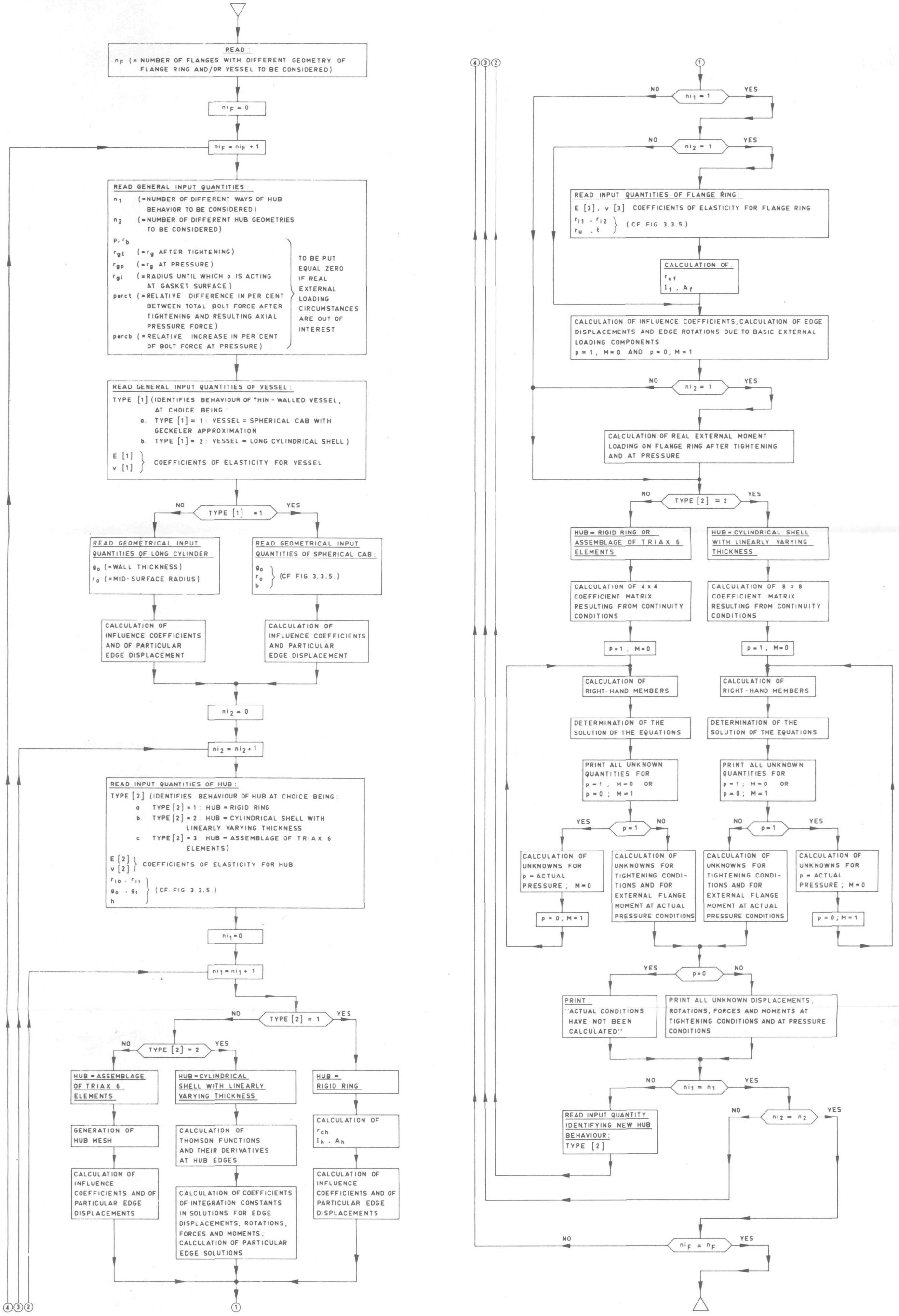

FIGURE 3.3.4.

Flowchart of general computer program for flange analysis under mechanical loading.

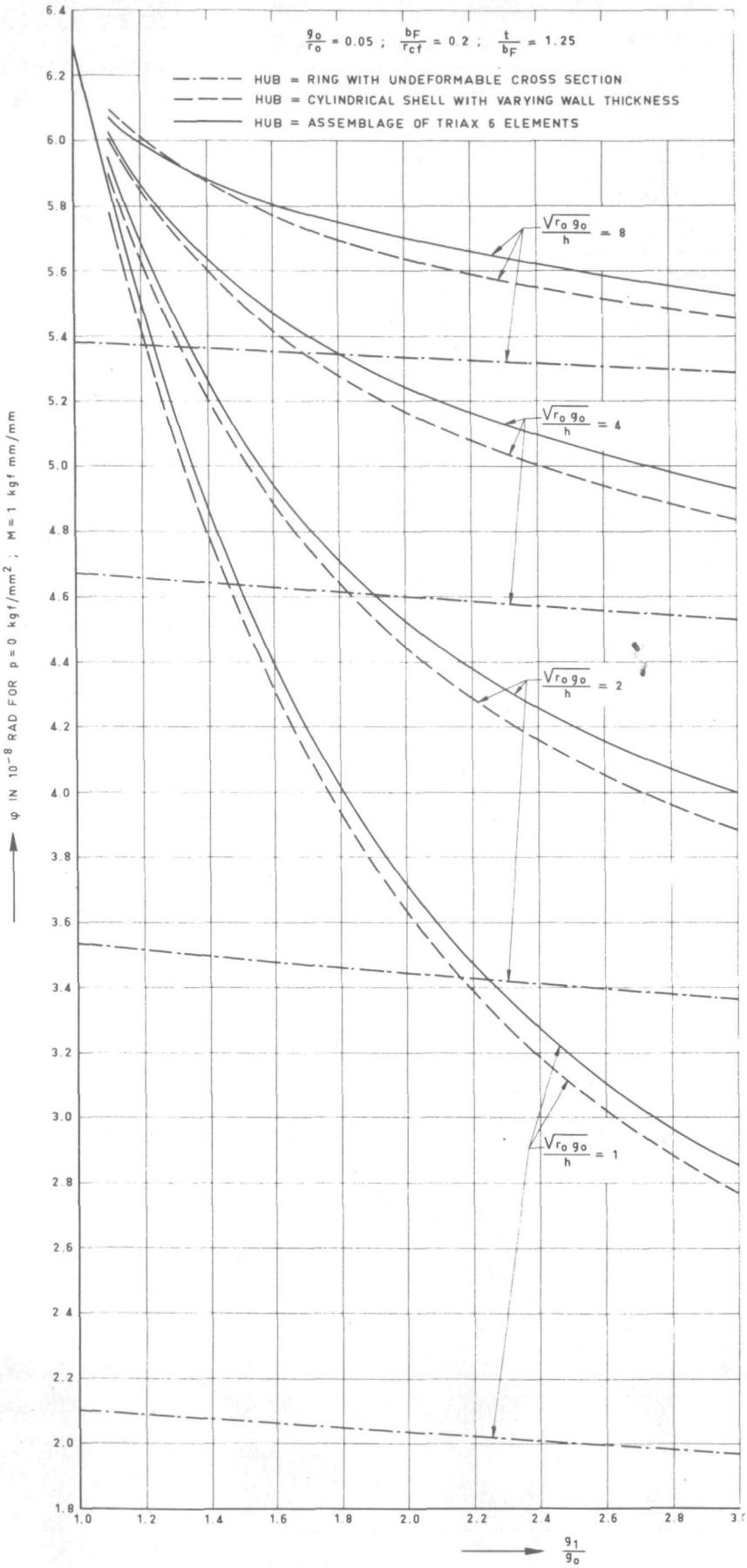

FIGURE 3.3.6.

Flange rotation for unit moment loading ($\frac{\sqrt{r_0 g_0}}{h} = 1, 2, 4$ *and* 8).

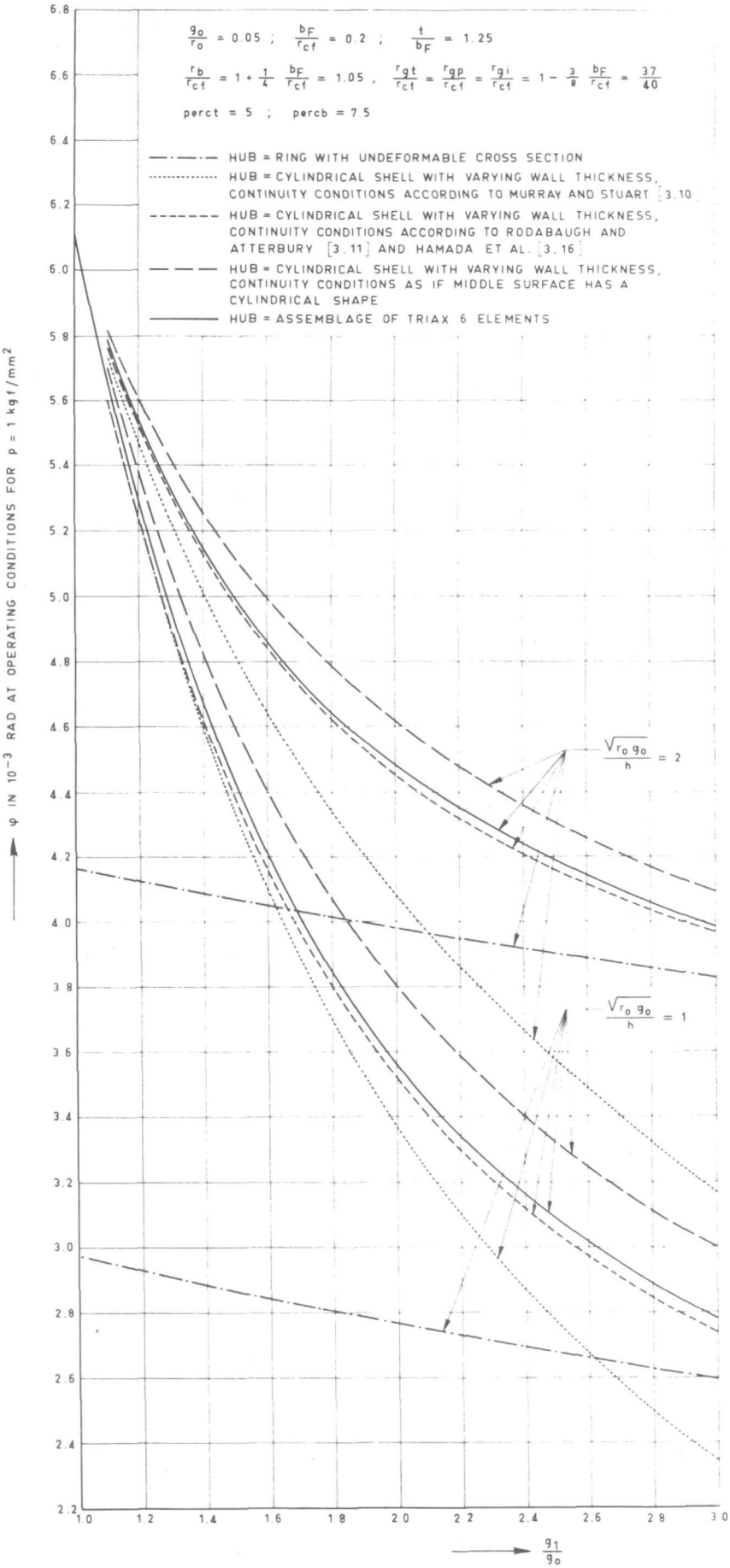

FIGURE 3.3.7.

Flange rotation for operating conditions ($\frac{\sqrt{r_o g_o}}{h} = 1$ *and* 2).

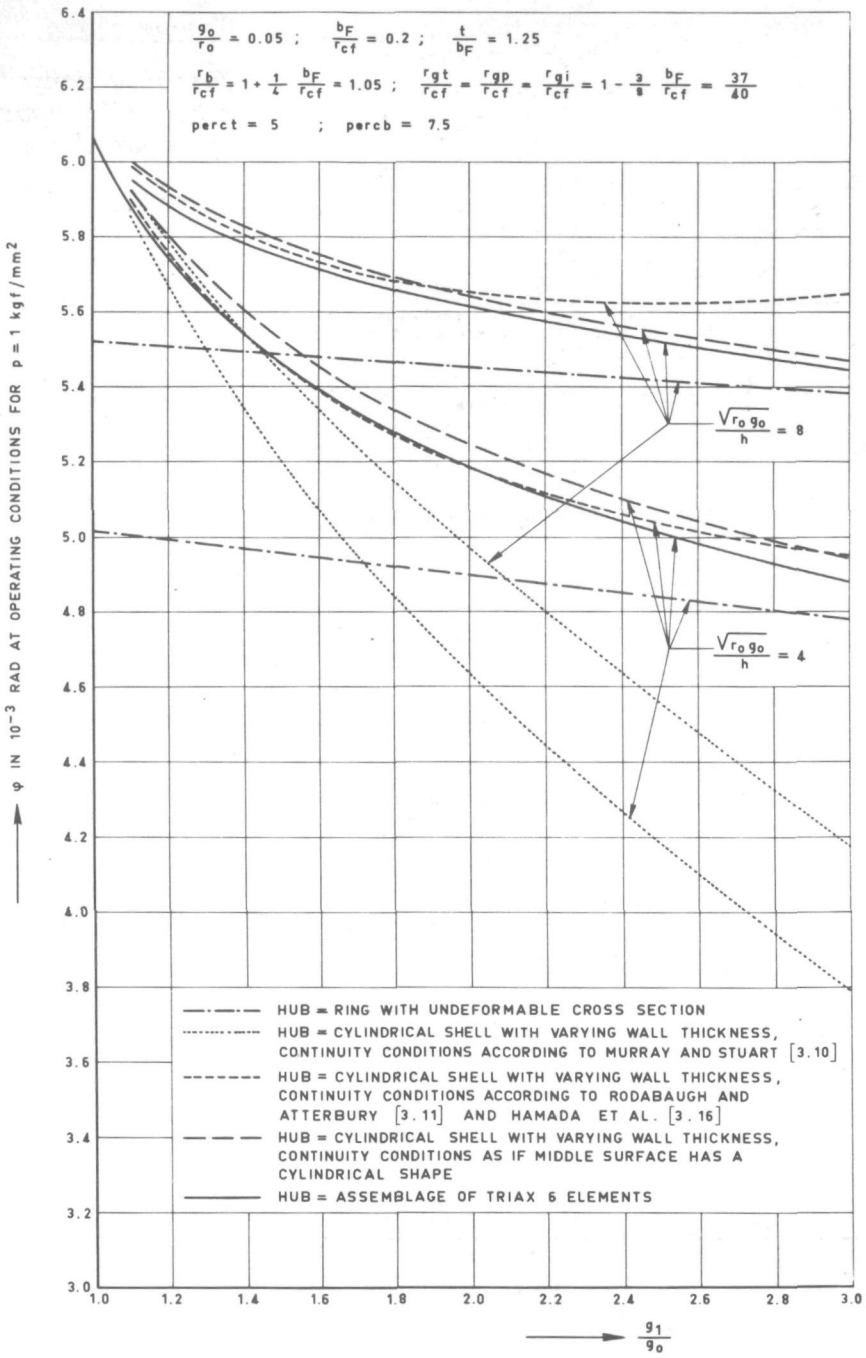

FIGURE 3.3.8.

Flange rotation for operating conditions ($\frac{\sqrt{r_0 g_0}}{h} = 4$ *and* 8).

The results of the comparison are given in figure 3.3.6 (see p. 67) for unit moment loading (representative for tightening conditions) and in figures 3.3.7 and 3.3.8 for representative operating conditions. The additional assumptions for some geometrical and loading parameters for the latter loading case are indicated in the figures. The results are presented in terms of the flange ring rotation as a function of g_1/g_0 for several values of the dimensionless parameter $\sqrt{r_0 g_0}/h$, covering the range of practical interest (i.e. $\sqrt{r_0 g_0}/h$ = 1, 2, 4, 8). It may be concluded from these figures that the thin shell approach developed by RODABAUGH and ATTERBURY [3.11] and utilized by HAMADA et al. [3.12, 3.16] gives the most accurate values for the flange ring rotation over nearly the whole range of these two dimensionless parameters, except for relatively large values of

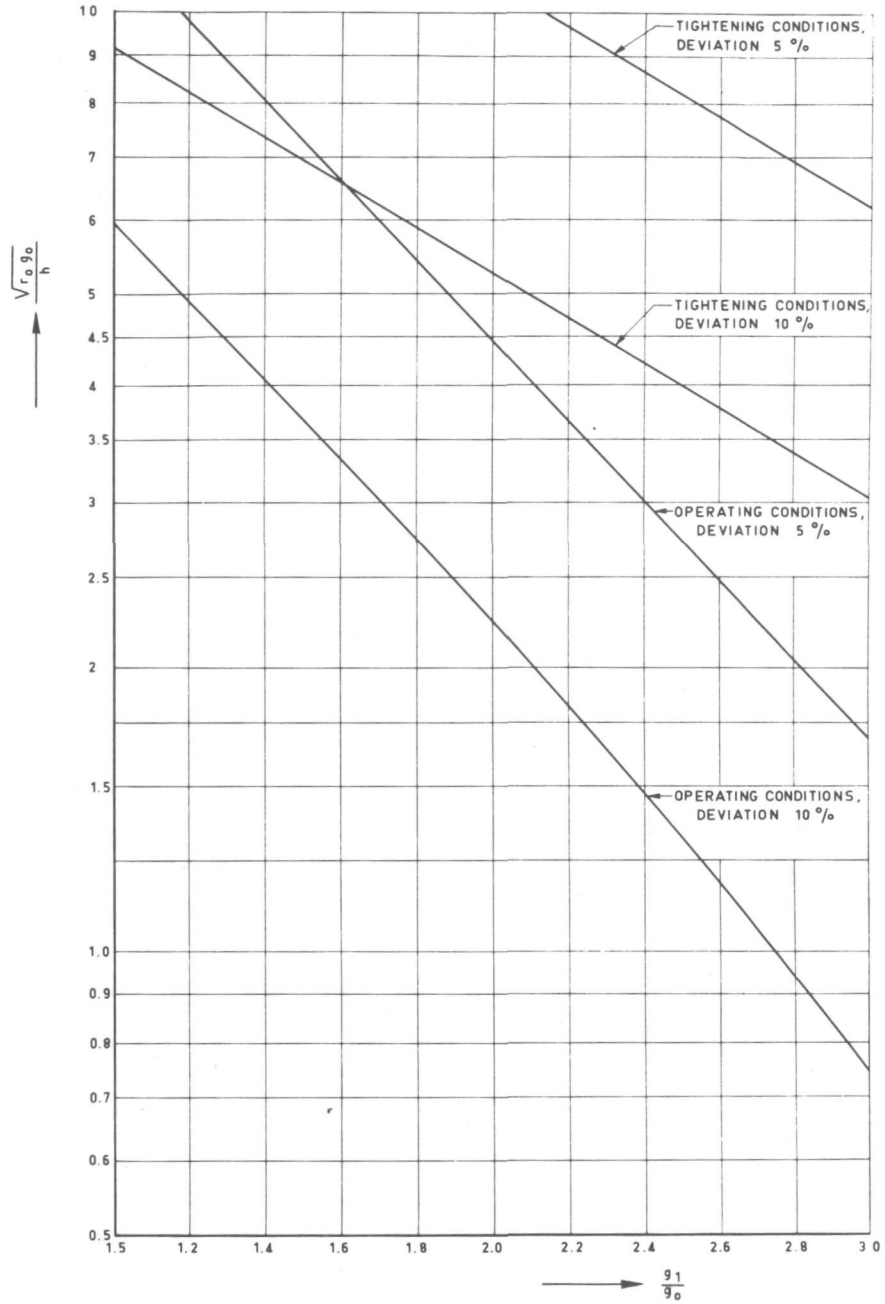

FIGURE 3.3.9.

Validity range for rigid ring approach of tapered hub.

$\sqrt{r_0 g_0}/h$ and correspondingly large values of g_1/g_0, i.e. for large values of the taper angle α (i.e. $\alpha \geq \sim 55^\circ$), where the approach considering the hub middle surface to be cylindrical in satisfying the continuity conditions gives the best results. However, this latter approach also gives results within a sufficiently accuracy from a practical point of view for other values of α. The thin shell approach used by MURRAY and STUART [3.10] underestimates the flange ring rotation considerably, particularly for relatively large values of the taper angle.

As regards the validity of the rigid ring approach for the hub, figure 3.3.9 shows the boundaries in the g_1/g_0 - $\sqrt{r_0 g_0}/h$ - plane where the relative deviation of the rigid ring approach under tightening conditions and operating conditions equals 5% and 10% respectively.

As can be seen from figure 3.3.4 an additional output obtainable from the finite element computations is formed by the influence coefficients for the tapered hub. These influence coefficients can be used in a very easy way by design engineers who do not generally have finite element programs at their disposal for including tapered hub behaviour in deformation analysis of flanges. They are therefore presented in graphical form in Appendix 4.

3.3.2. Experimental data on flange ring deformation and comparison with numerical results.

3.3.2.1. Test results on behaviour of metal-to-metal contact sealing faces and on bolt forces.

In Section 3.1 the importance has been illustrated quantitatively of knowing the exact location of the point of application of the gasket force P_g (cf. figure 3.1.2). Prior to comparing the analytical results obtained by the methods of the preceding sub-section with experimental evidence it is therefore desirable to obtain information on this point in order to insert correct values for M when utilizing the computer program of figure 3.3.4 for the flange geometry under consideration; such information will have to be of an experimental nature.

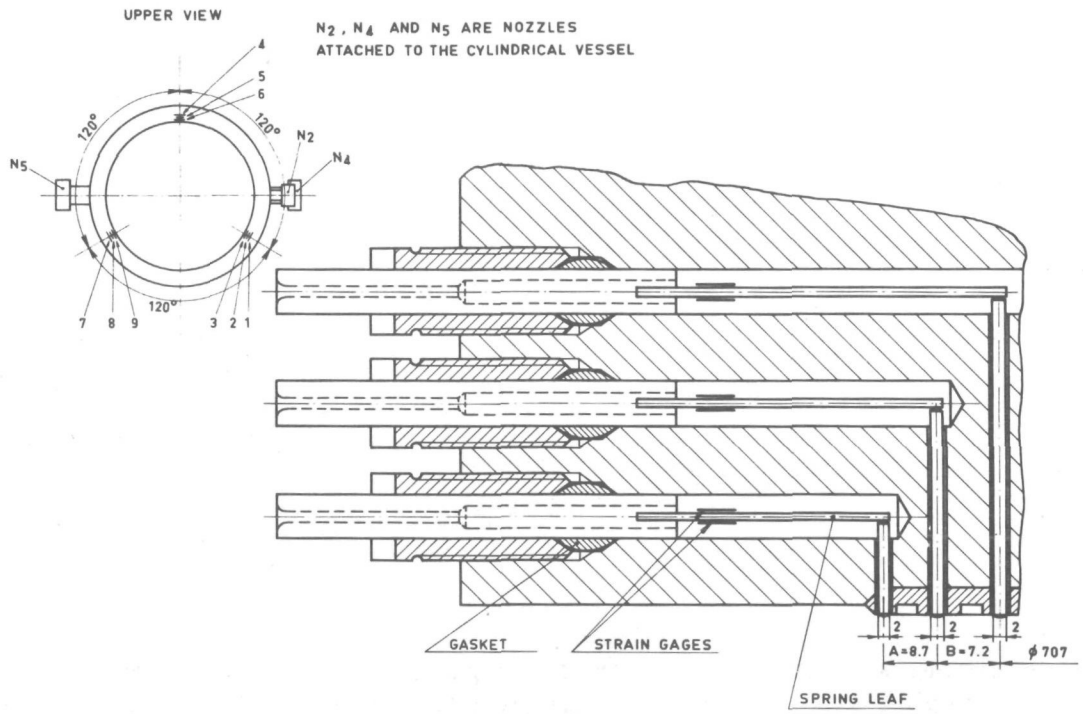

FIGURE 3.3.10.

Measuring device for gasket face rotation.

To obtain experimental information on the gasket face behaviour, the device shown in figure 3.3.10 was mounted in three longitudinal head flange cross sections (120° apart) of the 1:4 scale model (r_0 = 361 mm) of the Dodewaard BWR vessel investigated in the author's laboratory [3.8]. From the vertical displacements of the sensing pins resting on the vessel flange gasket face,

the rotations of parts A and B relative to their initial position *) can be obtained in the manner described in Appendix 5, provided that the rotation of the outer flange rim, where the leaf springs are clamped, is known. This rotation, which is also required for comparison with the analytical results obtained by the methods of the preceding sub-section, was measured by means of tangential strain gauges on the outer flange rims (2 gauges each at the 3 longitudinal cross sections mentioned above). The data mentioned above were obtained successively for two geometries of the upper (head flange) gasket face: perpendicular to the vessel centerline, i.e. parallel to the lower gasket face in the unbolted condition, and with an outward taper of about 3.5×10^{-3} rad, intended to obtain parallelism of the gasket faces under design conditions. The selection of this taper angle was made on the basis of measurements performed on the untapered gasket geometry; for brevity's sake, these measurements are omitted from the present text.
Figure 3.3.11 shows the schematized position of the vessel flange gasket face after tightening the flange connection for the design pressure of 90 bar and obtained from the mean values of the sensing pin displacements over the three longitudinal cross sections. Inasmuch as ϕ_A is seen to exceed ϕ_B it can be concluded from this figure that the point of application of the gasket force P_g after the tightening procedure for 90 bar is located between the points Q_m and Q_ℓ, i.e. between the inner rim and halfway the gasket surface.

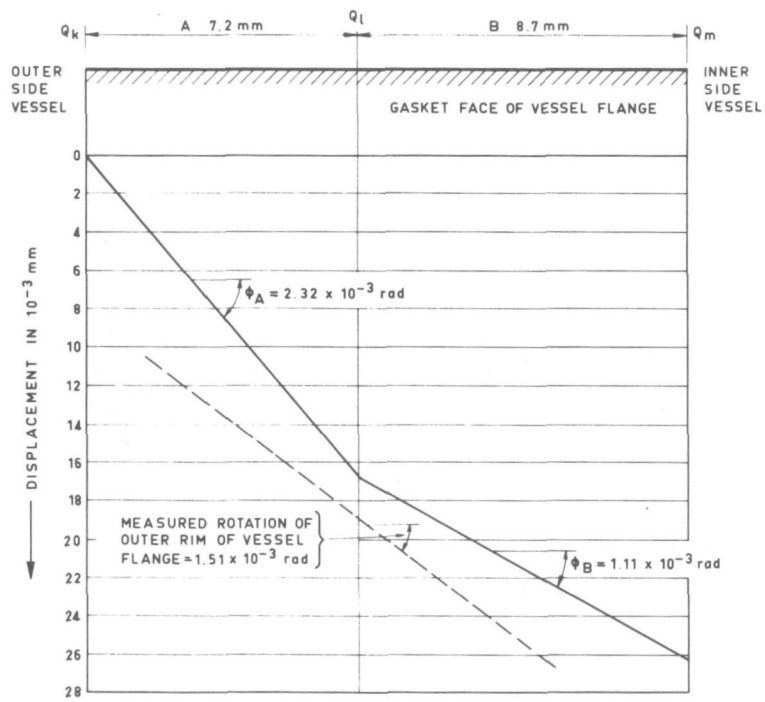

FIGURE 3.3.11.

Schematized position of vessel flange gasket face after tightening for 90 bar.

Figure 3.3.12 shows the change in the angles of rotation for parts A and B of the vessel flange gasket face during pressurization up to 90 bar vessel pressure. This pressurization process took place in the following pressure steps: 0 bar - $22\frac{1}{2}$ bar - 0 bar - 45 bar - 0 bar - $67\frac{1}{2}$ bar - 0 bar - 90 bar. The relatively large scatter in the results for the three sections (in particular for part B of the gasket face, which contains the point of application of P_g after tightening) is probably caused by sliding of the gasket faces along each other due to different radial expansions of the head and vessel flanges during pressurizing. Although this phenomenon could

*) *E.g. after bolt tightening relative to their untightened position and during pressurizing relative to their position after bolt tightening.*

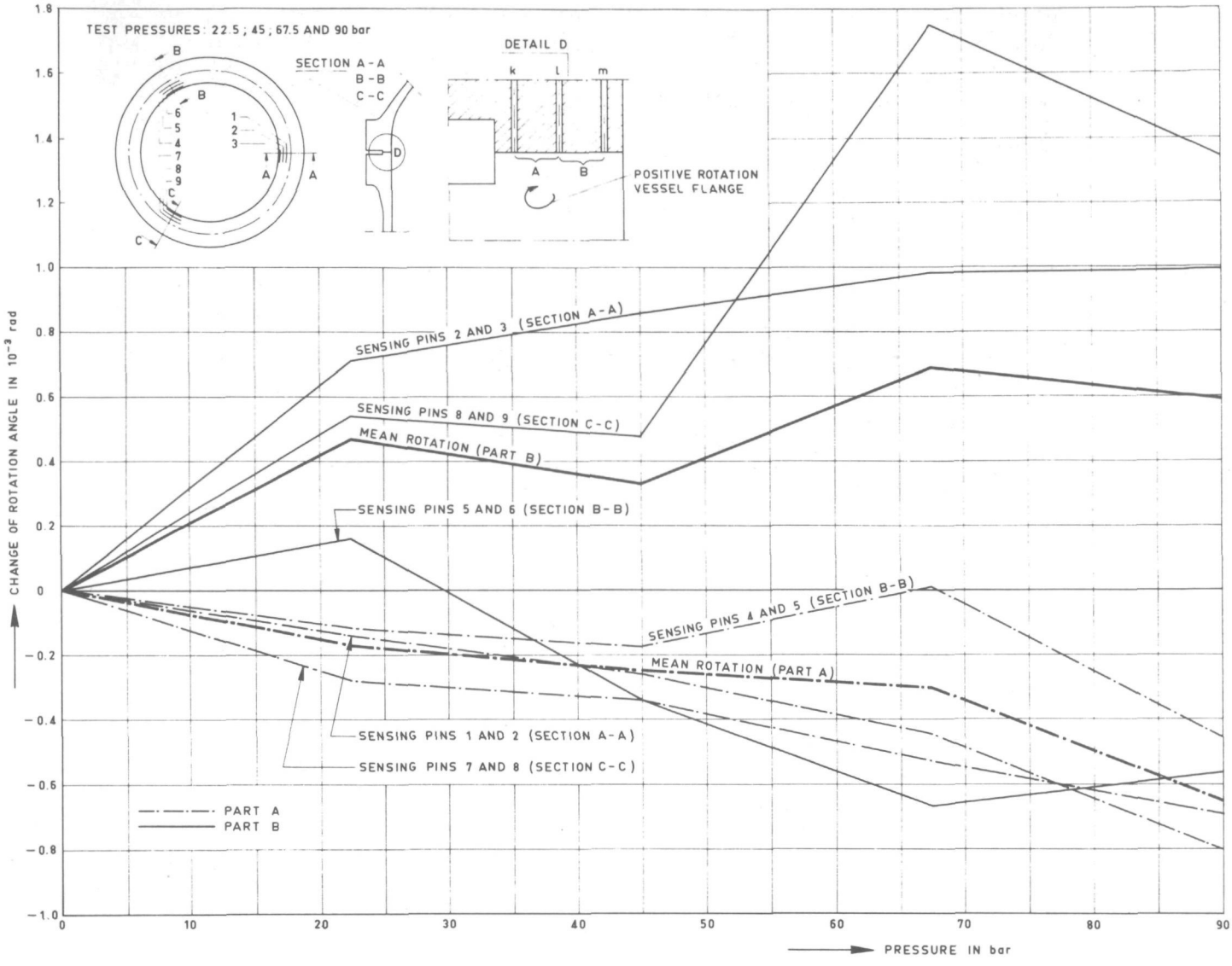

FIGURE 3.3.12.

Measured gasket face behaviour during pressurization of BWR model vessel.

not be observed explicitely during the experiments, it has been observed recently during the hydro tests for a number of large scale LWR vessels investigated by the author's laboratory at the pressure vessel manufacturer. Moreover it should be realized that errors up to about 25% of the maximum value can be expected to occur in the measured rotations shown in figure 3.3.12 because of their relatively small values. In conjunction with experimental and numerical results on the flange ring rotations further conclusions from the above experiments on the gasket face behaviour will be drawn in the next paragraph.

Not only its plane of application but also the value to be taken for P_g requires experimental information, at least for pressurized conditions, where it cannot be obtained from simple considerations of equilibrium unless one knows the actual value of the bolting force P_b. This value has been obtained for the above model vessel by means of the strain gauges mentioned in Section 3.2.1.
Figure 3.3.13 (see p. 74) shows some typical bolt stresses at tightening

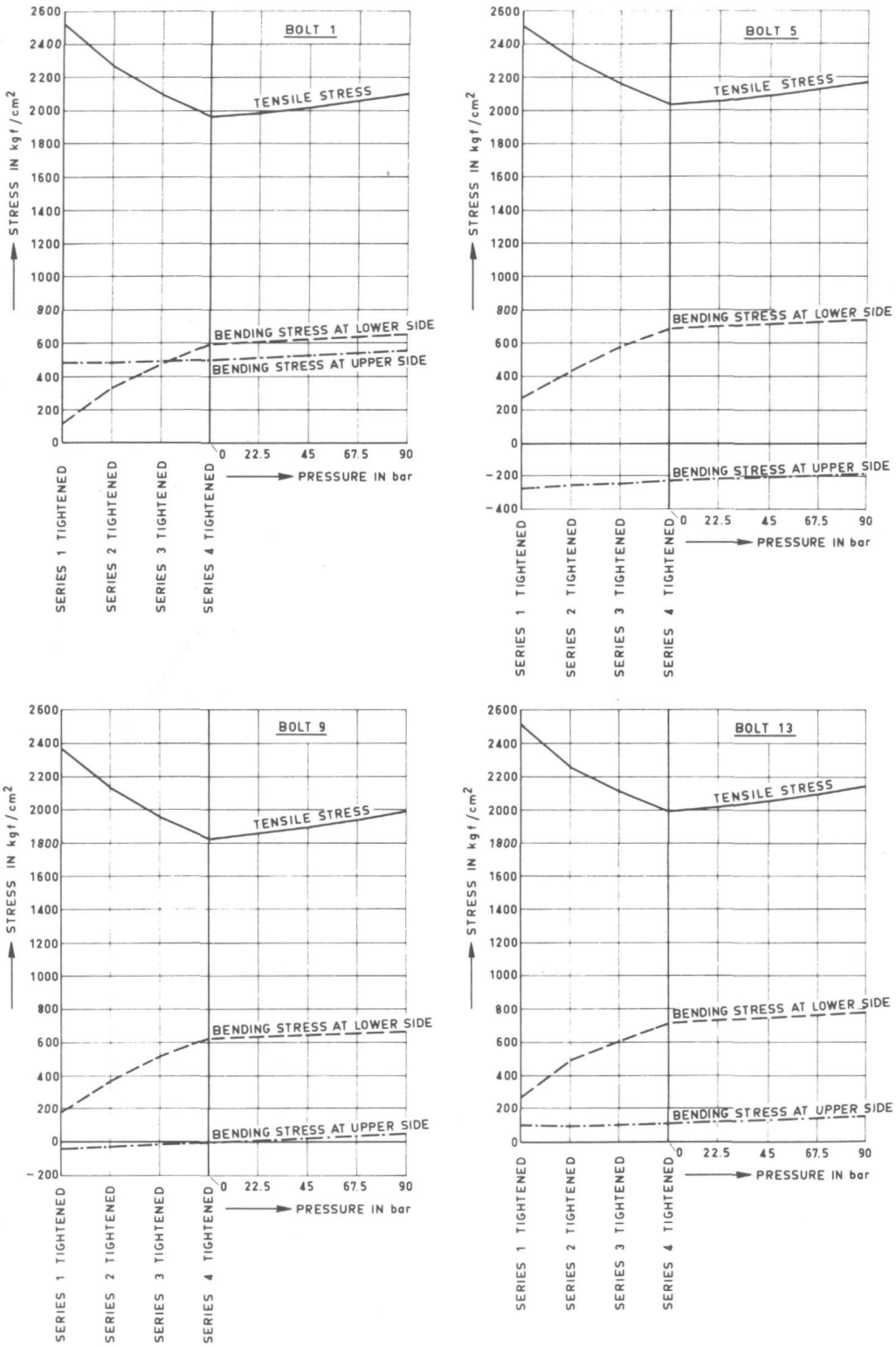

N.B. BENDING STRESSES ARE DEFINED TO BE POSITIVE AT THE INNER VESSEL SIDE
THE NUMBERING OF BOLTS AND GROUPS OF BOLTS IS INDICATED IN FIG. 3.2.3
THE STRAIN GAUGE LOCATIONS ARE INDICATED IN FIG. 3.2.1

FIGURE 3.3.13.

Typical bolt stresses at tightening and during pressuring.

and during pressurizing of the model vessel. The increase in the bolt force P_b from preloading to design conditions turned out to be about 7.5 percent, for a preloading force equal to 1.125 times the final axial hydrostatic force.
The large scatter in the bending stresses, occurring in particular at the upper side of the bolts, is caused by the differences in the measures of the spherical washers under the nuts already mentioned in Section 3.2.2 (discussion of experiment 1) *). From the experiments the bending stresses could be seen to mount up to about 35% of the tensile stresses. Although these bending stresses are of extreme importance in bolt design, it can be concluded from their values that the influence of the bending moments transferred by the bolts to the flanges on the overall deformations (rotations) of the flanges is negligibly small. Assuming for example the bending stress *in each bolt* at the vessel flange juncture to be 1000 kgf/cm^2, the total moment transferred from the bolts to the vessel flange and measured per unit arc length of the cylindrical vessel middle surface amounts to about 300 kgf cm/cm, while the moment $M_b + M_g$ (cf. figure 3.1.2) after tightening equals about 7000 kgf cm/cm. In conclusion it can be stated that the moment M_b^{ex} and the force Q_b defined in figure 3.1.2 can be neglected in the deformation analysis of flanges whose dimensions are of interest for the present thesis.

3.3.2.2. Comparison of numerical and experimental results on flange deformation.

The validity of the computational method underlying the computer program of figure 3.3.4 has been tested by comparing the numerical results obtained from this computer program with the experimental information obtained for the 1:4 scale model **) of the Dodewaard BWR vessel shown in figures 3.1.1 and 3.2.2. As indicated by the title of this paragraph this comparison has been restricted to the rotations of the vessel and head flange rings, thereby excluding a comparison for the stresses, which generally are of lesser importance in the design of the large-diameter, high-pressure vessel flanges of interest for the present thesis. In the computations the hub was considered as an assemblage of TRIAX 6 elements (third option of flowchart figure 3.3.4).

The calculations have been carried out for two geometries of the vessel and head flange rings. The first of these is identical to the one shown in figure 3.1.1, while the outside flange ring diameters of the second geometry have been reduced in such a way that the reduction in volume of each flange ring equals the volume of the bolt holes in that ring. It can be concluded from an analysis given by BICKELL and DANCE [3.19], utilizing the plain strain elastic solution for an infinitely long straight strip of finite width containing an eccentrically located infinite series of holes, that this correction yields a valid first approximation for the influence of bolt holes on flange deformation behaviour.
The calculations have been carried out for three locations of the point of application of the gasket force P_g, i.e. at the inner rim (r_g = 351 mm), at halfway the gasket surface (r_g = 361 mm) and at the outer rim (r_g = 371 mm) respectively.

---

*) *This is also the reason for the negative bending stress occurring at the upper side of bolt 5.*

**) *$E = 2{,}100{,}000$ kgf/cm^2; $\nu = 0.29$.*

In accordance with the results of the experiments described in the preceding paragraph the increase in the bolt force from preloading to design conditions (design pressure 90 bar) has been taken equal to 7.5 percent, for a preloading force equal to 1.125 times the final axial hydrostatic force. The moments and the shear forces transferred from the bolts to the flanges have been neglected in accordance with the findings of the preceding paragraph. As the tapered hub has been considered as an assemblage of TRIAX 6 elements, special caution is required in formulating the shear force continuity condition at the juncture between the tapered hub of the head flange and the spherical shell, where the membrane vessel force has, in general, a component in the direction perpendicular to the vessel axis, which has to be added to the edge effect solution for the vessel.

The rotations of the vessel and head flange rings were measured by means of tangential strain gauges mounted on the outer flange rims in the three longitudinal cross sections indicated in figure 3.3.10.

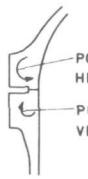

		FLANGE RING ROTATION IN 10^{-3} rad				CALCULATED RADIAL DISPLACEMENT AT GASKET FACE IN 10^{-1} mm		
		NUMERICAL			EXPERIMENTAL			
		r_g = 351 mm	r_g = 361 mm	r_g = 371 mm		r_g = 351 mm	r_g = 361 mm	r_g = 371 mm
VESSEL FLANGE	WITHOUT CORRECTION FOR BOLT HOLES	1.58	1.17	0.76	1.51	-1.22	-0.90	-0.59
	WITH CORRECTION FOR BOLT HOLES	1.63	1.21	0.78		-1.28	-0.95	-0.62
HEAD FLANGE	WITHOUT CORRECTION FOR BOLT HOLES	2.01	1.49	0.97	1.98	-1.45	-1.07	-0.70
	WITH CORRECTION FOR BOLT HOLES	2.14	1.59	1.03		-1.56	-1.16	-0.75

TABLE 3.3.3.

Comparison between calculated and measured flange ring deformations after bolt tightening the model vessel.

Table 3.3.3 gives a comparison between the numerical and experimental flange ring rotations after tightening the flange connection of the model vessel. In calculating these rotations it has been assumed that no friction force develops at the gasket faces during the tightening process (i.e. $Q_g = 0$ in figure 3.1.2). The measured rotations have been obtained from the mean strain gauge values over the three longitudinal cross sections.
It can be concluded from these results that, as already predicted by the test results on the deformation of the vessel flange sealing face presented in the preceding paragraph (cf. figure 3.3.11), the point of application of the gasket force P_g is indeed located between the inner rim and halfway the gasket face. The location calculated after combining the numerical and the experimental results from the table appears, as it should be, the same for both flanges, i.e. r_g = 354 mm, which corroborates the validity of the numerical and the experimental results. This validity is corroborated furthermore by the fact that the calculated rotation of the vessel flange ring after bolt tightening is in between the corresponding vessel flange gasket face rotations ϕ_A and ϕ_B indicated in figure 3.3.11.

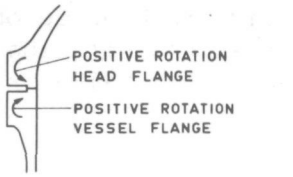

		FLANGE RING ROTATION IN 10^{-3} rad				CALCULATED RADIAL DISPLACEMENT AT GASKET FACE IN 10^{-1} mm		
		NUMERICAL			EXPERIMENTAL			
		r_g = 351 mm	r_g = 361 mm	r_g = 371 mm		r_g = 351 mm	r_g = 361 mm	r_g = 371 mm
VESSEL FLANGE	WITHOUT FRICTION	1.76	1.68	1.60	1.79	-0.38	-0.32	-0.26
	f_g = 0.3	1.93	1.85	1.76		-0.57	-0.51	-0.45
HEAD FLANGE	WITHOUT FRICTION	2.18	2.08	1.97	1.80	-1.15	-1.08	-1.00
	f_g = 0.3	1.98	1.87	1.77		-0.95	-0.87	-0.80

TABLE 3.3.4.

Comparison between calculated and measured flange ring deformations after pressurizing the model vessel.

Table 3.3.4 gives a comparison between the numerical and the experimental flange ring rotations after pressurizing up to 90 bar vessel pressure. As regards the calculated rotations, only the values obtained by correcting for the influence of the bolt holes are indicated in the table.
The calculations have been carried out for two values of the friction force Q_g at the gasket faces. The first of these was equal to zero, while the second equalled an arbitrary friction coefficient $f_g = 0.3$ times the gasket force P_g at 90 bar.
By combining the numerical and the experimental results from the table both the actual location of the point of application of the gasket force P_g and the magnitude of the friction force Q_g can be computed. For this purpose the numerical results for each of the two flanges have to be re-interpreted as follows

$$\phi\begin{bmatrix}\text{actual}\\ \text{numerical}\end{bmatrix} = \phi\begin{bmatrix}\text{numerical}\\ P_g \text{ located at } r_{i2} \text{ and } f_g = 0\end{bmatrix}^{+}$$

$$+ \Delta r_g\ \phi\begin{bmatrix}\text{numerical}\\ \text{no bolt forces and internal pressure}\\ P_g \text{ moves in outward direction for a}\\ \text{distance } \Delta r_g = 1\\ f_g = 0\end{bmatrix}^{+}$$

$$+ f_g\ \phi\begin{bmatrix}\text{numerical}\\ \text{no bolt forces and internal pressure}\\ P_g = 0\\ f_g = 1\end{bmatrix} \qquad (3.3.7)$$

where r_{i2} is defined in figure 3.3.5, while $\Delta r_g = [r_{g_{actual}} - r_{i2}]$ and the

magnitude of the three rotations defined in the right-hand side of (3.3.7) can be obtained from the table. By putting the numerical rotations on the basis of (3.3.7) equal to the corresponding experimental values a system of two equations is obtained, which yields the solution

$$r_{g_{actual}} = 369 \text{ mm}, \qquad f_g = 0.31$$

Thus it seems justified to conclude from the results given in the tables 3.3.3 and 3.3.4 that the point of application of the gasket force P_g moves in outward direction along the gasket faces during pressurizing. This conclusion is at least not contradicted by the test results on the deformation of the vessel flange sealing face presented in figure 3.3.12 which show the inner half B of this face to rotate in the same direction as the complete vessel and head flange rings.
In addition it can be concluded from the results presented in table 3.3.4 that the influence of the friction force Q_g is not negligibly small. The value chosen for Q_g (i.e. 0.3 P_g) seems to give a reasonably good description of the deformation behaviour of the flange connection under consideration because, after combining the numerical and the experimental results, it yields, as it should, about the same location of the point of application of P_g for both flanges, i.e. r_g = 368 mm (between halfway the gasket face and its outer rim).

Comparison of the results of table 3.3.3 and 3.3.4 confirms that the influence of the location of the point of application of the gasket force P_g on the resulting flange ring rotations is considerable after tightening, while it is much smaller after pressurizing.
The sum of flange ring rotations of the model vessel after pressurizing fits with the outward taper angle of the head flange gasket face. Therefore, perhaps somewhat prematurely and at least anticipating further experimental evidence on gasket face deformation to be gathered in the author's laboratory, it may tentatively be stated at this stage that a first approximation for satisfactorily tapering the head flange gasket face can be found by choosing the taper angle equal to the sum of the calculated rotations of the head flange ring and the vessel flange ring under a representative (operating!) condition.

4.1. Introduction.

The availability of an accurate computational method for determining both the maximum elastic stress concentration factor and the stress distribution in the neighbourhood of nozzle-to-cylinder connections is essential for designing against the various possible modes of failure at such intersections. In particular, to predict the formation of plastic hinge circles at the onset of plastic collapse caused either by a single overload (bursting) or by thermal ratcheting (incremental collapse) in a reliable manner knowledge of the elastic stress distribution across the entire load-bearing cross section is a prerequisite. On the other hand the prediction of fatigue crack formation and growth requires knowledge of the maximum local elastic stress occurring anywhere in the structure.
However, due to the non-axisymmetric character of the geometry and the loading, the elasticity problem for nozzle-to-cylinder connections is very complicated. Consequently, until only a few years ago the investigations reported in literature were nearly all experimental (cf. e.g. [4.1], [4.2], [4.3], [4.4], [4.5], [4.6], [4.7], [4.8]). The following computational methods with a more or less approximate character are known from literature and design practice:

1. The area method. This method, developed by LIND [4.9], gives some useful design formulae for the maximum stress concentration factor at internal pressure loading. These are, however, not based on a more or less rigorous analytical treatment but on a rough estimation of the stress raising effect. A basic assumption in this method is the occurrence of the maximum stress in the longitudinal section, while the shell behaviour is supposed to be dominant.

2. The thin shell theory method. An extensive historical survey of the thin shell theory analyses reported in literature has been given by LEKKERKERKER [4.10]. For the small nozzle-to-cylinder diameter ratios relevant in the context of the present thesis the treatment developed by LEKKERKERKER in his doctoral thesis [4.11] seems the most promising one. This analysis utilizes shallow shell theory for the main shell, whereas the branch pipe is approximated by a flat-ended tube.

By their very nature the above two methods lack the possibility to predict the highly localized peak stresses -occurring e.g. at the in- and outside fillets- required for fatigue analyses. The computation of these stresses requires the use of

3. The finite element method.
   3.1. Application of two-dimensional elements. Approximations utilizing ring elements under axisymmetric loading are sometimes used by design engineers, who replace the cylindrical vessel by a spherical shell with a radius of 1.5 or 2 times the vessel radius.
   3.2. Application of three-dimensional finite elements. Approaches using these elements have been reported by ARGYRIS [4.13, 4.14], by HELLEN and MONEY [4.15], by RASHID and GILMAN [4.16] and by KRISHNAMURTHY [4.17]. They offer a rigorous solution of the problem but a disadvantage, of course, is the large number of elements and nodal points needed. Therefore this approach is generally too expensive for practical applications.

The present thesis proposes a combination of the second and third methods for obtaining the stress distribution in the reinforced nozzle-to-cylinder

attachments of interest in high-pressure vessel technology, where the ratio between the outer diameter of the nozzle and the diameter of the cylinder does not exceed a value of e.g. 1/4 *). From a typical configuration shown in figure 4.1.1 it becomes clear that the thick-walled reinforced nozzle part excludes a two-piece thin shell analysis. Consequently, the connection will be schematized into its three constituent elements, viz. cylindrical shell, reinforced section and branch pipe. As a first step the present chapter investigates the potential of the flat plate analogy for the analysis of the above mentioned nozzle-to-cylinder intersections. This analogy permits to treat the structure as a solid of revolution under non-axisymmetric loading.
Subsequently the nozzle-to-flat plate computational method is extended to the nozzle-to-cylindrical vessel geometry. This generalization still treats the nozzle itself as geometrically rotationally symmetric, but considers the cylindrical vessel as a shallow cylindrical shell with a circular cutout.

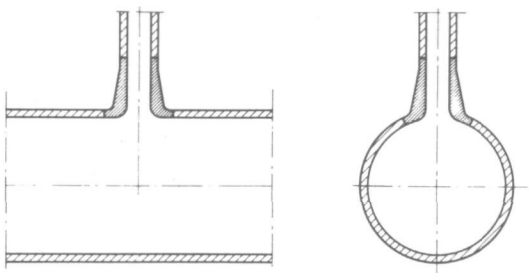

FIGURE 4.1.1.

Typical reinforced nozzle configuration.

4.2. Computational method for the biaxially loaded nozzle-to-flat plate connection.

The computational method for the nozzle-to-flat plate connection is based in principle upon the finite element method for solids of revolution under non-axisymmetric loadings. The general outline of this method has been given in Chapter 2.2.1 and implies a Fourier's series solution for the deformations and stresses in a direction tangential to the nozzle axis. Starting from this general outline the computational method proceeds to divide the structure into its three constituent elements, i.e. flat plate, reinforced section and cylindrical pipe and to determine the stiffness of each of these. In the case of the reinforced section this is done by subdividing it into the triangular ring elements developed in for this purpose in Chapter 2.2.2. The stiffnesses of the flat plate and the cylindrical pipe are determined by using the analytical solutions of the plate and shell equations for these elements in the way shown in the Chapters 2.3.2, 2.3.3 and 2.3.4.

---

*) *For the sake of completeness it should be remarked that large branch pipe-to-cylinder diameter ratios, of particular interest in piping systems, present an even more difficult problem. The applicability of shallow shell theory for the main shell becomes doubtful, while the intersecting shell is not nearly flat-ended. Therefore all numerical results reported in literature for this structure are obtained via the utilization of shell elements in a finite element approach. One of the best currently available shell elements has been developed by CLOUGH and JOHNSON [4.12], being of arbitrary quadrilateral shape and assembled from four triangular flat sub-elements which do not necessarily lie in the same plane.*

Once the elastic stiffnesses of the elements introduced before have been determined the compatibility conditions between the different elements have to be satisfied. The compatibility conditions between the triangular ring elements of the reinforced section can be satisfied by a suitable arrangement of the displacement parameters of each element in one displacement vector for the entire reinforced section. At the juncture of the reinforced section and the flat plate c.q. the cylindrical pipe the displacement parameters of the triangular ring elements should depend on the edge displacements and edge rotations of the flat plate c.q. the cylindrical pipe. This dependence has been expressed by specifying the general formulae developed in Appendix 1, i.e. by taking into account the basic Kirchhoff-Love assumptions from linear thin shell theory. Thus, as may be shown, complete compatibility is ensured over the whole boundary length at the two junctures between the constituent elements. It should be kept in mind that in satisfying the above compatibility conditions the particular part of the analytical plate and shell solutions (i.e. the free displacements due to the external loadings) enters the picture. For the cylindrical pipe under internal pressure loading the well-known particular solution for the radial displacement can be used (cf. [2.8, p. 482]), while the free edge displacements of a circular hole in an infinitely large rectangular plate under 1:2 biaxial tension are as follows (cf. e.g. [4.18])

$$\overset{0}{u} = \frac{r_0 \sigma_\infty}{E} \left[3 - 2 \cos 2\theta\right] \tag{4.2.1}$$

$$\overset{0}{v} = \frac{r_0 \sigma_\infty}{E} 2 \sin 2\theta \tag{4.2.2}$$

r_0 being the hole radius, σ_∞ the smallest tensile stress, θ the circumferential angle measured from the direction in which the smallest tensile stress is acting, $\overset{0}{u}$ the radial displacement, $\overset{0}{v}$ the circumferential displacement and E Young's modulus. The part of this solution that does not depend on θ represents the edge displacements of the hole due to 1.5:1.5 biaxial plate tension (i.e. axisymmetric loading), while the remaining part represents the corresponding displacements due to -0.5:0.5 biaxial plate tension (cf. figure 4.2.1).

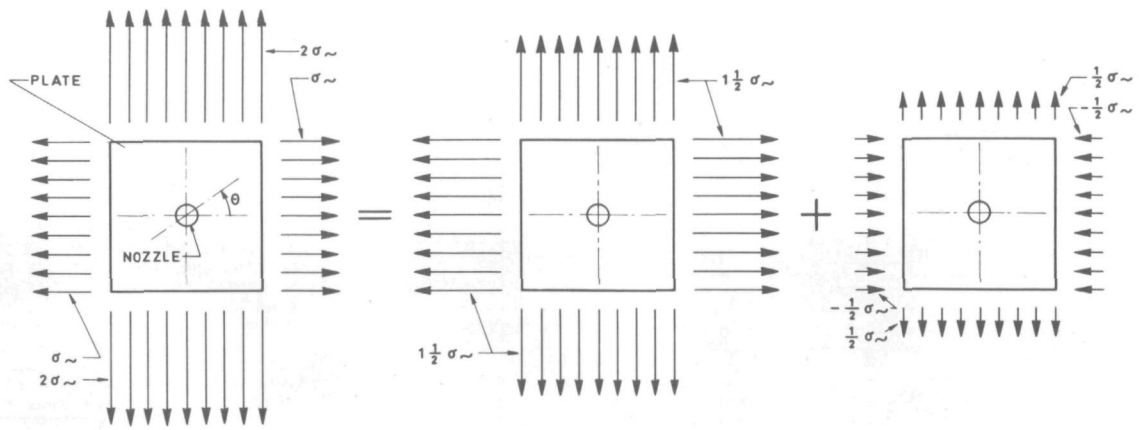

FIGURE 4.2.1.

Types of symmetry of the plate load.

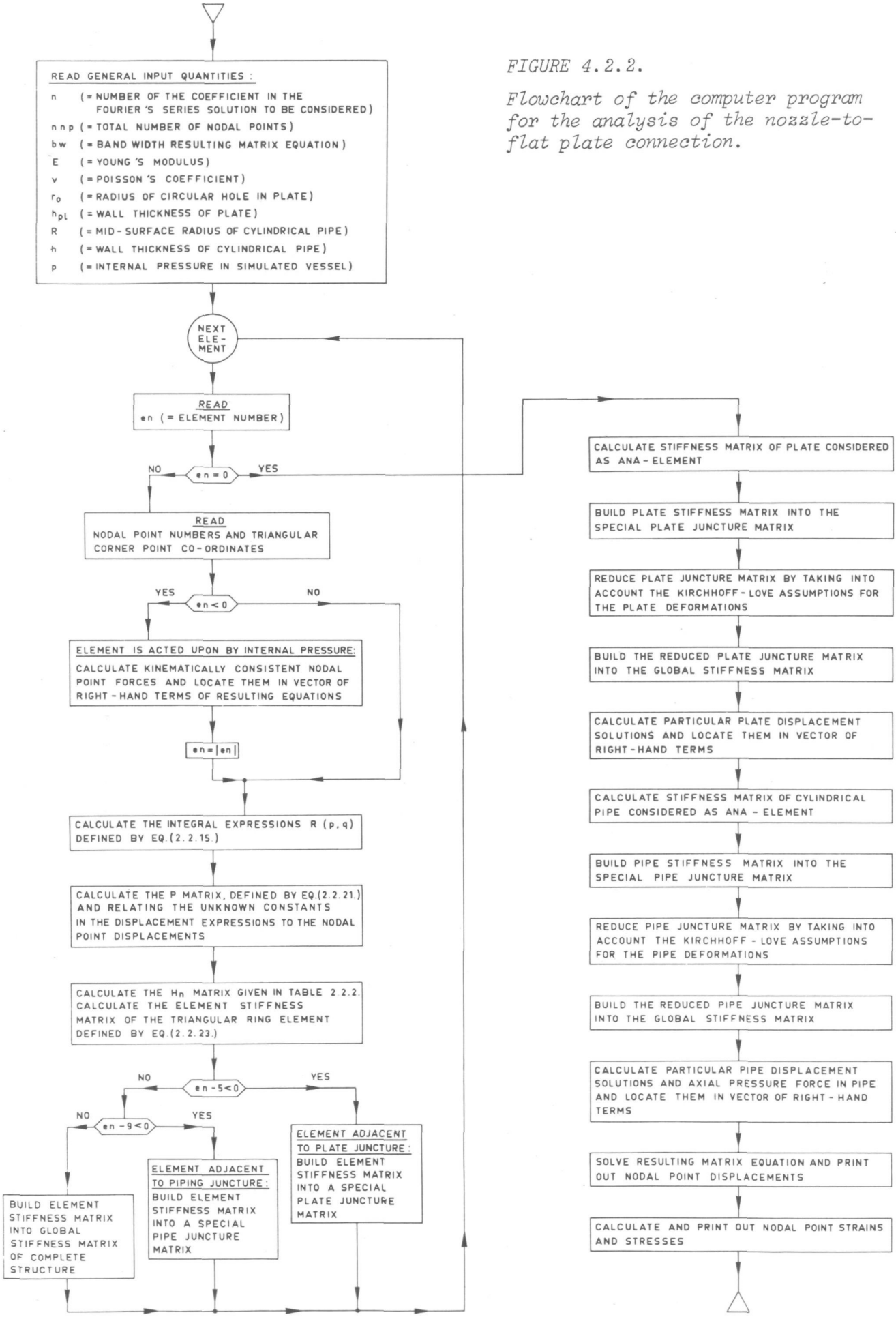

FIGURE 4.2.2.

Flowchart of the computer program for the analysis of the nozzle-to-flat plate connection.

Therefore it may be concluded from these formulae that the original three-dimensional finite element problem is split into two *uncoupled* quasi-two-dimensional problems, one of which is a real physical axisymmetric problem, while the other contains only solutions of the type $\{^{\cos}_{\sin}\}2\theta$. "Uncoupled" means that each external boundary loading of a certain harmonic type causes only displacements of the same type.
The virtual work equation for the nozzle-to-flat plate structure can now be completed by:

- putting the displacement at the plate juncture parallel to the nozzle axis equal to zero, thereby excluding the corresponding rigid body displacement
- introducing the so-called kinematically consistent loadings (cf. Chapter 2.3.1) in the relevant nodal points of the triangular ring elements subject to internal pressure
- taking into account the axial pressure force in the cylindrical pipe as a kinematically consistent force acting at the nodal points at the pipe juncture.

Figure 4.2.2 shows the flowchart of the computer program developed on the basis of the computational method described above. This flowchart needs no supplementary information, except for the following points:

- the number of elements adjacent to the plate juncture is equal to 4, while the same holds for the number of elements adjacent to the pipe juncture
- the elements adjacent to the plate juncture are numbered 1, 2, 3 and 4, while the elements adjacent to the pipe juncture are numbered 5, 6, 7 and 8
- after numbering the elements, the numbers of those elements which are subject to internal pressure receive a negative sign.

4.3. Generalization for the nozzle-to-cylinder connection.

4.3.1. Introductory remarks.

As mentioned before, in extending the preceding computational method to the nozzle-to-cylindrical vessel problem the assumption of completely axi-symmetric geometry with regard to the nozzle axis is maintained for the reinforced nozzle part. Therefore the analysis of the reinforced nozzle and cylindrical pipe part is identical, in principle, to the one described in the preceding section. In order to save computer time and memory the best way to incorporate this in the present context is to introduce a series of boundary loadings at the juncture with the cylindrical vessel and to calculate influence coefficients referring to a Fourier's series expansion. This has been worked out in the next sub-section.

The cylindrical vessel is treated separately and considered as a shallow thin circular cylindrical shell with a circular cutout. The stress distribution in this shell is written as the combination of a membrane state of stress (as would be present in the unweakened shell) and a stress distribution ensuing from a self-equilibrating boundary load along the edge of the circular hole. The latter problem is solved on the basis of the method developed by LEKKERKERKER [4.19, 4.10]. For this purpose a computer program [4.20] has been utilized which enables to evaluate influence coefficients referring to a Fourier's series expansion of the boundary loadings along the circular cutout. This program has been somewhat adapted for our purposes,

by transferring the boundary loadings acting in the sense of the shell surface co-ordinates to a statically equivalent system of loads acting in a plane z = constant in the sense of the cylindrical nozzle co-ordinates r, θ, z, viz. the plane that is tangent to the shell middle surface. This adaptation is described in Section 4.3.3. The corresponding adaptation for the membrane solution in the unweakened shell is described in Section 4.3.4. At this point the important difference with the computational method for the nozzle-to-flat plate structure becomes clear, as each separate boundary loading of the type $\{^{\cos}_{\sin}\}n\theta$ gives rise to a number of Fourier's coefficients in the series solutions for the boundary displacements and the edge rotation. This coupling effect influences the stress distribution in the reinforced nozzle and cylindrical pipe part via the last step in the computational method, where the continuity of the boundary loadings and the compatibility requirements at the cylindrical vessel juncture have to be satisfied. These requirements are specified in Section 4.3.5.

4.3.2. Influence coefficients for the reinforced nozzle and cylindrical pipe part.

As pointed out in the preceding sub-section the analysis of the reinforced nozzle and cylindrical pipe part does not differ, in principle, from the one described in Section 4.2. In fact, the flat plate ana-element in the latter analysis is replaced by a system of boundary forces and moments (cf. figure 4.3.1), which is written as a Fourier's series expansion in a direction tangential to the nozzle axis *)

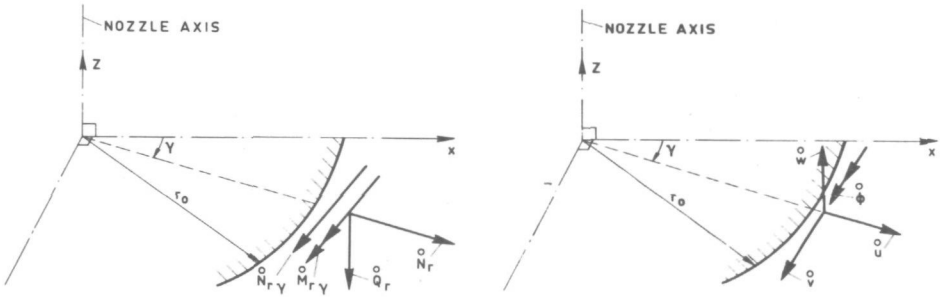

FIGURE 4.3.1.

Loadings and deformations along the edge of the reinforced nozzle part.

$$
\begin{aligned}
{}^{0}N_r &= \sum_{\ell=0}^{n_1} {}^{0}N_{r\ell} \cos 2\ell\gamma & {}^{0}N_{r\gamma} &= \sum_{\ell=1}^{n_1} {}^{0}N_{r\gamma\ell} \sin 2\ell\gamma \\
\frac{1}{r_0}\,{}^{0}M_r &= \sum_{\ell=0}^{n_1} \frac{1}{r_0}\,{}^{0}M_{r\ell} \cos 2\ell\gamma & {}^{0}Q_r &= \sum_{\ell=0}^{n_1} {}^{0}Q_{r\ell} \cos 2\ell\gamma
\end{aligned}
\qquad (4.3.1)
$$

where the integer number ℓ is related to the integer number n used in Chapter 2 in that $2\ell = n$. It should be noticed that the co-ordinate γ in these

*) *The superscript 0 refers to the value of a quantity at the boundary* r_0.

expressions differs from the co-ordinate θ defined in Chapter 2, i.e. $\gamma = -\theta$. This has been done in order to obtain the same positive sense for both the reinforced nozzle and the cylindrical vessel co-ordinate system.
The expansions (4.3.1) restrict the solution of the nozzle-to-cylindrical vessel problem to external loadings on the structure, containing two planes of symmetry, i.e. the plane $\gamma = 0$ through the nozzle axis and the vessel axis and the plane $\gamma = \frac{\pi}{2}$ through the nozzle axis perpendicular to the vessel axis. These symmetry aspects are not found in the cases of moment and shear force loadings on the nozzle. It is shown, however, in [3.8] by experimental evidence that the peak strains and stresses for internal pressure loading exceed by far those resulting from all other kinds of external loadings to be expected in practice. So these cases of mechanical loading seem to be of less importance and they will not be treated here.

In analogy with the analysis of the nozzle-to-flat plate connection the deformation of the reinforced nozzle edge plane at the cylindrical vessel juncture is completely described by the middle surface displacements and the edge rotation (cf. figure 4.3.1) by prescribing this plane to have a Kirchhoff-Love type of deformation. Again these middle surface edge deformations are written as Fourier's series expansions

$$\overset{0}{u} = \sum_{\ell=0}^{n_1} \overset{0}{u}_\ell \cos 2\ell\gamma \qquad \overset{0}{v} = \sum_{\ell=1}^{n_1} \overset{0}{v}_\ell \sin 2\ell\gamma$$

$$\overset{0}{w} = \sum_{\ell=0}^{n_1} \overset{0}{w}_\ell \cos 2\ell\gamma \qquad r_0 \overset{0}{\phi} = \sum_{\ell=0}^{n_1} r_0 \overset{0}{\phi}_\ell \cos 2\ell\gamma \qquad (4.3.2)$$

In accordance with the nozzle-to-flat plate analysis the original three-dimensional finite element problem for the reinforced nozzle and cylindrical pipe part is split into a series of uncoupled quasi-two-dimensional problems, the solutions of which may be written as follows

$$\left.\begin{aligned} \overset{0}{u}_0 &= \alpha_{110} \overset{0}{N}_{r0} + \alpha_{120} \frac{1}{r_0} \overset{0}{M}_{r0} + \overset{0}{u}_p \\ r_0 \overset{0}{\phi}_0 &= \alpha_{210} \overset{0}{N}_{r0} + \alpha_{220} \frac{1}{r_0} \overset{0}{M}_{r0} + r_0 \overset{0}{\phi}_p \end{aligned}\right\} \qquad (4.3.3)$$

$$\left.\begin{aligned} \overset{0}{u}_\ell &= \alpha_{11\ell} \overset{0}{N}_{r\ell} + \alpha_{12\ell} \overset{0}{N}_{r\gamma\ell} + \alpha_{13\ell} \overset{0}{Q}_{r\ell} + \alpha_{14\ell} \frac{1}{r_0} \overset{0}{M}_{r\ell} \\ \overset{0}{v}_\ell &= \alpha_{21\ell} \overset{0}{N}_{r\ell} + \alpha_{22\ell} \overset{0}{N}_{r\gamma\ell} + \alpha_{23\ell} \overset{0}{Q}_{r\ell} + \alpha_{24\ell} \frac{1}{r_0} \overset{0}{M}_{r\ell} \\ \overset{0}{w}_\ell &= \alpha_{31\ell} \overset{0}{N}_{r\ell} + \alpha_{32\ell} \overset{0}{N}_{r\gamma\ell} + \alpha_{33\ell} \overset{0}{Q}_{r\ell} + \alpha_{34\ell} \frac{1}{r_0} \overset{0}{M}_{r\ell} \\ r_0 \overset{0}{\phi}_\ell &= \alpha_{41\ell} \overset{0}{N}_{r\ell} + \alpha_{42\ell} \overset{0}{N}_{r\gamma\ell} + \alpha_{43\ell} \overset{0}{Q}_{r\ell} + \alpha_{44\ell} \frac{1}{r_0} \overset{0}{M}_{r\ell} \end{aligned}\right\} \quad \text{if } \ell > 0 \qquad (4.3.4)$$

In these solutions $\overset{0}{u}_p$ and $r_0 \overset{0}{\phi}_p$ represent the free edge deformations, i.e. the deformations due to the external loadings on the reinforced nozzle and cylindrical pipe part of the complete structure (e.g. internal pressure). As becomes clear from (4.3.2) these loadings are subjected to the (not essential) restriction that they are axisymmetric with regard to the nozzle axis. They are necessarily in equilibrium with the boundary force $\overset{0}{Q}_{r0}$.

The influence coefficients $\alpha_{ij\ell}$ (= $\alpha_{ji\ell}$) can now be determined by replacing the contribution of the flat plate to the virtual work equation of the nozzle-to-flat plate structure by the virtual work done by the boundary loadings (4.3.1) and by solving the resulting set of linear equations in the displacement parameters for unit loading systems. It results from (4.3.3) and (4.3.4) that we have three loading systems for $\ell = 0$ and four loading systems for $\ell > 0$. It should be noticed that solving a large set of linear equations for a number of right-hand members (i.e. 3 for $\ell = 0$ and 4 for $\ell > 0$) with the existing standard computer programs (Gauss, Cholesky) does hardly increase the computing time required.

4.3.3. Influence coefficients for the cylindrical vessel.

4.3.3.1. Loadings and deformations in Lekkerkerker's notation.

A symmary of Lekkerkerker's shallow thin shell theory method, utilized for the evaluation of appropriate influence coefficients for the cylindrical vessel part, is given in Appendix 6. The influence coefficients resulting from LEKKERKERKER's original analysis [4.19] refer to the following system of loadings, acting in the sense of the cylindrical shell surface co-ordinates *) along the edge of the circular cutout, and to the edge deformations resulting therefrom (cf. figure 4.3.2)

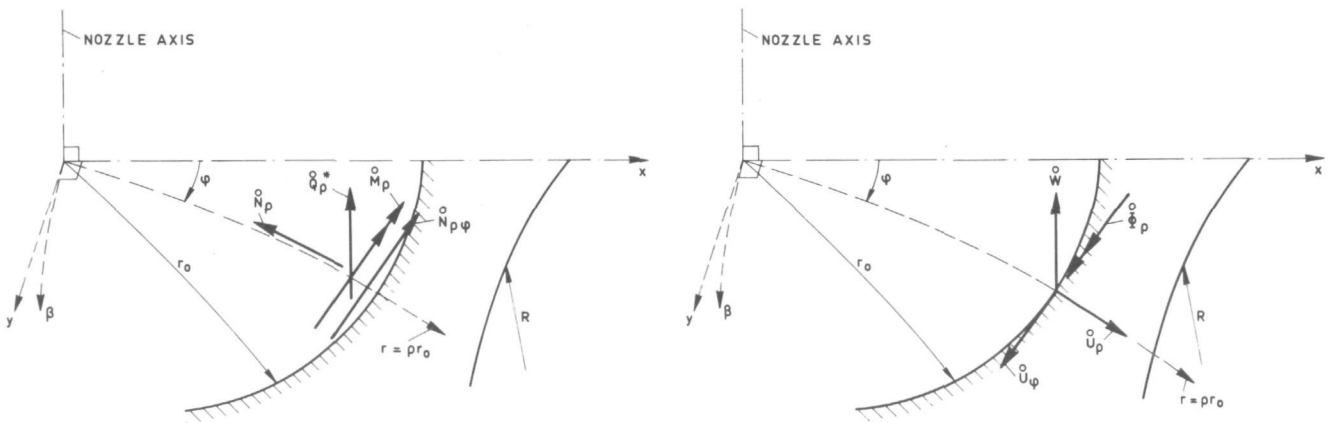

FIGURE 4.3.2.

Loadings and deformations along the edge of a circular cutout in the cylindrical shell.

*) *We shall use the non-dimensional co-ordinate* $\rho = r/r_0$.

$$
\left.
\begin{aligned}
{}^{0}N_{\rho} &= \sum_{\ell=0}^{n_1} {}^{0}N_{\rho}^{(\ell)} \cos 2\ell\phi & {}^{0}N_{\rho\phi} &= \sum_{\ell=1}^{n_1} {}^{0}N_{\rho\phi}^{(\ell)} \sin 2\ell\phi \\
\frac{1}{r_0}\,{}^{0}M_{\rho} &= \sum_{\ell=0}^{n_1} \frac{1}{r_0}\,{}^{0}M_{\rho}^{(\ell)} \cos 2\ell\phi & {}^{0*}Q_{\rho} &= \sum_{\ell=0}^{n_1} {}^{0*}Q_{\rho}^{(\ell)} \cos 2\ell\phi
\end{aligned}
\right\} \quad (4.3.5)
$$

$$
\left.
\begin{aligned}
{}^{0}U_{\rho} &= \sum_{\ell=0}^{n_1} {}^{0}U_{\rho}^{(\ell)} \cos 2\ell\phi & {}^{0}U_{\phi} &= \sum_{\ell=1}^{n_1} {}^{0}U_{\phi}^{(\ell)} \sin 2\ell\phi \\
{}^{0}W &= \sum_{\ell=0}^{n_1} {}^{0}W^{(\ell)} \cos 2\ell\phi & r_0\,{}^{0}\Phi_{\rho} &= \sum_{\ell=0}^{n_1} r_0\,{}^{0}\Phi_{\rho}^{(\ell)} \cos 2\ell\phi
\end{aligned}
\right\} \quad (4.3.6)
$$

where within the assumptions underlying the shallow thin shell theory

$$
{}^{0}\Phi_{\rho} = \left[\frac{\partial W}{\partial r}\right]_{r = r_0} \quad (4.3.7)
$$

Before formulating the continuity conditions for the boundary loadings and deformations at the reinforced nozzle juncture the above quantities have to be replaced by equivalent edge loadings and deformations acting in the sense of the cylindrical nozzle co-ordinates (cf. figure 4.3.1).

4.3.3.2. Adaptation of the boundary loadings.

Considering first the boundary loadings, this transformation may be accomplished most conveniently in the following consecutive steps:

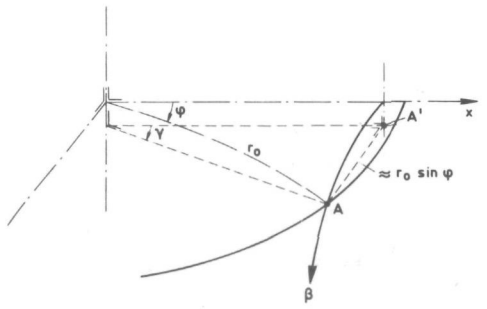

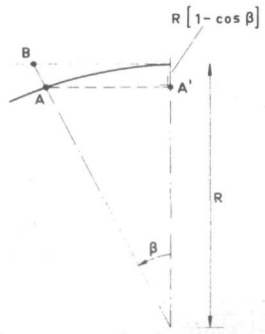

FIGURE 4.3.3.

Co-ordinates and notations for cylindrical shell edge.

1. Transferring the loading system shown in figure 4.3.2 from point A in the cylindrical shell mid-surface (cf. figure 4.3.3) to point B in the reinforced nozzle mid-surface (cf. figure 4.3.3), without changing the directions of the forces and the bending moments. This results in the following modified quantities, indicated by a superscript m

$$N_{\rho}^{0\,m} = N_{\rho}^{0} \qquad N_{\rho\phi}^{0\,m} = N_{\rho\phi}^{0}$$

$$\frac{1}{r_0} M_{\rho}^{0\,m} = \frac{1}{r_0} \left[M_{\rho}^{0} + N_{\rho}^{0} R \frac{1 - \cos \beta}{\cos \beta} \right] \tag{4.3.8}$$

$$Q_{\rho}^{0*m} = Q_{\rho}^{0*} + \frac{1}{r_0} \frac{\partial}{\partial \phi} \left[N_{\rho\phi}^{0} R \frac{1 - \cos \beta}{\cos \beta} \right]$$

The second term in the latter expression takes into account the effect of the change of the torsional edge moment on the reduced transverse shear force.

2. Replacement of the forces $N_{\rho}^{0\,m}$ and $N_{\rho\phi}^{0\,m}$ in a plane through point B parallel to the tangent plane through A by two equivalent forces $N_{x}^{0\,m}$ and $N_{\beta}^{0\,m}$ in the same plane, parallel and perpendicular to the x axis respectively

$$N_{x}^{0\,m} = N_{\rho}^{0\,m} \cos \phi - N_{\rho\phi}^{0\,m} \sin \phi$$

$$N_{\beta}^{0\,m} = N_{\rho\phi}^{0\,m} \cos \phi + N_{\rho}^{0\,m} \sin \phi \tag{4.3.9}$$

3. Replacement of the forces $N_{x}^{0\,m}$, $N_{\beta}^{0\,m}$ and Q_{ρ}^{0*m}, acting in point B, by three equivalent forces $N_{r}^{0\,c}$, $N_{r\gamma}^{0\,c}$ and $Q_{r}^{0\beta c}$, also acting in point B, in the directions r, γ and z (or the radial, tangential and axial directions) respectively of the cylindrical nozzle co-ordinate system

$$N_{r}^{0\,c} = N_{x}^{0\,m} \cos \gamma + \left[N_{\beta}^{0\,m} \cos \beta - Q_{\rho}^{0*m} \sin \beta \right] \sin \gamma$$

$$N_{r\gamma}^{0\,c} = \left[N_{\beta}^{0\,m} \cos \beta - Q_{\rho}^{0*m} \sin \beta \right] \cos \gamma - N_{x}^{0\,m} \sin \gamma \tag{4.3.10}$$

$$Q_{r}^{0\,c} = Q_{\rho}^{0*m} \cos \beta + N_{\beta}^{0\,m} \sin \beta$$

The modified boundary loadings $N_{r}^{0\,c}$, $N_{r\gamma}^{0\,c}$, $\frac{1}{r_0} M_{\rho}^{0}$ and $Q_{r}^{0\,c}$ can be expressed in the original dynamic boundary quantities (4.3.5) after substitution of (4.3.8) and (4.3.9) into (4.3.10). The co-ordinate β can be eliminated from the resulting expressions by taking into account the relationship between β and ϕ following from figure 4.3.3

$$\sin\beta = \frac{r_0}{R}\sin\phi \tag{4.3.11}$$

The resulting expressions can be modified by a simplification that is consistent with the inaccuracies due to the *shallow* shell theory underlying the analysis. It may be concluded from the discussion given in Chapter 6 of [4.11] that the main additional quantitative consequence of these inaccuracies, as compared to the basic errors underlying thin shell theory (cf. Chapter 1.2), is the neglection of r_0^2/R^2 with respect to 1 if $\mu = \frac{1}{2}\sqrt[4]{12(1-\nu^2)}\, r_0/\sqrt{hR}$ is small (h being the vessel thickness) or the neglection of $\mu\, r_0^2/R^2$ with respect to 1 if μ is large. Consequently, the contribution of the original reduced transverse shear force Q_ρ^{0*} to the first two expressions of (4.3.10) can be neglected, while the factors cos β in (4.3.10) can be replaced by 1 and the factors $(1 - \cos\beta)/\cos\beta$ in (4.3.8) can be replaced by $r_0^2 \sin^2\phi/(2R^2)$.

After utilizing the goniometrical relationships

$$\begin{aligned}
\sin 2\ell\gamma \cos 2\gamma &= \tfrac{1}{2}\left[\sin 2(\ell+1)\gamma + \sin 2(\ell-1)\gamma\right]\\
\cos 2\ell\gamma \sin 2\gamma &= \tfrac{1}{2}\left[\sin 2(\ell+1)\gamma - \sin 2(\ell-1)\gamma\right]\\
\cos 2\ell\gamma \cos 2\gamma &= \tfrac{1}{2}\left[\cos 2(\ell+1)\gamma + \cos 2(\ell-1)\gamma\right]\\
\sin 2\ell\gamma \sin 2\gamma &= -\tfrac{1}{2}\left[\cos 2(\ell+1)\gamma - \cos 2(\ell-1)\gamma\right]
\end{aligned} \tag{4.3.12}$$

the following final expressions for the modified boundary loadings are obtained

$$\boxed{\begin{aligned}
{}^{0c}N_r &= \sum_{\ell=0}^{n_1} {}^{0}N_\rho(\ell)\cos 2\ell\gamma & {}^{0c}N_{r\gamma} &= \sum_{\ell=1}^{n_1} {}^{0}N_{\rho\phi}(\ell)\sin 2\ell\gamma\\
\frac{1}{r_0}{}^{0m}M_\rho &= \sum_{\ell=0}^{n_1} \frac{1}{r_0}{}^{0m}M_\rho(\ell)\cos 2\ell\gamma & {}^{0c}Q_r &= \sum_{\ell=0}^{n_1} {}^{0c}Q_r(\ell)\cos 2\ell\gamma
\end{aligned}} \tag{4.3.13}$$

where

$$\begin{aligned}
{}^{0m}M_\rho(0) &= {}^{0}M_\rho(0) + \frac{r_0^2}{8R}\left[2\,{}^{0}N_\rho(0) - {}^{0}N_\rho(1)\right]\\
{}^{0m}M_\rho(1) &= {}^{0}M_\rho(1) + \frac{r_0^2}{8R}\left[-2\,{}^{0}N_\rho(0) + 2\,{}^{0}N_\rho(1) - {}^{0}N_\rho(2)\right]\\
{}^{0m}M_\rho(\ell) &= {}^{0}M_\rho(\ell) + \frac{r_0^2}{8R}\left[-{}^{0}N_\rho(\ell-1) + 2\,{}^{0}N_\rho(\ell) - {}^{0}N_\rho(\ell+1)\right], \quad \text{if } \ell > 1
\end{aligned} \tag{4.3.14}$$

and

$$
\begin{aligned}
{}^{0c}_{r}Q\,(0) &= {}^{0*}_{\rho}Q\,(0) + \frac{r_0}{4R}\left[2\,{}^{0}_{\rho}N\,(0) - {}^{0}_{\rho}N\,(1) + {}^{0}_{\rho\phi}N\,(1)\right] \\
{}^{0c}_{r}Q\,(1) &= {}^{0*}_{\rho}Q\,(1) + \frac{r_0}{4R}\left[-2\,{}^{0}_{\rho}N\,(0) + 2\,{}^{0}_{\rho}N\,(1) - {}^{0}_{\rho}N\,(2) + 2\,{}^{0}_{\rho\phi}N\,(1)\right] \\
{}^{0c}_{r}Q\,(\ell) &= {}^{0*}_{\rho}Q\,(\ell) + \frac{r_0}{4R}\left[-{}^{0}_{\rho}N\,(\ell-1) + 2\,{}^{0}_{\rho}N\,(\ell) - {}^{0}_{\rho}N\,(\ell+1) + \right. \\
&\quad \left. - (\ell+1)\,{}^{0}_{\rho\phi}N\,(\ell-1) + 2\,\ell\,{}^{0}_{\rho\phi}N\,(\ell) - (\ell-1)\,{}^{0}_{\rho\phi}N\,(\ell+1)\right], \quad \text{if } \ell > 1
\end{aligned}
\tag{4.3.15}
$$

It should be noticed that the reduced transverse shear force ${}^{0c}_{r}Q\,(0)$ vanishes automatically because of the self-equilibrating character of the boundary loadings mentioned in Section 4.3.1.

4.3.3.3. Adaptation of the edge deformations.

The transformation of the edge deformations (4.3.6) can be accomplished in the following consecutive steps:

1. Replacement of the edge deformations shown in figure 4.3.2 by the corresponding modified deformations in point B in the reinforced nozzle mid-surface (cf. figure 4.3.3), taking into account the Kirchhoff-Love assumptions for the deformations

$$
\begin{aligned}
{}^{0m}_{\rho}U &= {}^{0}_{\rho}U - {}^{0}_{\rho}\Phi\, R\,\frac{1-\cos\beta}{\cos\beta} \\
{}^{0m}_{\phi}U &= {}^{0}_{\phi}U - {}^{0}_{\phi}\Phi\, R\,\frac{1-\cos\beta}{\cos\beta} \\
{}^{0m}W &= {}^{0}W \qquad\qquad {}^{0m}_{\rho}\Phi = {}^{0}_{\rho}\phi
\end{aligned}
\tag{4.3.16}
$$

where within the assumptions underlying the shallow thin shell theory

$$
{}^{0}_{\phi}\Phi = \left[\frac{1}{r}\,\frac{\partial W}{\partial \phi}\right]_{r=r_0}
\tag{4.3.17}
$$

2. Replacement of the displacements ${}^{0m}_{\rho}U$ and ${}^{0m}_{\phi}U$ of point B parallel to the tangent plane through point A by two equivalent displacements ${}^{0m}_{x}U$ and ${}^{0m}_{\beta}U$ in the same plane, parallel and perpendicular to the x axis respectively

$$
\begin{aligned}
{}^{0m}U_x &= {}^{0m}U_\rho \cos\phi - {}^{0m}U_\phi \sin\phi \\
{}^{0m}U_\beta &= {}^{0m}U_\phi \cos\phi + {}^{0m}U_\rho \sin\phi
\end{aligned}
\qquad (4.3.18)
$$

3. Replacement the three displacement components ${}^{0m}U_x$, ${}^{0m}U_\beta$ and ${}^{0m}W$ of point B by three equivalent components ${}^{0c}U_r$, ${}^{0c}U_\gamma$ and ${}^{0c}W$ of the same point in the directions r, γ and z respectively of the cylindrical nozzle co-ordinate system

$$
\begin{aligned}
{}^{0c}U_r &= {}^{0m}U_x \cos\gamma + \left[{}^{0m}U_\beta \cos\beta + {}^{0m}W \sin\beta\right] \sin\gamma \\
{}^{0c}U_\gamma &= \left[{}^{0m}U_\beta \cos\beta + {}^{0m}W \sin\beta\right] \cos\gamma - {}^{0m}U_x \sin\gamma \\
{}^{0c}W &= {}^{0m}W \cos\beta - {}^{0m}U_\beta \sin\beta
\end{aligned}
\qquad (4.3.19)
$$

The modified edge deformations ${}^{0c}U_r$, ${}^{0c}U_\gamma$, ${}^{0c}W$ and ${}^{0m}\Phi_\rho$ can be expressed in the original kinematic boundary quantities (4.3.6) after substitution of (4.3.16) and (4.3.18) into (4.3.19). The resulting expressions can again be modified by a simplification that is consistent with the inaccuracies due to the shallow thin shell theory. Consequently the following final expressions for the modified edge deformations are obtained

$$
\begin{aligned}
{}^{0c}U_r &= \sum_{\ell=0}^{n_1} {}^{0c}U_r^{(\ell)} \cos 2\ell\gamma & {}^{0c}U_\gamma &= \sum_{\ell=1}^{n_1} {}^{0c}U_\gamma^{(\ell)} \sin 2\ell\gamma \\
{}^{0c}W &= \sum_{\ell=0}^{n_1} {}^{0}W^{(\ell)} \cos 2\ell\gamma & r_0\,{}^{0m}\Phi_\rho &= \sum_{\ell=0}^{n_1} r_0\,{}^{0}\Phi_\rho^{(\ell)} \cos 2\ell\gamma
\end{aligned}
\qquad (4.3.20)
$$

where

$$
{}^{0c}U_r^{(0)} = {}^{0}U_\rho^{(0)} + \frac{r_0}{4R}\left[2\,{}^{0}W^{(0)} - {}^{0}W^{(1)} + \tfrac{1}{2} r_0 \left\{-2\,{}^{0}\Phi_\rho^{(0)} + {}^{0}\Phi_\rho^{(1)}\right\}\right]
\qquad (4.3.21a)
$$

$$\overset{0}{U}{}^{c}_{r}(1) = \overset{0}{U}_{\rho}(1) + \frac{r_0}{4R}\left[-2\,\overset{0}{W}(0) + 2\,\overset{0}{W}(1) - \overset{0}{W}(2) + \right.$$

$$\left. + \tfrac{1}{2} r_0 \{2\,\overset{0}{\Phi}_{\rho}(0) - 2\,\overset{0}{\Phi}_{\rho}(1) + \overset{0}{\Phi}_{\rho}(2)\}\right] \qquad (4.3.21b)$$

$$\overset{0}{U}{}^{c}_{r}(\ell) = \overset{0}{U}_{\rho}(\ell) + \frac{r_0}{4R}\left[-\overset{0}{W}(\ell-1) + 2\,\overset{0}{W}(\ell) - \overset{0}{W}(\ell+1) + \right.$$

$$\left. + \tfrac{1}{2} r_0 \{\overset{0}{\Phi}_{\rho}(\ell-1) - 2\,\overset{0}{\Phi}_{\rho}(\ell) + \overset{0}{\Phi}_{\rho}(\ell+1)\}\right], \quad \text{if } \ell > 1 \qquad (4.3.21c)$$

and

$$\overset{0}{U}{}^{c}_{\gamma}(1) = \overset{0}{U}_{\phi}(1) + \frac{r_0}{4R}\left[2\,\overset{0}{W}(0) + 2\,\overset{0}{W}(1) - 3\,\overset{0}{W}(2)\right]$$

$$\overset{0}{U}{}^{c}_{\gamma}(\ell) = \overset{0}{U}_{\phi}(\ell) + \frac{r_0}{4R}\left[-(\ell-2)\,\overset{0}{W}(\ell-1) + 2\ell\,\overset{0}{W}(\ell) - (\ell+2)\,\overset{0}{W}(\ell+1)\right], \text{ if } \ell > 1 \qquad (4.3.22)$$

4.3.4. Adaptation of the internal pressure membrane solution.

As pointed out in Section 4.3.1 the above self-equilibrating boundary loadings (4.3.13) and the corresponding edge deformations (4.3.20) -to which we shall refer as the homogeneous solution- have to be increased by the membrane loadings and deformations as would be present in the unweakened shell -to which we shall refer as the particular solution. This unweakened shell solution should again refer to the polar nozzle co-ordinate system because of the assumed axisymmetric geometry of the reinforced nozzle part.

As the membrane solution for the unweakened cylindrical shell does not possess only membrane characteristics with regard to the middle surface of the reinforced nozzle model at the cylindrical vessel juncture two possible internal pressure membrane solutions appear to be of interest.

The first of these, which one would think to be the most consistent and to give the most reliable results, originates from the well-known membrane solution for an unweakened circular cylindrical shell in the x-β co-ordinate system. This solution transforms as follows in the ρ-φ co-ordinate system

$$\left.\begin{aligned} N_{\rho,p} &= \tfrac{1}{4} p R \left[3 - \cos 2\phi\right] \qquad N_{\phi,p} = \tfrac{1}{4} p R \left[3 + \cos 2\phi\right] \\ N_{p\phi,p} &= \tfrac{1}{4} p R \sin 2\phi \end{aligned}\right\} \qquad (4.3.23)$$

$$\left.\begin{aligned} U_{\rho,p} &= \frac{r_0\rho}{Eh} p R \tfrac{1}{2}(\tfrac{1}{2} - \nu)(1 + \cos 2\phi) \\ U_{\phi,p} &= -\frac{r_0\rho}{Eh} p R \tfrac{1}{2}(\tfrac{1}{2} - \nu) \sin 2\phi \\ W_{p} &= \frac{R}{Eh} p R (1 - \tfrac{1}{2}\nu) \end{aligned}\right\} \qquad (4.3.24)$$

Applying the same transformation procedure as described before for the self-equilibrating boundary loadings and the corresponding edge deformations the following non-zero boundary quantities in the r-γ co-ordinate system are obtained

$$
\left.
\begin{aligned}
&{}^{0c}N_{r,p} = {}^{0c}N_{r,p}(0) + {}^{0c}N_{r,p}(1)\cos 2\gamma \\
&{}^{0c}N_{r\gamma,p} = {}^{0c}N_{r\gamma,p}(1)\sin 2\gamma \\
&\frac{1}{r_0}\,{}^{0m}M_{\rho,p} = \frac{1}{r_0}\,{}^{0m}M_{\rho,p}(0) + \frac{1}{r_0}\,{}^{0m}M_{\rho,p}(1)\cos 2\gamma + \frac{1}{r_0}\,{}^{0m}M_{\rho,p}(2)\cos 4\gamma \\
&{}^{0c}Q_{r,p} = {}^{0c}Q_{r,p}(0) + {}^{0c}Q_{r,p}(1)\cos 2\gamma + {}^{0c}Q_{r,p}(2)\cos 4\gamma
\end{aligned}
\right\} \quad (4.3.25)
$$

where

$$
\left.
\begin{aligned}
&{}^{0c}N_{r,p}(0) = \tfrac{3}{4}\,p\,R \qquad {}^{0c}N_{r,p}(1) = -\,{}^{0c}N_{r\gamma,p}(1) = -\tfrac{1}{4}\,p\,R \\
&\frac{1}{r_0}\,{}^{0m}M_{\rho,p}(0) = \frac{7}{32}\,p\,r_0 \qquad \frac{1}{r_0}\,{}^{0m}M_{\rho,p}(1) = -\tfrac{1}{4}\,p\,r_0 \\
&\frac{1}{r_0}\,{}^{0m}M_{\rho,p}(2) = \frac{1}{32}\,p\,r_0 \\
&{}^{0c}Q_{r,p}(0) = \tfrac{1}{2}\,p\,r_0 \qquad {}^{0c}Q_{r,p}(1) = -\frac{3}{8}\,p\,r_0 \\
&{}^{0c}Q_{r,p}(2) = -\frac{1}{8}\,p\,r_0
\end{aligned}
\right\} \quad (4.3.26)
$$

and

$$
\left.
\begin{aligned}
&{}^{0c}U_{r,p} = {}^{0c}U_{r,p}(0) + {}^{0c}U_{r,p}(1)\cos 2\gamma \\
&{}^{0c}U_{\gamma,p} = {}^{0c}U_{\gamma,p}(1)\sin 2\gamma \\
&{}^{0c}W_{p} = W_{p} = \frac{R}{Eh}\,p\,R\,(1 - \tfrac{1}{2}\nu)
\end{aligned}
\right\} \quad (4.3.27)
$$

where

$$U^{0\,c}_{r,p}(0) = \frac{r_0}{Eh}\, p\, R\, \tfrac{3}{4}\,(1-\nu)$$

$$U^{0\,c}_{r,p}(1) = -\,U^{0\,c}_{\gamma,p}(1) = -\,\frac{r_0}{Eh}\, p\, R\, \tfrac{1}{4}\,(1+\nu) \qquad (4.3.28)$$

The second internal pressure membrane solution of interest originates from the infinitely large unweakened flat plate under 1:2 biaxial tension. Again the corresponding boundary quantities can be written as (4.3.25) and (4.3.27), where the Fourier's coefficients do not differ from (4.3.26) and (4.3.28), except that *)

$$\frac{1}{r_0}\, M^{0\,m}_{\rho,p}(0) = \frac{1}{r_0}\, M^{0\,m}_{\rho,p}(1) = \frac{1}{r_0}\, M^{0\,m}_{\rho,p}(2) = 0$$

$$Q^{0\,c}_{r,p}(0) = Q^{0\,c}_{r,p}(1) = Q^{0\,c}_{r,p}(2) = 0 \qquad (4.3.29)$$

and

$$W^{0\,c}_{p} = 0 \qquad (4.3.30)$$

The reliability of the two above approaches, i.e. their influence on the behaviour of the reinforced nozzle part, will be tested by experimental evidence in Section 4.4.3.

4.3.5. Continuity conditions at the cylindrical vessel juncture.

In order to satisfy the continuity conditions at the cylindrical vessel juncture the influence coefficients for the cylindrical vessel part, resulting from the analysis described in Sub-section 4.3.3, will be located into a $((4n_1+2) \times (4n_1+2))$ flexibility matrix MC. This matrix relates the vector of homogeneous (i.e. self-equilibrating) boundary loadings $\overline{q^c_h}$, defined by

$$\overline{q^c_h}' = \left| N^0_\rho(0)\;\; \frac{1}{r_0} M^{0\,m}_\rho(0)\;\; N^0_\rho(1)\;\; N^0_{\rho\phi}(1)\;\; Q^{0\,c}_r(1)\;\; \frac{1}{r_0} M^{0\,m}_\rho(1)\;\; \ldots\ldots \right.$$

$$\left. \ldots\ldots\; N^0_\rho(n_1)\;\; N^0_{\rho\phi}(n_1)\;\; Q^{0\,c}_r(n_1)\;\; \frac{1}{r_0} M^{0\,m}_\rho(n_1) \right| \qquad (4.3.31)$$

*) *Apart from a co-ordinate definition these results do not differ from the corresponding solution utilized by LEKKERKERKER in Chapter 5.4 of [4.11] for the analysis of a thin-walled circular cylindrical branch pipe attached to the main shell.*

to the vector of corresponding homogeneous edge deformations $\overline{w_h^c}$, defined by

$$\overline{w_h^c}' = \left| {}^{0}_{U_r}{}^{c}(0) \quad r_0 {}^{0}_{\Phi_\rho}(0) \quad {}^{0}_{U_r}{}^{c}(1) \quad {}^{0}_{U_\gamma}{}^{c}(1) \quad {}^{0}_{W}(1) \quad r_0 {}^{0}_{\Phi_\rho}(1) \quad \ldots\ldots \right.$$

$$\left. \ldots\ldots \; {}^{0}_{U_r}{}^{c}(n_1) \quad {}^{0}_{U_\gamma}{}^{c}(n_1) \quad {}^{0}_{W}(n_1) \quad r_0 {}^{0}_{\Phi_\rho}(n_1) \right| \tag{4.3.32}$$

viz.

$$\overline{w_h^c} = MC \; \overline{q_h^c} \tag{4.3.33}$$

Introducing the vector of particular boundary loadings $\overline{q_p^c}$, defined by

$$\overline{q_p^c}' = \left| {}^{0}_{N_{r,p}}{}^{c}(0) \quad \frac{1}{r_0} {}^{0}_{M_{\rho,p}}{}^{m}(0) \quad {}^{0}_{N_{r,p}}{}^{c}(1) \quad {}^{0}_{N_{r\gamma,p}}{}^{c}(1) \quad {}^{0}_{Q_{r,p}}{}^{c}(1) \quad \frac{1}{r_0} {}^{0}_{M_{\rho,p}}{}^{m}(1) \right.$$

$$\left. 0 \quad 0 \quad {}^{0}_{Q_{r,p}}{}^{c}(2) \quad \frac{1}{r_0} {}^{0}_{M_{\rho,p}}{}^{m}(2) \quad \ldots\ldots \quad 0 \quad 0 \quad 0 \quad 0 \right| \tag{4.3.34}$$

and the vector of corresponding particular edge deformations $\overline{w_p^c}$, defined by

$$\overline{w_p^c}' = \left| {}^{0}_{U_{r,p}}{}^{c}(0) \quad 0 \quad {}^{0}_{U_{r,p}}{}^{c}(1) \quad {}^{0}_{U_{\gamma,p}}{}^{c}(1) \quad 0 \quad 0 \quad \ldots\ldots \right.$$

$$\left. \ldots\ldots \quad 0 \quad 0 \quad 0 \quad 0 \right| \tag{4.3.35}$$

the resulting boundary loadings (located in a vector $\overline{q^c}$) and the resulting edge deformations (located in a vector $\overline{w^c}$) are equal to

$$\overline{q^c} = \overline{q_h^c} + \overline{q_p^c} \qquad \overline{w^c} = \overline{w_h^c} + \overline{w_p^c} \tag{4.3.36}$$

From (4.3.33) and (4.3.36) the following relationship can be obtained between the vector of resulting boundary loadings and the vector of resulting edge deformations for the cylindrical vessel

$$\overline{w^c} = MC \left[\overline{q^c} - \overline{q_p^c} \right] + \overline{w_p^c} \tag{4.3.37}$$

The second step before satisfying the continuity conditions at the cylindrical vessel juncture consists of locating the influence coefficients for the reinforced nozzle and cylindrical pipe part, resulting from the analysis described in Section 4.3.2, into a $((4n_1+2) \times (4n_1+2))$ flexibility matrix MN. This matrix relates the vector of homogeneous (i.e. self-equilibrating) boundary loadings $\overline{q_h^n}$, defined by

$$\overline{q_h^n}' = \left| {}^0N_{r0} \quad \frac{1}{r_0}{}^0M_{r0} \quad {}^0N_{r1} \quad {}^0N_{r\gamma 1} \quad {}^0Q_{r1} \quad \frac{1}{r_0}{}^0M_{r1} \quad \ldots\ldots \right.$$

$$\left. \ldots\ldots \; {}^0N_{rn_1} \quad {}^0N_{r\gamma n_1} \quad {}^0Q_{rn_1} \quad \frac{1}{r_0}{}^0M_{rn_1} \right| \qquad (4.3.38)$$

to the vector of homogeneous edge deformations $\overline{w_h^n}$, defined by

$$\overline{w_h^n}' = \left| {}^0(u_0 - u_p) \quad {}^0r_0(\phi_0 - \phi_p) \quad u_1 \quad v_1 \quad w_1 \quad r_0\phi_1 \quad \ldots\ldots \right.$$

$$\left. \ldots\ldots \; u_{n_1} \quad v_{n_1} \quad w_{n_1} \quad r_0\phi_{n_1} \right| \qquad (4.3.39)$$

viz.

$$\overline{w_h^n} = MN \; \overline{q_h^n} \qquad (4.3.40)$$

The structure of the MN matrix is shown in table 4.3.1.

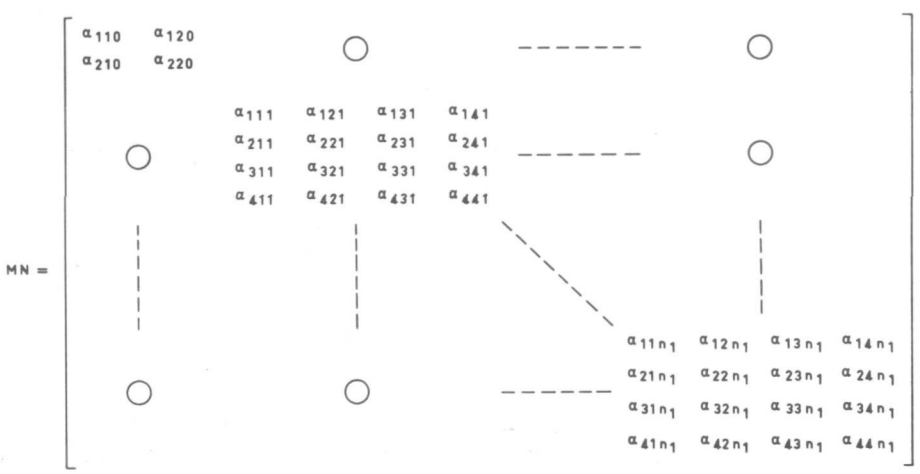

TABLE 4.3.1. The MN matrix.

It can be concluded from the analysis given in Section 4.3.2 (cf. (4.3.3) and (4.3.4)) that the vector of homogeneous boundary loadings $\overline{q_h^n}$ equals the corresponding vector of total boundary loadings $\overline{q^n}$, while the total edge

deformations (located in a vector $\overline{w^n}$) can be obtained by increasing the vector $\overline{w_h^n}$ by the vector of particular edge deformations

$$\overline{w_p^n}' = \left| \begin{matrix} 0 & 0 \\ u_p & r_0\phi_p \end{matrix} \quad 0 \quad 0 \quad 0 \quad 0 \quad \ldots\ldots \right.$$

$$\left. \ldots\ldots 0 \quad 0 \quad 0 \quad 0 \right| \tag{4.3.41}$$

i.e.

$$\overline{w^n} = \overline{w_h^n} + \overline{w_p^n} \tag{4.3.42}$$

From (4.3.40) and (4.3.42) the following relationship can be obtained between the vector of resulting boundary loadings and the vector of resulting edge deformations for the reinforced nozzle and cylindrical pipe part

$$\overline{w^n} = MN\ \overline{q^n} + \overline{w_p^n} \tag{4.3.43}$$

From figures 4.3.1 and 4.3.2 the continuity conditions for the boundary loadings and the edge deformations at the cylindrical vessel juncture read

$$\overline{q^c} = \overline{q^n} \qquad \overline{w^c} = \overline{w^n} \tag{4.3.44}$$

By means of (4.3.37), (4.3.43) and (4.3.44) the following set of equations can be obtained for the unknown boundary loadings located in the vector $\overline{q^c}$

$$[MC - MN]\ \overline{q^c} = MC\ \overline{q_p^c} - \overline{w_p^c} + \overline{w_p^n} \tag{4.3.45}$$

It should be remarked that the coupling effect, mentioned in Section 4.3.1, which makes the nozzle-to-cylindrical vessel computational method essentially different from the nozzle-to-flat plate computational method, is ensured in (4.3.45) by the nature of matrix MC.
Once the boundary loadings have been solved from (4.3.45) the complete distribution of strain and stress in the nozzle-to-cylinder connection can be determined.

4.4. Evaluation by comparison with experimental results.

4.4.1. Description of test arrangement.

To provide a basis for comparison with the computational results, two series of experiments have been carried out, both referring to the three nozzles N2, N4, and N5 attached to the cylindrical part of the 1:4 scale model (internal diameter 702 mm) of the 50 MWe Dodewaard BWR vessel (design pressure 87.9 atm; design temperature 301.6 °C) shown in figure 3.2.2.
One of these series refers to the internal pressure loading of the nozzles

in their actual location in the vessel. The second refers to the simulated internal pressure loading of identical nozzles *) attached to a flat plate. In both cases the nozzles were fabricated to identical drawings *) prescribing extremely close tolerances. In actual fact the nozzles welded into the vessel were fabricated with the aid of replicas taken off the corresponding nozzles in the flat plate.
The shape and dimensions of the nozzles mentioned above are indicated in figure 4.4.1, while figure 4.4.2 (see p. 100) shows the locations of the strain gauges attached to the model vessel nozzles. These gauges had a filament length of about 0.5 mm.
The strain gauge locations for the inner surfaces of the flat plate nozzles were practically identical to those for the model vessel nozzles, while the locations for the outer surfaces were practically identical to the corresponding locations for the sections through the nozzle axis and the vessel axis. The exact locations of the strain gauges have been determined after the attachment by means of the optical instruments shown in figure 4.4.3 (see p. 101). The strains were measured by means of the automatic installation mentioned in Chapter 3.2.1.

To simulate the static load in the pressurized vessel for the flat plate nozzles each of these has been exposed to the following consecutive loading modes:

- uniaxial tension of the plate to a stress equal to the tangential membrane stress in the undisturbed pressurized vessel
- internal hydraulic pressurization of the nozzle (cf. figure 4.4.4, see p. 101)
- axial tensile load on the nozzle equal to $\frac{\pi}{4} d_i^2 p$, d_i being the internal nozzle diameter.

Superposition of the strains measured at these loadings and of those which would have resulted from uniaxial tension of the plate in a direction perpendicular to the above to cause a stress equal to the axial membrane stress results in total strains directly comparable to those in the actual pressurized vessel.
The uniaxial tensioning of the plate has been performed by means of a 200 tf uniaxial tensile machine shown in figure 4.4.5 (see p. 102). The equipment for axial tensioning of the nozzle is shown in figure 4.4.6 (see p. 102), where the diameter of the cylinder transferring the tensile load to the plate equals 90 cm.

A detailed description of the above experiments can be found in [4.21] for the three flat plate nozzles and in [4.22] for the corresponding three model vessel nozzles. At each test a positive load (internal pressure or tension) was applied and increased stepwise after measuring the strains. After reaching the maximum the load was again reduced stepwise. At each step the strains were measured and from these data the representative elastic strains and stresses at a pressure of 90 kgf/cm^2 (about the design pressure) were computed by applying a least squares technique. Thereby possible deviations from the desired proportionality between the applied load and the corresponding strains have been eliminated. Such (small) deviations occurred e.g. during the uniaxial plate tensioning at small tension loads. The results of the experiments will be discussed in the next two sub-sections in conjunction with the results of the numerical predictions.

---

*) *Of course only the longitudinal cross sections of the model vessel nozzles are identical to those of the flat plate nozzles.*

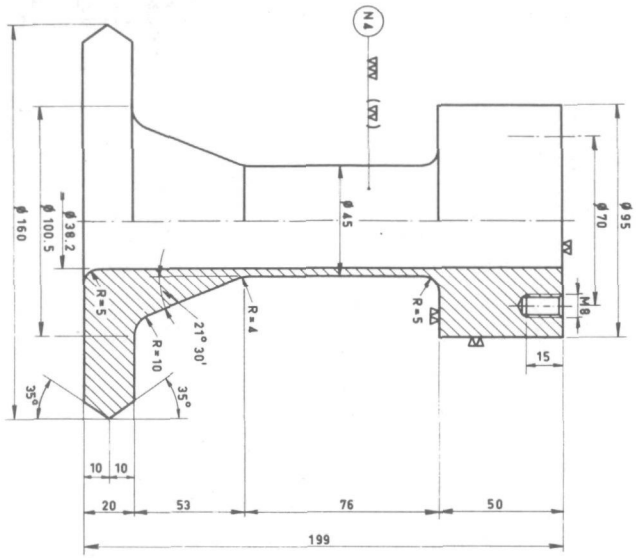

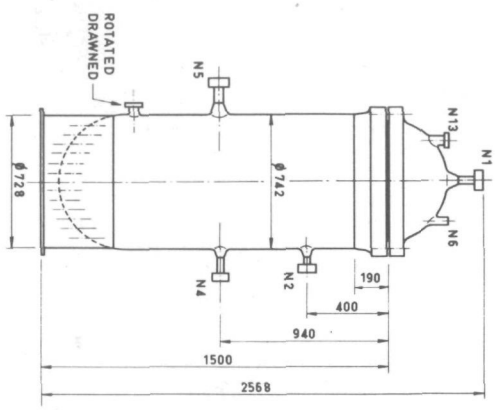

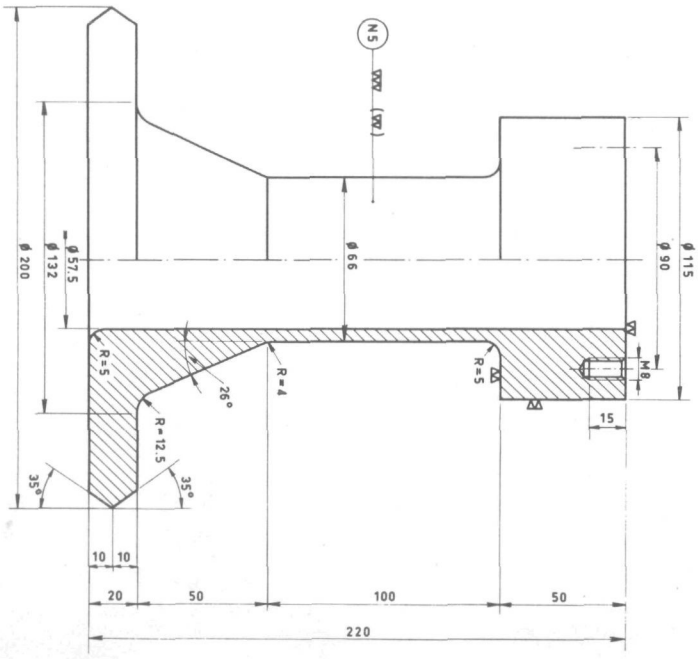

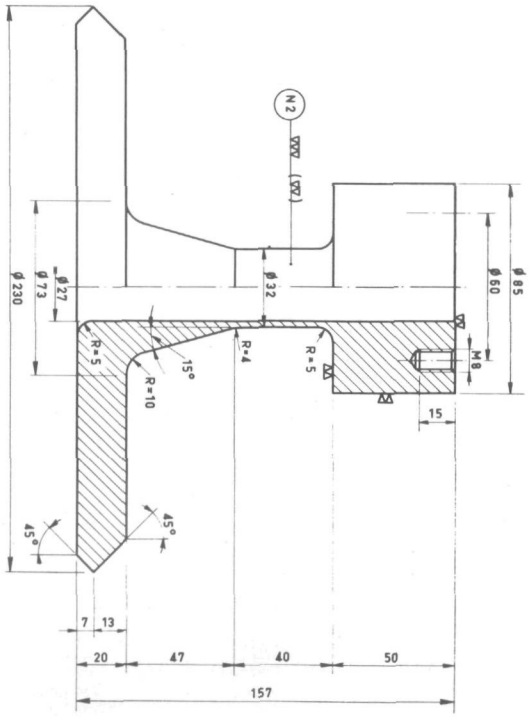

FIGURE 4.4.1.

Dimensions of model vessel nozzles N2, N4 and N5.

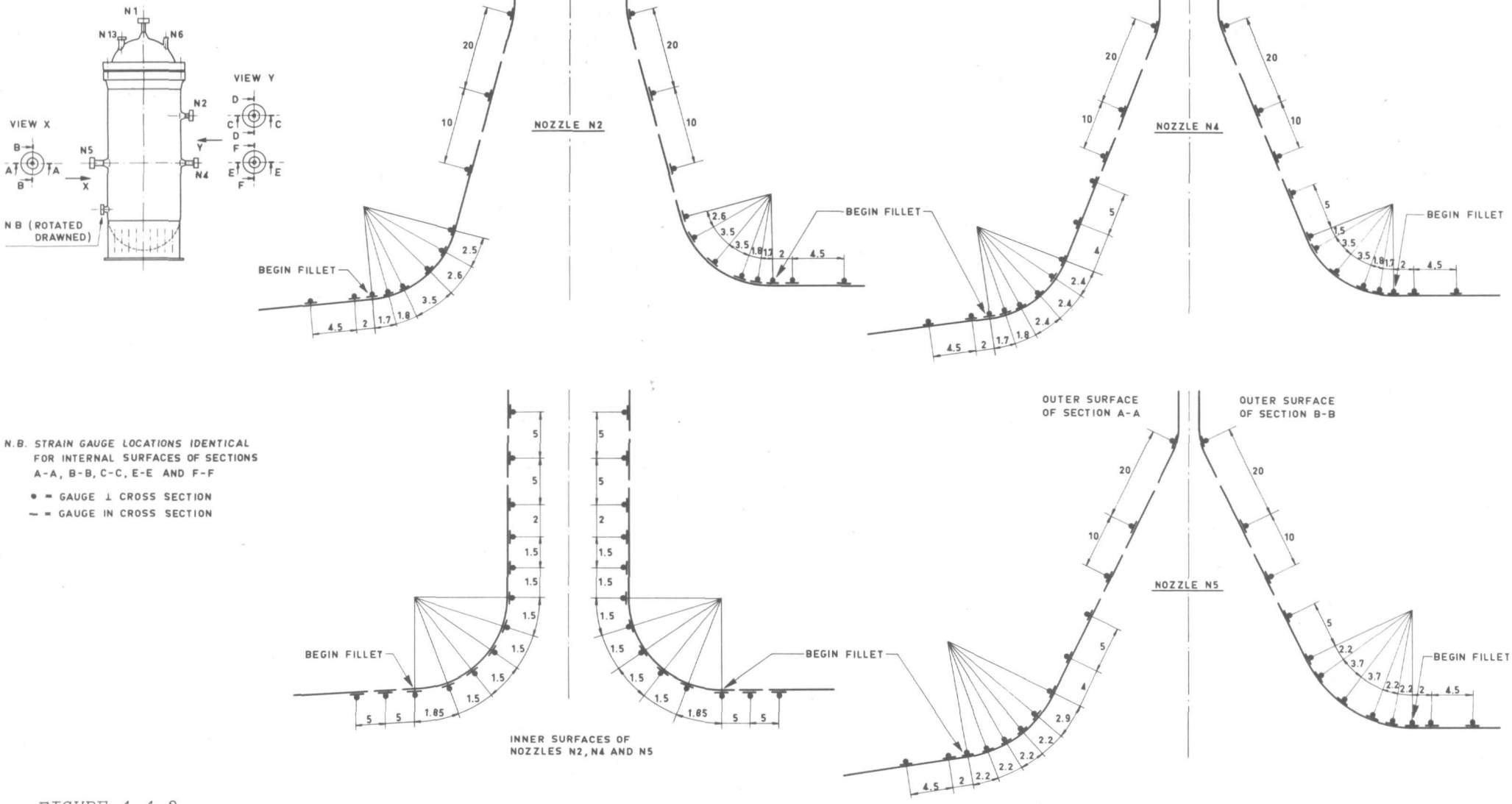

FIGURE 4.4.2.

Strain gauge locations for model vessel nozzles.

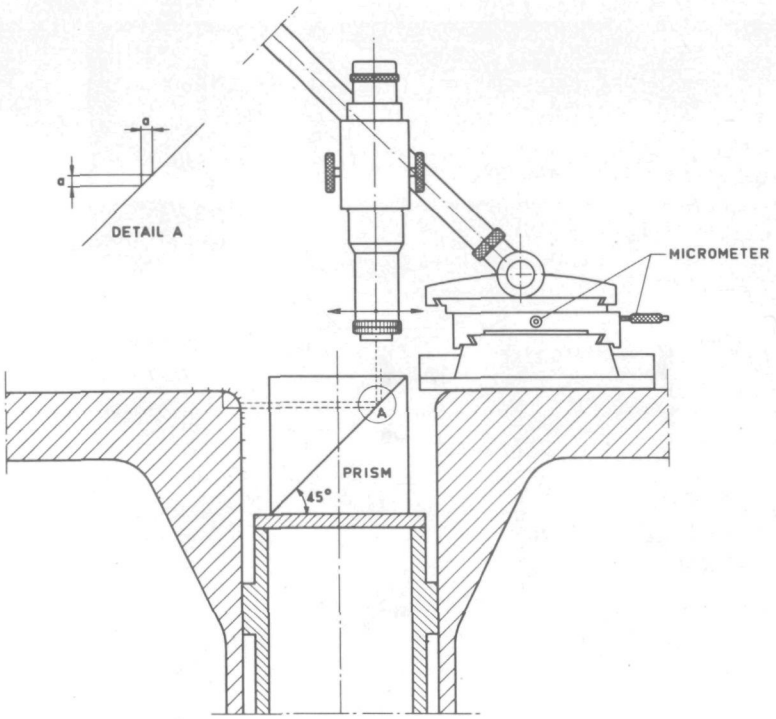

FIGURE 4.4.3.

Determination of exact location of strain gauges.

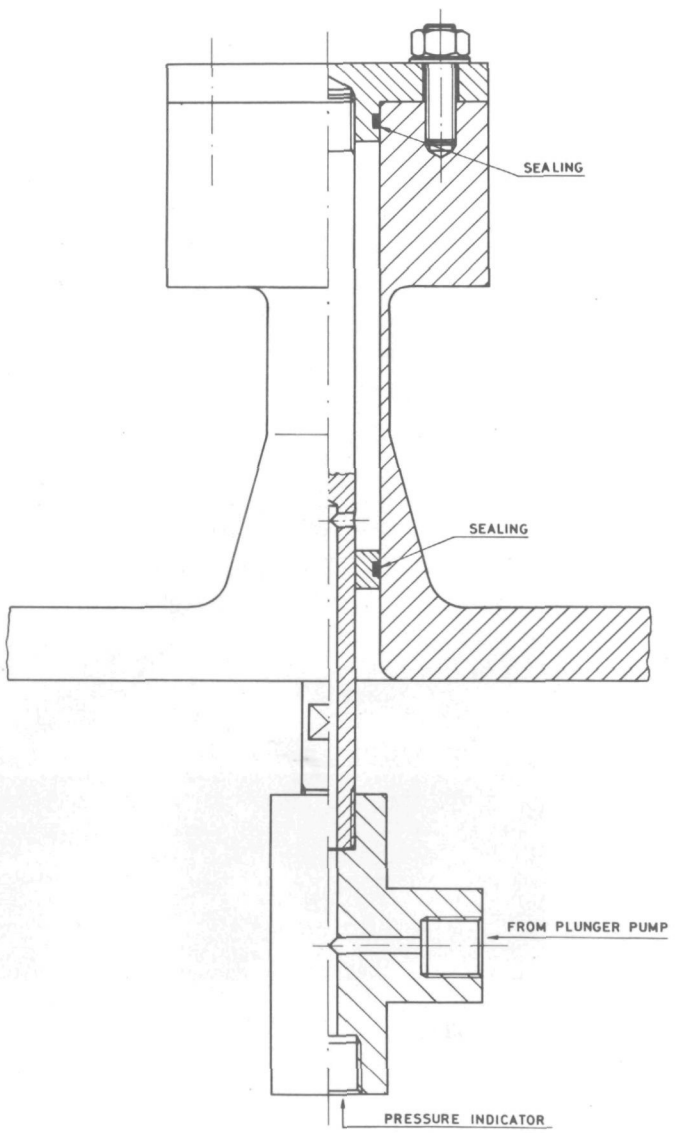

FIGURE 4.4.4.

Internal hydraulic pressurization of nozzle.

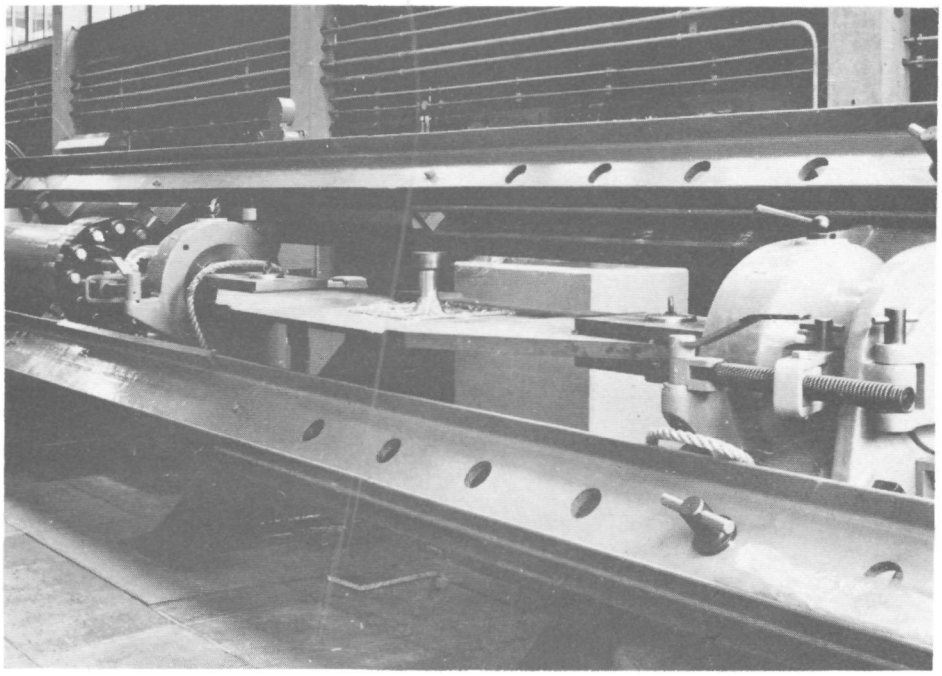

FIGURE 4.4.5.

Plate with nozzle in 200 tf tensile machine.

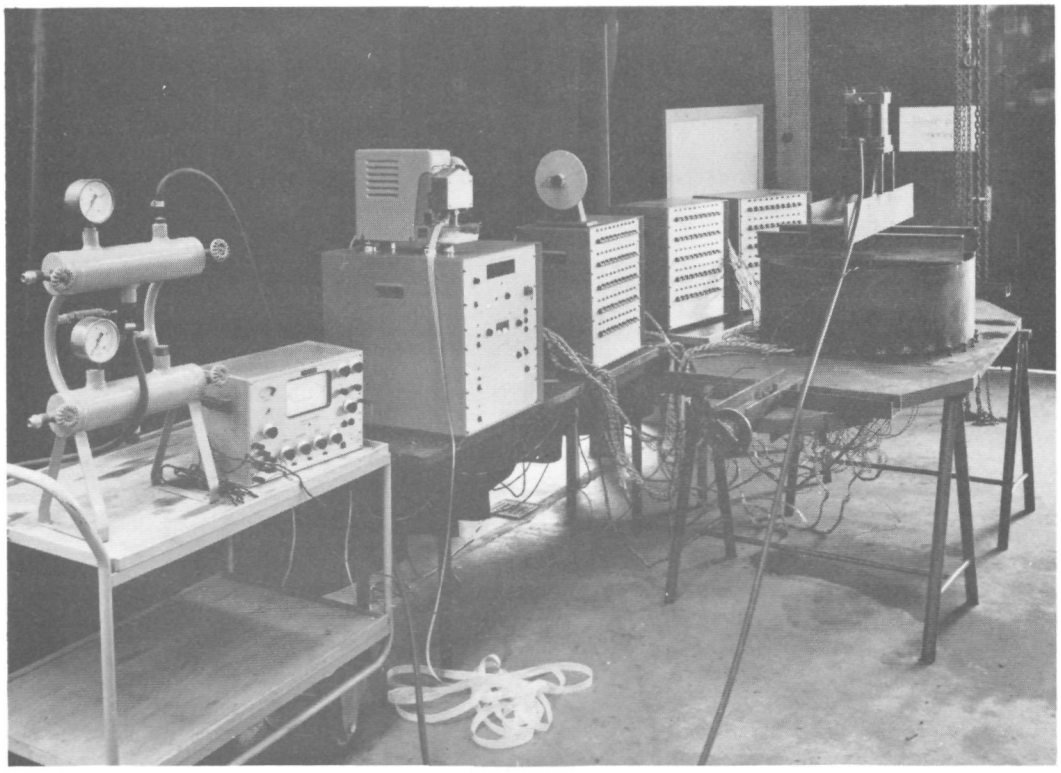

FIGURE 4.4.6.

Test-arrangement for axial nozzle tensioning.

As regards the test *accuracy* it can be concluded from a detailed discussion in [4.21] that errors up to 3% of the measured strains must be accounted for because of the accuracy of the gauge factor, the transverse sensitivity of the strain gauges and the accuracy of the test apparatus *). This value may be exceeded for the strain gauges attached to the inner and outer nozzle fillets due to the fact that these gauges are attached to strongly curved surfaces.

4.4.2. Comparison of experimental and numerical model vessel and flat plate results.

4.4.2.1. Introductory remarks.

A detailed comparison of the calculated and measured strain distributions for both the model vessel and the flat plate nozzles N2, N4 and N5 at a pressure of 90 kgf/cm^2 is shown in the figures 4.4.7, 4.4.8 and 4.4.9 respectively. The right-hand side of each of these figures gives the strain distributions for the longitudinal section (γ = 0 rad), while the left-hand side shows the distributions for the transversal section ($\gamma = \pi/2$ rad). The finite element mesh underlying the computations is indicated for each of the nozzles in the right-hand side of the corresponding figure.

The calculations for the three model vessel nozzles have been carried out utilizing the influence coefficients for the cylindrical vessel derived in Section 4.3.3 and the corresponding consistent membrane solution for the unweakened shell given in the first part of Section 4.3.4. The series solutions (4.3.13) and (4.3.20) for the boundary loadings and the edge deformations at the cylindrical vessel juncture have been truncated at a value $n_1 = 1$. It was found during the numerical investigations that truncating at a higher value of n_1 does not affect the relevant strains in the reinforced nozzle part within 0.03% for nozzle N2, within 0.07% for nozzle N4 and within 1% for nozzle N5. Thus truncating at $n_1 = 1$ is admissible from a practical point of view and consequently mainly terms for $\ell = 0$ and $\ell = 1$ play a role in the solution.
In addition it could be concluded from the computations that truncating at a value of n_1 exceeding 2 does not affect the results within 0.05% as compared with truncating at $n_1 = 2$. This conclusion is completely in accordance with the numerical results given in Chapter 5.4 of [4.11] for the analysis of a thin-walled circular cylindrical branch pipe attached to the main shell.

---

*) *The effect of hydrostatic pressure on the electric strain gauge resistance has been tested for gauges attached to a flat surface and appeared to be negligibly small in that case.*

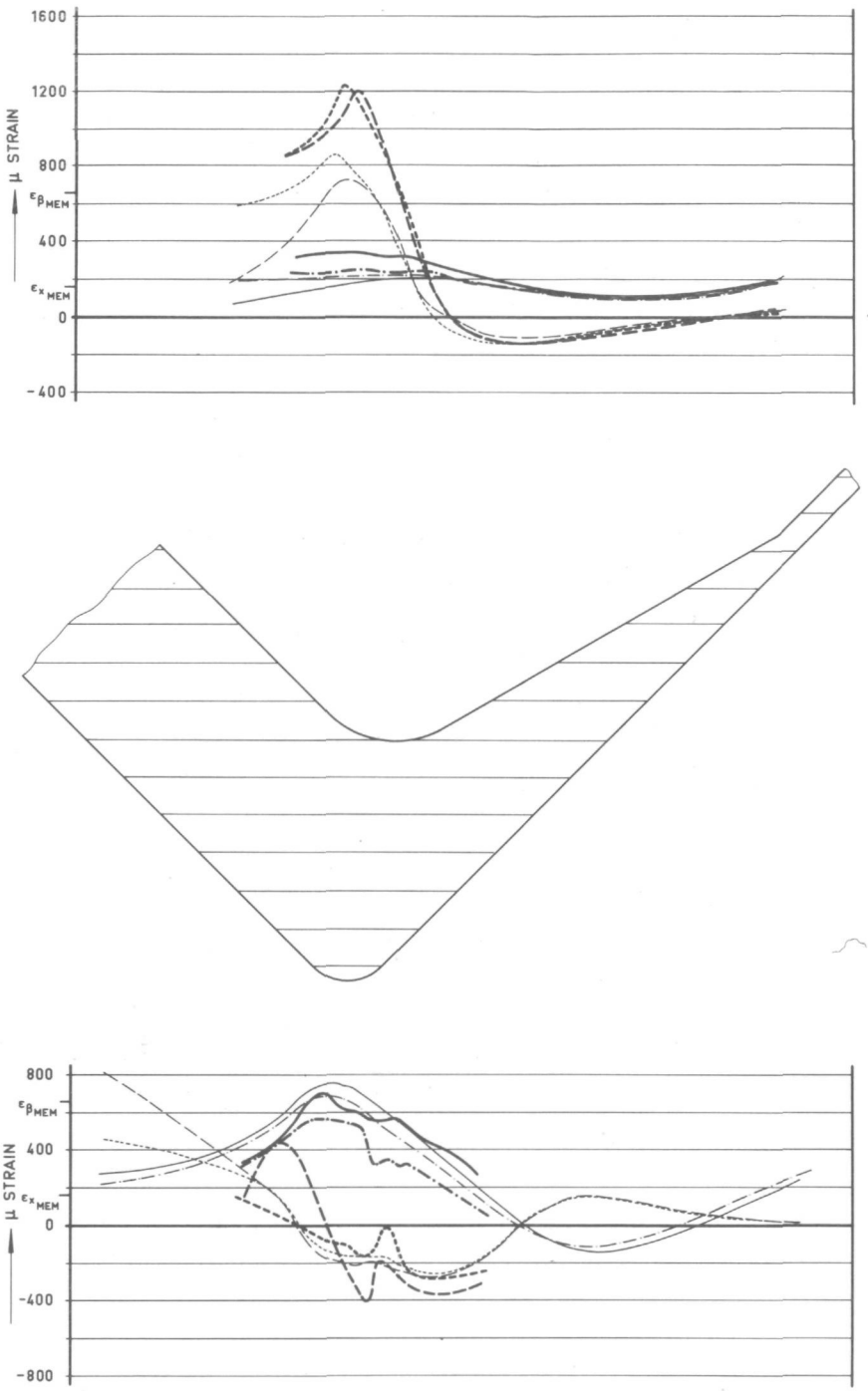

TRANSVERSAL SECTION C-C (cf. FIG. 4.4.2)

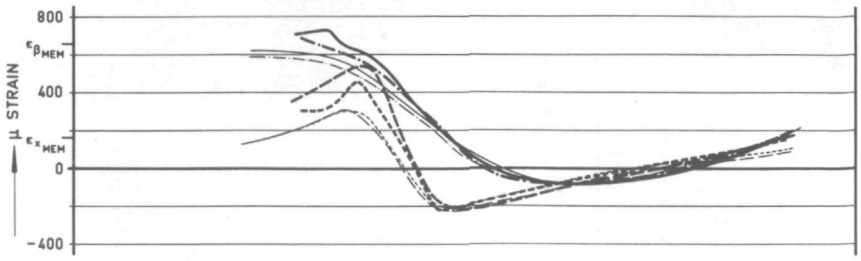

STRAIN ⊥ CROSS SECTION
STRAIN IN CROSS SECTION
} EXPERIMENTAL

STRAIN ⊥ CROSS SECTION
STRAIN IN CROSS SECTION
} NUMERICAL

} MODEL VESSEL

Influence coefficients : Section 4.3.3
Membrane solution for unweakened shell :
first part of Section 4.3.4

STRAIN ⊥ CROSS SECTION
STRAIN IN CROSS SECTION
} EXPERIMENTAL

STRAIN ⊥ CROSS SECTION
STRAIN IN CROSS SECTION
} NUMERICAL

} FLAT PLATE

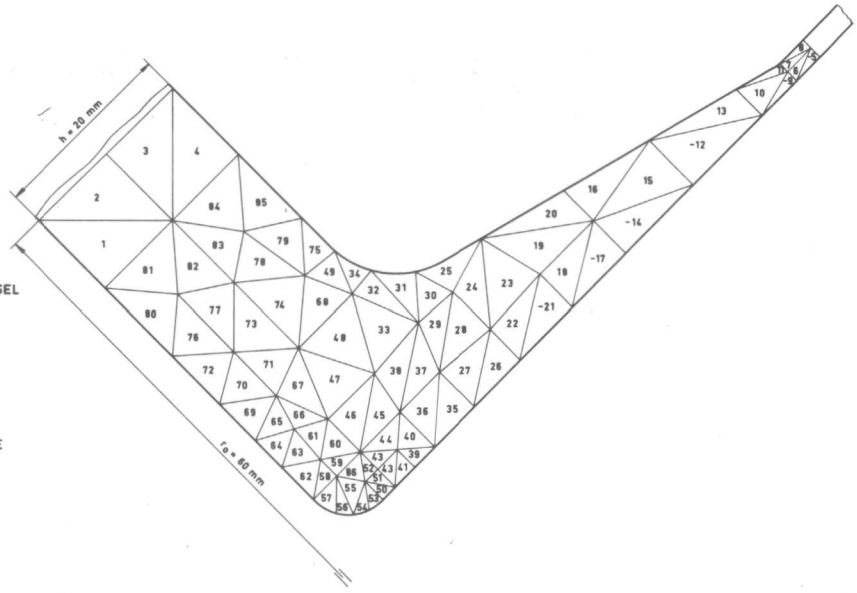

$E = 2{,}100{,}000\ kgf/cm^2$

$\nu = 0.29$

$\mu = \frac{\sqrt[4]{12(1-\nu^2)}}{2} \frac{r_o}{\sqrt{Rh}} = 0.64$

$\frac{R}{r_o} = 6.01$

INTERNAL PRESSURE : $90\ kgf/cm^2$

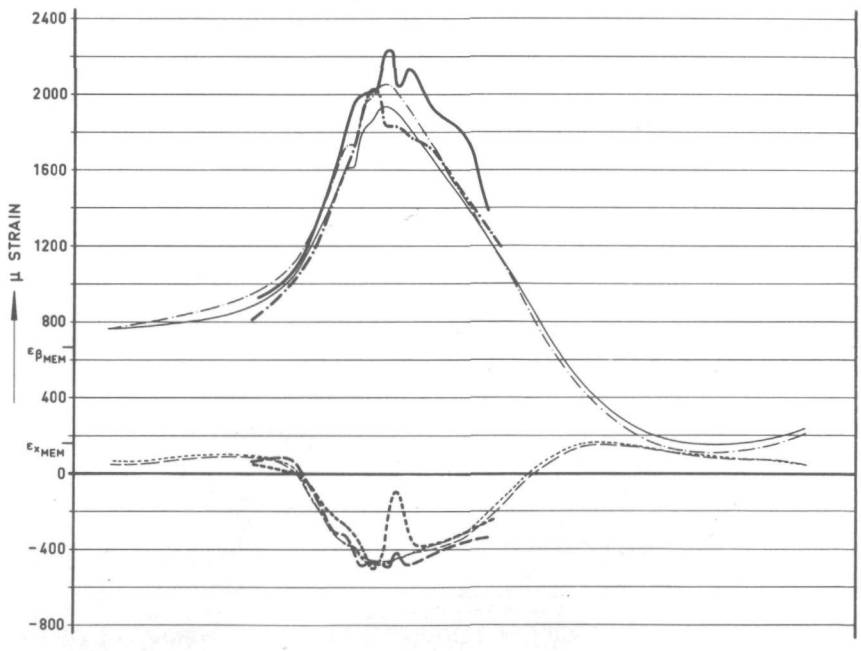

LONGITUDINAL SECTION D - D (cf. FIG. 4.4.2)

FIGURE 4.4.7.

Comparison of experimental and numerical results of nozzle N2.

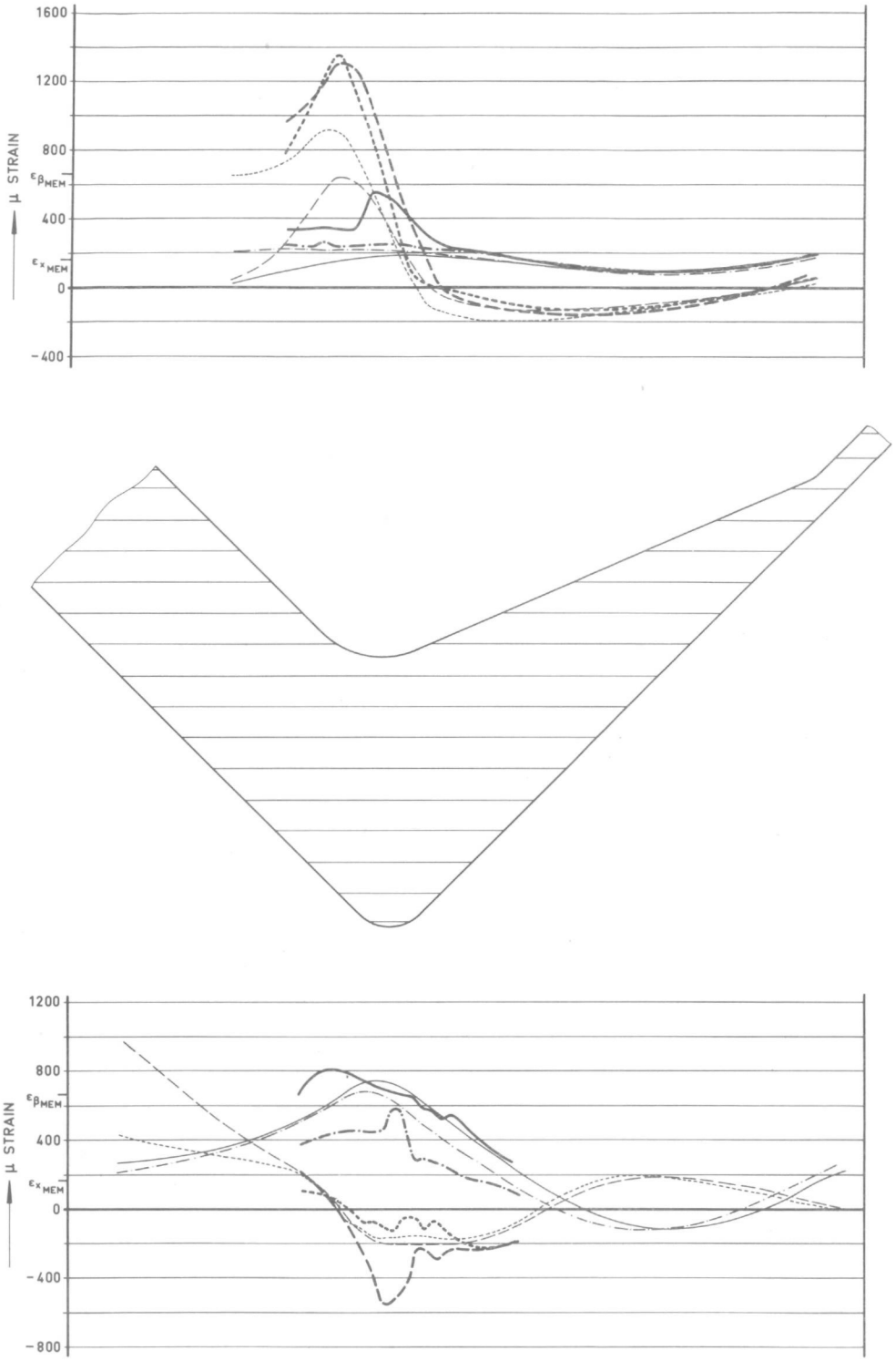

TRANSVERSAL SECTION E - E (cf. FIG. 4.4.2)

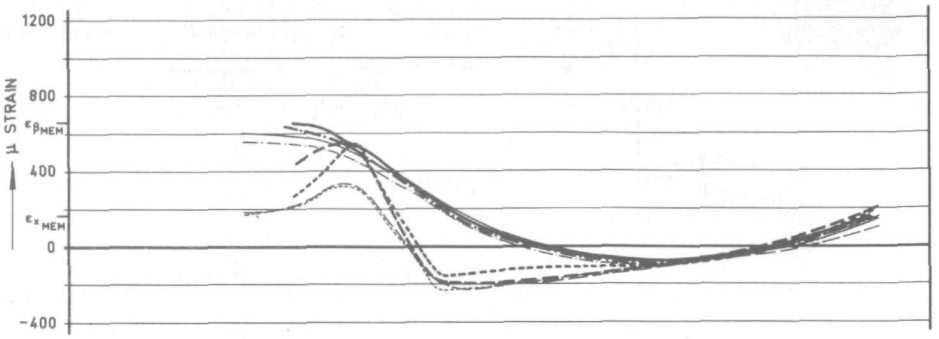

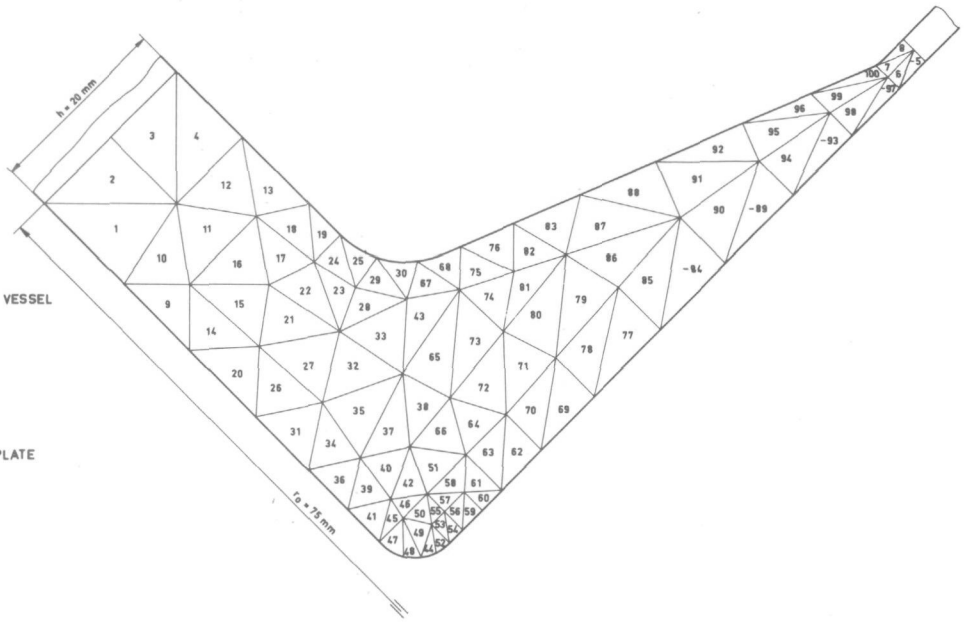

STRAIN ⊥ CROSS SECTION
STRAIN IN CROSS SECTION
} EXPERIMENTAL

STRAIN ⊥ CROSS SECTION
STRAIN IN CROSS SECTION
} NUMERICAL

} MODEL VESSEL

Influence coefficients: Section 4.3.3
Membrane solution for unweakened shell:
first part of Section 4.3.4

STRAIN ⊥ CROSS SECTION
STRAIN IN CROSS SECTION
} EXPERIMENTAL

STRAIN ⊥ CROSS SECTION
STRAIN IN CROSS SECTION
} NUMERICAL

} FLAT PLATE

$E = 2{,}100{,}000\ kgf/cm^2$

$\nu = 0.29$

$\mu = \frac{\sqrt[4]{12(1-\nu^2)}}{2} \frac{r_o}{\sqrt{Rh}} = 0.80$

$\frac{R}{r_o} = 4.81$

INTERNAL PRESSURE : $90\ kgf/cm^2$

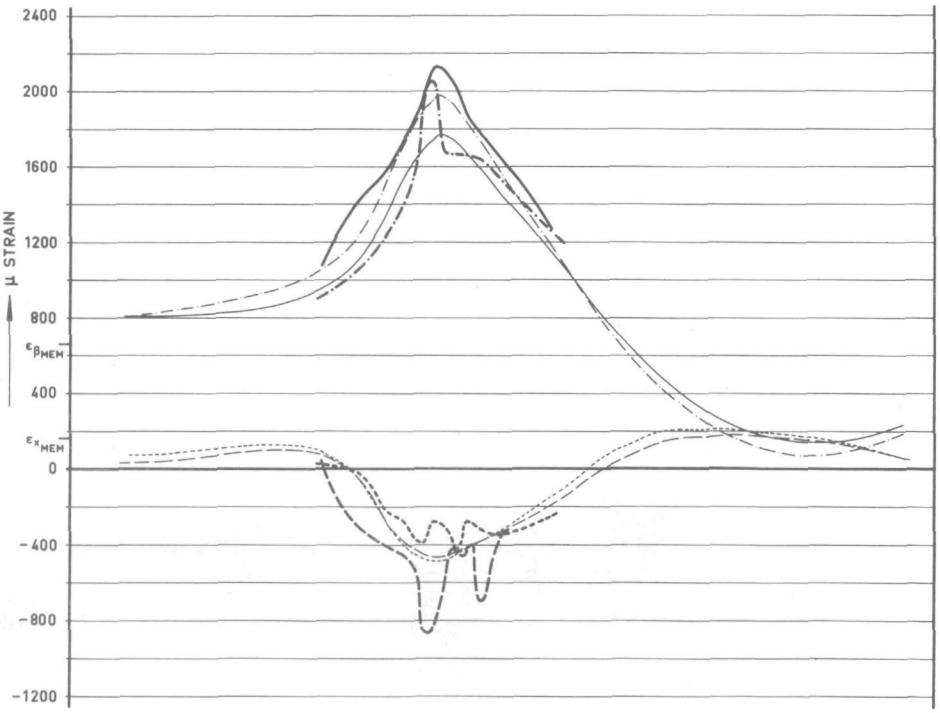

LONGITUDINAL SECTION F-F (cf. FIG. 4.4.2)

FIGURE 4.4.8.

Comparison of experimental and numerical results of nozzle N4.

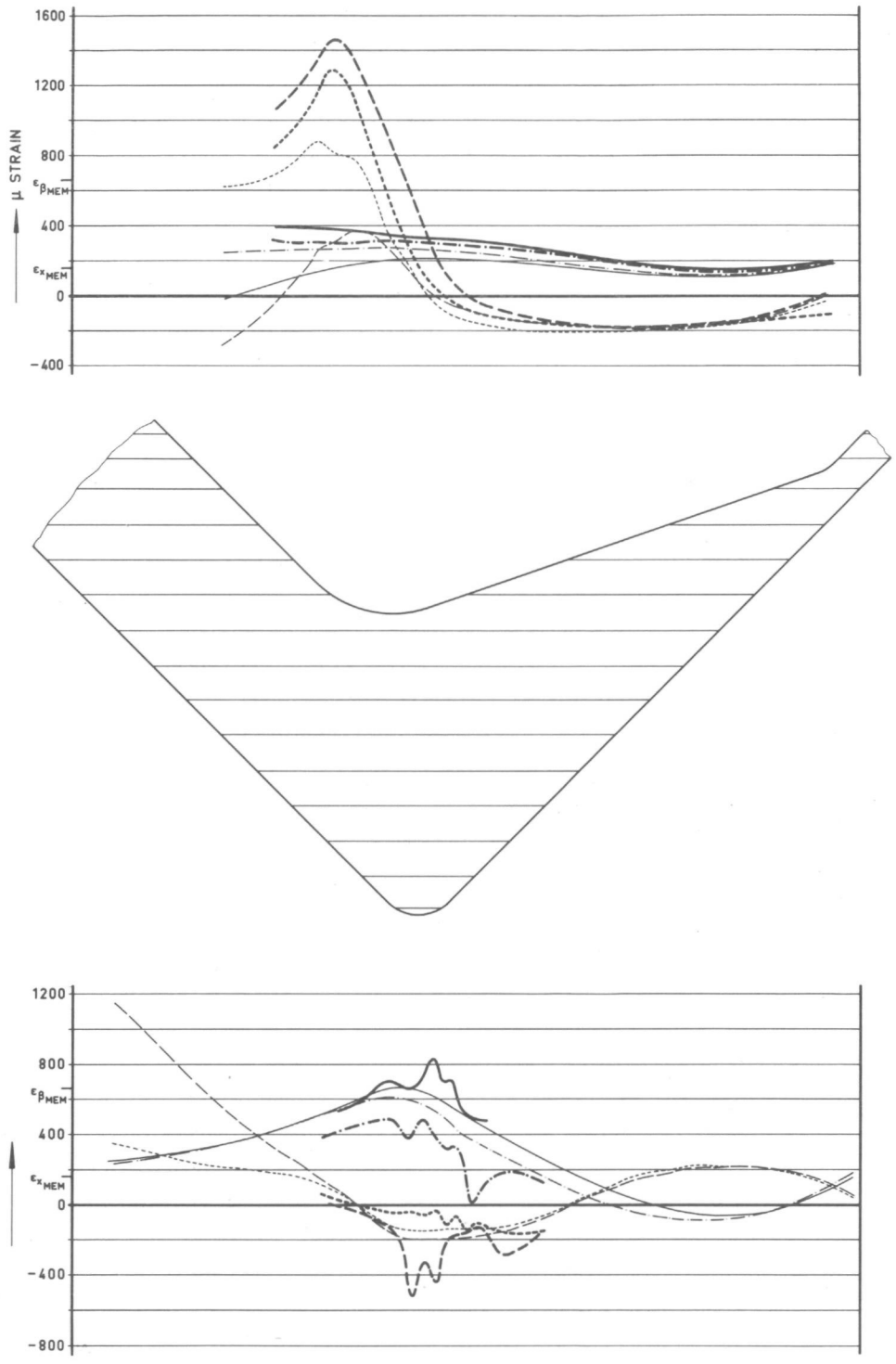

TRANSVERSAL SECTION A-A (cf. FIG. 4.4.2)

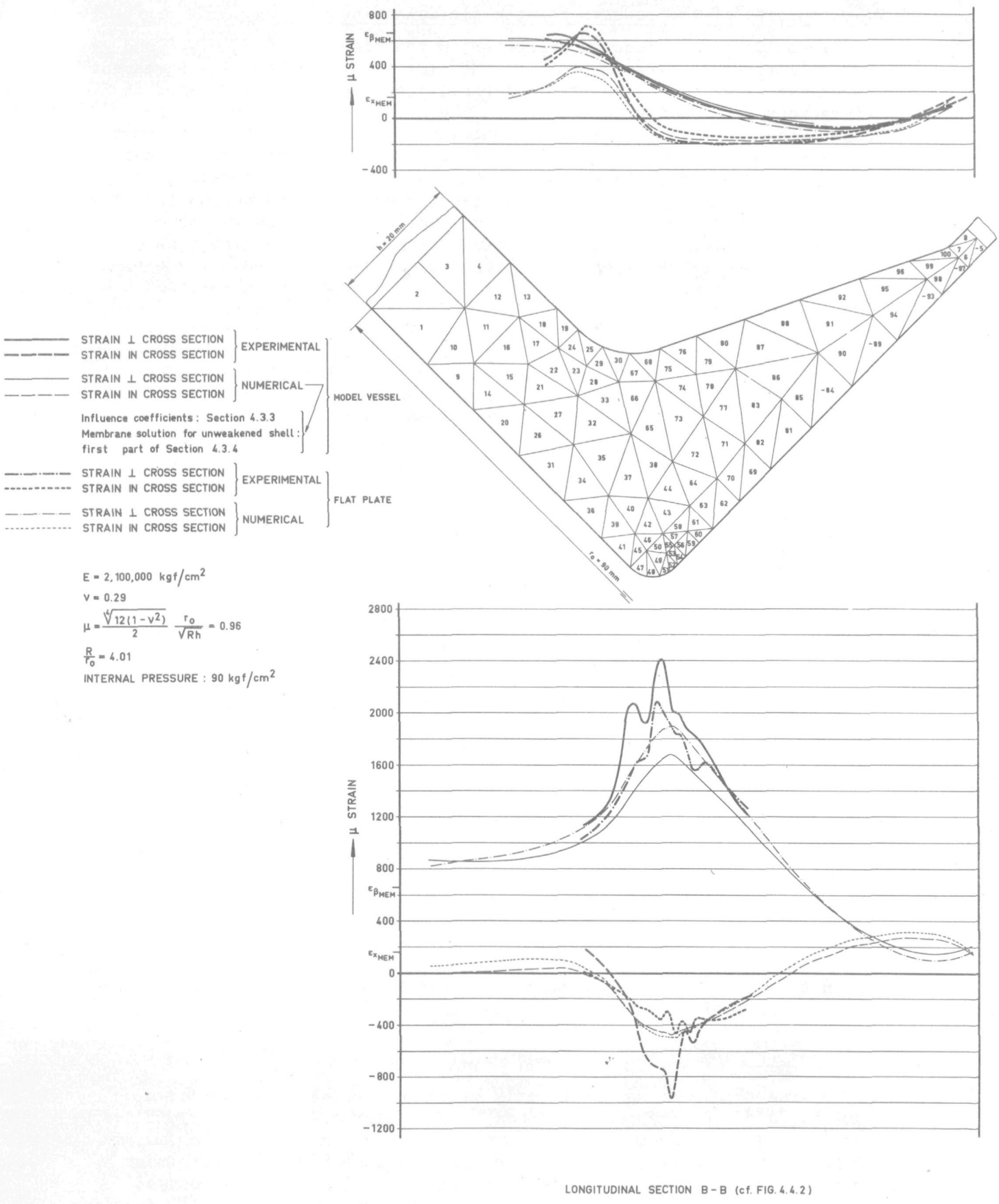

FIGURE 4.4.9.

Comparison of experimental and numerical results of nozzle N5.

4.4.2.2. Discussion of the results for the flat plate nozzles.

The discussion of the results presented in the figures 4.4.7, 4.4.8 and 4.4.9 will first be directed towards the flat plate nozzles. The agreement between the experimental and the numerical results for these nozzles is satisfactory outside the regions where the strain peaks occur *). The highest strain peak at the longitudinal inner surface, which is the most important one in nozzle design, is predicted by the computations with a very high accuracy for the smallest nozzle N2 and with a decreasing accuracy for the larger nozzles N4 (relative discrepancy 3.8%) and N5 (relative discrepancy 8.8%). Whereas the measured values show a trend to increase slightly, the calculated maximum strain decreases at increasing nozzle dimensions. Although the experimental results may represent relative errors up to 3% of the measured strains for reasons mentioned in Sub-section 4.4.1, the main reason for the increasing discrepancies is thought to be of numerical nature. Comparing the element networks for the three flat plate nozzles, the element dimensions are seen to be identical for the elements at the inner fillet (radius 5 mm for all nozzles), whereas the element dimensions increase with increasing nozzle dimensions for elements adjacent to the former ones in the plate direction. Apparently this results in a decrease of the maximum strain and the element grids for the nozzles N4 and N5 in the neighbourhood of the inner fillet have to be refined to obtain better results. In addition to the above it can be remarked that the relatively small differences between the measured and calculated location of the highest strain peak never exceed the mutual strain gauge distance of 1.5 mm (cf. figure 4.4.2) at this location.
As regards the strain peaks at the longitudinal and transversal outer fillets of the three flat plate nozzles, which are of lesser importance in nozzle design, the considerable differences between the experimental and numerical results are mainly caused by the fact that the element networks in the neighbourhood of these regions are too rough. This conclusion is corroborated by the deviations between the in-plane strains at identical (nodal) triangular corner points of different elements near the outer fillets, mounting up to 200 μ strain **).
A final point worth noticing in the discussion of the results for the flat plate nozzles is formed by the irregularities in the distributions of the experimental in-plane strains at the inner fillets, which are not predicted by the computations. Although these (relatively small) strain peaks may probably be predicted numerically by refining the element mesh, their influence in the context of the present thesis is minor.

4.4.2.3. Discussion of the results for the model vessel nozzles.

The discussion of the results presented in the figures 4.4.7, 4.4.8 and 4.4.9 will next be directed towards the model vessel nozzles. *The agreement between the predicted and the measured strains does not appear very satisfactory*. Considering in particular the maximum strains at the longitudinal

---

*) *Of course this conclusion can only be drawn for the outer surfaces on the basis of the information given in the figures 4.4.7, 4.4.8 and 4.4.9, as the inner surfaces were not completely provided with strain gauges (cf. figure 4.4.2). However, the results of a preliminary experiment carried out on a less accurately fabricated replica of model vessel nozzle N5, completely provided with 1.5 mm strain gauges [4.23], justify the same conclusion for the inner surfaces.*

**) *The values for the in-plane strains at the element corner points indicated in the figures are mean values.*

inner surfaces, which have been indicated already as the most important in nozzle design, the deviation between the numerical and the experimental values is seen to increase rapidly at increasing r_0/R ratios. Although the inaccuracy of the shallow thin shell theory underlying the cylindrical vessel analysis increases at increasing r_0/R ratios while the hole is no longer a circle in the developed middle surface of the cylindrical shell in that case (cf. Appendix 6), it is thought that the deviation between the numerical and the experimental maximum strain for nozzle N5 ($r_0/R = 0.25$) is too large to be caused by these effects only. Apparently the deviation of the reinforced nozzle geometry from the assumed axisymmetric one constitutes the main reason for the above discrepancies. As a consequence of this deviation the boundary loadings and the edge deformations of the cylindrical vessel at the reinforced nozzle juncture have been adapted following the processes described in the Sections 4.3.3.2 and 4.3.3.3 *). Sub-section 4.4.3 therefore offers a comparison of the influence of various boundary conditions at the cylindrical vessel juncture on the numerical strain distribution in the reinforced nozzle.

4.4.2.4. Comparison of experimental model vessel and flat plate results.

The final part of the discussion of the results presented in the figures 4.4.7, 4.4.8 and 4.4.9 consists of a comparison between the measured strain distributions for the model vessel nozzles and those for the flat plate nozzles. Considered as a whole the potential of the flat plate analogy can be concluded to yield a convenient first approximation for the strain distribution in reinforced nozzle-to-cylinder attachments, where the ratio between the outer diameter of the nozzle and the diameter of the cylinder does not exceed a value of e.g. $\frac{1}{4}$. This conclusion may be of particular use for experimental investigations on the fatigue behaviour of these nozzles, where the flat plate approach leads to a (relatively) cheap and simple experimental arrangement [4.8].
The magnitude of the highest strain peak in the above nozzle-to-cylinder intersections is predicted by the flat plate approach with an accuracy which is thought to be an increasing function of the reinforcement volume and a decreasing function of the ratio between the outer diameter of the nozzle and the diameter of the cylinder. The measured relative discrepancy rises from 9.4% for the smallest nozzle N2 via 3.1% for the larger nozzle N4 to 13.5% for the largest nozzle N5. It will be pointed out in the next sub-section how the flat plate approach for the nozzle-to-cylindrical vessel problem can be slightly improved.

A final point worth noticing in the experimental results concerns the maximum stress concentration factor for model vessel nozzle N5 (i.e. referred to the tangential membrane stress in the undisturbed vessel), which can be concluded to amount to 3.10 at the longitudinal inner fillet and thus exceeds the experimental values commonly reported in literature.

---

*) *As a matter of fact it can already be expected that the experimental and the numerical strain distributions in the transversal cross section near the cylindrical vessel juncture will not coincide for the larger nozzles, because of the geometrical discontinuity in the middle surface of the computational model at this location. This expectation is completely confirmed by the results given in the figures.*

4.4.3. Comparison of various boundary conditions in the computational method for the nozzle-to-cylinder connection.

In order to check whether or not the transformation of the boundary loadings and the edge deformations of the cylindrical vessel at the reinforced nozzle juncture, described in Section 4.3.3 and in the first part of Section 4.3.4, is the most reliable one of all possible (consistent *) adaptations of the (homogeneous and particular) cylindrical shell solutions, the following additional modified transformations have been considered subsequently:

first modification.
The adaptation processes for the (self-equilibrating and internal pressure membrane) boundary loadings and edge deformations are identical, in principle, to those described in the Sections 4.3.3.2 and 4.3.3.3, except that the first step in these processes is deleted. Thus only the change in direction of the boundary forces and edge displacements is accounted for.

second modification.
The continuity conditions for the self-equilibrating boundary loadings and the resulting edge deformations are identical to those of the original calculations, while the adaptation of the internal membrane solution is identical to the one used in the first modification mentioned before.

		MAXIMUM STRAIN IN μ strain FOR MODEL VESSEL NOZZLE		
		N2	N4	N5
MEASURED VALUE		2240	2121	2410
CALCULATED VALUE	ORIGINAL CONTINUITY CONDITIONS	1935	1777	1673
	FIRST MODIFICATION	1771	1616	1513
	SECOND MODIFICATION	1804	1671	1602

TABLE 4.4.1.

Influence of continuity conditions at cylindrical vessel juncture on maximum strain.

Table 4.4.1 compares the measured maximum strains for the three model vessel nozzles with those computed on the basis of the different adaptations described above. As could already be expected it can indeed be concluded that the original continuity conditions at the cylindrical vessel juncture yield the best approximation for the maximum strain.
In addition to the above modifications the sensitivity of the solution to different locations of the reinforced nozzle part in the computational model has been assessed by transferring the reinforced nozzle mid-surface at the cylindrical vessel juncture (i.e. the plane z = 0, tangent to the middle surface of the shell) to the plane perpendicular to the nozzle axis through the point $\phi = \pi/2$ rad (cf. figures 4.3.2 and 4.3.3) of the cylindrical shell edge. Thereby in the first step of the original adaptation

*) *A consistent adaptation yields a shear force in the transformed membrane solution for the unweakened cylindrical shell, which is in equilibrium with the resulting pressure force* $\pi\, p\, r_0^2$ *in the axial direction of the reinforced nozzle.*

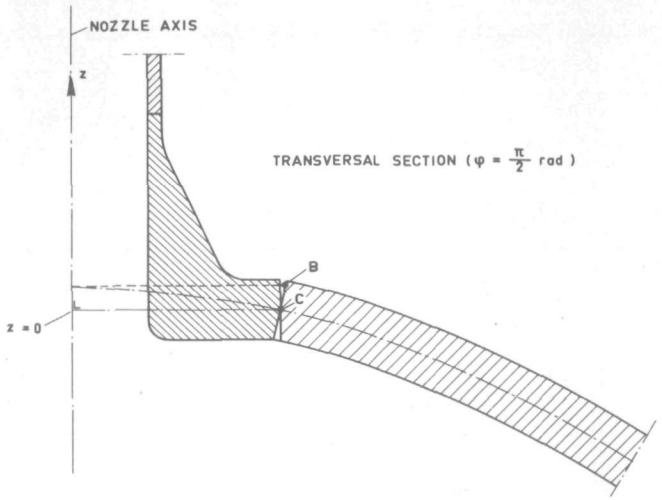

FIGURE 4.4.10

Location of nozzle in additional modified computational model.

processes point B is replaced by point C, as indicated in figure 4.4.10. This resulted in a considerable increase of the maximum strain (by about 50% for nozzle N2), whereas its location shifted from the inner fillet in the longitudinal section to a point of the inner surface of the same section above the plane z = 0 (i.e. the point z = 16 mm for nozzle N2).

As mentioned before the main reason for the unsatisfactory numerical results probably originates from the assumed axisymmetric reinforced nozzle geometry. In particular, the transformation of the *membrane* solution for the unweakened cylindrical shell yields an adapted solution, which includes *bending* as well as *membrane* characteristics with regard to the middle surface of the reinforced nozzle at the cylindrical vessel juncture (i.e. the plane z = 0). Therefore, in a perhaps somewhat unscientific attempt to obtain a better approximation this solution has been replaced by the membrane solution for the infinitely large unweakened flat plate under 1:2 biaxial tension given in the second part of Section 4.3.4. The influence coefficients for the cylindrical shell have been kept identical to those derived in Section 4.3.3. As regards the particular (internal pressure) solution for the reinforced nozzle and cylindrical pipe part the following possibilities have been investigated:

first particular reinforced nozzle solution
The pressure is acting at the complete inner surface of the cylindrical pipe and the reinforced nozzle. Consequently an equilibrium shear force perpendicular to the reinforced nozzle mid-surface is acting along the edge at the cylindrical vessel juncture. The magnitude of this force is $\frac{1}{2}\ p\ r_0$ per unit length along this edge.

second particular reinforced nozzle solution
The pressure is only acting at the complete inner surface of the cylindrical pipe and that part of the reinforced nozzle being parallel to the nozzle axis. The resulting axial pressure force is in equilibrium with a shear force acting along the edge at the cylindrical vessel juncture, whose magnitude per unit arc length along this edge equals

$$\frac{\pi}{4}\ d_i^2\ p\ /\ (2\pi\ r_0),$$

d_i being the internal nozzle diameter.

third particular reinforced nozzle solution
The pressure is acting at the same part of the inner surface as in the preceding approximation. The resulting axial pressure force is in equilibrium with a normal force acting along the cylindrical pipe edge at

the reinforced nozzle juncture, whose magnitude per unit arc length along this edge equals

$$\frac{\pi}{4} d_i^2 p / [\pi (d_i + h_{pipe})],$$

h_{pipe} being the wall thickness of the pipe.

fourth particular reinforced nozzle solution
No pressure is acting at the inner surface of the reinforced nozzle and cylindrical pipe.

		MAXIMUM STRAIN IN μ strain FOR MODEL VESSEL NOZZLE		
		N2	N4	N5
MEASURED VALUE		2240	2121	2410
CALCULATED VALUE FOR ORIGINAL CONTINUITY CONDITIONS		1935	1777	1673
CALCULATED VALUE FOR PARTICULAR SOLUTION ON THE BASIS OF THE UNWEAKENED FLAT PLATE	FIRST APPROXIMATION	2002	1964	1982
	SECOND APPROXIMATION	2121	2069	2075
	THIRD APPROXIMATION	2146	2097	2119
	FOURTH APPROXIMATION	2103	2056	2078

TABLE 4.4.2.

Influence of particular reinforced nozzle solution on maximum strain.

Table 4.4.2 compares the measured maximum strains for the three model vessel nozzles with those computed on the basis of the different approximations described above. It can be concluded from the results given in the table that for all four possibilities given above the particular unweakened shell solution on the basis of the infinitely large flat plate yields an improved approximation for the maximum strain in the three nozzles. The improved results confirm the somewhat surprisingly experimental tendency that the maximum strain for the nozzles N2 and N5 exceeds that for the nozzle N4.
As regards the influence of the different particular reinforced nozzle solutions the best results are believed to be obtained by applying the third approximation described above. In the context of the motivation of the utilization of the *membrane* solution for the unweakened flat plate given before it should be realized here that in this particular reinforced nozzle solution (and also in the one used for the fourth approximation) no shear force (giving rise to *bending* effects) is acting along the edge at the cylindrical vessel juncture.
In addition it can be concluded from the results listed in the table that the flat plate approach for the reinforced nozzle-to-cylindrical vessel configurations of interest for the present thesis can be improved by replacing the particular reinforced nozzle solution resulting from the description given in Sub-section 4.4.1 by the third approximation defined above. Indeed, this adaptation resulted in an increase of the calculated maximum strain by 1.6% for flat plate nozzle N2, by 1.9% for flat plate nozzle N4 and by 3.0% for flat plate nozzle N5. The consequence of this improvement for experimental investigations on the fatigue behaviour of reinforced cylindrical vessel nozzles based on the flat plate approach should be a modification of the axial nozzle tensioning arrangement shown in figure 4.4.6.

The figures 4.4.11, 4.4.12 and 4.4.13 show a comparison between the calculated original strain distributions, the calculated strain distributions on the basis of the above mentioned third approximation, and the measured strain distributions for the three model vessel nozzles N2, N4 and N5, respectively. The relative discrepancies between the measured and the calculated improved maximum strains are seen to amount to 4.2% for the smallest nozzle N2, 1.1% for the larger nozzle N4 and 12.1% for the largest nozzle N5. In view of the discussion of the experimental and the numerical results for the flat plate nozzles given in the preceding sub-section it seems evident that the relatively large discrepancies between the experimental and the improved numerical maximum strains for model nozzle N5 must for the greater part be blamed on the fact that the finite element mesh near the inner fillet of this nozzle is too rough. Summarizing the results it can be concluded that the third approximation defined above predicts, for an appropriate choice of the finite element mesh, the maximum strain in the reinforced nozzle configurations of interest for the present thesis with an inaccuracy not exceeding 5% even if r_0/R gets near $\frac{1}{4}$. The validity of this conclusion for r_0/R ratios of about 1/3, of interest for large PWR vessels is presently under investigation in the author's laboratory by experimental and numerical means.

In spite of the (relatively small) inaccuracies the improved computational method is believed to constitute a powerful tool for design engineers in predicting the peak strains and the strain distributions in reinforced nozzle-to-cylinder attachments. As compared with three-dimensional finite element approaches, the major advantage of the present method is the *reduction of the computing time by a factor of about 10*, whereas the preparation of the input data is considerably simplified.

It can be concluded from the discussion given in Sub-section 4.4.2.1 that truncating of the series solutions (4.3.13) and (4.3.20) for the boundary loadings and the edge deformations at a value $n_1 = 1$ is admissable from a practical point of view and consequently mainly terms for $\ell = 0$ and $\ell = 1$ play a role in the solution. The original three-dimensional finite element problem for the nozzle-to-flat plate structure being split into two *uncoupled* quasi-two-dimensional problems for $\ell = 0$ and $\ell = 1$ (cf. Section 4.2), the computational method for the nozzle-to-cylinder attachment, as compared with the computational method for the former structure, does hardly more than couple the Fourier's coefficients in the series solutions for the displacements of the reinforced nozzle part for $\ell = 0$ and $\ell = 1$. The incorporation of this coupling effect appears to be possible without a relevant increase in computing time, due to the fact that the calculation of the influence coefficients for the cylindrical vessel on the basis of the formulae given in Section 4.3.3 requires only a few seconds computing time on an IBM 360/65 computer, while the calculation of the displacement parameters of the reinforced nozzle part for a number of unit boundary loading systems hardly increases the computing time at all (cf. Section 4.3.2).

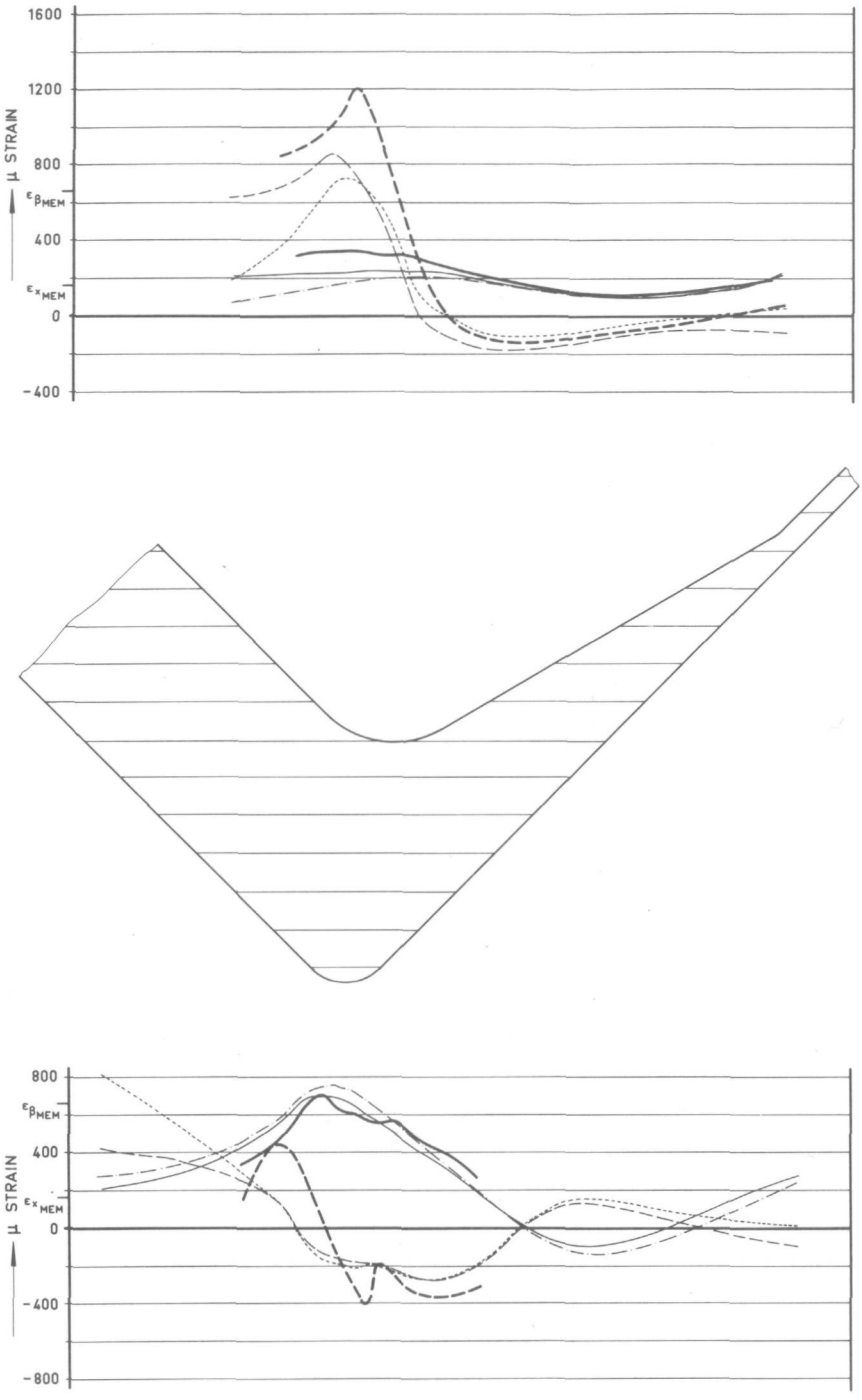

TRANSVERSAL SECTION C-C (cf. FIG. 4.4.2)

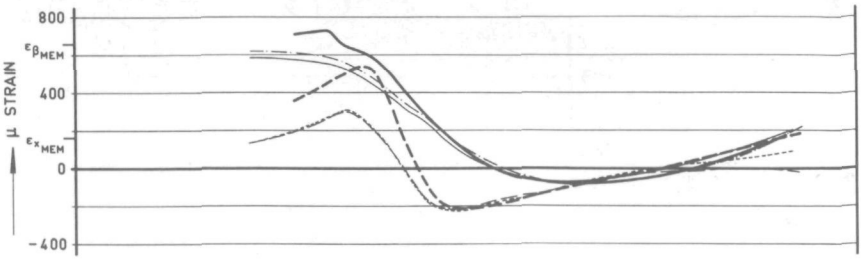

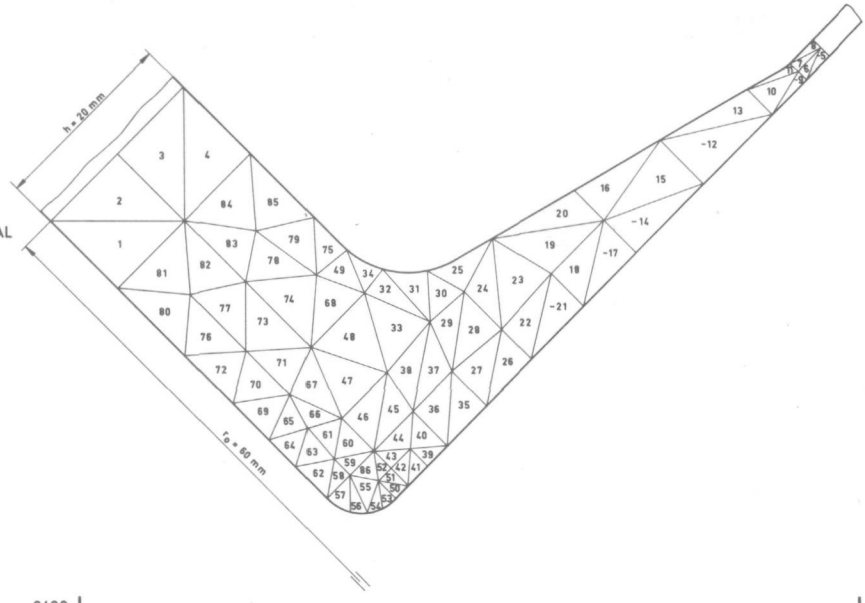

STRAIN ⊥ CROSS SECTION
STRAIN IN CROSS SECTION
} EXPERIMENTAL

STRAIN ⊥ CROSS SECTION
STRAIN IN CROSS SECTION

Influence coefficients: Section 4.3.3
Membrane solution for unweakened shell:
second part of Section 4.3.4
} NUMERICAL

STRAIN ⊥ CROSS SECTION
STRAIN IN CROSS SECTION

Influence coefficients: Section 4.3.3
Membrane solution for unweakened shell:
first part of Section 4.3.4
} NUMERICAL

$E = 2{,}100{,}000\ kgf/cm^2$

$\nu = 0.29$

$\mu = \frac{\sqrt[4]{12(1-\nu^2)}}{2} \frac{r_o}{\sqrt{Rh}} = 0.64$

$\frac{R}{r_o} = 6.01$

INTERNAL PRESSURE : $90\ kgf/cm^2$

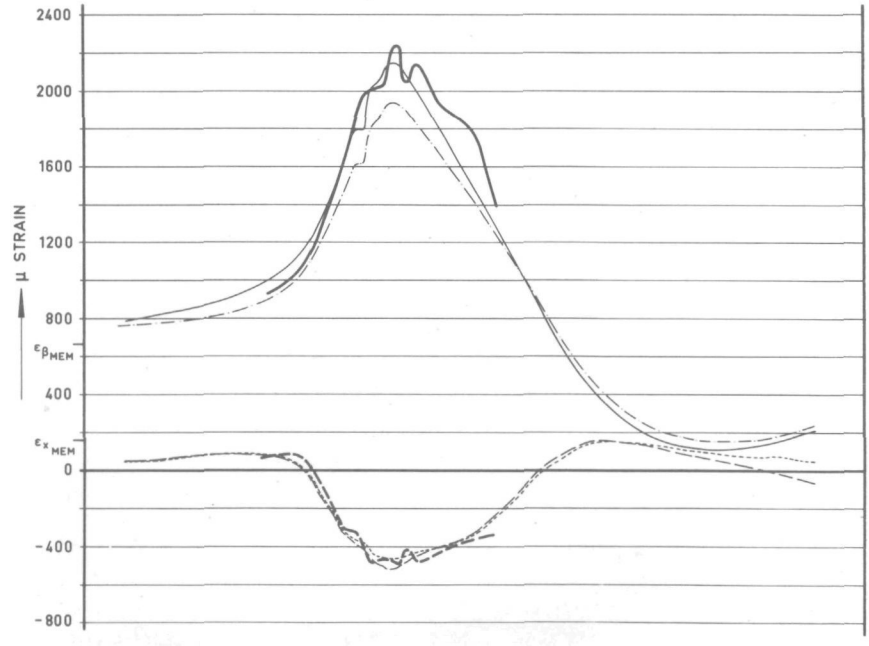

LONGITUDINAL SECTION D-D (cf. FIG. 4.4.2)

FIGURE 4.4.11.

Influence of various boundary conditions on numerical strain distribution for model vessel nozzle N2.

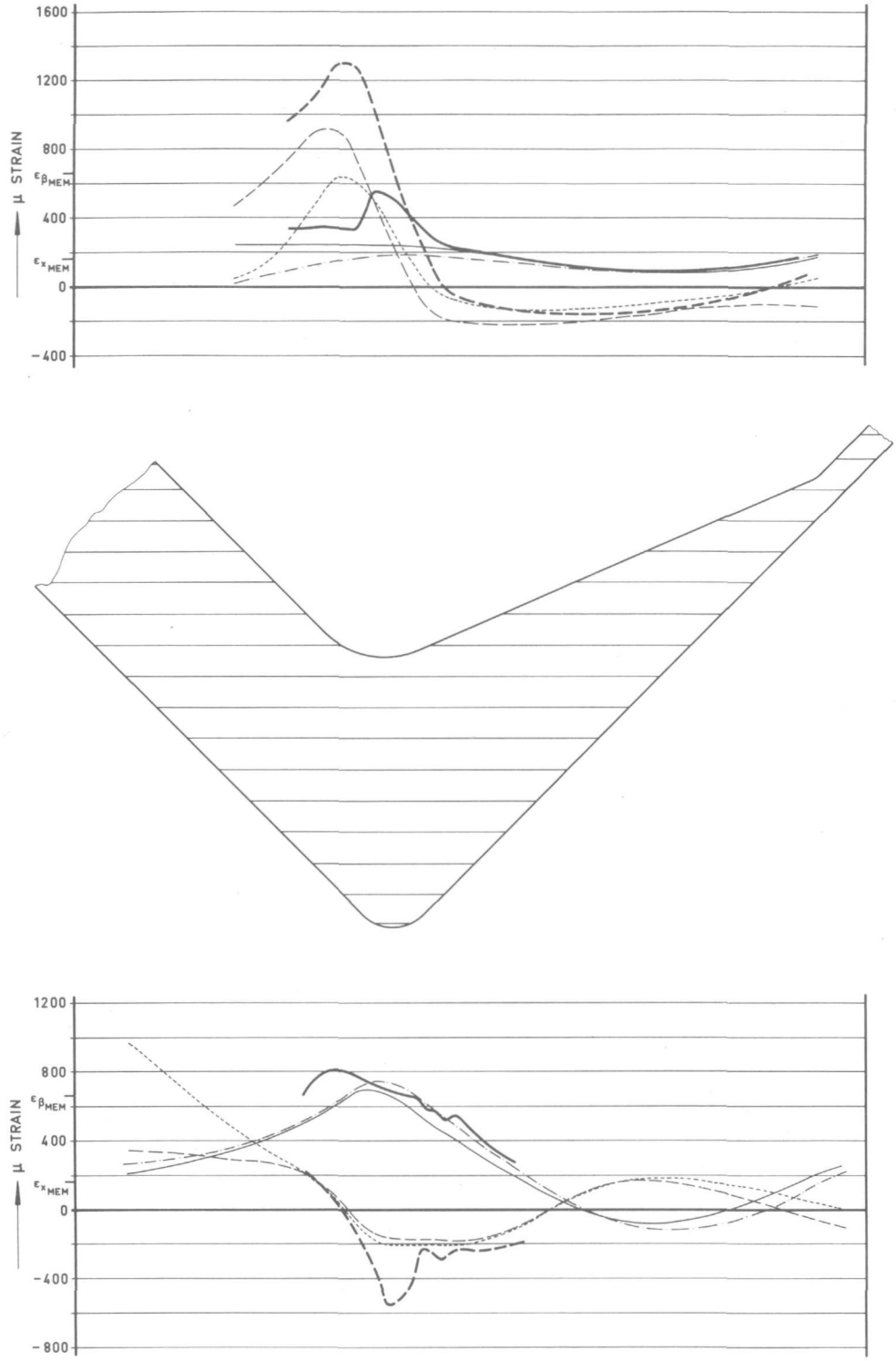

TRANSVERSAL SECTION E - E (cf. FIG. 4.4.2)

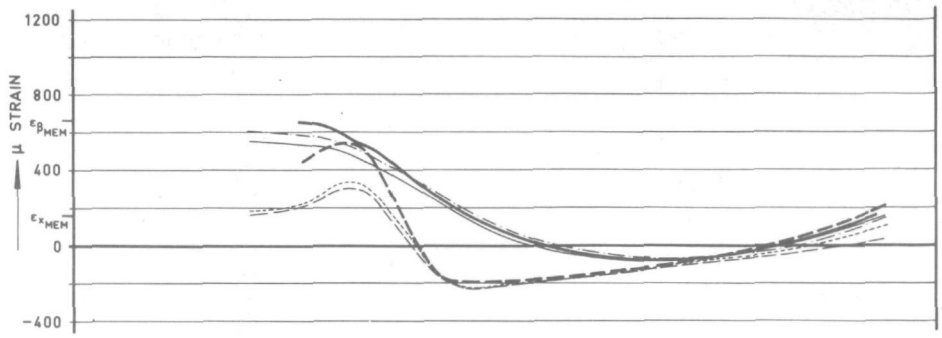

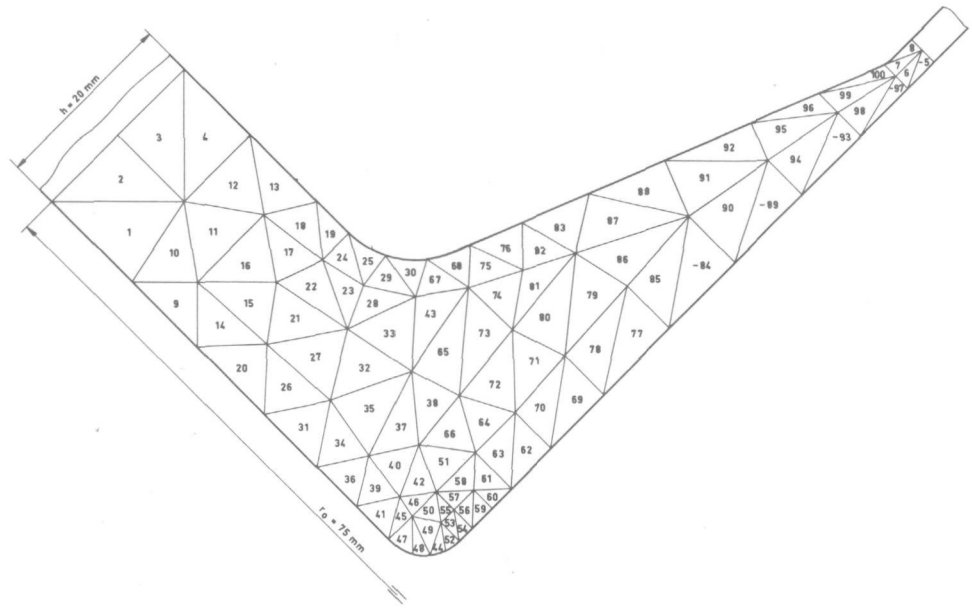

STRAIN ⊥ CROSS SECTION
STRAIN IN CROSS SECTION
} EXPERIMENTAL

STRAIN ⊥ CROSS SECTION
STRAIN IN CROSS SECTION
} NUMERICAL

Influence coefficients : Section 4.3.3
Membrane solution for unweakened shell :
second part of Section 4.3.4

STRAIN ⊥ CROSS SECTION
STRAIN IN CROSS SECTION
} NUMERICAL

Influence coefficients : Section 4.3.3
Membrane solution for unweakened shell :
first part of Section 4.3.4

$E = 2,100,000\ kgf/cm^2$

$\nu = 0.29$

$\mu = \frac{\sqrt[4]{12(1-\nu^2)}}{2} \frac{r_o}{\sqrt{Rh}} = 0.80$

$\frac{R}{r_o} = 4.81$

INTERNAL PRESSURE : $90\ kgf/cm^2$

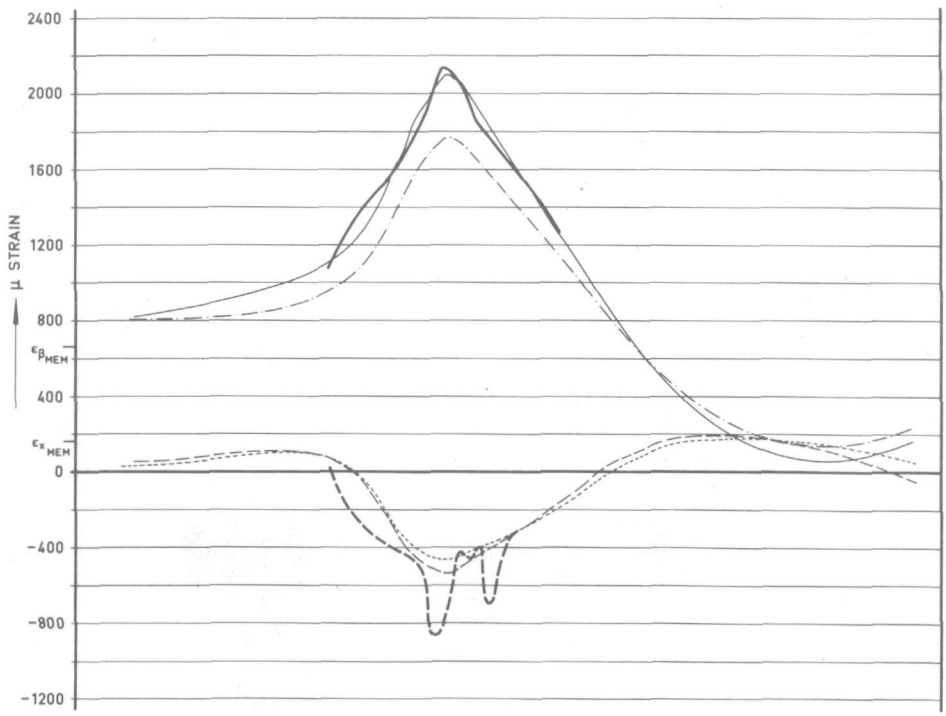

LONGITUDINAL SECTION F-F (cf. FIG. 4.4.2)

FIGURE 4.4.12.

Influence of various boundary conditions on numerical strain distribution for model vessel nozzle N4.

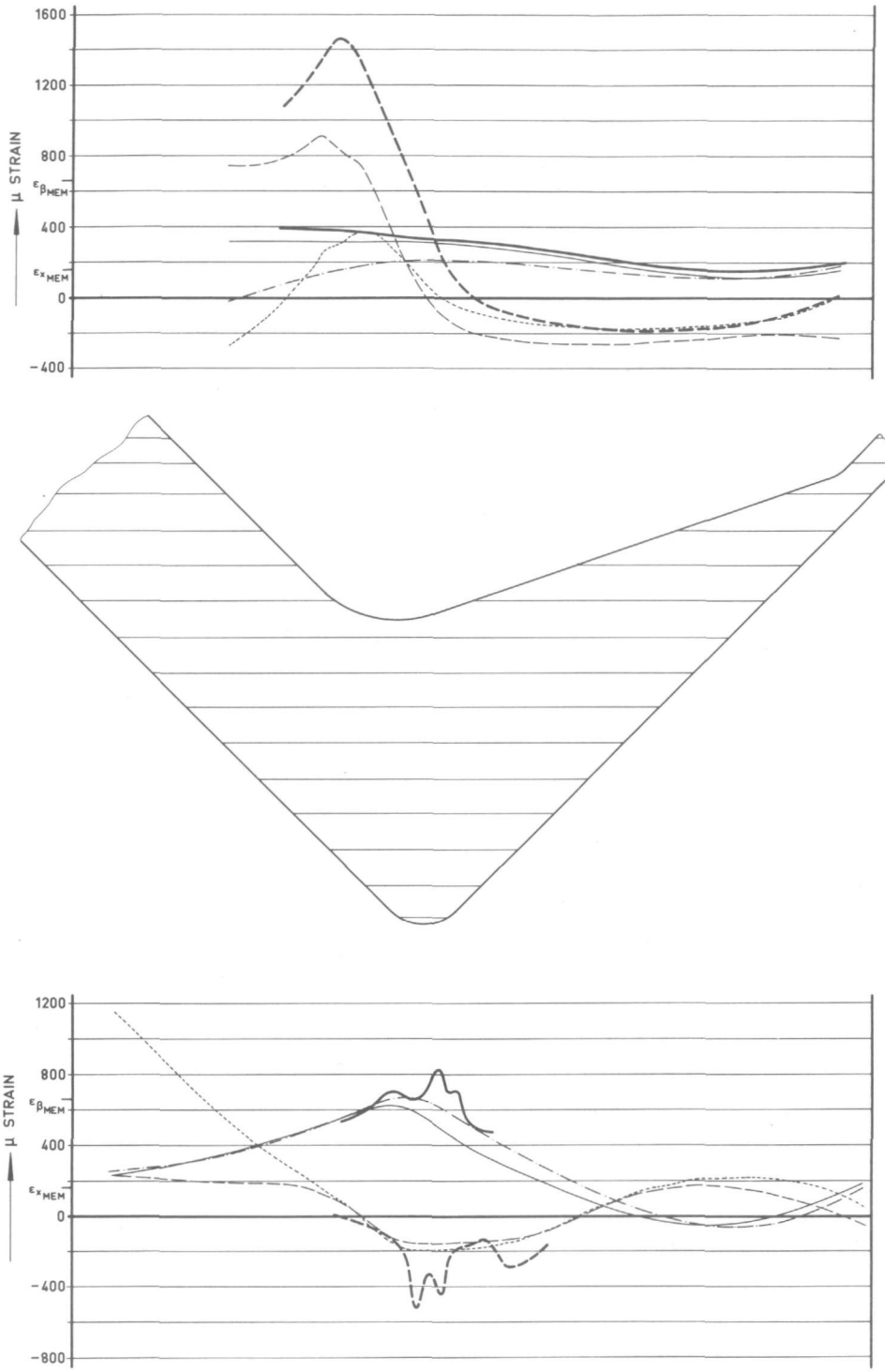

TRANSVERSAL SECTION A - A (cf. FIG. 4.4.2)

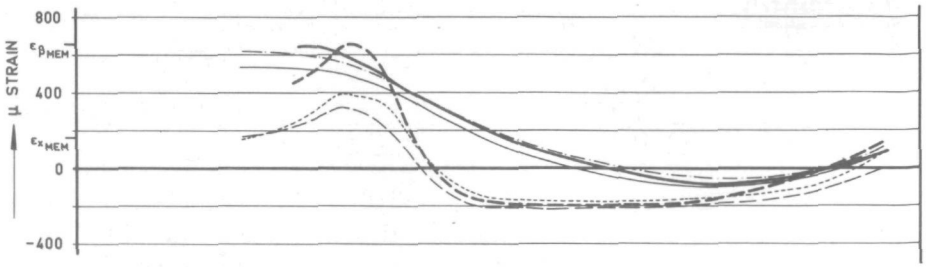

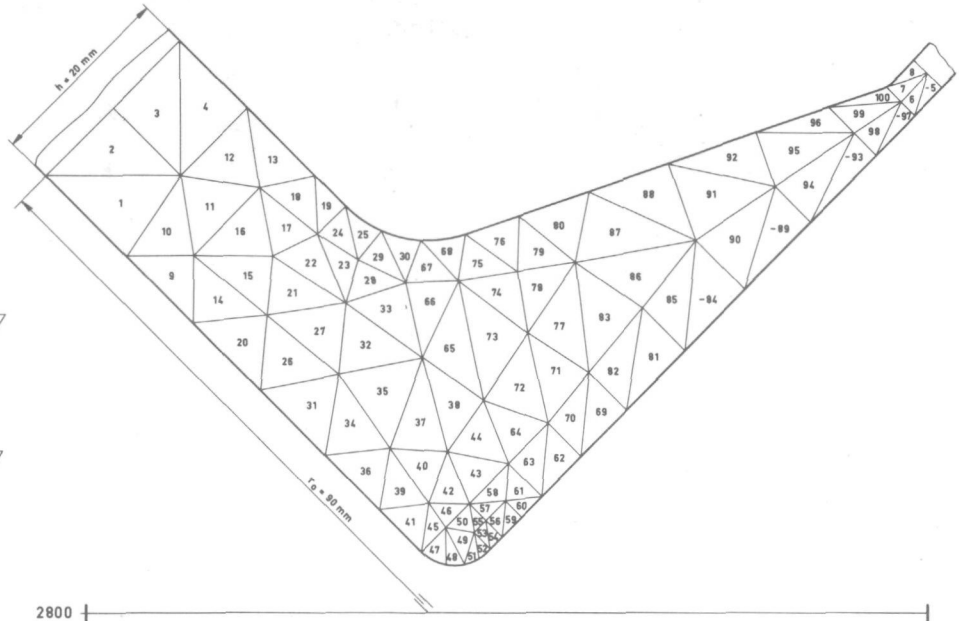

STRAIN ⊥ CROSS SECTION
STRAIN IN CROSS SECTION
} EXPERIMENTAL

STRAIN ⊥ CROSS SECTION
STRAIN IN CROSS SECTION
} NUMERICAL

Influence coefficients: Section 4.3.3
Membrane solution for unweakened shell:
second part of Section 4.3.4

STRAIN ⊥ CROSS SECTION
STRAIN IN CROSS SECTION
} NUMERICAL

Influence coefficients: Section 4.3.3
Membrane solution for unweakened shell:
first part of Section 4.3.4

$E = 2,100,000\ kgf/cm^2$

$\nu = 0.29$

$\mu = \frac{\sqrt[4]{12(1-\nu^2)}}{\sqrt{Rh}} \frac{r_o}{} = 0.96$

$\frac{R}{r_o} = 4.01$

INTERNAL PRESSURE : $90\ kgf/cm^2$

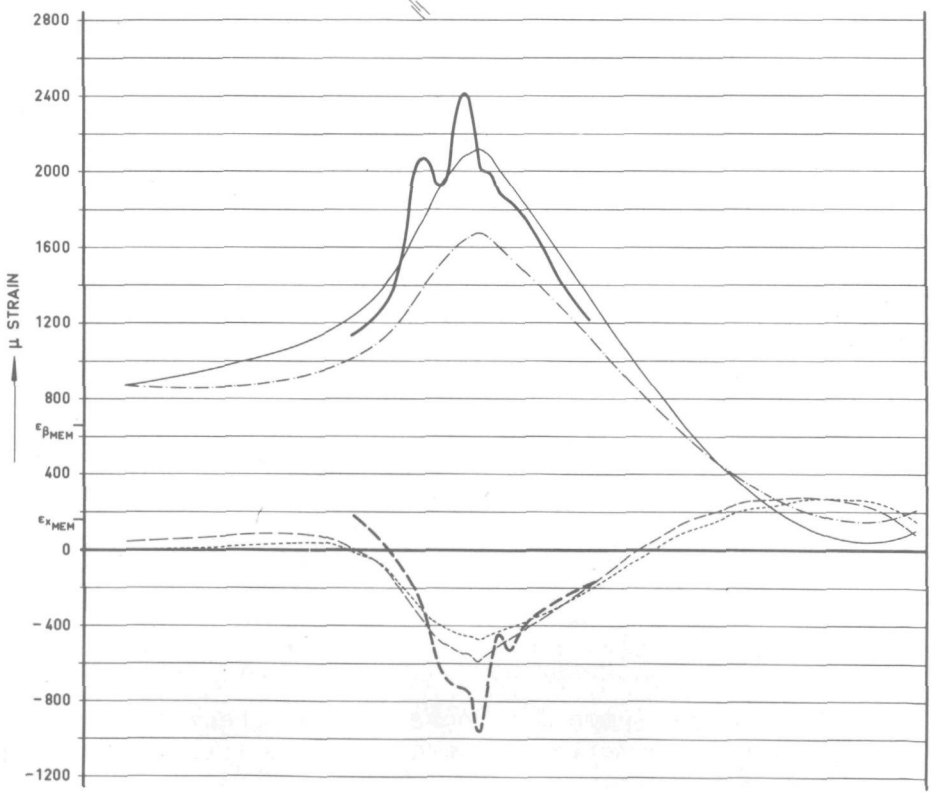

LONGITUDINAL SECTION B - B (cf. FIG. 4.4.2)

FIGURE 4.4.13.

Influence of various boundary conditions on numerical strain distribution for model vessel nozzle N5.

Appendix 1. Compatibility conditions at the intersection between a shell element and other finite elements.

In this appendix the compatibility conditions shall be derived at the intersection between a shell element and other finite elements. The general compatibility conditions will be specified for the case of solids of revolution under non-axisymmetric loads.

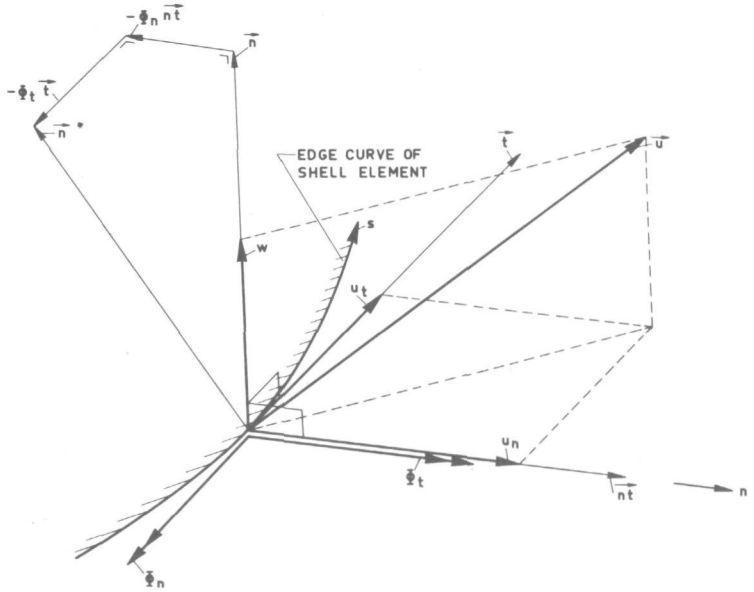

FIGURE A.1.1.

Edge displacements and edge rotations of a shell element.

Let $\vec{nt}$ denote the outward normal unit vector in the tangent plane to the edge curve in the undeformed middle surface of a shell element, and $\vec{t}$ the unit tangent vector to this curve (cf. figure A.1.1). The unit normal vector $\vec{n}$ to the undeformed middle surface at the edge curve is defined by means of the cross product of these two vectors

$$\vec{n} = \vec{nt} \times \vec{t} \qquad (A.1.1)$$

where the right-hand screw rule applies between $\vec{nt}$, $\vec{t}$ and $\vec{n}$ in this sequence. The three vectors $\vec{nt}$, $\vec{t}$ and $\vec{n}$ will be decomposed with respect to the three unit base vectors $\vec{e}_i$ (i = 1, 2, 3) in a fixed global co-ordinate system $0\ x_1\ x_2\ x_3$ in space

$$\vec{nt} = nt_i\ \vec{e}_i \qquad \vec{t} = t_i\ \vec{e}_i \qquad \vec{n} = n_i\ \vec{e}_i \qquad (A.1.2)$$

where the summation convention has been applied for a repeated index, which implies summation of an index from 1 to 3 if this index occurs twice in a product term.

Let $\vec{u}(z)$ denote the displacement vector of a material point of the boundary section of our shell element at a distance z above the middle surface, while $\vec{u}$ is the value of $\vec{u}(z)$ for z = 0. This displacement vector will be decomposed with respect to the three unit vectors $\vec{nt}$, $\vec{t}$ and $\vec{n}$ as follows

$$\vec{u} = u_n\ \vec{nt} + u_t\ \vec{t} + w\ \vec{n} \qquad (A.1.3)$$

The unit normal vector $\vec{n}^{*}$ to the deformed middle surface at the edge curve will also be decomposed with respect to the three vectors $\vec{nt}$, $\vec{t}$ and $\vec{n}$

$$\vec{n}^{*} = \vec{n} - \Phi_n \vec{nt} - \Phi_t \vec{t} \tag{A.1.4}$$

where Φ_n and Φ_t are the physical components of the rotation of the normal to the middle surface at the edge curve (cf. figure A.1.1). General expressions for Φ_n and Φ_t as a function of the middle surface displacements are given e.g. in [1.16] and have the following form

$$\Phi_n = \frac{\partial w}{\partial n} + \frac{u_n}{R_n} + \frac{u_t}{T} \tag{A.1.5}$$

$$\Phi_t = \frac{\partial w}{\partial s} + \frac{u_t}{R_t} + \frac{u_n}{T} \tag{A.1.6}$$

where R_n, R_t and T are the radii of curvature and the radius of torsion along the parametric curves n and s shown in figure A.1.1.

By taking into account the Kirchhoff-Love assumptions from linear thin shell theory, discussed in Chapter 1.2, the displacement vector $\vec{u}(z)$ can be expressed as a function of the middle surface edge displacements and edge rotations

$$\begin{aligned}\vec{u}(z) &= \vec{u} + z\,[\vec{n}^{*} - \vec{n}] = \\ &= [u_n - z\,\Phi_n]\,\vec{nt} + [u_t - z\,\Phi_t]\,\vec{t} + w\,\vec{n} = \\ &= \{[u_n - z\,\Phi_n]\,nt_i + [u_t - z\,\Phi_t]\,t_i + w\,n_i\}\,\vec{e}_i\end{aligned} \tag{A.1.7}$$

Let $\vec{u}_k$ denote the displacement vector of a nodal point, identified by the index k, of a finite element adjacent to the shell element under consideration. This nodal point is assumed to be located in the plane of intersection with the shell element at a distance z_k above the shell middle surface, where the co-ordinate s along the edge curve (cf. figure A.1.1) equals s_k. The displacement vector $\vec{u}_k$ will be decomposed with respect to the three unit base vectors $\vec{e}_i$

$$\vec{u}_k = u_{ki}\,\vec{e}_i \tag{A.1.8}$$

By means of the vector equation, resulting from (A.1.7) and (A.1.8), we arrive at the general formulae for the compatibility requirements

$$u_{ki} = [u_{nk} - z_k\,\Phi_{nk}]\,nt_{ki} + [u_{tk} - z_k\,\Phi_{tk}]\,t_{ki} + w_k\,n_{ki} \tag{A.1.9}$$

where the subscript k refers to the value of a quantity at the point $s = s_k$. At this point the reader should recall that the only independent kinematic boundary quantities of the shell element, occurring in the right-hand member of (A.1.9), are u_{nk}, u_{tk}, w_k and Φ_{nk}. With the three displacements prescribed along the edge curve, the rotation Φ_t follows from (A.1.6) to be a known quantity.

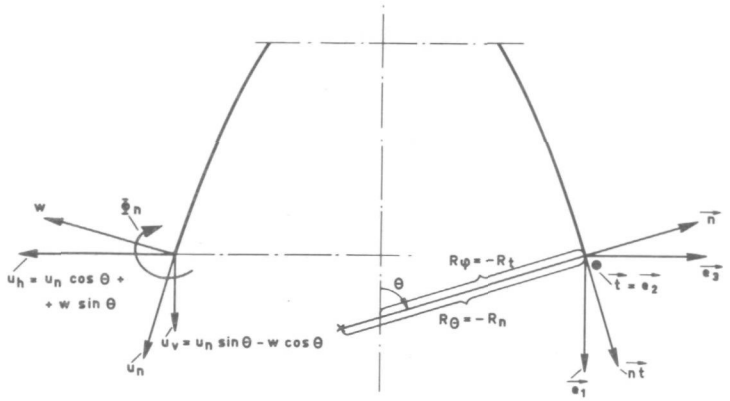

FIGURE A.1.2.

Co-ordinate and displacement notations for shell of revolution.

In order to specify the general formulae (A.1.9) for the case of solids of revolution under non-axisymmetric loads, we introduce the co-ordinate definitions shown in figure A.1.2. The components nt_i, t_i and n_i of the unit vectors $\vec{nt}$, $\vec{t}$ and $\vec{n}$, defined by (A.1.3), are specified as follows

$$\begin{aligned} nt_1 &= \sin\theta & nt_2 &= 0 & nt_3 &= \cos\theta \\ t_1 &= 0 & t_2 &= 1 & t_3 &= 0 \\ n_1 &= -\cos\theta & n_2 &= 0 & n_3 &= \sin\theta \end{aligned} \qquad \text{(A.1.10)}$$

Substitution from (A.1.10) into (A.1.9) leads to

$$u_{k1} = u_{vk} - z_k \Phi_{nk} \sin\theta \qquad \text{(A.1.11)}$$

$$u_{k2} = u_{tk} - z_k \Phi_{tk} \qquad \text{(A.1.12)}$$

$$u_{k3} = u_{hk} - z_k \Phi_{nk} \cos\theta \qquad \text{(A.1.13)}$$

where u_h and u_v are defined in figure A.1.2, while

$$\Phi_n = \frac{\partial w}{\partial n} - \frac{u_n}{R_\theta} \qquad \text{(A.1.14)}$$

$$\Phi_t = \frac{\partial w}{\partial s} - \frac{u_t}{R_\phi} \qquad \text{(A.1.15)}$$

Appendix 2. Formulae for the integral expressions R(p,q).

In this appendix the formulae shall be given for the integral expressions

$$R(p,q) = \int_\Delta \int r^p z^q \, r dr dz$$

occuring in the coefficients of the H_n matrix defined in table 2.2.2. The sequence in the numbering of the triangular corner points shall always be assumed to be counter clockwise (cf. figure A.2.1).

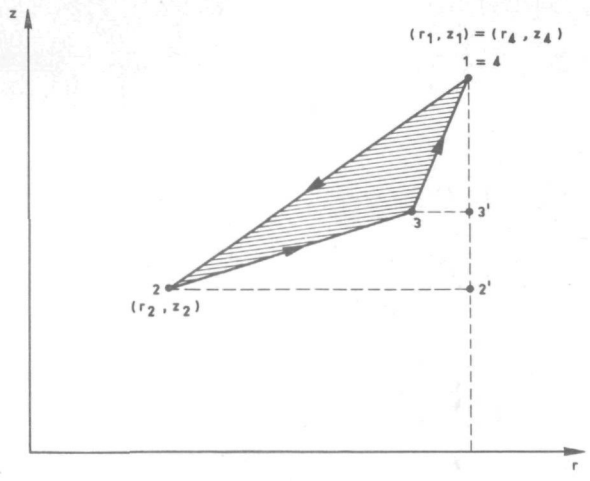

FIGURE A.2.1.

Numbering of triangular corner points.

A general expression for R(p,q), where $p \geq -1$, $q \geq 0$, has been developed by ALMERING [A.1], making use of the series expansion for the beta function for positive integer arguments

$$R(p,q) = \frac{2\,(p+1)!\;q!}{(p+q+3)!} \sum_{\ell=1}^{3} A_\ell \times$$

$$\times \sum_{i=0}^{p+1} \sum_{j=0}^{q} \binom{i+j}{i} \binom{p+1+q-i-j}{p+1-i} r_\ell^{p+1-i}\, r_{\ell+1}^{i}\, z_\ell^{q-j}\, z_{\ell+1}^{j} \qquad \text{(A.2.1)}$$

where

$$A_\ell = \frac{1}{2}\,(r_\ell\, z_{\ell+1} - r_{\ell+1}\, z_\ell) \qquad \text{(A.2.2)}$$

is the area of the triangle (0, ℓ, ℓ+1), while

$$\binom{n}{k} = \frac{n!}{k!\;(n-k)!}$$

As can be seen from table 2.2.2 the case $p \geq -1$, $q \geq 0$ covers all possibilities, with the exception of R(-2,q), $q \geq 0$. The expression for R(-2,q), where $0 \geq q \geq 4$, has been developed by MEIJERS [A.2]. Assuming r_1 to be the largest of the corner point radii and assuming also the smallest of these radii to be nonzero, he defined

$$R(-2,q) = I_{21}(q) - I_{23}(q) - I_{31}(q) \qquad \text{(A.2.3)}$$

where $I_{21}(q)$ is the integral over the area 22'1, $I_{23}(q)$ the integral over the area 22'3'3 and $I_{31}(q)$ the integral over the area 33'1 (cf. figure A.2.1). A detailed analysis of these integrals leads to the following results

$$I_{ij}(q) = \sum_{n=0}^{q} \binom{q}{n} z_{ij}^{q-n}\, \bar{I}_{ij}(n) \qquad \text{(A.2.4)}$$

where

$$z_{ij} = \frac{1}{2}(z_i + z_j) \tag{A.2.5}$$

while

$$\left.\begin{aligned}
\bar{I}_{ij}(2q) &= -\frac{2}{(2q+1)}\left[\frac{z_i - z_j}{2}\right]^{2q+1} \ln\left[\frac{2r_1}{r_i + r_j}\right] + \\
&\quad - \left[\frac{z_i - z_j}{2}\right]^{2q+1} \sum_{n=1}^{\infty} \frac{1}{n(2n+2q+1)}\left[\frac{r_i - r_j}{r_i + r_j}\right]^{2n} \\
\bar{I}_{ij}(2q+1) &= 2\left[\frac{z_i - z_j}{2}\right]^{2q+2} \sum_{n=1}^{\infty} \frac{1}{(2n-1)(2n+2q+1)}\left[\frac{r_i - r_j}{r_i + r_j}\right]^{2n-1}
\end{aligned}\right\} \tag{A.2.6}$$

Appendix 3. Summary of governing equations for circular cylindrical shells.

For circular cylindrical shells the relations between the components of the rotation vector and the displacements resulting from the general linear theory of thin elastic shells have the following form (see [1.16], equations (3.10), (3.11) and (3.12))

$$\phi_x = \frac{w'}{R} \qquad \phi_y = \frac{w^{\cdot} - v}{R} \qquad \Omega = \frac{v' - u^{\cdot}}{2R} \tag{A.3.1}$$

Starting from a modified expression for the strain energy for circular cylindrical shells, including no other assumptions than those basic to linear thin shell theory (cf. Chapter 1.2), KOITER [A.3] defined the following modified stress resultants and stress couples

$$\left.\begin{aligned}
N_x^* &= \frac{Eh}{(1-\nu^2)R}\left[u' + \nu(v^{\cdot} + w) + (1-\nu)\frac{h^2}{12R^2}(v^{\cdot} - w^{\cdot\cdot})\right] \\
N_y^* &= \frac{Eh}{(1-\nu^2)R}\left[\nu u' + (v^{\cdot} + w) + (1-\nu)\frac{h^2}{12R^2}(u' + w'')\right] \\
N_{xy}^* &= \frac{Eh}{(1-\nu^2)R}\left[\frac{1}{2}(1-\nu)(u^{\cdot} + v') - (1-\nu)\frac{h^2}{12R^2}(u^{\cdot} + w^{\cdot\cdot})\right] \\
N_{yx}^* &= \frac{Eh}{(1-\nu^2)R}\left[\frac{1}{2}(1-\nu)(u^{\cdot} + v') + (1-\nu)\frac{h^2}{12R^2}(w^{\cdot\cdot} - v')\right] \\
M_x^* &= \frac{Eh^3}{12(1-\nu^2)R^2}\left[w'' + \nu w^{\cdot\cdot} + w + (1-\nu)v^{\cdot}\right] \\
M_y^* &= \frac{Eh^3}{12(1-\nu^2)R^2}\left[\nu w'' + w^{\cdot\cdot} + w - (1-\nu)u'\right] \\
M_{xy}^* &= M_{yx}^* = \frac{Eh^3}{12(1-\nu^2)R^2}\left[(1-\nu)w^{\cdot\cdot} + \frac{1}{2}(1-\nu)(u^{\cdot} - v')\right]
\end{aligned}\right\} \tag{A.3.2}$$

In combination with the modified stress couples, the associated modified transverse shear forces are defined in [A.3]

$$Q_x^* = -\frac{1}{R}\left[M_x^{*\prime} + M_{yx}^{*\cdot}\right] = -\frac{Eh^3}{12(1-\nu^2)R^3}\left[(\Delta w+w)' + \frac{1}{2}(1-\nu)(u^{\cdot}+v')^{\cdot}\right]$$

$$Q_y^* = -\frac{1}{R}\left[M_{xy}^{*\prime} + M_y^{*\cdot}\right] = -\frac{Eh^3}{12(1-\nu^2)R^3}\left[(\Delta w+w)^{\cdot} - \frac{1}{2}(1-\nu)(u^{\cdot}+v')'\right] \qquad \text{(A.3.3)}$$

From the principle of virtual work we obtain the following three homogeneous equations of equilibrium

$$N_x^{*\prime} + N_{yx}^{*\cdot} = 0 \qquad N_{xy}^{*\prime} + N_y^{*\cdot} = 0$$

$$\frac{Eh}{(1-\nu^2)R}\left[\nu u' + v^{\cdot} + w + \frac{h^2}{12R^2}(\Delta w+w)\right] - Q_x^{*\prime} - Q_y^{*\cdot} = 0 \qquad \text{(A.3.4)}$$

and the following four dynamic boundary conditions along an arbitrary edge curve (cf. figure 2.3.4)

$$N_x^* n_x + N_{yx}^* n_y = \overline{N}_x \qquad N_{xy}^* n_x + N_y^* n_y = \overline{N}_y - \frac{1}{R}\left[M_n n_y + M_t n_x\right] = \overline{N}_{y_{red}}$$

$$M_x^* n_x^2 + 2M_{xy}^* n_x n_y + M_y^* n_y^2 = M_n \qquad \text{(A.3.5)}$$

$$Q_x^* n_x + Q_y^* n_y - \frac{\partial}{\partial s}\left[(M_y^* - M_x^*)\, n_x n_y + M_{xy}^* (n_x^2 - n_y^2)\right] = \overline{Q} - \frac{\partial M_t}{\partial s} = \overline{Q}_{red}$$

Substitution from (A.3.2) and (A.3.3) into (A.3.4) leads to three homogeneous equations for the displacements u, v, and w

$$u'' + \frac{1}{2}(1-\nu)u^{\cdot\cdot} + \frac{1}{2}(1+\nu)v^{\cdot\cdot} + \nu w' = 0$$

$$\frac{1}{2}(1+\nu)u^{\cdot\cdot} + \frac{1}{2}(1-\nu)v'' + v^{\cdot\cdot} + w^{\cdot} = 0 \qquad \text{(A.3.6)}$$

$$\nu u' + v^{\cdot} + w + \frac{h^2}{12R^2}(\Delta+1)^2 w = 0$$

Expressing u and v in w by means of the two first equations we obtain

$$\Delta^2 u = -\nu w''' + w^{\cdot\cdot\cdot} \qquad \Delta^2 v = -(2+\nu)w''^{\cdot} - w^{\cdot\cdot\cdot} \qquad \text{(A.3.7)}$$

Substitution from this equation into the last equation of (A.3.6) leads to the following equation for w

$$(1-\nu^2)w'''' + \frac{h^2}{12R^2}\Delta^2(\Delta+1)^2 w = 0 \qquad \text{(A.3.8)}$$

The partial differential equations (A.3.7) and (A.3.8) are the so-called Morley equations. However, MORLEY [A.4] derived his equations in a rather opaque way, being different from the above summarized derivation, proposed by KOITER [A.3]. Morley proposed his equations as a correction on the well-known DONNELL equations [A.5], which imply the following assumption

$$|\Delta w| >> |w| \tag{A.3.9}$$

SIMMONDS [A.6] developed a fourth order equation for a complex-valued displacement-stress function, being equivalent to (A.3.8). However, where a stress function is occurring in this equation, it is more straight-forward to use (A.3.8) as a starting point for practical applications.

Appendix 4. Influence coefficients for the tapered hub considered as an assemblage of TRIAX 6 elements.

In this appendix the influence coefficients will be presented for the tapered hub considered as an assemblage of TRIAX 6 elements. At first glance, one would think that these influence coefficients should refer to the hub boundary loadings Q_0, M_0, Q_1 and M_1 shown in figure 3.1.2 and the edge deformations w_0, ϕ_0, w_1 and ϕ_1 resulting therefrom. However, in this case these influence coefficients can be shown to depend on the three dimensionless parameters

$$\frac{g_0}{r_0}, \qquad \frac{g_1}{g_0} \qquad \text{and} \qquad \sqrt{r_0 g_0}/h$$

A closer inspection of the equations underlying the thin shell analysis discussed in Chapter 3.3.1 reveals that appropriately defined influence coefficients only depend on the two dimensionless parameters g_1/g_0 and $\sqrt{r_0 g_0}/h$. As the thin shell behaviour of the tapered hub has been shown dominant in Chapter 3.3.1 it can be stated with sufficient accuracy from a practical point of view that these influence coefficients will also only depend on the above parameters when the hub is considered as an assemblage of TRIAX 6 elements.
The modified influence coefficients $\alpha_{ij} = \alpha_{ji}$ $(i = 1, .., 4;\ j = 1, .., 4)$ are defined as follows

$$w_0 = \frac{1}{E}\left(\frac{r_0}{g_0}\right)^2 \left[- \alpha_{11} Q_0 \sqrt{\frac{g_0}{r_0}} + \alpha_{12} \frac{M_0}{r_0} - \alpha_{13} Q_1 \sqrt{\frac{g_0}{r_0}} + \right.$$

$$\left. - \alpha_{14} \frac{M_1}{r_0} \right] + \alpha_{1p} \frac{p\, r_0^2}{E\, g_0} \tag{A.4.1}$$

$$\sqrt{r_0 g_0}\,\phi_0 = \frac{1}{E}\left(\frac{r_0}{g_0}\right)^2 \left[- \alpha_{21} Q_0 \sqrt{\frac{g_0}{r_0}} + \alpha_{22} \frac{M_0}{r_0} - \alpha_{23} Q_1 \sqrt{\frac{g_0}{r_0}} + \right.$$

$$\left. - \alpha_{24} \frac{M_1}{r_0} \right] + \alpha_{2p} \frac{p\, r_0^2}{E\, g_0} \tag{A.4.2}$$

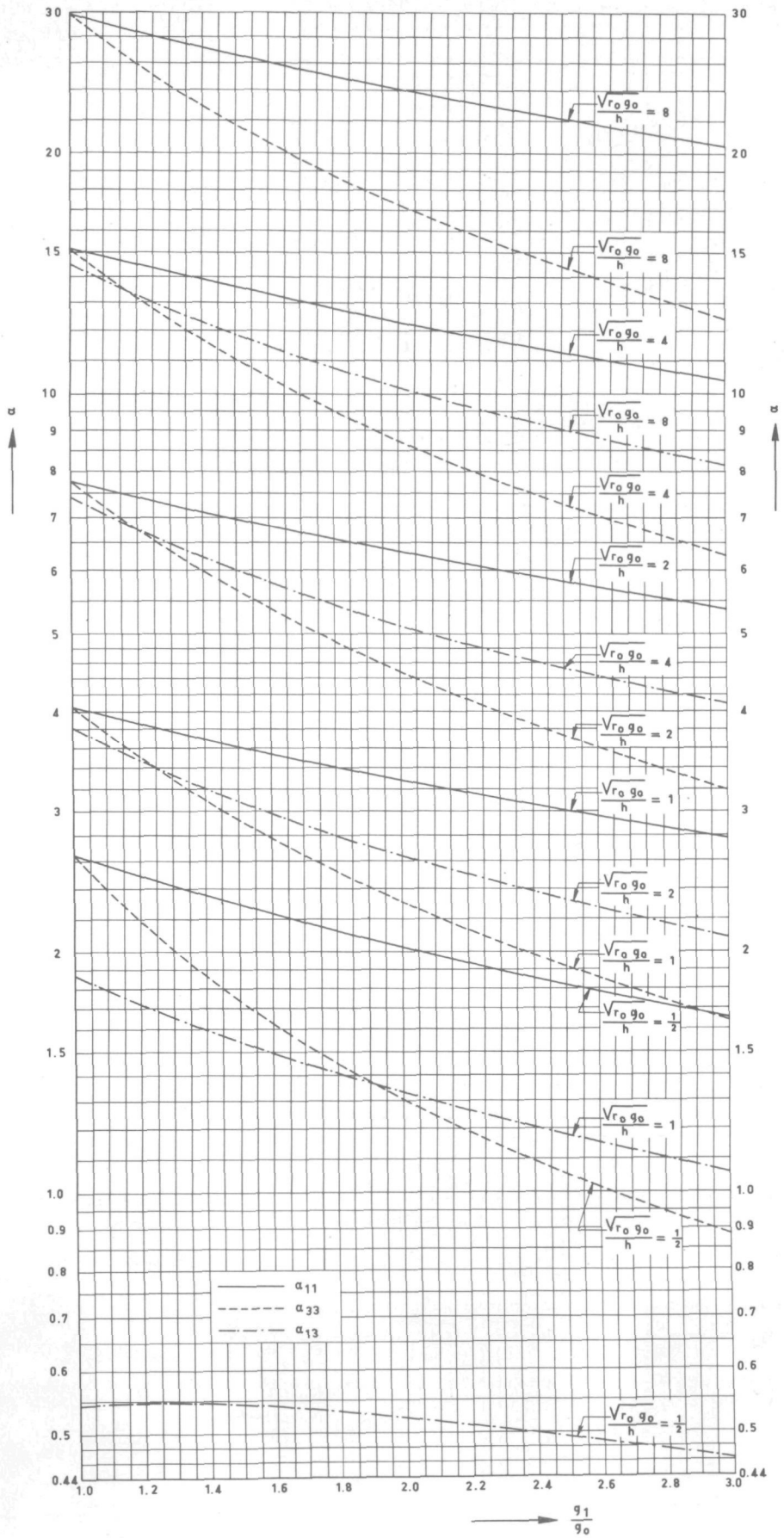

FIGURE A.4.1.

The influence coefficients α_{11}, α_{33} *and* α_{13}.

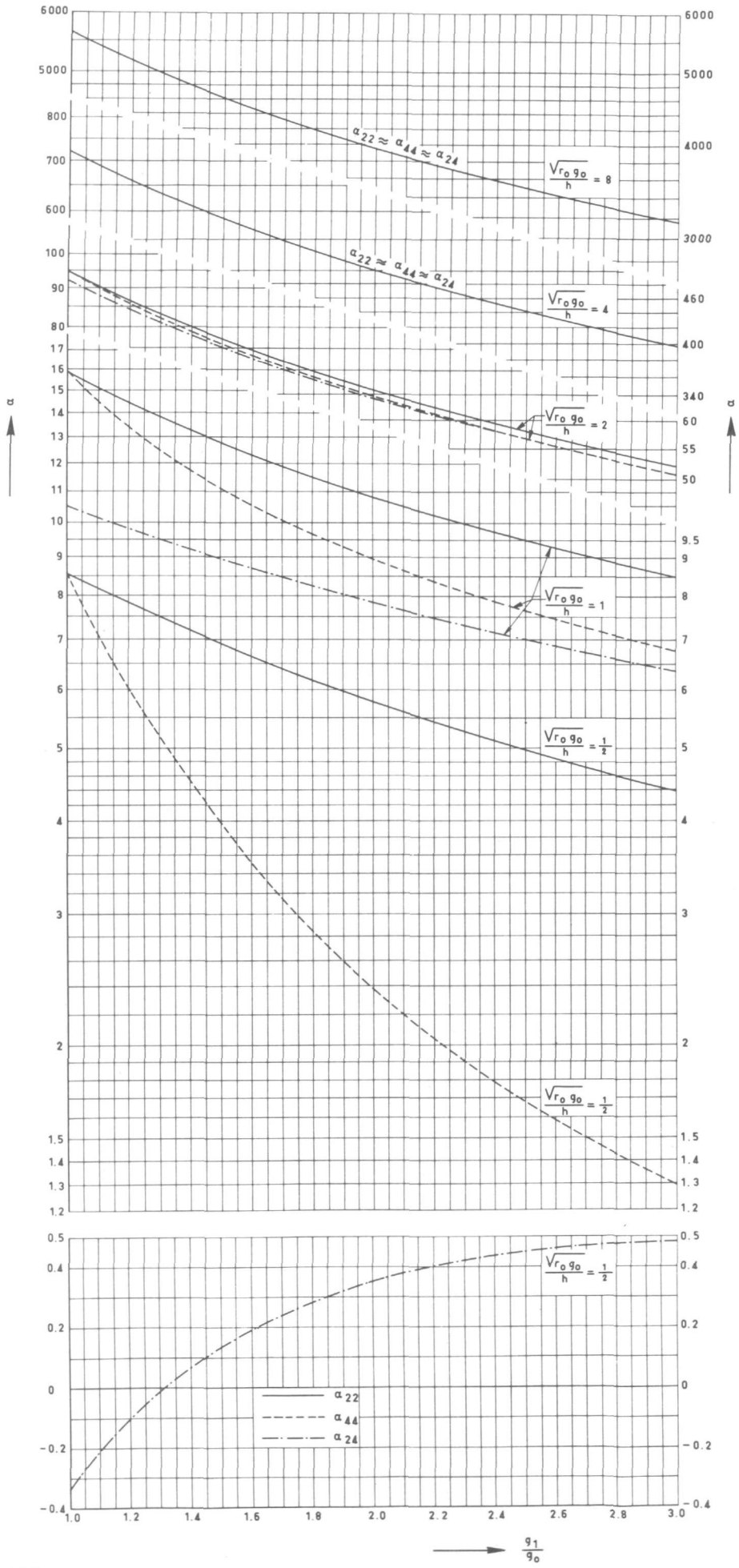

FIGURE A.4.2.

The influence coefficients α_{22}, α_{44} and α_{24}.

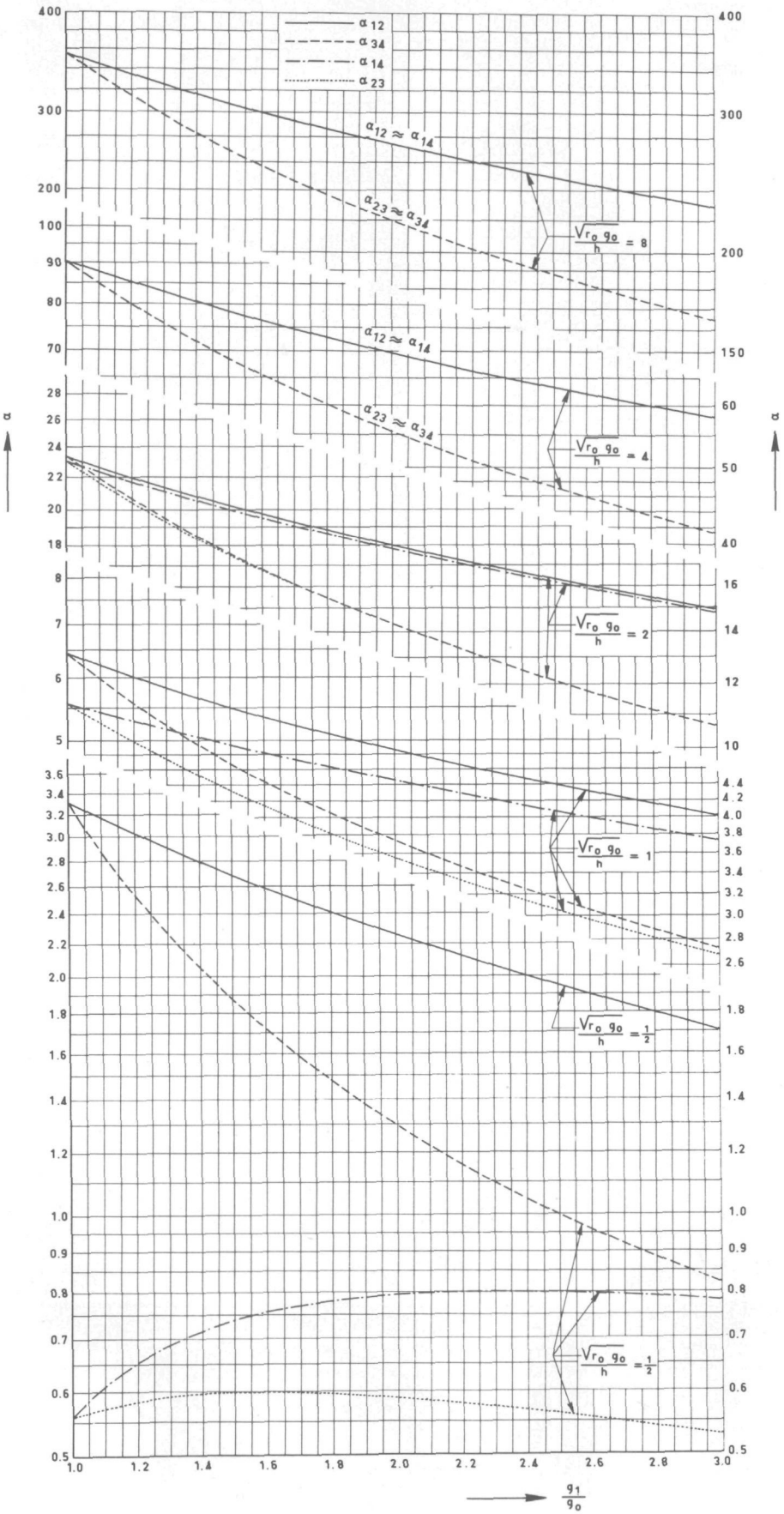

FIGURE A.4.3.

The influence coefficients α_{12}, α_{34}, α_{14} *and* α_{23}.

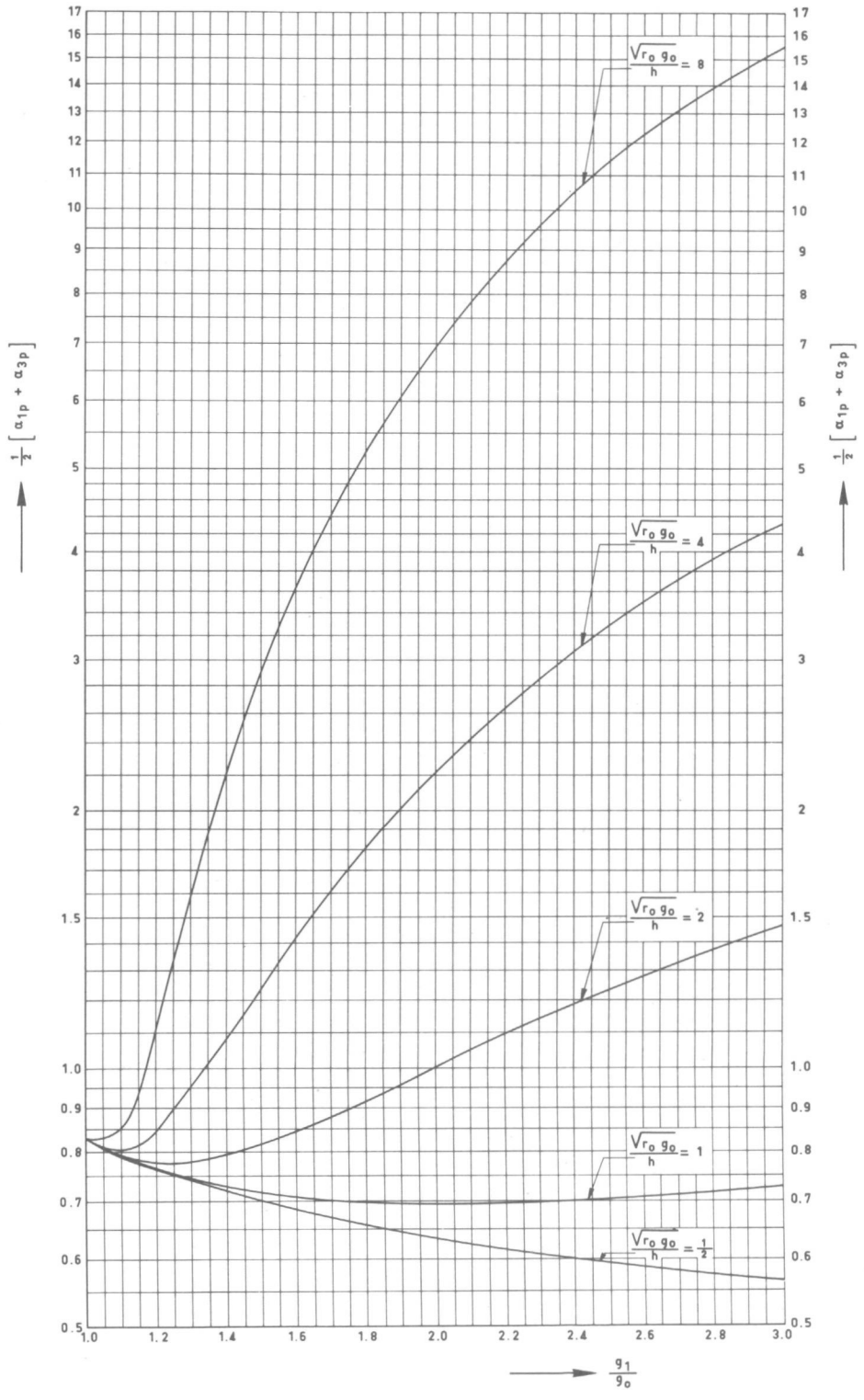

FIGURE A.4.4.
The coefficient $\frac{1}{2}\left[\alpha_{1p} + \alpha_{3p}\right]$.

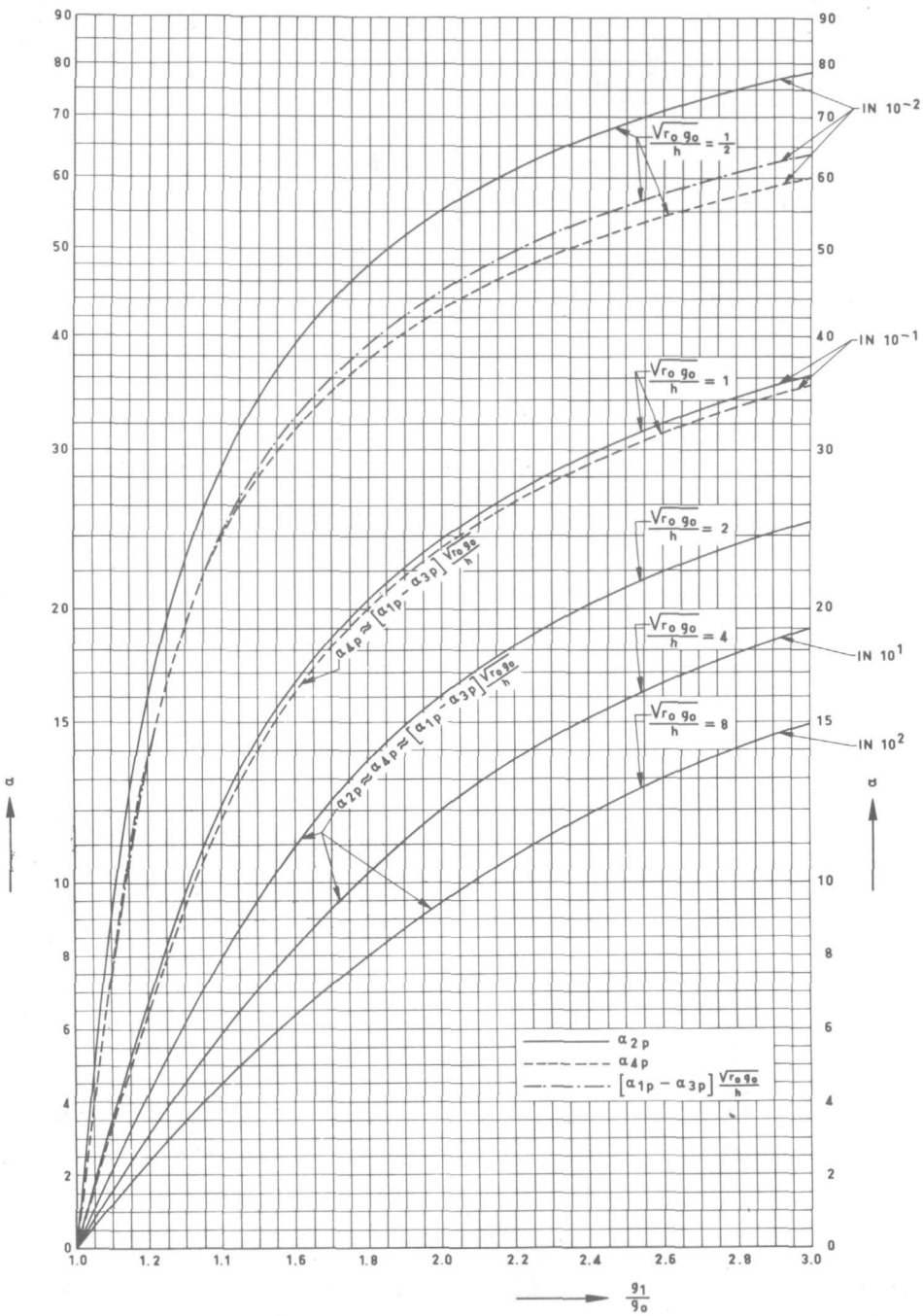

FIGURE A.4.5.

The influence coefficients α_{2p}, α_{4p} *and* $[\alpha_{1p} - \alpha_{3p}] \frac{\sqrt{r_0 g_0}}{h}$

$$w_1 = \frac{1}{E}\left(\frac{r_0}{g_0}\right)^2 \left[\alpha_{31}\, Q_0 \sqrt{\frac{g_0}{r_0}} - \alpha_{32}\frac{M_0}{r_0} + \alpha_{33}\, Q_1 \sqrt{\frac{g_0}{r_0}} + \right.$$

$$\left. + \alpha_{34}\frac{M_1}{r_0}\right] + \alpha_{3p}\frac{p\, r_0^2}{E\, g_0} \qquad \text{(A.4.3)}$$

$$\sqrt{r_0 g_0}\,\phi_1 = \frac{1}{E}\left(\frac{r_0}{g_0}\right)^2 \left[-\alpha_{41}\, Q_0 \sqrt{\frac{g_0}{r_0}} + \alpha_{42}\frac{M_0}{r_0} - \alpha_{43}\, Q_1 \sqrt{\frac{g_0}{r_0}} + \right.$$

$$\left. - \alpha_{44}\frac{M_1}{r_0}\right] + \alpha_{4p}\frac{p\, r_0^2}{E\, g_0} \qquad \text{(A.4.4)}$$

where α_{1p}, α_{2p}, α_{3p} and α_{4p} are proportional to the free edge deformations due to the internal loading (including the axial pressure force) acting on the tapered hub. The modified influence coefficients are given in graphical form in figures A.4.1 through A.4.5 (cf. pp. 129-133) as a function of g_1/g_0 for several values of $\sqrt{r_0 g_0}/h$ (i.e. $\sqrt{r_0 g_0}/h = \frac{1}{2}$, 1, 2, 4, 8) and intend to cover the range of practical interest. In order to obtain a systematic presentation the coefficients α_{1p} and α_{3p} have been replaced by $\frac{1}{2}[\alpha_{1p} + \alpha_{3p}]$ and $[\alpha_{1p} - \alpha_{3p}]\sqrt{r_0 g_0}/h$ *). For values of $\sqrt{r_0 g_0}/h$ between the values mentioned above the influence coefficients can be obtained via interpolation.

Appendix 5. Determination of relative gasket face rotations from sensing pin displacements.

Figure A.5.1 shows a schematic representation of the leaf spring deformation and the sensing pin displacement during an experiment. Part a of this figure shows an arbitrary starting position, while part b shows the final position after the experiment during which the rotation of the head flange at the clamping point of the leaf spring on the outside is ϕ_F radians.
With the strain gages being attached on the leaf spring we measure the difference m between the vertical displacement w of point Q *relative to point P*, and the product of ϕ_F and the sensing pin length ℓ

$$m = w - \phi_F.\ell \qquad \text{(A.5.1)}$$

In considering (cf. figure A.5.2) three sensing pins in one longitudinal section it is possible to determine the relative vertical displacement $\Delta_{k\ell}$ between the points Q_k and Q_ℓ (positively if Q_k moves away from Q_ℓ in head flange direction) as well as the relative vertical displacement $\Delta_{\ell m}$ between

*) *The first of these quantities is proportional to the mean value of the two free edge displacements, while the second is proportional to the free rotation obtained by dividing the difference between these displacements by the axial length of the hub.*

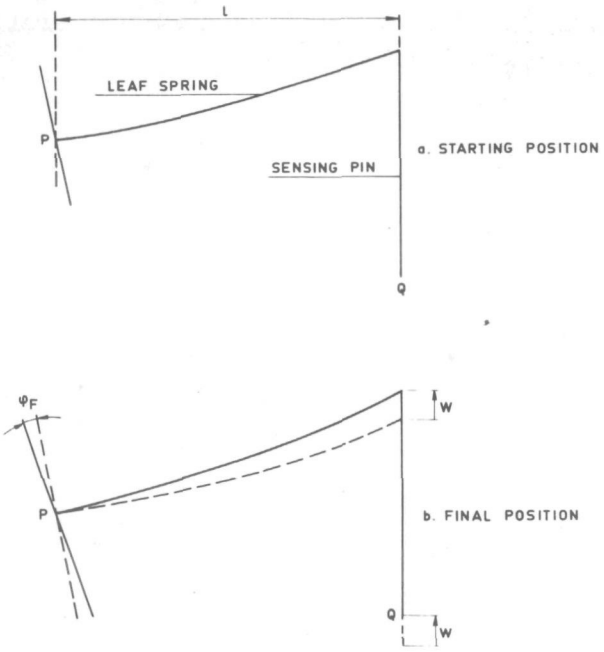

FIGURE A.5.1.

Schematic representation of the deformation of leaf spring and sensing pin during an experiment.

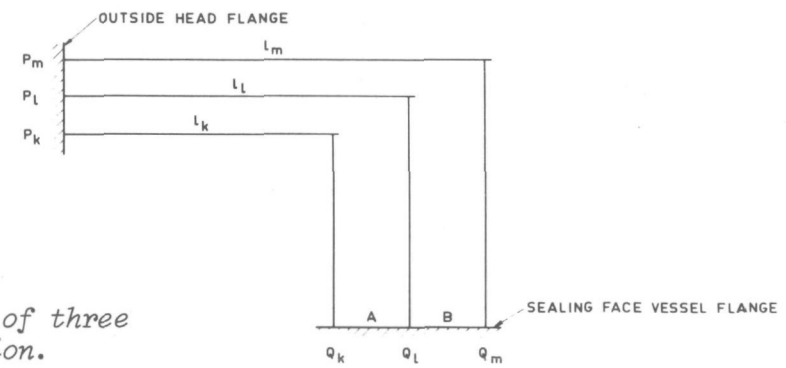

FIGURE A.5.2.

Schematic representation of three sensing pins in one section.

the points Q_ℓ and Q_m (positively if Q_ℓ moves away from Q_m in head flange direction). For this purpose the following assumptions have been made:

1. The relative vertical displacements between the points P_k and P_ℓ (cf. figure A.5.2) and between the points P_ℓ and P_m are negligible.
2. The change in rotation of the head flange at the points P_k, P_ℓ and P_m is identical and equal to ϕ_F during the experiment.

From (A.5.1) follows

$$\Delta_{k\ell} = w_k - w_\ell = m_k - m_\ell - \phi_F (\ell_\ell - \ell_k) \qquad (A.5.2)$$

$$\Delta_{\ell m} = w_\ell - w_m = w_\ell - m_m - \phi_F (\ell_m - \ell_\ell) \qquad (A.5.3)$$

The rotations ϕ_A and ϕ_B of the parts A and B of the vessel flange sealing face have been defined in the following way

$$\phi_A = \frac{\Delta_{k\ell}}{\ell_\ell - \ell_k} = \frac{m_k - m_\ell}{\ell_\ell - \ell_k} - \phi_F \qquad (A.5.4)$$

$$\phi_B = \frac{\Delta_{\ell m}}{\ell_m - \ell_\ell} = \frac{m_\ell - m_m}{\ell_m - \ell_\ell} - \phi_F \qquad (A.5.5)$$

Appendix 6. Summary of Lekkerkerker's shallow thin shell theory method.

In this appendix the analysis is summarized of a thin circular cylindrical shell, weakened by a circular hole, and subjected to a self-equilibrating boundary load along the edge of the hole. The method of analysis, developed by LEKKERKERKER [4.10, 4.11], is based on shallow shell theory and consequently the deformation pattern has to be rapidly varying, i.e. the wave length of the deformation pattern must be small with respect to the shell radius R (cf. Chapter 1.2). A second essential approximation in the analysis is connected with the employed polar co-ordinate system in the developed middle surface of the shell. As a consequence the actual cylindrical shell is replaced by a hypothetical spiral shell model where the actual connection along the generator opposite the hole centre is neglected, while furthermore the hole is assumed to be circular in the developed shell surface as this coincides with one of the co-ordinate lines. A comprehensive qualitative study of the inaccuracies due to the approximate character of the theory underlying the analysis in Chapter 6 of [4.11] indicates that the analysis can be expected accurate if the hole radius to shell radius ratio r_0/R is comparatively small, e.g. smaller than $\frac{1}{4}$.

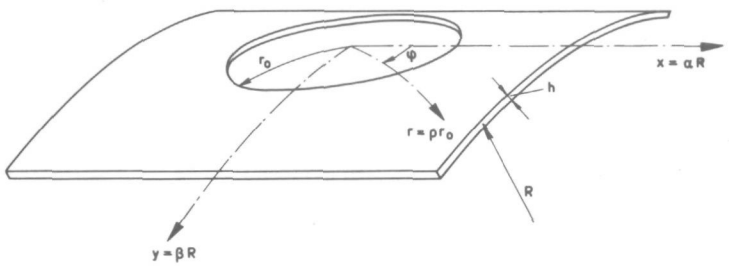

FIGURE A.6.1.

Geometry and co-ordinate systems of a cylindrical shell with a circular hole.

The geometry of the shell middle surface is described with respect to the rectangular co-ordinates x, y, and in addition with respect to the polar co-ordinates r, ϕ (cf. figure A.6.1). The origin of both co-ordinate systems coincides with the centre of the circular hole, while instead of the co-ordinates x, y and r the non-dimensional co-ordinates $\alpha = x/R$, $\beta = y/R$ and $\rho = r/r_0$ are introduced.

Following shallow shell theory for cylindrical shells the displacements and stresses can be expressed in terms of one complex function ψ. The real part of this function denotes the non-dimensional radial displacement component

$$\mathrm{Re}\ (\psi) = -\frac{W}{r_0} \qquad (A.6.1)$$

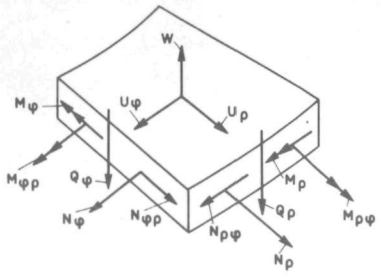

FIGURE A.6.2.

Cylindrical shell element in polar co-ordinates with displacements, stress resultants and stress couples.

The stress couples and the transverse shear forces indicated in figure A.6.2, together with the reduced transverse shear force

$$Q_\rho^* = Q_\rho - \frac{\partial M_{\rho\phi}}{\partial \phi} \tag{A.6.2}$$

are expressed in terms of W by expressions identical to those used in Kirchhoff's flat plate theory (cf. Chapter 2.3.3, equations (2.3.33) and (2.3.34)). The imaginary part of ψ is proportional to Airy's stress function Φ (cf. Chapter 2.3.2) for the direct and shear stress resultants N_ρ, N_ϕ and $N_{\rho\phi} = N_{\phi\rho}$ indicated in figure A.6.2

$$\mathrm{Im}\,(\psi) = \frac{\sqrt{12(1-\nu^2)}}{r_0\, E\, h^2}\,\Phi \tag{A.6.3}$$

The compatibility condition for the middle surface strains and the force equilibrium equation of a shell element in normal direction lead to the basic complex partial differential equation for ψ of fourth order (cf. e.g. GREEN and ZERNA [A.7, p. 418])

$$\Delta\Delta\psi + 4\,i\,\mu^2 \frac{R^2}{r_0^2} \frac{\partial^2 \psi}{\partial \alpha^2} = 0 \tag{A.6.4}$$

where Δ denotes the Laplacian operator

$$\Delta = \frac{\partial^2}{\partial \alpha^2} + \frac{\partial^2}{\partial \beta^2} = \frac{R^2}{r_0^2}\left(\frac{\partial^2}{\partial \rho^2} + \frac{1}{\rho}\frac{\partial}{\partial \rho} + \frac{1}{\rho^2}\frac{\partial^2}{\partial \phi^2}\right) \tag{A.6.5}$$

while the non-dimensional curvature parameter μ is equal to

$$\mu = \frac{\sqrt[4]{12(1-\nu^2)}}{2}\,\frac{r_0}{\sqrt{R\,h}} \tag{A.6.6}$$

It is shown in Chapter 3.2 of [4.11] and in Section 3 of Part II of [4.10] that the complete solutions of the two partial differential equations of second order.

$$(\Delta + 2\, i\, \sqrt{i}\, \mu \frac{R}{r_0} \frac{\partial}{\partial \alpha})\, \psi = 0 \qquad (A.6.7)$$

$$(\Delta - 2\, i\, \sqrt{i}\, \mu \frac{R}{r_0} \frac{\partial}{\partial \alpha})\, \psi = 0 \qquad (A.6.8)$$

together represent the complete solution of the basic equations (A.6.4).

The solutions of the differential equations (A.6.7) and (A.6.8) are written as a series of products of Hankel functions and exponential functions, while the latter functions are expanded as Fourier Bessel series. Within the restriction to functions ψ that are single-valued (in order that the normal displacements are single-valued) and that are bounded at infinity the following expression represents the complete solution of the basic equation

$$\psi = \sum_{n=-\infty}^{\infty} \sum_{k=-\infty}^{\infty} i^k \left[\tilde{A}_n + (-1)^k \tilde{B}_n\right] e^{i(n-k)\phi}\, H_n^{(1)}(\mu\rho\sqrt{i})\, J_k(\mu\rho\sqrt{i}) \qquad (A.6.9)$$

In this solution $\tilde{A}_n$ and $\tilde{B}_n$ are complex integration constants to be determined by the boundary conditions, while $H_n^{(1)}(\mu\rho\sqrt{i})$ and $J_k(\mu\rho\sqrt{i})$ represent the Hankel and Bessel functions with argument $\mu\rho\sqrt{i}$.

Since the region occupied by the middle surface of the spiral shell model is doubly-connected, the restriction to single-valued functions ψ does not necessarily give rise to single-valued in-plane displacements. It is shown in Chapter 3.4 of [4.11] and in Section 4 of Part II of [4.10] that the uniqueness of the axial displacement is ensured automatically by single-valued functions ψ, while the uniqueness of the circumferential displacement is only ensured if the integration constants in the solution (A.6.9) satisfy the condition

$$\mathrm{Im}\left\{(1+i) \sum_{n=-\infty}^{\infty} i^n \left[-\tilde{A}_n + (-1)^n \tilde{B}_n\right]\right\} = 0 \qquad (A.6.10)$$

In addition to the above it is shown in Chapter 3.3 of [4.11] and in Section 5 of Part II of [4.10] that the solution (A.6.9) restricts the analysis to self-equilibrating loads along the hole boundary, except for the resulting moment M of the edge load about the y-axis, which is equal to

$$M = \frac{8\, E\, h^3}{12(1-\nu^2)}\, \mathrm{Re}\left\{\mu\sqrt{i} \sum_{n=-\infty}^{\infty} i^n \left[-\tilde{A}_n + (-1)^n \tilde{B}_n\right]\right\} \qquad (A.6.11)$$

In view of the practical application of the analysis to the pressurized nozzle-to-cylindrical-vessel attachment in Chapter 4 of the present thesis, this limitation is not too serious. In the case of loading by internal pressure the stress distribution and consequently the solution of the basic differential equation will be symmetric with respect to both the generator ($\phi = 0$, $\phi = \pi$) and the parallel circle ($\phi = \pi/2$, $\phi = 3\pi/2$) that pass through the hole centre. It follows immediately from (A.6.9) that this doubly symmetric solution is culled out of the complete solution (A.6.9) by imposing the following condition for the complex integration constants

$$[\tilde{A}_n + (-1)^k \tilde{B}_n] = 0 \qquad \text{for odd values of } (n-k),$$

or (A.6.12)

$$\tilde{A}_n - (-1)^n \tilde{B}_n = 0$$

With this restriction the requirement (A.6.10) ensuring the uniqueness of the displacements is automatically met.
Defining a new complex integration constant

$$\tilde{C}_n = \tilde{A}_n + (-1)^n \tilde{B}_n \tag{A.6.13}$$

we obtain from (A.6.9) and (A.6.12)

$$\psi = \sum_{n=\text{even}} \sum_{k=\text{even}} i^k \tilde{C}_n e^{i(n-k)\phi} H_n J_k +$$

$$+ \sum_{n=\text{odd}} \sum_{k=\text{odd}} i^k \tilde{C}_n e^{i(n-k)\phi} H_n J_k \tag{A.6.14}$$

where we wrote, in view of conciseness

$$H_n \equiv H_n^{(1)} (\mu\rho\sqrt{i}) \text{ and } J_k \equiv J_k (\mu\rho\sqrt{i}) \tag{A.6.15}$$

As the factor n-k is always an even integer in (A.6.14), we can introduce the integer number ℓ, defined by $n-k = 2\ell$, and write ψ as a double summation with respect to n and ℓ. Truncating at $n = 2n_1$ and at $\ell = n_1$ we obtain

$$\psi = \tfrac{1}{4} \sum_{n=0}^{2n_1} \sum_{\ell=0}^{n_1} i^{n+2\ell} (2-\delta_{n0})(2-\delta_{\ell 0}) \times$$

$$\times \left[\{(\cos 2\ell\phi + i \sin 2\ell\phi) J_{n-2\ell} + (\cos 2\ell\phi - i \sin 2\ell\phi) J_{n+2\ell}\} \tilde{C}_n H_n + \right.$$

$$\left. + \{(\cos 2\ell\phi + i \sin 2\ell\phi) J_{n+2\ell} + (\cos 2\ell\phi - i \sin 2\ell\phi) J_{n-2\ell}\} \tilde{C}_{-n} H_{-n}\right] \tag{A.6.16}$$

where the Kronecker's delta is defined as

$$\delta_{kj} = \begin{cases} 0 \text{ if } k \neq j \\ 1 \text{ if } k = j \end{cases} \tag{A.6.17}$$

while the following well-known relation for the Bessel functions has been utilized

$$(-1)^n J_{-n+2\ell} = J_{n-2\ell} \tag{A.6.18}$$

In view of the doubly symmetric character a second restriction upon the complex integration constant follows from (A.6.16) by noticing that the

coefficient of sin $2\ell\phi$ must vanish for all possible values of ρ, i.e.

$$[J_{n-2\ell} + J_{n+2\ell}] \; [\tilde{C}_n H_n - \tilde{C}_{-n} H_{-n}] \equiv 0 \tag{A.6.19}$$

In view of a relation for the Hankel functions similar to (A.6.18) the condition (A.6.19) is identical to

$$\tilde{C}_n = (-1)^n \, \tilde{C}_{-n} \tag{A.6.20}$$

Introducing the real integration constants A_n and B_n as follows

$$A_n + i \, B_n = i^n \, (2-\delta_{n0}) \, \tilde{C}_n \tag{A.6.21}$$

and defining furthermore the function λ_{mnj} of ρ

$$\lambda_{mnj} = i^m \, (1-\tfrac{1}{2} \, \delta_{n0}) \, (J_{n-m} + J_{n+m}) \, H_{n+j} \tag{A.6.22}$$

we arrive at the following solution of the basic equation

$$\psi = \sum_{n=0}^{2n_1} \sum_{\ell=0}^{n_1} (A_n + i \, B_n) \, \lambda_{(2\ell)n0} \cos 2\ell\phi \tag{A.6.23}$$

Substitution from the solution (A.6.23) into the relationships between the stress resultants and stress couples on the one hand and the complex function ψ on the other hand mentioned previously leads to expressions of these dynamic quantities in terms of the integration constants. The normal displacement W and the slope $\frac{\partial W}{\partial r}$ can also be expressed directly into the integration constants by means of (A.6.23). Finally the in-plane displacement components U_ρ and U_ϕ are obtained by integrating the constitutive relations expressed in terms of the displacements and their derivatives.
All expressions of stress and displacement quantities are written as

$$f_p = d_p \sum_{n=0}^{2n_1} \sum_{\ell=0}^{n_1} [\mathrm{Im} \, (h^p_{mn}) \, A_n + \mathrm{Re} \, (h^p_{mn}) \, B_n] \, G^p \, (m\phi) \quad (p = 1, 2, .., 10) \tag{A.6.24}$$

where $m = 2\ell$.
Here d_p is a dimensional factor listed together with the complex functions h^p_{mn} and the trigonometric functions $G^p \, (m\phi)$ in table A.6.1.
In the formal expressions of the functions h^p_{mn} derivatives of the functions λ are denoted by superscripts as follows

$$\lambda^{(p)}_{mnj} = \rho^p \, \frac{d^p \lambda_{mnj}}{d\rho^p} = \frac{\mu\rho \, \sqrt{i}}{2} \, [\lambda^{(p-1)}_{m(n-1)(j+1)} - \lambda^{(p-1)}_{m(n+1)(j-1)} + \tag{A.6.25}$$

$$+ \lambda^{(p-1)}_{mn(j-1)} - \lambda^{(p-1)}_{mn(j+1)}]$$

p	f_p	d_p	h^p_{mn}	G^p
1	N_ρ	$\frac{Eh^2}{\sqrt{12(1-\nu^2)}r_0}$	$\frac{1}{\rho^2}\left[\lambda^{(1)}_{mn0} - m^2\lambda_{mn0}\right]$	cos
2	N_φ	$\frac{Eh^2}{\sqrt{12(1-\nu^2)}r_0}$	$\frac{1}{\rho^2}\left[\lambda^{(2)}_{mn0}\right]$	cos
3	$N_{\rho\varphi}$	$\frac{Eh^2}{\sqrt{12(1-\nu^2)}r_0}$	$\frac{1}{\rho^2}\left[m\left\{\lambda^{(1)}_{mn0} - \lambda_{mn0}\right\}\right]$	sin
4	M_ρ	$\frac{Eh^3}{12(1-\nu^2)r_0}$	$-\frac{i}{\rho^2}\left[\lambda^{(2)}_{mn0} + \nu\lambda^{(1)}_{mn0} - \nu m^2\lambda_{mn0}\right]$	cos
5	M_φ	$\frac{Eh^3}{12(1-\nu^2)r_0}$	$-\frac{i}{\rho^2}\left[\nu\lambda^{(2)}_{mn0} + \lambda^{(1)}_{mn0} - m^2\lambda_{mn0}\right]$	cos
6	Q^*_ρ	$\frac{Eh^3}{12(1-\nu^2)r_0^2}$	$\frac{i}{\rho^3}\left[-\lambda^{(3)}_{mn0} - \lambda^{(2)}_{mn0} + \left\{1+(2-\nu)m^2\right\}\lambda^{(1)}_{mn0} - (3-\nu)m^2\lambda_{mn0}\right]$	cos
7	W	r_0	$-i\lambda_{mn0}$	cos
8	$\frac{\partial W}{\partial r}$	1	$-\frac{i}{\rho}\lambda^{(1)}_{mn0}$	cos
9	U_ρ	$\frac{r_0^2}{R}$	$\frac{\rho}{4(m^2-1)}\left\{\frac{1}{\mu^2\rho^2}\left[\lambda^{(3)}_{mn0} - \left\{1-\nu+(2+\nu)m^2\right\}\lambda^{(1)}_{mn0} + 3m^2\lambda_{mn0}\right] + i\left[(1-\delta_{m0}+\delta_{m2})\left(\lambda^{(1)}_{(m-2)n0} - (2m-1)\lambda_{(m-2)n0}\right) + 2\left(\lambda^{(1)}_{mn0} - \lambda_{mn0}\right) + \lambda^{(1)}_{(m+2)n0} + (2m+1)\lambda_{(m+2)n0}\right]\right\}$	cos
10	U_φ	$\frac{r_0^2}{R}$	$\frac{\rho}{4m}\left\{\frac{1}{\mu^2\rho^2}\left[\lambda^{(2)}_{mn0} - \nu\lambda^{(1)}_{mn0} + \nu m^2\lambda_{mn0}\right] + i\left[(1-\delta_{m0}+\delta_{m2})\cdot\lambda_{(m-2)n0} + 2\lambda_{mn0} + \lambda_{(m+2)n0}\right] - \frac{4}{\rho}h^{(9)}_{mn}\right\}$	sin

TABLE A.6.1.

Dimensional factors and complex functions in the expressions (A.6.24).

where use has been made of a well-known recurrent formula for the derivatives of Bessel functions, while

$$\lambda^{(0)}_{mnj} \equiv \lambda_{mnj} \tag{A.6.26}$$

The displacements and stresses in the cylindrical shell are known as soon as we know the $(4n_1+2)$ integration constants A_n and B_n occurring in (A.6.23) and in all subsequent expressions listed in table A.6.1. The equations by which these constants are determined arise from boundary conditions to be enforced. For the present thesis are of interest the dynamic boundary conditions, where at first glance we would think of prescribing along the hole boundary $\rho = 1$ the value of each separate term in the Fourier's series expansions of N_ρ, $N_{\rho\phi}$, M_ρ and Q^*_ρ. However, in view of the utilization of the analysis summarized in this appendix for the nozzle-to-cylindrical vessel problem it is more convenient to replace the above dynamic boundary quantities by equivalent edge loadings acting in the sense of the cylindrical nozzle co-ordinates (cf. Chapter 4.3.3). Thereby a system of $(4n_1+2)$ linear equations is obtained, determining uniquely the $(4n_1+2)$ integration constants.

REFERENCES

References Chapter 1.

1.1. DIENST VOOR HET STOOMWEZEN (Boiler Inspection Department).
Grondslagen waarop de beoordeling van de constructie en het materiaal van stoomtoestellen, damptoestellen en drukhouders berust (in Dutch).
Staatsuitgeverij, 's-Gravenhage, The Netherlands, 1965.

1.2. AMERICAN SOCIETY OF MECHANICAL ENGINEERS.
Division 1 of Section VIII (Pressure Vessels) of the ASME Boiler and Pressure Vessel Code.
ASME United Engineering Center, New York, 1968.

1.3. AMERICAN SOCIETY OF MECHANICAL ENGINEERS.
Section III (Nuclear Vessels) of the ASME Boiler and Pressure Vessel Code.
ASME United Engineering Center, New York, 1968.

1.4. AMERICAN SOCIETY OF MECHANICAL ENGINEERS.
Criteria of the ASME Boiler and Pressure Vessel Code for design by analysis in Sections III and VIII, Division 2.
ASME United Engineering Center, New York, 1969.

1.5. GAINES, A.L. and PORSE, L.
Problems in the design and construction of large reactor vessels.
Nuclear Structural Engineering, Vol. 1, 1965, pp. 457-466.

1.6. AMERICAN SOCIETY OF MECHANICAL ENGINEERS.
Division 2 of Section VIII (Alternative Rules for Pressure Vessels) of the ASME Boiler and Pressure Vessel Code.
ASME United Engineering Center, New York, 1968.

1.7. BICKELL, M.B. and RUIZ, C.
Pressure vessel design and analysis.
Mac-Millan, London, Melbourne, Toronto & St. Martin's Press, New York, 1967.

1.8. LOVE, A.E.H.
A treatise on the mathematical theory of elasticity.
4th edition, Cambridge University Press (1927), reprinted by Dover Publications Inc., New York, 1944.

1.9. GOL'DENVEIZER, A.L.
The equations of the theory of shells (in Russian).
Prikl. Mat. Mekh., Academia Nauk. U.S.S.R., Vol. 4, No. 2, 1940.

1.10. LUR'E, A.J.
The general theory of thin elastic shells (in Russian).
Prikl. Mat. Mekh., Academia Nauk. U.S.S.R., Vol. 4, No. 2, 1940.

1.11. NOVOZHILOV, V.V.
The theory of thin shells.
P. Noordhoff Ltd., Groningen, The Netherlands (1959), second edition, 1964.

1.12. KOITER, W.T.
On the nonlinear theory of thin elastic shells, Part II Basic shell equations.
Proc. Kon. Ned. Ak. Wet., series B, Vol. 69, No. 1, 1966, pp. 18-32.

1.13. THOMSON, W. and TAIT, P.G.
Treatise on natural philosophy.
Vol. 1, part 2, arts 645-648, Cambridge University Press (1867), second edition, 1883.

1.14. KOITER, W.T.
On the dynamic boundary conditions in the theory of thin shells.
Proc. Kon. Ned. Ak. Wet., series B, Vol. 67, No. 8, 1964, pp. 117-126.

1.15. KOITER, W.T.
A consistent first approximation in the general theory of thin elastic shells.
Proc. IUTAM Symposium on the Theory of Thin Shells, Delft (August 1959).
North-Holland Publishing Cy., Amsterdam, 1960, pp. 12-33.

1.16. KOITER, W.T.
A consistent first approximation in the general theory of thin elastic shells, Part I Foundations and linear theory.
Report of Laboratory of Applied Mechanics, University of Technology, Delft (August 1959).
This report gives a more detailed derivation of the results presented in [1.15].

1.17. JOHN, F.
Estimates for the derivatives of the stresses in a thin shell and interior shell equations.
Comm. Pure and Appl. Math., Vol. 18, 1965, pp. 235-267.

1.18. KOITER, W.T.
On the foundations of the linear theory of thin elastic shells.
Proc. Kon. Ned. Ak. Wet., series B, Vol. 73, No. 12, 1970, pp. 169-195.

1.19. KOITER, W.T.
A systematic simplification of the general equations in the linear theory of thin shells.
Proc. Kon. Ned. Ak. Wet., series B, Vol. 64, 1961, pp. 612-619.

1.20. ARGYRIS, J.H.
Energy theorems and structural analysis, Part I General theory.
Aircraft Engineering, Vol. 26 (1954), Oct. pp. 347-356, Nov. pp. 383-387, 394, Vol. 27 (1955), Feb. pp. 42-58, March pp. 80-94, April pp. 125-134, May pp. 145-158.
ARGYRIS, J.H. and KELSEY, S.
Energy theorems and structural analysis, Part II Applications to thermal stress analysis and to upper and lower limits of st. venant torsion constant.
Aircraft Engineering, Vol. 26 (1954), Dec. pp. 410-422.
Also published Butterworths, London, 1960, third edition 1965.

1.21. TURNER, M.J., CLOUGH, R.W., MARTIN, H.C. and TOPP, L.J.
Stiffness and deflection analysis of complex structures.
J. Aero, Sci., Vol. 23, (1956), No. 9, pp. 805-823.

1.22. CLOUGH, R.W.
The finite element method in structural analysis.
Chapter 7 of Stress Analysis, ed. O.C. Zienkiewicz and G.S. Holister.
John Wiley & Sons, New York, London, Sidney, 1965.

1.23. BESSELING, J.F.
The complete analogy between the matrix equations and the continuous field equations of structural analysis.
Proc. Int. Symp. on Analogue and Digital Techniques applied to Aeronautics.
Liege, 1963, pp. 223.

1.24. MELOSH, R.W.
Basis for the derivation of matrices for the direct stiffness method.
J. Am. Inst. Aero. Astro., Vol. 1, 1963, pp. 1631-1637.

References Chapter 2.

2.1. WILSON, E.L.
Structural analysis of axisymmetric solids.
J. Am. Inst. Aero. Astro, Vol. 3, No. 12, 1965, pp. 2269-2274.

2.2. ARGYRIS, J.H.
The TRIAX 6 element for axisymmetric analysis by the matrix displacement method, Part I Foundations.
The Aeronautical Journal of the Royal Aeronautical Society, Vol. 70, December 1966, pp. 1102-1105.
ARGYRIS, J.H.
The TRIAX 6 element for axisymmetric analysis by the matrix displacement method, Part II
Elastic stiffness and influence of initial strains.
The Aeronautical Journal of the Royal Aeronautical Society, Vol. 70, December 1966, pp. 1105-1106.

2.3. BUCK, K.E.
Zur Berechnung der Verschiebungen und Spannungen in rotationssymmetrischen Körpern unter beliebiger Belastung.
Dr.-Ing. Thesis submitted at the University of Stuttgart, January 1970.

2.4. VAN CAMPEN, D.H.
On the stress distribution in an arbitrarily loaded nozzle-to-flat plate connection.
Nucl. Eng. Design, Vol. 11, 1970, pp. 495-516.

2.5. LIVESLEY, R.K.
Matrix methods of structural analysis.
Pergamon Press, The Mac-Millan Company, 1964.

2.6. TIMOSHENKO, S. and GOODIER, J.N.
Theory of Elasticity.
Second edition, McGraw-Hill, New York, Toronto, London, 1951.

2.7. MICHELL, J.H.
On the direct determination of stress in an elastic solid with applications to the theory of plates.
Proc. London Math. Soc., Vol. 31, 1900, pp. 100-124.

2.8. TIMOSHENKO, S.P., WOINOWSKY-KRIEGER, S.
Theory of plates and shells.
Second edition, McGraw-Hill, New York, Toronto, London, 1959.

2.9. VAN CAMPEN, D.H.
Mechanical and thermal stresses in cylinder-to-cylinder intersections of equal or nearly equal diameters.
Proc. First International Conference on Pressure Vessel Technology, Delft, September 29 - October 2, 1969, Part I Design and Analysis, paper I - 25, pp. 293-307.

References Chapter 3.

3.1. WATERS, E.O., WESSTROM, D.B., ROSSHEIM, D.B. and WILLIAMS, F.S.G.
Formulas for stresses in bolted flanged connections.
Trans. ASME, Fuel and Steam Power, Vol. 59, No. 4, 1937, pp. 161-169.

3.2. LAKE, G.F. and BOYD, G.
Design of Bolted, Flanged Joints of Pressure Vessels.
Proc. Inst. Mech. Engrs., Vol. 171, 1957, pp. 843-858.

3.3. BRITISH STANDARDS INSTITUTION.
B.S. 1500, Part I, 1958.

3.4. SIEBEL, E. and KRÄGELOH, E.
Untersuchungen an Dichtungen für Rohrleitungen.
Konstruktion, No. 7, 1955, pp. 123-137 and pp. 187-196.

3.5. ARBEITSGEMEINSCHAFT DRÜCKBEHÄLTER.
AD-Merkblätter.

3.6. MENKEN, C.M.
Influence of bolt loading on deformation of pressure vessel flanges.
Proc. First International Conference on Pressure Vessel Technology, Delft, September 29 - October 2, 1969, Part I Design and Analysis, paper I - 11, pp. 143-153.

3.7. VISSER, W.
Calculation of flange deformation of Dodewaard reactor vessel by means of finite elements (in Dutch).
Report MORS-Ad-1, Laboratory for Nuclear Engineering, Delft University of Technology, 1968.

3.8. VAN CAMPEN, D.H. and BROEKHOVEN, M.J.G.
Final report concerning stress and strain analysis on models of the Dodewaard reactor pressure vessel (in Dutch), Part I, II and III.
Reports Laboratory for Nuclear Engineering, Delft University of Technology, 1968.

3.9. GECKELER, J.W.
Über die Festigkeit achsensymmetrischer Schalen.
Forschungsarbeiten auf den Gebiete des Ingenieurwesen, Vol. 276, Berlin 1926.

3.10. MURRAY, N.W. and STUART, D.G.
Behaviour of large taper hub flanges.
Proc. Symposium on Pressure Vessel Research towards Better Design, Inst. Mech. Eng., London, 1962, pp. 133-147.

3.11. RODABAUGH, E.C. and ATTERBURY, T.J.
Stresses in tapered transition joints in pipelines and pressure vessels.
Trans. ASME, series B, J. Eng. Indus., Vol. 84, 1962, pp. 321-328.

3.12. HAMADA, K., UKAJI, H. and HAYASHI, T.
Stress analysis of bolted flanges for pressure vessels.
Proc. First International Conference on Pressure Vessel Technology, Delft September 29 - October 2, 1969, Part I Design and Analysis, paper I-42, pp. 513-525.

3.13. VAN CAMPEN, D.H., DEEN, P.J. and LATZKO, D.G.H.
Deformation of large-diameter, high-pressure vessel flanges.
Proc. First International Conference on Pressure Vessel Technology, Delft, September 29 - October 2, 1969, Part I Design and Analysis, paper I-43, pp. 529-549.

3.14. VAN CAMPEN, D.H.
A systematic bolt-tightening procedure for reactor vessel flanges.
Proc. First International Conference on Pressure Vessel Technology, Delft, September 29 - October 2, 1969, Part I Design and Analysis, paper I-10, pp. 131-141.

3.15. VAN CAMPEN, D.H.
Author's closure to the paper "A systematic bolt-tightening procedure for reactor vessel flanges".
Proc. First International Conference on Pressure Vessel Technology, Delft, September 29- October 2, 1969, Part III Discussion, paper I-10, pp. 67-69.

3.16. HAMADA, K., HAYASHI, T. and OGUCHI, I.
Stress analysis of tapered transition joints in reactor pressure vessel.
Report ORNL-tr-1769, 1966, distributed by Clearinghouse, U.S. Department of Commerce.

3.17. FLÜGGE, W.
Stresses in shells.
Springer-Verlag, Berlin/Göttingen/Heidelberg, second edition, 1962.

3.18. BIEZENO, C.B. and GRAMMEL, R.
Technische Dynamik.
Springer-Verlag, Berlin/Göttingen/Heidelberg, second edition, 1939.

3.19. BICKELL, M.B. and DANCE, S.H.
An elastic analysis of axially perforated cylinders with applications to the design of reactor vessel flanges.
Proc. First International Conference on Structural Mechanics in Reactor Technology, Berlin, Germany, 20-24 September 1971, paper G 3/2 (to be published).

References Chapter 4.

4.1. RODABAUGH, E.C., ATTERBURY, T.J., CLOUD, R.L., and WITT, F.J.
Evaluation of experimental and theoretical data on radial nozzles in pressure vessels.
USAEC-report TID-24342, March 1966 - December 1967.

4.2. BERMAN, I. and PAI, D.H.
An experimental investigation of stresses in an HY-80 marine boiler drum.
The Welding Journal, No. 41, July 1962, Research Supplement, pp. 307S-321S.

4.3. KONO, K., IKI, T., NAKAMURA, H., TSUJITA, S. and SHIMAGUCHI, S.
Three-dimensional photoelastic investigation of stresses in nuclear reactor pressure vessels.
Mitsubishi Heavy Industries Technical Review, September 1966, pp. 173-184.

4.4. IWASAKI, T. and OUCHIDA, H.
Three-dimensional photoelastic study of stress around nozzles in pressure vessels (in Japanese).
Hitachi Hyoron, Special issue, November 1964, pp. 102-106.

4.5. VINING, R.E.
Model test for stresses and deflections in the N.S. Savannah reactor vessel model and attachments.
USAEC-report NYO 2856, 1961.

4.6. KAUFMAN, W.J., SMEITINK, G., ARAV, F. and BANNINK, G.H.
Vormgeving van stompen in stoomdrums in verband met de sterkte, de lastechnische fabrikage en het niet-destructief onderzoek (in Dutch).
VMF-mededelingen No. 24, December 1964, pp. 175-192.

4.7. LEVEN, M.M.
Photoelastic determination of the stress in reinforced openings in pressure vessels.
Welding Research Council Bulletin No. 113, 1966.

4.8. VAN CAMPEN, D.H. and LATZKO, D.G.H.
Stress concentrations at nozzle penetrations in high-pressure vessels.
Proc. Fourth International Conference on Experimental Stress Analysis.
Cambridge, England, 6th-10th April 1970, paper 31, pp. 348-362.

4.9. LIND, N.C.
Approximate stress-concentration analysis for pressurized branch pipe connections.
ASME publication 67-WA/PVP-7.

4.10. LEKKERKERKER, J.G.
The determination of elastic stresses near cylinder to cylinder intersections.
Paper G 2/1 presented at First International Conference on Structural Mechanics in Reactor Technology, Berlin, Germany, 20-24 September 1971, published in special conference issue of Nucl. Eng. Design, Vol. 20, No. 1, March 1972.

4.11. LEKKERKERKER, J.G.
On the stress distribution in cylindrical shells weakened by a circular hole.
Thesis Delft University of Technology, February 1965.

4.12. CLOUGH, R.W. and JOHNSON, C.P.
Finite element analysis of arbitrary thin shells.
Proc. ACI Symposium on Concrete Thin Shells, New York, April 1971.

4.13. ARGYRIS, J.H.
The LUMINA element for the matrix displacement method.
The Aeronautical Journal of the Royal Aeronautical Society, Vol. 72, June 1968, pp. 515-517.

4.14. ARGYRIS, J.H. and BUCK, K.E.
Modern developments in the stress analysis of pressure vessels.
Proc. First International Conference on Pressure Vessel Technology, Delft, September 29 - October 2, 1969, Part III Discussion, General Congress Lecture, pp. 33-49.

4.15. HELLEN, T.K. and MONEY, H.A.
The application of three-dimensional finite elements to a cylinder-cylinder intersection.
Int. Journal for Numerical Methods in Eng., Vol. 2, No. 3, 1970, pp. 415-418.

4.16. RASHID, Y.R. and GILMAN, J.D.
Three-dimensional analysis of reactor pressure vessel nozzles.
Proc. First International Conference on Structural Mechanics in Reactor Technology, Berlin, Germany, 20-24 September 1971, paper G 2/6 (to be published).

4.17. KRISHNAMURTHY, N.
Three-dimensional finite element analysis of thick-walled pipe-nozzle junctions with curved transitions.
Proc. First International Conference on Structural Mechanics in Reactor Technology, Berlin, Germany, 20-24 September 1971, paper G 2/7, (to be published).

4.18. SAWIN, G.N.
Spanningserhöhung am Rande von Löchern.
VEB-Verlage Technik, Berlin, 1956 (Translation of Russian edition).

4.19. LEKKERKERKER, J.G.
The analytical foundations of a computer program treating general boundary conditions along the edge of a circular hole in a cylindrical shell.
Report WTHD No. 20, Department of Mechanical Eng., Delft University of Technology, March 1970.

4.20. DOUMA, T. and LEKKERKERKER, J.G.
A computer program in ALGOL-60 treating dynamic boundary conditions along the boundary of a circular hole in a tube.
Report No. 427, Laboratory of Engineering Mechanics, Delft University of Technology, February 1970.

4.21. HARTEVELT, M.
Strain measurements on simulated nozzles (in Dutch).
Report DV-26, Laboratory for Nuclear Engineering, Delft University of Technology, October 1970.

4.22. HARTEVELT, M.
Strain measurements on the MORS nozzles by means of micro gauges (in Dutch).
Report DV-34, Laboratory for Nuclear Engineering, Delft University of Technology, October 1971.

4.23. KROON, J.P., SWART, W. and VAN WEELDEREN, A.B.
Measurements on simulated nozzles (in Dutch).
Report KR-162, Laboratory for Nuclear Engineering, Delft University of Technology, 1969.

References Appendices.

A.1. ALMERING, J.H.J.
Over de berekening van momenten van een willekeurige orde voor een veelhoek (in Dutch).
Heron, Vol. 15, No. 1, 1967, pp. 15-20.

A.2. MEIJERS, P.
Stresses in a centrifugal impellar with cover disk.
Report TNO-IWECO, Delft, December 1968.

A.3. KOITER, W.T.
Summary of equations for modified, simplest possible accurate linear theory of thin circular cylindrical shells.
Communication of the Laboratory of Applied Mechanics, University of Technology, Delft, 1968, to be published.

A.4. MORLEY, L.S.D.
An improvement on Donnell's approximation for thin-walled circular cylinders.
Quart. Journ. Appl. Math., Vol. 12, 1959, p. 89.

A.5. DONNELL, L.H.
A new theory for the buckling of thin cylinders under axial compression and bending.
Trans. Am. Soc. Mech. Engrs., Vol. 56, 1934, p. 795.

A.6. SIMMONDS, J.G.
A set of simple, accurate equations for circular cylindrical elastic shells.
Intern. Journ. Solids Structures, Vol. 2, 1966, pp. 525-541.

A.7. GREEN, A.E. and ZERNA, W.
Theoretical Elasticity.
Oxford at the Clarendon Press, second edition, 1968.

ACKNOWLEDGEMENTS

The work reported in this thesis was carried out in the Laboratory for Nuclear Engineering of the Delft University of Technology.

The author feels indebted to The Rotterdam Dockyard Company for their assistance in fabricating the model vessel nozzles and the flat plate nozzles.

The author is very grateful to Mr. M. Hartevelt, who was responsible for the experimental investigations and developed the measuring technique by means of micro gauges.
The author also wishes to thank Mr. M.J.G. Broekhoven for the many discussions and valuable suggestions in the course of the experimental work and Messrs R.A. Gerbrands, M.J. Hopma and H. v.d. Zwet for their active participation in the experimental investigations.

The author is much indebted to Mr. H.A.C.M. Spaas for his valuable contribution to the numerical analysis of the nozzle-to-cylindrical vessel connection.
Thanks also go to the students, who participated actively in several aspects of the work in the course of their studies.

The author is grateful to the staff of the computer centre of the Delft University of Technology for their assistance during carrying out the calculations.

Special thanks are due to Mr. W.H. van Velzen for his artistic contribution to the drawings and graphs and to Miss A.M. Aarssen and Miss M. Vrijenhoek for their typing of the manuscript and their contribution to the lay-out.

SAMENVATTING

Het primaire doel van deze dissertatie vormt het leveren van een bijdrage tot de elastische analyse van twee belangrijke drukvatcomponenten, te weten de flensverbinding en de radiaal op een cilindrisch vat geplaatste stomp. Ter realisering van deze doelstelling wordt in hoofdstuk 2 een tweevoudige bijdrage geleverd tot de vervormings- en spanningsanalyse middels de op energiecriteria gebaseerde eindige elementenmethode. Allereerst wordt een driehoekig ringelement ontwikkeld met zes knooppunten ter analysering van omwentelingslichamen onder niet axiaal-symmetrische belastingen (hoofdstuk 2.2). Tevens wordt het begrip ana-element op systematische wijze geïntroduceerd (hoofdstuk 2.3). Met behulp hiervan is het mogelijk constructiedelen, waarvan de elasticiteits-vergelijkingen een bekende analytische oplossing bezitten, in de eindige elementenformulering te integreren. Het begrip ana-element wordt nader uitgewerkt voor een aantal plaat- en schaalelementen welke van belang zijn bij de vervormings- en spanningsanalyse van drukvaten.

Voor wat betreft de analyse van flensverbindingen heeft de in hoofdstuk 3 gepresenteerde bijdrage betrekking op voor vaten met grote diameters (tot ca. 6,5 m) en hoge drukken (tot ca. 155 bar) gebruikelijke constructies. Allereerst wordt de ontwikkeling beschreven van een systematische semi-empirische procedure voor het vastzetten van de bouten van een dergelijke flensconstructie, indien het aanhalen groepsgewijs plaatsvindt (hoofdstuk 3.2). Deze procedure beoogt een zo gelijkmatig mogelijke verdeling van de boutbelasting over alle bouten te verkrijgen na het vastzetten in één rondgang.
Vervolgens wordt een vergelijking gegeven tussen twee alternatieve berekeningsmethoden voor het gedrag van het conische overgangsgedeelte (hals) tussen flensring en drukvat, waarbij de hals achtereenvolgens wordt opgevat als een dunwandige cilinderschaal met verlopende wanddikte en als een ring met onvervormbare diametraaldoorsnede (kantelring), terwijl een analyse volgens de eindige elementenmethode als vergelijkingsbasis wordt gebruikt (hoofdstuk 3.3.1). Voor relatief grote waarden van de hoek tussen binnen- en buitenoppervlak wordt een verbeterde versie gepresenteerd van de in de literatuur voorkomende op de schaaltheorie gebaseerde berekeningsmethoden, terwijl bovendien de invloedsgetallen, resulterend uit de analyse volgens de eindige elementenmethode, in grafische vorm worden weergegeven.
Tenslotte wordt enige experimentele informatie verstrekt welke betrekking heeft op de lokatie van het aangrijpingspunt van de pakkingvlakbelasting (hoofdstuk 3.3.2.1), terwijl gebruik makend van deze informatie, voor een concreet geval een vergelijking wordt gemaakt tussen berekende en gemeten flensringrotaties (hoofdstuk 3.3.2.2).

Voor wat betreft de analyse van drukvatstompen wordt in hoofdstuk 4 allereerst een behandeling gegeven van de vervormings- en spanningsanalyse van de loodrecht op een biaxiaal belaste vlakke plaat geplaatste stomp (biaxialiteit 1:2) welke een eerste benadering beoogt te zijn van de radiaal op een dunwandig cirkelcilindrisch vat geplaatste stomp voor voldoend kleine verhoudingen van stompdiameter (d) en vatdiameter (D): $d/D \lesssim \frac{1}{4}$ (hoofdstuk 4.2). De gepresenteerde berekeningsmethode is in beginsel gebaseerd op de eindige elementenmethode voor omwentelingslichamen onder niet axiaal-symmetrische belasting, waarbij het cilindrisch pijpdeel en de vlakke plaat worden opgevat als ana-elementen. In vervolg hierop wordt een verfijning van deze berekeningsmethode ontwikkeld voor de op een cilindrisch vat geplaatste stomp, waarbij de stomp zelf weer als geometrisch rotatie-symmetrisch wordt opgevat, terwijl het vat wordt beschouwd als zijnde een dunwandige flauwgekromde cirkelcilindrische schaal met een cirkelvormig gat (hoofdstuk 4.3). Tenslotte wordt de betrouwbaarheid van de beide bovengenoemde berekeningsmethoden getest aan de hand van metingen met zogenaamde micro-rekstrookjes,

waarvan de filamentlengte ongeveer $\frac{1}{2}$ mm bedraagt, terwijl tevens de beide berekeningsmethoden met elkaar worden vergeleken (hoofdstuk 4.4).

S T E L L I N G E N

1

De door NOVOZHILOV afgeleide oplossing voor het randstoringsprobleem zoals dat optreedt bij bolvormige schalen is onvolledig in dié zin dat de cotangens van de poolhoek welke de schaalrand vastlegt niet voorkomt in het merendeel der uitdrukkingen voor de spanningsresulanten benevens in elk der uitdrukkingen voor de spanningskoppels.

NOVOZHILOV, V.V., The theory of thin shells, Second edition, P. Noordhoff Ltd, Groningen, 1964.
Zie ook:
VAN CAMPEN, D.H., Bolvormige tanks, spanningsverdeling en ondersteuningsconstructie, Rapport No. 304, Laboratorium voor Technische Mechanica der T.H. Delft, december 1965.

2

Ofschoon de door VISSER in hoofdstuk 6.1.3 van diens proefschrift afgeleide energie-uitdrukking (6.14) voor de half oneindig lange cilinderschaal volledig correct wordt gebruikt ten behoeve van de analyse van een flensconstructie, dient ze met grote voorzichtigheid te worden gehanteerd bij de meer algemene incorporatie van deze cilinderschaal als ana-element in de eindige elementenmethode. De bedoeling energie-uitdrukking stelt namelijk niet, zoals door VISSER beweerd wordt, de in de schaal opgehoopte inwendige energie voor, noch representeert ze in het algemeen de bijdrage van de cilinderschaal tot de in de gehele constructie, waarvan deze schaal deel uitmaakt, opgehoopte potentiële energie.

VISSER, W., The finite element method in deformation and heat conduction problems, proefschrift T.H. Delft, maart 1968.

3

De door MURRAY en STUART voorgestelde berekeningsmethode voor het vervormingsgedrag van het konische overgangsgedeelte tussen flensring en drukvat bij vaten met grote diameters onder hoge drukken geeft te lage waarden voor de relevante vervorming van de flensring onder ontwerpcondities.

MURRAY, N.W. and STUART, D.G., Behaviour of large taper hub flanges, Proc. Symposium on Pressure Vessel Research towards Better Design, Inst. Mech. Eng., London, 1962, pp. 133-147.

4

Met behulp van de berekeningsmethode van DUDLEY kan op snelle wijze een eerste indruk verkregen worden van het vervormings- en spanningsbeeld van een flensverbinding onder invloed van thermische belasting, waarbij echter rekening moet worden gehouden met fouten tot ca. 60%. Vanwege de schematisering van bouten en pakking vanaf de aangehaalde toestand tot lineaire veren moet deze methode echter voor de in de reactordrukvattechniek voorkomende relatief smalle en hoge flenzen als niet aanbevelenswaardig bestempeld worden.

DUDLEY, W.M., Deflection of heat exchanger flanged joints as affected by barreling and warping, Trans. ASME, Series B, Vol. 83, No. 4, November 1961.
Zie ook:
VAN CAMPEN, D.H., Classificatie van berekeningsmethoden voor flensverbindingen onder statische omstandigheden, Rapport WTHD No.9, Afdeling der Werktuigbouwkunde der T.H. Delft, November 1968.

5

In de door LIND afgeleide benaderingsformule ter bepaling van de maximale spanningsconcentratiefactor in een aan inwendige druk onderhevig T-stuk impliceert de eis $n^2 \sqrt{h^2/(12R^2)} \ll 1$ (waarin n = laatst meegenomen term in Fourierontwikkeling, h/R = grootste wanddikte-straal verhouding) een te grote restrictie in een belangrijk aantal praktisch interessante gevallen.

LIND, N.C., An elastic-shell analysis of the stress concentration of a pressurized tee branch-pipe connection, Proc. First International Conference on Pressure Vessel Technology, Delft, September 29 - October 2, 1969, Part I Design and Analysis, paper I - 23, pp. 269-275.
Zie ook:
VAN CAMPEN, D.H., Discussion to paper I - 23, Proc. First International Conference on Pressure Vessel Technology, Delft, September 29 - October 2, 1969, Part III Discussion, pp. 89-90.

6

Een door ontwerpingenieurs veelvuldig gebruikte berekeningsmethode ter bepaling van de spanningsverdeling in de radiaal op een cilindrisch drukvat geplaatste stomp, welke stoelt op de vervanging van het cilindrisch drukvat door een bolvormig vat waarvan de straal van het middenvak gelijk is aan $1\frac{1}{2}$ maal die van de cilinder, kan aanleiding geven tot een onderschatting van de maximaal optredende spanning met 40%.

7

De versnippering van activiteiten in Nederland op het gebied van sterkteproblemen welke optreden bij componenten van nucleaire reaktorinstallaties werkt verlagend op het kennisniveau en impliceert een inefficiente besteding van industriële investeringen en van overheidsgelden.

8

De ontwikkeling van de ISO-code voor nucleaire vaten geschiedt te weinig vanuit het bewustzijn der enorme en systematische door de Verenigde Staten van Amerika in de ontwikkeling van de overeenkomstige ASME-code geïnvesteerde arbeid. Derhalve is de eerstgenoemde code gedoemd inferieur te blijven ten opzichte van de ASME-code voor nucleaire vaten tenzij de activiteiten in ISO-verband meer gericht worden op het leveren van een kritische bijdrage tot en een voortgezette ontwikkeling van de ASME-code.

9

Het verdient aanbeveling in het onderwijsprogramma voor het eerste studiejaar van de afdelingen der Technische Hogeschool Delft een college informatica op te nemen.

10

Het verdient aanbeveling bij de opleiding voor werktuigkundig ingenieur aan de Technische Hogeschool Delft de mogelijkheid te heropenen tot keuze tussen de vijf- en zesjarige opleiding na het met goed gevolg afleggen van het propaedeutisch examen.

11

Veel zogenaamde handboeken op het gebied der toegepaste wetenschappen zijn samengesteld door auteurs die hetzij lijden aan overschatting van eigen capaciteiten, dan wel uit zijn op goedkope wijze opbouwen van een reputatie. Lezing van dergelijke boeken door praktisch georiënteerde outsiders die op snelle wijze een inzicht in een bepaald vakgebied willen verkrijgen kan op zijn gunstigst aanleiding geven tot onnodig veel tijdsverlies en op zijn ongunstigst een verkeerd beeld van het betreffende vakgebied opwekken.

Het verdient aanbeveling in Nederland de investeringen op medisch terrein te bevorderen ten koste van die in het natuurkundige fundamenteel onderzoek der materie.